Morphology control of zinc oxide nanostructures for application in hybrid solar cells

Dissertation

von

Kun Wang

TECHNISCHE UNIVERSITÄT MÜNCHEN

PHYSIK-DEPARTMENT

TECHNISCHE UNIVERSITÄT MÜNCHEN

Physik-Department

Lehrstuhl für Funktionelle Materialien

Morphology control of zinc oxide nanostructures for application in hybrid solar cells

Kun Wang

Vollständiger Abdruck der von der Fakultät für Physik der Technischen Universität München zur Erlangung des akademischen Grades eines

Doktors der Naturwissenschaften (Dr. rer. nat.)

genehmigten Dissertation.

Vorsitzende:	Prof. Dr. Martin Zacharias
Prüfer der Dissertation:	1. Prof. Dr. Peter Müller-Buschbaum
	2. Prof. Dr. Reinhard Kienberger

Die Dissertation wurde am 23.11.2018 bei der Technischen Universität München eingereicht und durch die Fakultät für Physik am 07.01.2019 angenommen.

Abstract

In this thesis mesoporous zinc oxide (ZnO) films are prepared for being applied in solid-state dye-sensitized solar cells. Furthermore, ZnO/poly(3-hexylthiophene-2,5-diyl) (ZnO/P3HT) hybrid films are investigated for hybrid bulk heterojunction solar cells. The main focus is set to tailor the morphology of the mesoporous ZnO films and the ZnO/P3HT hybrid films to improve the corresponding photovoltaic performance. To achieve this, sol-gel synthesis is used in combination with a diblock copolymer assisted template to tune the morphology of the ZnO and ZnO/P3HT films. Various interconnected network morphologies including foam-, worm-, sphere- and sponge-like structures are obtained, which are favorable to increase the interface area between the n-type and p-type semiconductors. Moreover, characteristic parameters are investigated during synthesis, such as the composite ratio of the materials, the deposition method and the annealing temperature, to tune the morphology of the films. The ZnO based hybrid solar cells show an increased photovoltaic performance accordingly. A cost-effective low-temperature technique is employed to fabricate the mesoporous ZnO films and the ZnO/P3HT heterojunction. Furthermore, the ZnO film morphologies obtained with low-temperature UV-irradiation and high-temperature sintering as well as the corresponding photovoltaic performance are compared and discussed accordingly. It is demonstrated that the morphology of the ZnO and the ZnO/P3HT films significantly plays an indispensable role in improving the photovoltaic performance.

Zusammenfassung

In dieser Arbeit werden mesoporöse Zinkoxid (ZnO)-Filme für die Anwendung in hybriden Festkörper-Farbstoffsolarzellen hergestellt. Außerdem werden Gemische aus ZnO und poly(3-hexylthiophen-2,5-diyl) (P3HT) im Hinblick auf die Anwendung in sogenannten hybriden "Bulk-Heterojunction"-Solarzellen untersucht. Das Hauptaugenmerk liegt auf der Variation der Sturktur in mesoporösen ZnO- und ZnO/P3HT-Hybridschichten zur Verbesserung der entsprechenden photovoltaischen Eigenschaffen. Es werden verschiedene Netzwerkstrukturen (beispielsweise schaum-, wurm- und schwammartig) hergestellt, welche durch ihre große Oberfläche die Grenzfläche zwischen n-Typ- und p-Typ-Halbleiter vergrößern können. Außerdem werden charakteristische Parameter, die für die Synthese relevant sind, untersucht. Zu diesen gehören beispielsweise das Verhältnis der Materialien, die gewählte Methode der Filmfabrikation und die Temperatur, welche die Morphologie des Films maßgeblich beeinflussen. Dementsprechend zeigen ZnO-basierte Hybridsolarzellen eine verbesserte photovoltaische Leistung. Eine Niedrigtemperaturroute wird als kosteneffektive Methode benutzt, um ZnO- und ZnO/P3HT-Hybridfilme herzustellen. Die über UV-Bestrahlung bei niedrigen Temperatur und Sintern bei hohen Temperaturen erhaltenen ZnO-Morphologien, wie auch die entsprechende photovoltaische Leistung der Filme zeigen, dass die Morphologie in ZnO- und ZnO/P3HT-Hybridfilmen eine maßgebliche Rolle in der Verbesserung der photovoltaischen Eigenschaften spielt.

Contents

List of abbreviations

AFM: atomic force microscopy

DOS: density of states

DSSC: dye-sensitized solar cell

DWBA: distorted wave Born approximation

FF: fill factor

FTO: fluorine doped tin oxide

FWHM: full width at half maximum

GISAXS: grazing-incidence small-angle X-ray scattering

GIWAXS: grazing-incidence wide-angle X-ray scattering

HBSC: hybrid bulk heterojunction solar cell

I-V: current-voltage characteristics

J_{sc}: short circuit current

LMA: local monodisperse approximation

M_n: number average molecular weight

M_w: weight average molecular weight

PCE: power conversion efficiency

PS-*b*-PEO: polystyrene-block-poly(ethylene oxide)

PS-*b*-P4VP: polystyrene-block-poly(4-vinylpyridine)

P3HT: poly(3-hexylthiophene-2,5-diyl)

P3HT-*b*-PEO: poly(3-hexylthiophene-2,5-diyl)-*block*-poly(ethylene oxide)

SDD: sample detector distance

SEM: scanning electron microscopy

SLD: scattering length density

spiro-OMeTAD: 2,2',7,7'-tetrakis(N,N di-p-methoxyphenyl-amine)9,9'-spiro-bifluorene

ssDSSC: solid-state dye-sensitized solar cell

TOF-GISANS: time-of-flight grazing-incidence small-angle neutron scattering

V_{oc}: open circuit voltage

XRD: X-ray diffraction

1DDL: One-dimensional paracrystalline lattice

1. Introduction

With the development of a modern society, the global energy consumption has been increasing dramatically. Fossil fuels which can provide us the required energy for economical and industrial usage are becoming less and less, while on the contrary, the environmental pollution caused by the overexploitation of fossil fuels increases year by year. To solve these problems, it is required to use new approaches. Solar energy, which can be converted to electricity or chemical energy, is a kind of clean and sustainable energy and has gained great attention in recent years. Among the different technologies, solar cells, which can directly convert light into electricity via the photovoltaic effect, show great potential in the development of our society.

Since the first observation of the photovoltaic effect by Alexandre-Edmond Becquerel in 1839, an enormous amount of research activities to convert sunlight into electricity has been developed.[1] The first generation solar cells were produced based on silicon wafers. It is the most established technology and very popular due to regular high power conversion efficiencies. However, due to the poor absorption of light, a thick Si film on the order of hundreds of micrometers is required to absorb the light sufficiently, which leads to memorial inflexibility and high production costs.[2] In contrast, second generation solar cells, which are based on good absorbers such as amorphous silicon (a-Si), cadmium telluride (CdTe) and copper indium (gallium) diselenide (CIS or CIGS), can be made as thin film solar cells, generally in the order of 1 μm thickness. However, the rare elements used in these materials and the mechanical inflexibility limit the wide spread usage of this kind of solar cells.

To increase the efficiency with low costs, third generation solar cells were developed. Conducting polymers are used in this kind of solar cells since the discovery of conducting polymers in 1977.[3] With the advantages of organic materials, such as a good mechanical flexibility and low weight, it is possible to make flexible solar cells with potential application in many fields, e.g. in building-integration. However, due to the instability of organic materials, hybrid solar cells have gained in interest. A combination of organic and inorganic semiconductors offers outstanding potential due to their minor investment as compared to inorganic solar cells and higher chemical stability as compared to organic solar cells. In the present thesis, solid-state dye-sensitized solar cells (ssDSSCs) and hybrid bulk heterojunction solar cells (HBSCs) are investigated, both, with organic materials to transport the positive charge carriers and inorganic materials to transport the negative charge carriers.

Since the pioneering work about DSSCs introduced by O'Regan and Grätzel in 1991,[4] extensive researches ranging from liquid electrolyte DSSCs to solid-state DSSCs, have been stimulated. More than 13% of efficiency can be achieved.[5] HBSCs, which use p-type organic semiconductors instead of the dye molecules to absorb light, are a simplification of ssDSSCs. For both types of solar cells, inorganic materials such as titanium dioxide (TiO_2), zinc oxide (ZnO), silicon (Si) and germanium (Ge) are necessary to transport the charge carriers. The interface between these inorganic materials and the organic semiconductors is of great significance as excitons are generated in the organic materials (dye molecules in ssDSSCs and p-type organic semiconductors in HBSCs) and can only be separated at the interface of donor and acceptor. Moreover, after the exciton dissociation, the charge carriers will be transported to their corresponding electrodes along the inorganic and organic materials and finally be extracted. Due to the fabrication technique, the interface is formed by backfilling of the organic materials into the pre-fabricated inorganic materials. Thus, the structure of the inorganic materials plays an important role in the performance of the final devices. To improve the photovoltaic performance, an interconnected mesoporous inorganic nanostructure is favorable, which can provide a high surface-to-volume ratio for exciton separation within their lifetime and a good pathway for charge carrier transport. To fabricate the mesoporous inorganic semiconductors, various methods can be employed, such as chemical vapor deposition, wet chemical method, hydrothermal synthesis, *etc*.[6-9] Among these methods, sol-gel synthesis, as a solution-processed self-organization technique, shows great potential in large-scale production. To tune the morphology of the inorganic materials for application in solar cells, a diblock copolymer is used as a template in combination with an inorganic precursor for the sol-gel synthesis. Applying a diblock copolymer, more ordered mesoporous structures can be obtained and a diblock copolymer can be used as a compatibilizer to modify the interfaces between the n-type inorganic and the p-type organic semiconductors.[10-14]

So far, great efforts have been made for the development of hybrid solar cells using high-temperature fabricated inorganic semiconductors. In general, a calcination step with temperatures in the range of 350-500 °C is needed.[15-18] Such high-temperature routes exclude the application in flexible solar cells on polymer substrates due to their heat-sensitivity. Moreover, the high energy input during fabrication is also a drawback for real world applications of solar cells. Instead, low-temperature fabricated solar cells have the advantages of significantly lower production costs, short payback time and low environmental impact. They can be an alternative for the successfully emerging organic solar cells. In the present thesis, ZnO, an inorganic semiconductor, is able to be used as electron transport material in hybrid solar cells due to the better electron mobility and the lower crystallization temperature

as compared to TiO_2.[19-23] All processing temperatures used to prepare the ZnO films are well below 240 °C. Due to the important role of annealing temperature, the ZnO films and ZnO/P3HT hybrid films are prepared at different temperatures to compare the resulting structures. Moreover, the structures obtained from both high- and low-temperature processing are compared as well to investigate the influence of the post-treatment method on the morphology of the ZnO films.

The main focus is set on improving the photovoltaic performance via tailoring the morphology of the ZnO films and the corresponding active layers. The morphology of the films is modified by tuning the parameters for synthesis, such as the ratio of the inorganic and organic materials, the annealing temperature, the film deposition technique and the post-treatment method. Accordingly, the correlation between the film morphology and the photovoltaic performance is investigated to gain a deep understanding of the photovoltaic effect. First, the theoretical background is introduced in chapter 2. The theory about polymer physics covers mainly diblock copolymers and conducting polymers, which are used in the present work. Moreover, the structure and synthesis of ZnO and ZnO-based ssDSSCs and HBSCs are described as well. The scattering theory which is necessary to understand the applied scattering methods is also introduced in chapter 2. Chapter 3 describes the used characterization methods, including the basic working principle and the parameters for measuring samples. In chapter 4, the experimental part is covered, where the sample preparation process is introduced in detail. Then the research results are discussed from chapter 5 to chapter 8. In Figure 1.1 an overview of the related four projects is schematically depicted.

As mentioned before, the morphology of the ZnO films are of great importance for application in solar cells as the excitons can only dissociate at the interface between the n-type and p-type semiconductors and the charge carrier transport can only occur along the interconnected pathways. For ssDSSCs, both dye molecules and the p-type organic semiconductors are backfilled into the mesoporous ZnO films. Therefore, the morphology of ZnO films should be optimized. Since in most research work ZnO films are prepared at high temperature which is energy- and time-consuming and inapplicable to the polymer substrates to fabricate flexible solar cells as well, a low-temperature route is aimed to fabricate the ZnO films in the first project. Based on a method using sol–gel chemistry combined with PS-*b*-PEO as a template, in chapter 5 I mainly aim at tailoring the morphologies of the ZnO films and improving the corresponding photovoltaic performance for ssDSSCs.

To realize an efficient backfilling of dye molecules and p-type organic semiconductors for application in ssDSSCs, the pore size plays a significant, indispensable role in improving the solar cell efficiency. On one hand, increased pore sizes have the tendency to enhance the

backfilling capability. On the other hand, large pores reversely reduce the surface-area-to-volume-ratio, which is unfavorable for exciton separation at ZnO and dye molecule interface. The second project covers nanoporous ZnO films that are prepared using sol-gel synthesis in combination with PS-*b*-P4VP as a template. In chapter 6, the ZnO pore sizes prepared from two different template removal techniques, one with low-temperature UV irradiation and the other one with high-temperature sintering, are compared. Moreover, the influence of the template-to-ZnO precursor ratio on the pore size is investigated. Accordingly, the correlation between the pore sizes of sol-gel synthesized ZnO films and photovoltaic performance of fabricated ssDSSCs is discussed as well.

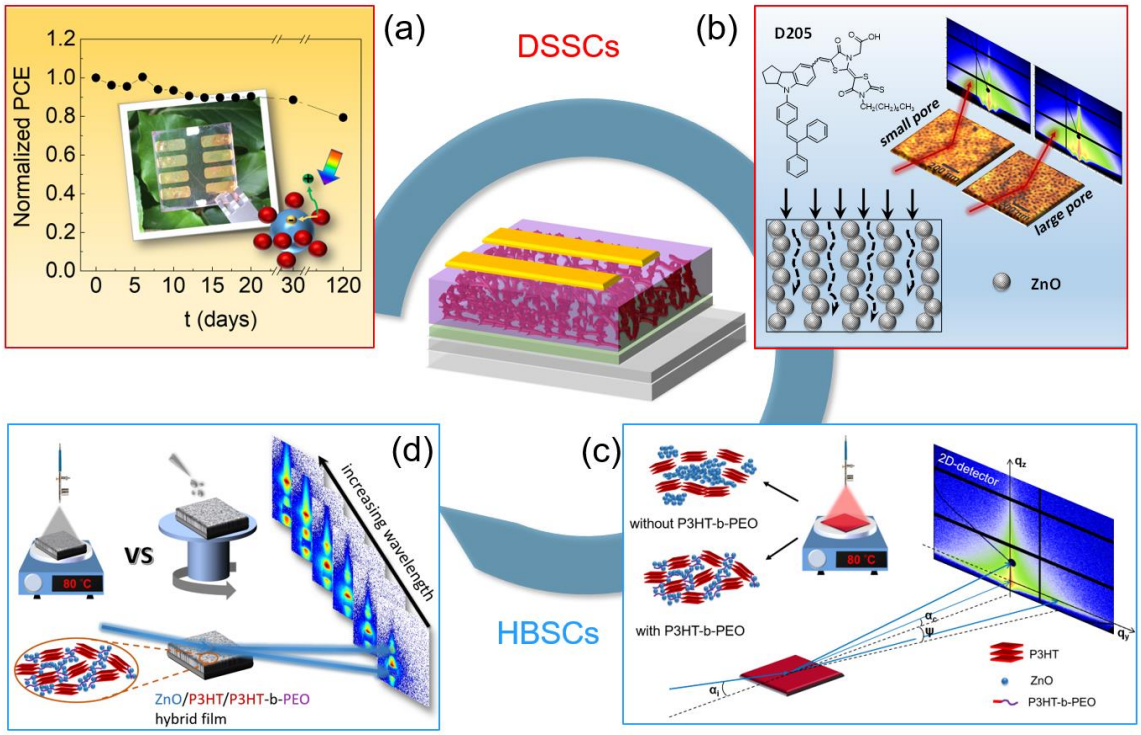

Figure1.1 A schematic illustration of a ZnO-based thin film solar cell (in the center) along with the different research projects included in the present thesis. The topics from (a) to (d) are presented in chapter 5 to chapter 8, respectively.

For HBSCs, hybrid films of ZnO/P3HT show promising characteristics. Most researchers prepare this bulk heterojunction via two steps, namely first prepare ZnO films and then backfill P3HT into the mesoporous ZnO films. This technique results in a poor interface due to the limited backfilling of P3HT, thus, reducing the probability of exciton separation and consequently lowering solar cell efficiencies. Moreover, if one directly mixes ZnO and P3HT together, a poor interface will be obtained as well due to the incompatibility of ZnO and P3HT. Thus, in chapter 7, the diblock copolymer poly(3-hexylthiophene-2,5-diyl)-block-

poly(ethylene oxide) (P3HT-*b*-PEO) is used to modify the morphology of the ZnO/P3HT hybrid films. The corresponding optoelectronic properties are discussed.

Although it is reported that the deposition method plays a significant role in the film morphology, researches on the comparison of the morphologies using different deposition methods are seldom reported. In chapter 8, two deposition methods, namely spray and spin coating are compared with respect to the resulting film structure. Both, the surface and inner morphologies prepared from the two deposition methods are discussed. Moreover, the morphologies of the spray coated samples by changing the weight fraction of ZnO in the films are revealed using time-of-flight grazing-incidence small-angle neutron scattering (TOF-GISANS).

Finally, chapter 9 gives a conclusion of the thesis. The challenges mentioned in this chapter are solved and the obtained results based on various investigations are summarized. In addition, a brief outlook for further studies is given as well.

2. Theoretical aspects

Theoretical background, on the materials, methods and processes used in dye-sensitized solar cells (DSSCs) and hybrid bulk heterojunction solar cells (HBSCs), is discussed in this chapter. Some basic concepts of polymer physics are given in section 2.1. Since block copolymers (mainly used as a template) and conducting polymers (as light absorbers and hole transport materials) are primarily used in this work, more details about these two parts are discussed individually. Afterwards, the electron transport material, ZnO, is introduced in section 2.2. The properties of ZnO and the mostly used sol-gel method, along with the diblock copolymer templating are discussed in this section. For the background of photovoltaic devices, an overview about DSSCs and HBSCs is given in section 2.3. Lastly, the basic principles of different scattering techniques (including different sources: X-rays and neutrons) to probe the structure of thin films are discussed in section 2.4.

2.1 Polymer basics

In this section, fundamental aspects of polymer physics are introduced. Basic principles including basic definitions and crystallization behavior of polymers are present in section 2.1.1. The descriptions about block copolymers, especially about diblock copolymers are given in detail in section 2.1.2, followed by the theoretical background of conducting polymers in section 2.1.3.

2.1.1 Basic definitions

Polymers are large molecules (macromolecules) composed of one or more types of repeating structuring units. These subunits are called monomers, which are connected with each other by covalent chemical bonds. The process of polymerization means transition of low molecular weight constitutes (monomers) into high molecular weight constitutes (polymers) via a chemical reaction. The number of monomeric units in a polymer is defined as the degree of polymerization (*N*). Generally, polymers have a molecular weight larger than 10000 g mol^{-1}.[24] It can only be referred as oligomers if the molecular mass is less than 10000 g mol^{-1}.[24] Typically, oligomers show different physical properties compared to polymers.

At present, polymers obtained via a synthesis process usually have various chain lengths and thereby have various molar masses.[25] Only some bio-polymers (*e.g.* enzymes) are monodisperse *i.e.*, all molecules possess the same degree of polymerization and the same

molecular weight. Therefore, statistical mean values are used to describe the mass of the polymers.

The number average molar mass M_n is the average of the molecular masses of the individual polymers, which is defined as the first central moment of the statistical distribution of the molar masses as seen in Equation 2.1

$$M_n = \frac{\sum_i n_i M_i}{\sum_i n_i}, \tag{2.1}$$

where M_i and n_i are the molar mass and chain number of component i, respectively. Thus, the total mass of macromolecules of the ith component is $w_i = n_i M_i$. With this, another molar mass can be defined as the weight average molar mass M_w, which is defined as the ratio of the second central moment to the first central moment, as seen in Equation 2.2

$$M_w = \frac{\sum_i w_i M_i}{\sum_i w_i} = \frac{\sum_i n_i M_i^2}{\sum_i n_i M_i}. \tag{2.2}$$

The ratio of M_w to M_n is called polydispersity index (*PDI*, Equation 2.3), which is used to describe the width of the distribution of the molar masses as follows

$$PDI = \frac{M_w}{M_n} = U + 1, \tag{2.3}$$

where U is the inconsistency. As M_w is larger than M_n, the value of *PDI* is always equal to or larger than 1. For the case of $U = 0$, a polymer shows lowest inconsistency value, which is called monodisperse ($P = 1$). However, as mentioned above, all synthesized polymers present a certain distribution of the chain lengths. Thus, these polymers are polydisperse, with $PDI > 1$. Different molar mass distributions can be obtained via different synthesis methods. The most commonly used methods in polymerization synthesis are step polymerization and chain polymerization. For step polymerization, which is also called poly-condensation, monomers or polymer fragments react with each other randomly. Thus, the molar mass distribution is very broad, yielding a Schulz-Zimm-distribution. Generally, the high polydispersity index makes it only applicable for industry. However, concerning chain polymerization, the molar mass distribution is very narrow, with a small polydispersity index close to 1. Each time a new monomer is linked to reactive centers, which contributes to the Poisson-distribution. Therefore, this synthesis method is typically used for scientific applications.

Due to variable ordering possibilities and multiple monomers, a large amount of polymer structures can be obtained, such as chain-like structure, the simplest one as well as ring-like, brush-like and star-like structures which grow by substituting the hydrogen atoms initially on side groups,[25] as seen in Figure 2.1. If the polymer consists of only one type of monomer, a

homopolymer is formed. Instead, more commonly used, more than one type of monomers connect with each other, yielding a copolymer. In the case of two kinds of monomers, if a homopolymer subunit PA is linked with the other homopolymer subunit PB, a diblock copolymer PA-*b*-PB is formed. If a polymer consists of alternating monomers A and B, alternating copolymers appear. Additionally, the so-called graft copolymer illustrates that some hydrogen atoms of homopolymer PA are replaced by long side chains with monomer B, forming a special branched copolymer. More complicated, random copolymers can be obtained if monomers A and B connect with each other without a specific order.

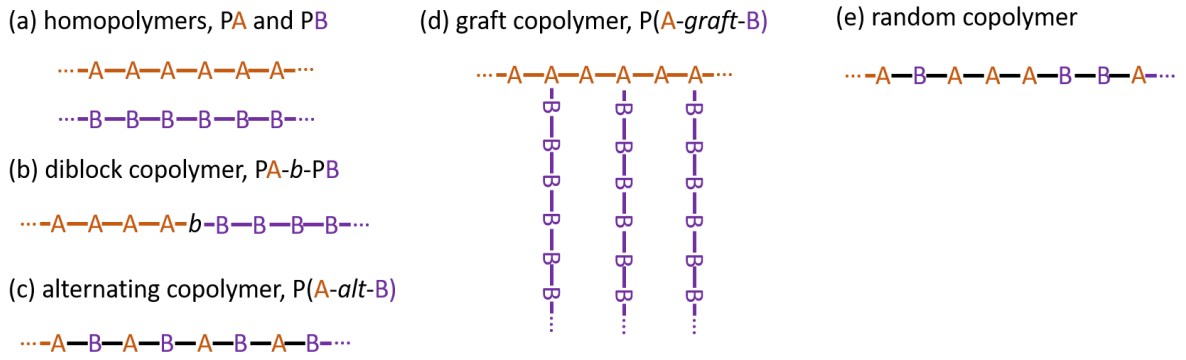

Figure 2.1 Commonly observed constitutions of polymers with two different components A and B: (a) homopolymers, (b) diblock copolymer, (c) alternating copolymer, (d) graft copolymer and (e) random copolymer.

Crystallization

Unlike small organic molecules or oligomers which can form complete crystals, polymers can only form crystals in a semi-crystalline state. The crystallization of polymers is mainly hindered by two factors. One is the high entropic activation barrier which hampers the complete disentanglement of the coiled polymer chains before crystallization. The second factor which hinders the full crystallization of polymers is the polydispersity of the synthesized polymers, which show different length of polymer chains. Thus, polymers always crystallize in a semi-crystalline state which consists of polymer crystals separated by amorphous regions of the same polymer. This state is kinetically determined, instead of a thermally equilibrated state.

In Equation 2.4, the crystallinity ϕ_c of polymers is defined as the volume fraction of the crystalline part in the polymer matrix, *i.e.* the volume of the crystalline part divided by the total volume:

$$\phi_c = \frac{V_c}{V_a + V_c}, \tag{2.4}$$

where V_c and V_a are the volume of crystalline phase and amorphous phase, respectively. The amorphous part mainly includes chain ends, entangled chains, impurities and other defects. Polymer crystals show a layered structure with a layer thickness of d_c. The crystals can extend along the direction perpendicular to the polymer chains to several micrometers. Independent of the molecular weight M_w, the crystal thickness d_c mainly depends on the crystallization temperature T_c of the polymers.[26] Generally, T_c lies between the glass transition temperature T_g and the melting temperature T_m. Below the temperature of T_g, polymers are in the glass state, where the chains lose their large scale mobility completely. The polymer chains are frozen until reaching T_g, where the polymers switch from a solid, glassy state to a more soft, rubber-like state. The chains can rearrange themselves if the polymers are heated up above T_g. When the temperature reaches T_m, polymers are in the liquid phase, where the polymer chains lose their molecular ordering and become mobile. For semi-crystalline polymers, decreasing the temperature below T_m, the crystallization process starts at the temperature of T_c. The polymer crystallinity increases with further decrease of the temperature. Once the temperature reaches T_g, no more crystalline regions can form, which means the crystallinity does not increase any more due to the motionless polymer chains.

The crystallinity of polymers plays a critical role for conducting polymers, as higher ordering due to crystallization contributes to higher mobility of charge carriers in these polymers,[27, 28] which is beneficial for improving the photovoltaic performance. More details of conductivity in polymers are discussed in section 2.1.3. Regarding the growth mechanism of polymer crystals, a multi-stage growth model proposed by Strobl is described here as this model is widely accepted nowadays.[29] However, it has to be mentioned that the validity is still debated. With the multi-stage growth model, the first step of polymer crystallization is nucleation, which can be initiated by dust particles, impurities, or defects. This way, starting from the pre-existing nuclei, is called heterogenous nucleation. In another case, the thermal fluctuations of the system can lead to an ordered arrangement of polymer chains, which serve as nuclei.[29] This type of nucleation is known as homogenous nucleation. Along the process of increasing the amount of nuclei, a transient mesomorphic layer establishes where the structure shows an intermediate between crystal and melt. In this aligned state, the epitaxial forces make not only single polymer chains but also several neighboring chains fold back and forth to form the mesomorphic layer.[30] Afterwards, this preliminary lamellar stacks formed in the mesomorphic state solidify via the core crystallization which leads to the observation of a block, as shown in the stage II in Figure 2.2. Finally, the crystal structures are stabilized via increasing the order of the polymer chains on the surface. The crystallization starts at a nucleation point, and the growth is always perpendicular to the chain direction. Generally, a spherulite structure resulting

from branching and splaying during the crystal growth is observed if no temperature gradient is employed. As shown in Figure 2.2b, amorphous regions are located in between the highly ordered lamellar stacks in this semi-crystalline structure.

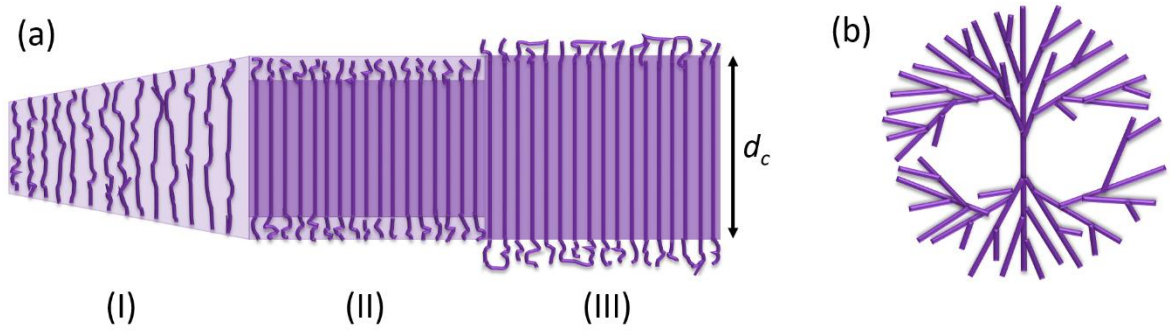

Figure 2.2 (a) Polymer crystallization described by a multi-stage model with three different phases: (I) formation of a mesomorphic layer, (II) solidification of the core, and (III) stabilization via surface ordering. d_c represents the thickness of the crystal. (b) Schematic model of a spherulite. Lines indicate direction of crystal alignment. The image is based on Ref.[31]

2.1.2 Diblock copolymers

As introduced in section 2.1.1, diblock copolymers are macromolecules which contains two chemically different subunits which are covalently bound together. PolyA-*block*-polyB, shortened as PA-*b*-PB is generally used in the case of Figure 2.1b. The volume fractions f_A and f_B can be obtained from Equation (2.5) and (2.6)

$$f_A = \frac{V_A}{V_A+V_B}, \tag{2.5}$$

$$f_B = \frac{V_B}{V_A+V_B} = 1 - f_A. \tag{2.6}$$

When the two blocks in the diblock copolymer are chemically fixed together, there is generally some degree of incompatibility between them. In order to decrease the incompatibility, the diblock copolymers self-assemble into various structures as shown in Figure 2.3. Competing forces arise from the enthalpic contribution of mixing (or de-mixing) and the entropic penalty associated with elongating the polymer chains. Therefore, depending on the balance between these two factors the structures show very well-defined spacing and size on the nanometer length scale. This local reorganization is called microphase separation. The morphology of the diblock copolymer depends on many parameters, such as the Flory-Huggins interaction

parameter χ, the overall degree of polymerization N, the relative fraction of the component blocks f, and the particular polymer architecture. The Flory-Huggins interaction parameter χ determined by Equation 2.7, is found as an important parameter for diblock copolymers,[32, 33] which describes the interaction between two homopolymers PA and PB.

$$\chi = \frac{\chi_H}{T} + \chi_S, \tag{2.7}$$

with χ_S and χ_H being the entropic and enthalpic contribution, respectively.

Normally, the degree of microphase separation in a diblock copolymer greatly depends on the factor χ_N. Generally, for a symmetric diblock copolymer, the critical value of χ_N is about 10.5, below which an intermixed phase is obtained. For $\chi_N \approx 10.5$, a weak segregation limit (WSL) is observed in case of symmetric blocks (f = 0.5). When increasing χ_N, the incompatibility between the two blocks increases and a strong segregation limit (SSL) is observed for $\chi_N >> 10.5$.[34]

A large collection of diblock copolymers is called a polymer melt, and above the transition temperature the amount of A and B is equally distributed throughout the material. This is the disordered state of the material and exhibits no spatial variance, and thus, possesses the same type of translational symmetry found in liquids. Below a certain transition temperature the polymer melt gets ordered. The ordering results in the formation of a periodic distribution of A and B, and many different geometries have been observed in experiment. This temperature is called order-disorder transition temperature (T_{ODT}), below which the monomer segments will segregate and form regular, periodic structures. The block fraction plays an important role in the structure tuning. As shown in the theoretical phase diagram of a diblock copolymer PA-*b*-PB, with increasing the fraction of f_A, the morphology changes from spheres via hexagonal cylinders to gyroids with A domains in the matrix of B. When increasing the fraction of the B block further, the structures change in the opposite way, namely from gyroids, hexagonal cylinders to spheres with B block in the matrix of A.

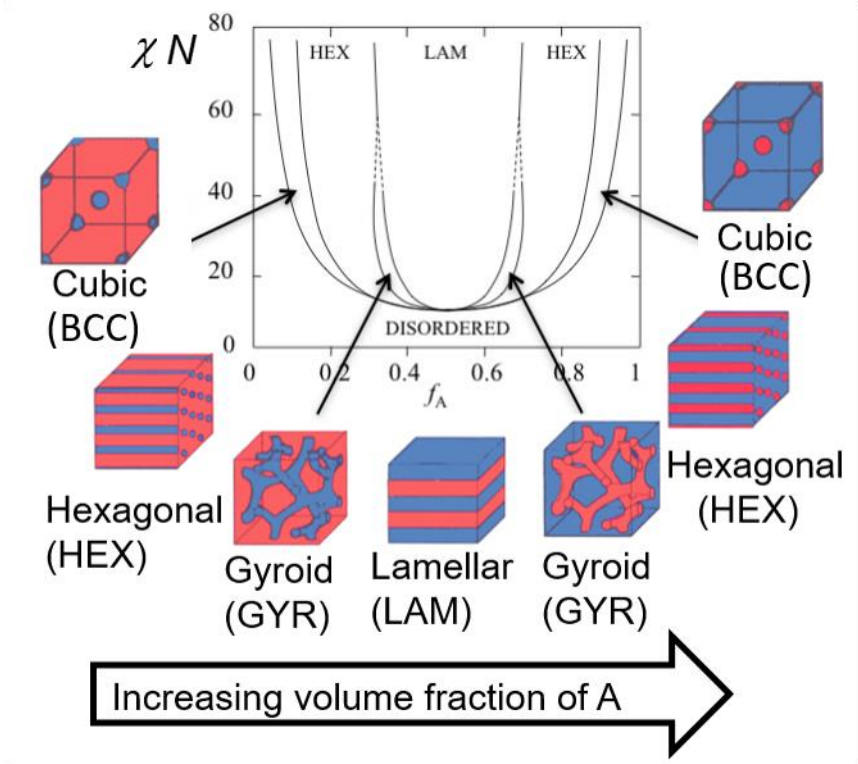

Figure 2.3 Theoretical phase diagram and corresponding morphologies for diblock copolymers. The phases are indicated as follows: body centered cubic (BCC), hexagonal cylinders (HEX), gyroid (GYR) and lamellar (LAM). f_A is the volume fraction of polymer block A, χ the Flory-Huggins interaction parameter, and N the total degree of polymerization. The image is based on Ref.[35]

In general, due to the possibility of the conformationally different polymer blocks and different behaviors shown by the blocks, such as crystallization, an asymmetric phase diagram is more frequently observed. Moreover, the structure of a diblock copolymer in a thin film may be quite different to the phase diagram shown above because of the interfacial interactions.[36-38]

2.1.3 Conducting polymers

Traditionally, polymers are considered to be insulators, which are used in many fields, *e.g.* as housing for electrical appliances. However, in 1977, conducting behavior of doped polyacetylene was found by Shirakawa, MacDiarmid and Heeger, who were jointly awarded with the Nobel Prize in chemistry in the year 2000 for this discovery.[3] Since polymers are typically insulators, they gain more attention for using as electronic materials. With doping, the electrical conductivity of polymers can potentially be tuned over a range of electrical conductivities from insulating to metallic behavior. For all conducting polymers, conjugated

double bonds, which consist of alternating single and double bonds in the polymer chains, are required. The presence of alternating double bonds refers to the presence of π-orbitals. In these conjugated polymers, the electrons resulting from the unsaturated sp^2 hybridization are delocalized in π-orbitals along the polymer chain, therefore, having an enhanced mobility along the chain. With the conjugated bonds, as shown in Figure 2.4 in the case of polyacetylene, the π-orbitals overlap with each, leading to the energy shift of bonding π- and antibonding π*-bands, which are referred as the highest occupied molecular orbital (HOMO) and the lowest unoccupied molecular orbital (LUMO), respectively, and therefore, a decreased band gap forms.

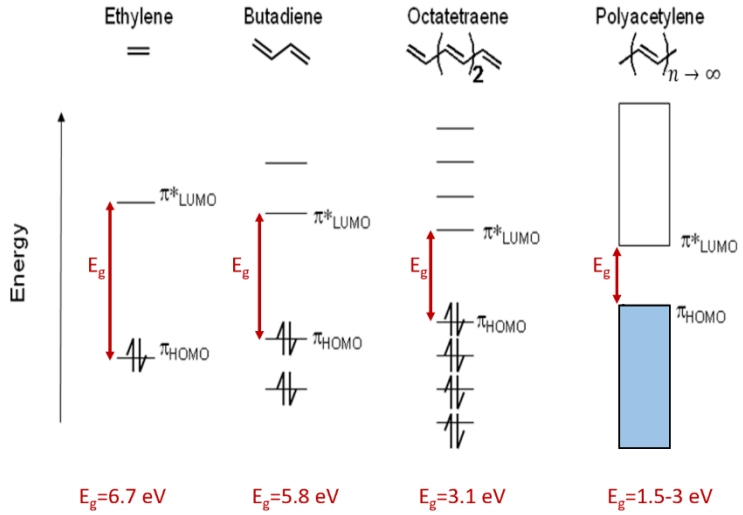

Figure 2.4 Schematic illustration of bonding π- and antibonding π-bands along with the band gap of the ethylene, butadiene, octatetraene and polyacetylene, based on photonicswiki.org.*

Band structure and charge carriers

To explain the band structure of conjugated polymers, Peierl's instability theorem is typically used. As shown in Figure 2.5, for a one-dimensional metallic lattice of *N* atoms, each atom possesses one electron and the periodic distance a is constant, due to which a half-filled energy band up to Fermi level E_F is obtained. Whereas for the conducting polymers, the conjugation or dimerization leads to a new periodic distance of 2a. To decrease the total energy of the system, the Brillouin zone is bisected at the position of $k = \pm\pi/2a$ as shown in Figure 2.5b. Therefore, a new band gap ΔE_{gap} appears. For polymers, the band gap strongly depends on the structure, degree of polymerization and doping. Such as P3HT shows a band gap about 2 eV, PTB7 about 1.8 eV and PTB7-*th* about 1.6 eV.[39, 40]

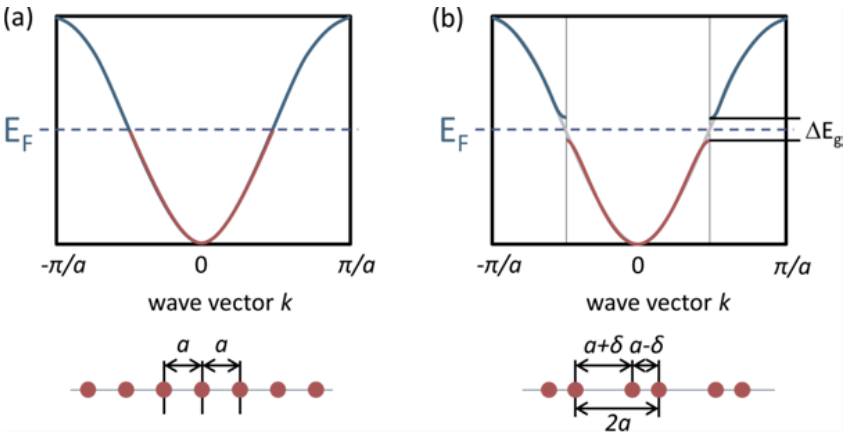

Figure 2.5 Schematic illustration of the band structure with Peierl's theorem of (a) an undistorted one-dimensional metal chain with lattice spacing a, and (b) a distorted one-dimensional lattice with distortion of δ and periodicity of 2a. This picture is based on Ref.[41]

In conducting polymers, quasiparticles which combine charges and lattice distortions are considered as charge carriers. Generally, in systems with an energetically degenerated ground state, the most commonly found charge carriers are solitons, polarons and bipolarons. In systems without an energetically degenerated ground state, solitons are not observed. Polyacetylene is used as an example to see these three quasiparticles in Figure 2.6. Here it is important to note that the quasiparticles are not fixed at one position, but are delocalized, and thus, can extend over several atoms. In case of polyacetylene, it is possible for a soliton to extend over 14 carbon atoms. For polyacetylene, neutral solitons (S^0) are always present due to its two degenerated ground states. When doped or excited by light, charged solitons (S^+ or S^-) are created. Unlike electrons and holes in inorganic materials, solitons with a charge are spin-less, while solitons without charge show spin ½. A polaron can be considered as a combination of a neutral soliton and a charged soliton as shown in Figure 2.6b, exhibiting charge and a spin of ½. In contrast, bipolarons (Figure 2.6c) can be thought as a bond of two polarons, showing charged and spin-less properties.

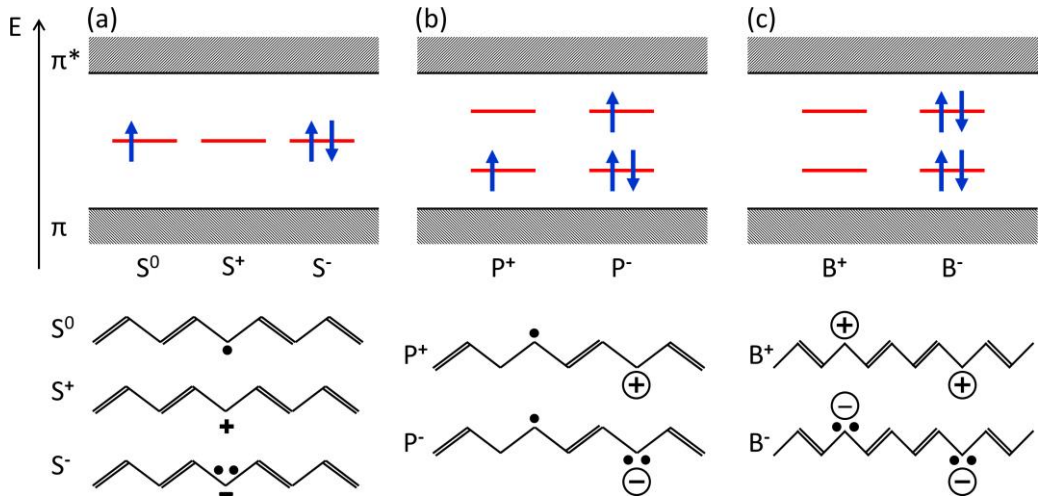

Figure 2.6 Energetic states of the three quasiparticles for the example of polyacetylene. (a) Solitons are shown in their neutral state S^0, positively charged S^+, and negatively charged S^-. (b) Polarons are only observed with either a positive P^+ or negative charge P^-. (c) Bipolarons are observed with either two positive B^+ or two negative charges B^-. The horizontal lines represent the energetic band states of all quasiparticles which stay within the band gap E_g. The black dots depict electrons which are part of a π-bond, and the + and – signs indicate the charge of the quasiparticle. This picture is based on Ref.[31]

Charge transport

The charge transport in conducting polymers is quite different from that in inorganic materials due to several factors. Instead of electrons and holes in inorganic materials, generally polarons and bipolarons are transported in the conducting polymers. Moreover, in inorganic lattices, atoms are strongly bound and can only move slightly around their lattice position. While for polymeric systems, the chains are able to change their conformation and thereby move quite freely which can lead to much stronger polarization effects. Even for the semi-crystalline polymers, amorphous regions are always present. In conducting polymers, the conduction of charges along the backbone is most efficient due to the presence of the delocalized π-orbitals as mentioned above. However, regarding the charge transport from one chain to another, the hopping mechanism is important. Because of the spatial or energetic disorders in the polymer, localized states are present as illustrated as red lines in Figure 2.7. To illustrate the hopping mechanism, the Gaussian disorder model is used with a Gaussian distribution of density of states with the width σ to describe the energetic disorder of hopping sites. Under steady-state conditions, the charge density lies below the center of density of states by a thermal activation energy – σ^2/k_BT, leading to the transport energy as indicated by the dashed line in Figure 2.7.

Generally a charge is excited, for example by photons in the case of solar cells, to a higher energetic state. If the neighboring state shows a lower energy (the Boltzmann activation energy $k_BT=0$), it will relax and hop down in energy until it reaches a trap state. In this case, the trap state makes charge carriers motionless, thereby they do not contribute to the electrical conductivity any more. If the charge reaches the region between the centers of the charge carrier density and the density of states, it can potentially be thermalized (the Boltzmann activation energy $k_BT>0$). The charge will gain the thermal energy from the system and then it is able to hop from one localized state to another via absorbing or emitting of a phonon. It can even hop towards energetically higher states. Therefore, typically the conductivity for polymers increases with increasing temperature. Moreover, the crystallinity of the polymer is important to significantly increase the mobility of the charge carriers. Therefore, improving the crystallinity is considered promising to improve the performance of hybrid solar cells.

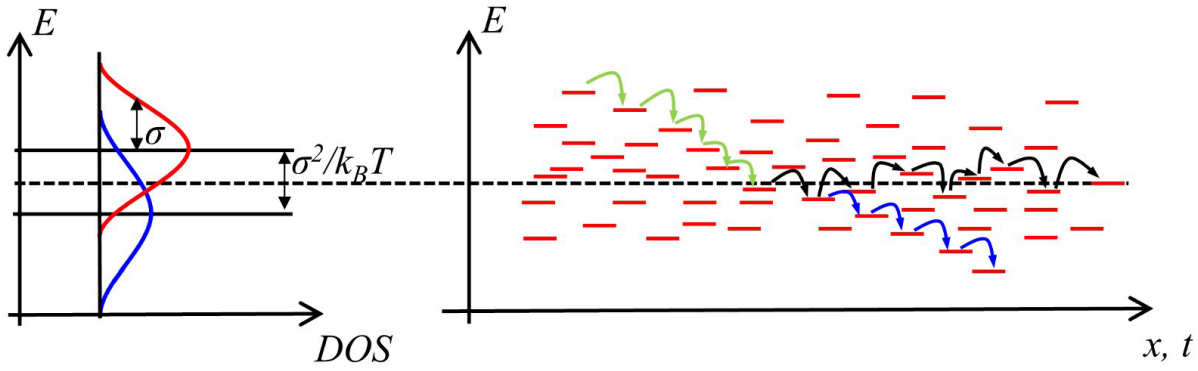

Figure 2.7 Schematic illustration of hopping transport: Gaussian distribution of density of states (red) and of charge carrier density (blue), and resulting hopping transport (black arrows) around the transport energy (indicated by the dashed line) as a function of space x and time t. The green arrows indicate the relaxation after the creation of an excited state, the blue arrows indicate the relaxation down to a trap state in case of the Boltzmann activation energy $k_BT=0$. Adapted from Ref.[42]

2.2 Zinc oxide and sol-gel synthesis

2.2.1 Zinc oxide properties

ZnO is a well-known material and the research on ZnO continues for many decades due to its wide applications. Most of the II-VI compound semiconductors crystallize in either cubic zincblende or hexagonal wurtzite structure. Tetrahedral coordination, in which each anion is surrounded by four cations at the corners of a tetrahedron, and vice versa, is observed. A typical

sp^3 covalent bonding exists in the materials, but also a substantial ionic character. ZnO is a II-VI compound semiconductor with the ionicity residing at the borderline between covalent and ionic semiconductor. Two crystal structures are discovered, namely wurtzite and zincblende as shown in Figure 2.8. Wurtzite ZnO is thermodynamically stable at ambient conditions. While the zincblende ZnO structure can only be stabilized by growing them on substrates with cubic lattice.

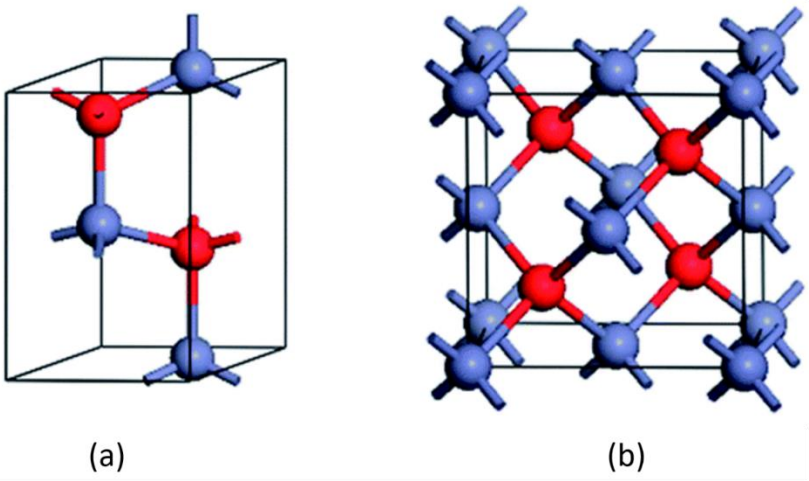

Figure 2.8 Crystal structures of ZnO with (a) hexagonal wurtzite and (b) zincblende. The blue and red spheres denote Zn and O atoms, respectively. Reproduced from Ref.[43] with permission from The Royal Society of Chemistry.

The wurtzite ZnO shows unique optical, semiconducting and electrical conducting properties. It is a natural n-type semiconductor with a direct wide band gap of 3.3 eV in the near-UV spectrum and a high exciton binding energy of 60 meV at room temperature.[44] These characteristics enable ZnO to have remarkable applications in various fields. The wide band gap of ZnO causes strong absorption in the UV spectral region, therefore allowing for protection of a sensitive polymer from degradation via UV irradiation when applied in solar cells. Its longer durability, higher selectivity, and better heat resistance are superior as compared to the organic materials.

Recently, nanostructured ZnO has been a subject of immense research due to the multifunctional properties in diverse applications, such as sensors, energy harvesting and many electronic devices. Many applications are being currently explored in the field of solar cells. The unique properties and versatility of ZnO provide a way to use various methods to synthesize manifold ZnO nanostructures. The properties can be tuned by tailoring shape and size of ZnO particles, which depend on the selected fabrication methods. The most commonly

used fabrication methods include thermal evaporation, hydrothermal synthesis, sol-gel technique, simple thermal sublimation, *etc*.[45, 46] Many factors such as solvent type, precursors, pH and temperature are highly influential. With these methods, an assortment of ZnO nanostructures with different morphologies such as nanorods, nanospheres, nanotubes, nanowires, nanoneedles and nanorings have been successfully synthesized.[20, 47] Each nanostructure shows unique optical and electrical properties, thus, paving a way for remarkable applications.

2.2.2 Basic principles of sol-gel synthesis

Sol-gel synthesis is a self-assembly method for producing solid materials from small molecules, which is used for fabricating metal oxides, such as SiO_2 networks, TiO_2 and ZnO.[48] It is essentially a bottom-up method where a network of the given material is obtained from initial small molecules, which are generally the precursors for the desired material. Basically, metal alkoxides are used as precursors to undergo hydrolysis reaction, through which nanoparticles form in the solution to produce the so-called "sol". Then nanoparticles cross-link with each other to form a three dimensional network in the solution with the remaining solvent trapping in the pores. Thus, a "gel" is obtained. In the case of ZnO, zinc acetate can be used as a precursor. The hydrolysis is depicted in equation 2.8.

$$(HCOO)Zn\text{-}OOCH + H_2O \rightleftharpoons (HCOO)Zn\text{-}OH + HCOOH \qquad (2.8)$$

Then, the condensation yields the hydrolyzed nanoparticles as shown in equation 2.9 and 2.10.

$$2\ (HCOO)Zn\text{-}OH \rightleftharpoons (HCOO)Zn\text{-}O\text{-}Zn(OOCH) + H_2O \qquad (2.9)$$

$$(HCOO)Zn\text{-}OH + (HCOO)Zn\text{-}OOCH \rightleftharpoons (HCOO)Zn\text{-}O\text{-}Zn(OOCH) + HCOOH \qquad (2.10)$$

All of the chemical species are in equilibrium in the sol-gel solution.

Due to the low volume fraction of the particles in the sol-gel, a significant amount of solvents need to be removed to bring forth the gel-like properties. For this, many methods can be used, of which the simplest is sedimentation and then removing the remaining liquid. Centrifugation can be used to accelerate this process. Spin-coating is also a good way to remove the excessive solvents. After this, a subsequent drying process is also needed to remove solvent residuals, which is typically accompanied by shrinkage and densification. It is reported that many factors such as the pH value, temperature, humidity and concentration have a great influence on the reaction kinetics which results in the formation of nanostructures with different length scales.[49]

2.2.3 Structure direction with block copolymer templates

With the sol-gel technique, ZnO nanostructures can be obtained and the morphology can be tuned finely through control of the reaction environment. However, available structures are still limited and often ill-defined, especially for gaining ordered structures. Therefore, to obtain ordered nanostructures, which can provide a large surface area for application in solar cells, a diblock copolymer is used as a template in combination with the sol-gel method. As introduced in section 2.1.2, diblock copolymers undergo micro-phase separation if χ_N is larger than 10.5. Through the self-assembly process, multiple morphologies can be obtained, such as spherical, cylindrical, lamella, and gyroid structures. For preparing n-type semiconductors used in solar cells, the selected diblock copolymer for the templates has an amphiphilic behavior, with a hydrophobic block covalently bond to a hydrophilic block. In this case, it can fulfill the requirement that the n-type semiconductor selectively agglomerates on one block, and thus, form ordered nanostructures along the self-assemble hydrophilic block of the copolymer.

To achieve a film with ordered nanostructures inside, first a "good" solvent is needed to dissolve the diblock copolymer. This is a non-selective solvent which can dissolve both of the two blocks of the copolymer. Moreover, a selective solvent, which can only dissolve one of the blocks in the diblock copolymer, is also required. This selective solvent is also called "poor" solvent, which can only dissolve the hydrophilic block in this case. Thus, with the addition of the poor solvent, the hydrophobic block tends to minimize its interface with the surrounding solvent environment to form the cores. The hydrophilic block will extend to form the micellar corona due to the favorable solvent around. As a result, with the introduction of the "good-poor" solvent pair, micelles are formed in solution, as a result of a complex thermodynamic process. It is a dynamic equilibrium where the fusion and separation of the micelles are reversible. If zinc precursor is added into the solution, it will undergo hydrolysis and condensation steps. The produced ZnO species will incorporate into the hydrophilic block preferentially via hydrogen bonds in combination with electrostatic and van-der-Waals interactions. This incorporation will in turn result in its selective swelling, which may have an influence on the micelle formation due to the different equilibrium conditions in the system. Hence, unique nanostructures can be achieved when deposited on a substrate. If the block lengths of the polymer or the ratio of the polymer and zinc precursor is changed, the size of the micelles and the cores will be tuned, therefore leading to tailored morphologies with different length scales. Apart from this, a high degree of control of the length scales can also be achieved by adjusting the concentration of the zinc precursor, PH value and reaction environment.

Regarding the deposition process to remove solvents and solidify samples, many factors need to be considered as well.[50] Generally, during drying, the diblock copolymer rearranges to

decrease the system energy and meanwhile the ZnO species tend to cross-link, therefore hampering the rearrangement of the diblock copolymer. The morphology of the films adopted to a large degree depends on the balance between this two processes. Ordered structures can be obtained if the former process dominates as the micro-phase separation favors the formation of ordered structure. In the other case, a less ordered structure will form. Different deposition techniques may lead to different morphologies. For fast deposition techniques, such as spin and spray coating, the diblock copolymer undergoes a non-equilibrium process, with the structures freezing within seconds. While for other deposition methods, like solution-casting, blade-casting and printing, the drying process is slow. Therefore, they result in more time for structural rearrangements, and in general more ordered structures.

After deposition of the sol-gel solution, the ZnO/diblock copolymer hybrid films can be further treated with solvent or thermal annealing to promote the structural rearrangement by improving the mobility of the polymer chains. Moreover, a high temperature above 400 °C can be applied to combust the polymer template from the hybrid films to get pure ZnO films. Further, it was reported that the polymers can be removed from the hybrid films with low-temperature methods, such as UV irradiation, oxygen plasma and solvent extraction.[51] Removal of the template from the hybrid films may lead to a change of the morphology due to the collapse of the materials left in the films after removal of the polymer matrix.[52]

2.3 Solar cells

A solar cell is an electronic device, which converts solar radiation into electricity by the photovoltaic effect. So far, many different kinds of solar cells, such as inorganic solar cells, organic solar cells and hybrid solar cells, are realized. Recently, hybrid solar cells have attracted great attention due to the advantages of their short payback time, high stability and flexibility, which results from the combination of inorganic and organic materials. For hybrid solar cells, DSSCs and HBSCs are mostly explored. In this section, the basic principles of DSSCs and HBSCs are introduced in section 2.3.1 and 2.3.2, respectively. For both of these kinds of solar cells, nanostructured ZnO is used as an electron transport material to provide a large interface area for exciton separation and electron extraction to their corresponding electrode.

2.3.1 Dye-sensitized solar cells

DSSCs have attracted a great attention since the pioneering work in 1991.[53] Recently more than 13% of efficiency is achieved.[5] However, due to the problems of electrolyte leakage and electrode corrosion, the stability is not good in long-term operation. To overcome these

limitations, ssDSSCs have been developed, in which the liquid electrolyte is replaced by a solid-state charge carrier transport material.[54] Generally, a ssDSSC is made up of several functional layers as shown in Figure 2.9. At the bottom is a transparent electrode, normally ITO or FTO, to allow the light to go through. On the top of the transparent electrode, a hole blocking layer is deposited to decrease the probability of charge carrier recombination at the electrode. As next there comes the so-called active layer, where actually the light absorption happens. It consists of ZnO, dye molecules (adsorbed at the surface of ZnO) and a p-type semiconductor (backfilled in the ZnO mesopores). The photon absorption is followed by the exciton generation and separation, and the charge carrier extraction to their corresponding electrodes as shown in Figure 2.10. The metal electrode serves as a counter electrode and consists normally of gold. By connecting the metal electrode and the transparent electrode with an external circuit, the generated electrical power can be used to run an external load.

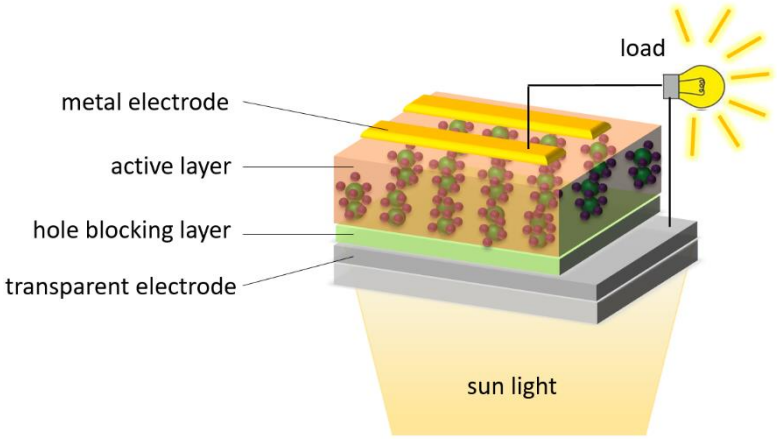

Figure 2.9 Schematic architecture of a DSSC under solar illumination. A hole blocking layer is deposited on transparent electrode to block the transport of positive charge carriers, thereby to decrease the recombination at the electrode. The active layer which consists of charge carrier transport materials and dye molecules will absorb light, generate excitons and the subsequent free charge carriers. The courter electrode is a metal electrode.

Light absorption, exciton generation and separation, and electron injection

In DSSCs, a monolayer of dye molecules, which are loaded on ZnO, absorb light with a photon energy that is equal to or larger than the band gap between the ground state and the excited state of the dye. This is referred as Equation 2.11,

$$E = \frac{hc}{\lambda} \geq \Delta E_{gap} \tag{2.11}$$

With the excitation of the sensitizers, an electron-hole pair, which is known as exciton, appears in the dye molecules. When the generated excitons go to the interface between ZnO and dye molecules, they will separate into negative and positive charge carriers. The electrons are injected to the conduction band of ZnO with the force of an inner electrical field built by the interface of ZnO/dye/p-type semiconductor. Gerischer's model is used to describe the electron transfer from the dye molecules to ZnO.[55] Due to thermal fluctuations, the energy levels of the ground and the excited states of dye molecules are assumed to have a Gaussian distribution. It is possible that the electrons are transferred from the valence band (VB) of ZnO to the ground state of the excited dye molecules. However, this process should be reduced, since it would increase the probability for the recombination of the separated charges. Thus, the ground states of the dye molecules are expected to be located in the band gap of ZnO and are supposed to be not overlapped with the VB of ZnO.

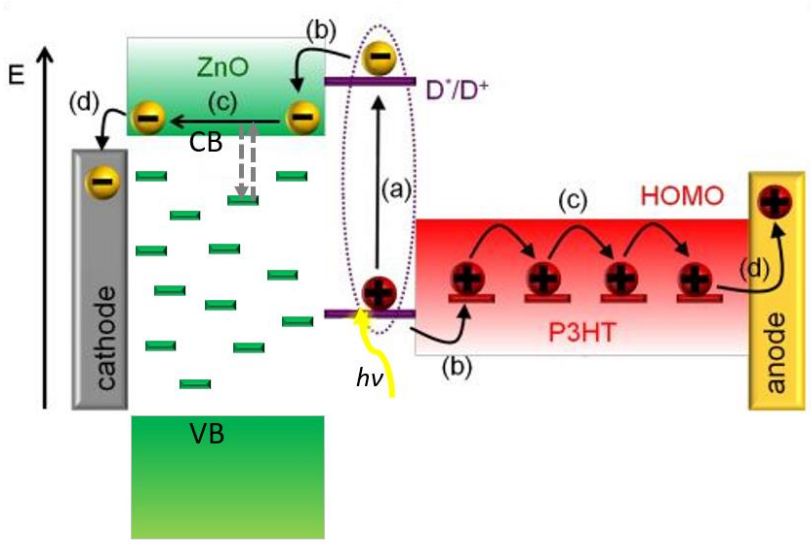

Figure 2.10 A detailed energy diagram of the electronic transport processes in a ssDSSC. (a) Photoexcitation of a dye by light absorption. (b) The injection of the charge carriers with the negative charge carriers to the conduction band of ZnO and positive charge carriers to the HOMO of a p-type semiconductor, such as P3HT. (c) Charge carrier transport through ZnO and P3HT. (d) Charge carrier extraction to the corresponding electrode. The green bars indicate the trap states in the band gap and the gray dashed arrows indicate the trapping and detrapping events. This picture is based on Ref.[31]

As light absorbers, dye molecules in this case, mononuclear and polynuclear dyes based on metals such as Ru^{II}, Os^{II}, Pt^{II}, Re^{I}, Cu^{I}, and Fe^{II} are well established.[56-65] Besides these transition-metal complexes, a range of organic molecules have been explored, such as

coumarin, squaraine, indoline, hemicyanine, and other conjugated donor–acceptor organic dyes.[66-69] Generally an electron acceptor moiety is required in the dye molecules to bind strongly to ZnO, thus ensuring efficient electron injection into the CB of ZnO. It is required that the dye molecules have a high absorption coefficient in the visible range or near-IR region, so that they can absorb light in a broad range of wavelengths. Moreover, the electron transfer from the excited state of dye molecules to the CB of ZnO should be fast as compared to the decay to the ground state of the dye molecules. The sensitizer used in the present thesis is indoline dye D205. The detailed description of D205 is given in section 4.1.

Charge carrier transport

After charge carrier injection into the CB of ZnO, the electrons are transported through ZnO to the transparent electrode. The generated electrons can only be transferred into the CB of ZnO. Therefore, the probability of electrons in the CB of ZnO determines the overall electron mobility. The probability of the electrons highly depends on the trapping and detrapping events as shown in Figure 2.10 marked with gray dashed arrows within the band gap of ZnO. Various defects contribute to the overall trap states, which would influence the final device performance. The traps are proportional to the roughness and porosity of the ZnO films. It has been proved that ZnO films with a high surface-to-volume ratio show a great advantage for loading dye molecules. However, the defects will also inevitably increase, therefore, leading to a low electron mobility in the mesoporous ZnO films. That is to say, the amount of dye adsorption on the surface of ZnO and the electron mobility of ZnO films are contradictory. Therefore, multiple morphologies should be investigated.

For the positive charge carriers, the transport occurs from the p-type semiconductors, generally conjugated polymers, to the metal electrode. To make the transport efficient, the HOMO of the conjugated polymers should be above the ground state of the dye molecules. Moreover, the conjugated polymers should be backfilled into the mesoporous ZnO films to make an efficient interface of ZnO/dye/conjugated polymers, therefore improving the positive charge carrier transport along the conjugated polymers. P3HT is one of the commonly used conjugated polymers to transport positive charge carriers via polaron hopping as described in section 2.1.3. However, as P3HT is a polymer material, which is challenging to be backfilled into the mesoporous ZnO efficiently due to the spatial limitation, spiro-OMeTAD is used in the present work for the fabrication of ssDSSCs, which is introduced in more detail in section 4.1. Due to the contradictory existence of the amount of dye adsorption on ZnO and the difficulty of backfilling for the solid state conjugated polymers with a relatively bad contact with dye

molecules (compared to liquid electrolytes), the optimum thickness of the active layer is about 2 μm.[70]

2.3.2 Hybrid bulk heterojunction solar cells

Different from the structure of organic bulk heterojunction solar cells, the active layer in HBSCs consists of inorganic and organic materials, which act as acceptor and donor, respectively, instead of two types of organic materials in organic solar cells. Therefore, HBSCs are supposed to have the advantages from both the inorganic and organic materials, such as high stability, tunable nanostructures, low costs, and ease of production. In the present thesis, ZnO and P3HT are used as the acceptor and donor, respectively, in which P3HT not only serves as a positive charge transport material but also as a light absorber to generate excitons inside.

The working mechanism of HBSCs is different from that of ssDSSCs. Instead of dye molecules, the P3HT serves as light absorber. Therefore, excitons are generated in P3HT when it is illuminated under light with the photon energy equal to or larger than the band gap of P3HT. When the excitons diffuse to the interfaces of ZnO and P3HT, they will separate into free charge carriers at the ZnO/P3HT interfaces. Then, these charge carriers will be extracted through ZnO and P3HT to their corresponding electrode. In order to obtain solar cells with high power conversion efficiency, loss mechanisms need to be minimized as much as possible, which is one of the biggest challenges in the production of HBSCs. There are mainly four processes which lead to charges being lost. They are depicted in Figure 2.11. After the creation of excitons, they start to roam inside the P3HT in a random way. It is of high probability that the excitons cannot reach the interface within their lifetime and therefore, the excitons will recombine, leading to the loss of the potential charge carriers. This gives a strong requirement for the morphology to be optimized within the exciton diffusion length, to split the excitons into free charge carriers. Therefore, the P3HT domain sizes should not be too large, as shown in Figure 2.11a. The second loss mechanism occurs due to the isolated islands, illustrated in Figure 2.11b, being created during the fabrication of the solar cells. In this case generated excitons are able to separate into free charge carriers. However, if the P3HT domain is isolated and has no connection to the metal electrode, the charge carriers will be trapped, which leads to recombination with the opposite charge carriers, making this dead areas. Therefore, interconnected pathways are required for both donor and acceptor. Moreover, due to the fabrication process, ZnO interconnected nanostructures with suitable percolation paths are fabricated first, leading to the subsequent backfilling steps of the P3HT being a main challenge. It has been shown in literature that there is a large probability that small pores result in an incomplete backfilling as shown in Figure 2.11c. Apart from this, the limited space of pores

can hinder the packing behavior of the polymer backbone, which will decrease the photovoltaic performance of the HBSCs. Besides the recombination inside the active layer, the recombination at the electrodes also contribute to the loss mechanisms. For example, in Figure 2.11d, P3HT is directly connected to the bottom electrode, which increases the probability for the generated positive charge carriers to recombine with the electrons from the bottom electrode. In order to improve the efficiency of the HBSCs, the morphology of the active layer is of great importance, which is also the main point being discussed in this thesis.

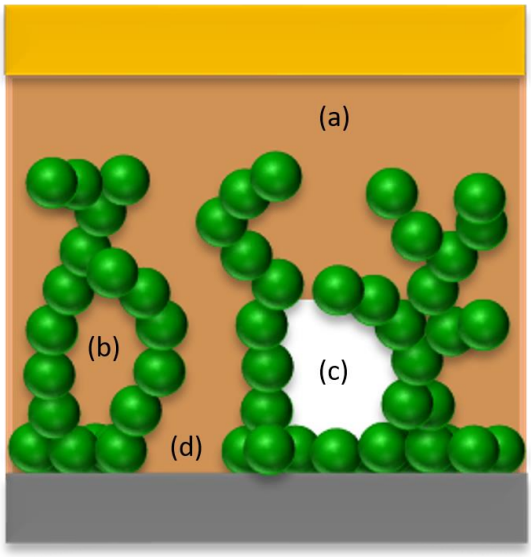

Figure 2.11 Schematic illustration of the four main problems present in HBSCs. The active layer is comprised of a blend of a donor (orange) and an acceptor (green) which is sandwiched between the two electrodes, the metal electrode (yellow) at the top and the transparent electrode (grey) at the bottom. (a) A large domain in the donor material; (b) isolated islands with no connection to the surrounding material; (c) incomplete backfilling of the acceptor material; (d) a recombination at the electrode. This picture is based on Ref.[41]

2.4 Scattering methods

As discussed in section 2.3.1 and 2.3.2, the morphology of the ZnO films plays a critical role in improving the photovoltaic performance of ZnO based solar cells. For investigating the morphology of the ZnO films, SEM and AFM are the mostly used technique to provide the structure information on nanometer length scale. However, these measurements are limited to surface morphology of the films. The inner morphology might be different from the surface which might be influenced by the surface energy. Apart from these real space measurements, in the present thesis, scattering methods using X-rays and neutrons are employed to probe the

inner morphology. Instead of measuring the morphology for a small area on a local scale, a high statistical relevance can be obtained via scattering methods. Moreover, the crystallization of the materials can be determined by X-ray diffraction (XRD). Some basic principles of scattering techniques are described in section 2.4.1, followed by an introduction of XRD in section 2.4.2. The description of grazing-incidence small-angle X-ray or neutron scattering will be given in section 2.4.3 and 2.4.4, respectively.

2.4.1 General principles

X-rays can be described as electromagnetic plane waves. It travels through a medium with a refractive index $n(\vec{r})$ and scattering events can only occur when the refractive index changes. For structural investigation, elastic X-ray scattering is used with the energies of the incoming (E_i) and the final (E_f) X-ray beam being the same. The refractive index $n(\vec{r})$ for X-rays in the investigated material can be given by

$$n(\vec{r}) = 1 - \delta(\vec{r}) + i\beta(\vec{r}) \tag{2.12}$$

where $\vec{r}$ is the position, δ and β are the dispersion and absorption part, respectively. Both δ and β depend on the wavelength λ of the X-rays and can be written as Equation 2.13 and 2.14, respectively, in the case of a homogeneous medium far away from the absorption edges.

$$\delta = \frac{\lambda^2}{2\pi}\rho, \tag{2.13}$$

$$\beta = \frac{\lambda}{4\pi}\mu, \tag{2.14}$$

with the scattering length density (SLD) $\rho = r_e\rho_e$ and the absorption coefficient μ.

Due to the constant classical electron radius r_e (being 2.814×10^{-5} Å), the SLD depends on the electron density ρ_e of the material greatly. Typically, δ is of the order of 10^{-6} and β 10^{-7} for X-rays in the used energy range. Scattering experiments can only be performed based on the different SLD of the investigated materials. The difference is regarded as scattering contrast.

General definitions

When the X-rays interact with the samples, two different cases of scattering, namely the specular and the diffuse scattering, will occur, as depicted in Figure 2.12. The X-ray beam $\overrightarrow{k_i}$ impinges on the sample with the incident angle of α_i. One part of the beam is transmitted with the angle of α_t and another part is reflected with the final angle of α_f. If the final angle α_f equals the incident angle α_i and the beam still stays in the xz-plane, it is called specular reflection. Otherwise, diffuse scattering will occur. The scattered beam is not restricted to the xz-plane

any more. Instead, an additional scattering angle ψ is observed in the xy-plane. The momentum transfer of the scattered beam is described by the scattering vector $\vec{q}$,

$$\vec{q} = \vec{k}_f - \vec{k}_i. \tag{2.15}$$

The modulus of the wavevector is $k = \frac{2\pi}{\lambda}$ for the X-rays with a wavelength of λ.

Snell's law (Equation 2.16), also called the law of refraction, is used to describe the refraction at the interface between air and a medium with a refractive index of *n*.

$$\cos(\alpha_i) = n\cos(\alpha_t), \tag{2.16}$$

where α_t is the exit angle of the transmitted beam $\vec{k}_t$. As the dispersion part $\delta > 0$ as described above, the refractive index of X-rays is less than 1 for most materials. As a result, the refractive index of most materials is smaller than that of air for X-rays. When decreasing the incident angle, the exit angle α_t will decrease as well. At a certain point, if the exit angle α_t=0, the beam is totally reflected when the beam travels from air to the material. In this case, the incident angle is called critical angle α_c. Under small angle approximation, the critical angle is determined by

$$\alpha_c = \alpha_i \approx \sqrt{2\delta} = \lambda\sqrt{\frac{\rho}{\pi}}, \tag{2.17}$$

where ρ is the scattering length density of the material for X-rays as described above. The incident angle α_i has a significant impact on the penetration depth of X-rays into the samples. When the incident angle is smaller than the critical angle of the material, the X-ray beam is totally reflected and can only penetrate a small depth. The intensity of X-rays decreases with increasing the penetration distance. The penetration depth is denoted as the point where the intensity of the evanescent wave decreases to 1/e of its original intensity. Moreover, due to a second damping when the X-rays go out of the sample, the escape depth should be considered. Therefore, the scattering depth is determined by both the penetration and the escape depth. Generally, the scattering depth is in the order of 50 Å for the studied materials and used X-ray energy, which is considered half of the penetration depth.[71] If the incident angle is larger than the critical angle, the X-rays will penetrate the whole film, therefore providing inner information of the sample.

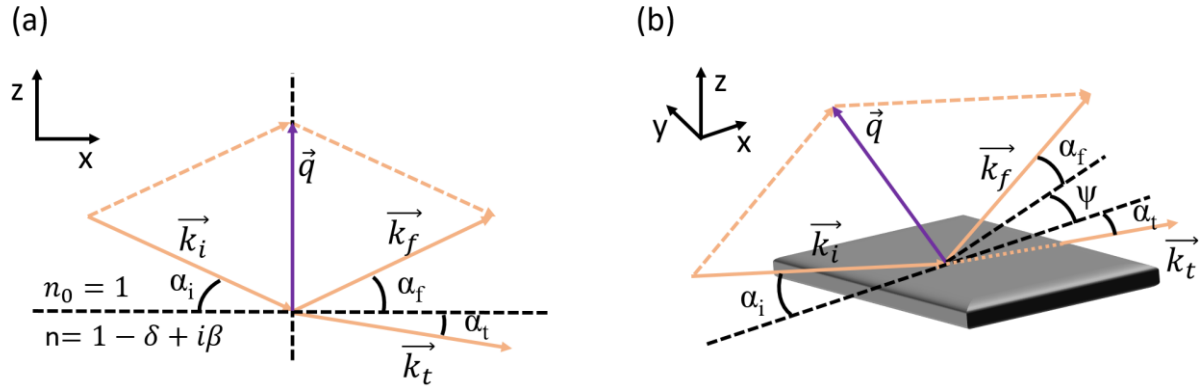

Figure 2.12 Schematic scattering geometry: (a) specular scattering $\alpha_i = \alpha_f$ and (b) diffuse scattering with basic definitions of directions and angles. This picture is based on Ref.[31]

2.4.2 X-ray diffraction

X-ray diffraction is used to investigate the crystal structure of the samples. The different lattice planes in the crystal structure show a periodic grating as shown in Figure 2.13. When a monochromatic X-ray beam impinges onto the lattice planes, scattering with spherical waves will be present. The scattering intensity depends on the electrons around the atoms of the crystal as well as the position of the atoms in the lattice. Therefore, the scattering pattern for the crystal structure is unique, which provides a way to determine the crystal phase of the material. When X-rays illuminate the crystal structure with its different planes, interference will occur as shown in Figure 2.13. Depending on the path difference 2S of the two beams with the same incident angle θ, either constructive or destructive will happen. The maximum intensity obtained for the constructive interference is defined by Bragg's equation (Equation 2.18):

$$2d_{hkl}\sin(\theta) = n\lambda. \tag{2.18}$$

In this equation, d_{hkl} is the lattice spacing of the crystal structure and λ is the wavelength of the X-rays. For polycrystalline materials, an isotropic scattering signal can be observed, which means the crystals are oriented randomly in all directions, therefore, leading to rings of scattered intensity known as Debye-Scherrer rings for each Bragg reflex. Moreover, the apparent size of the crystals can be obtained from the width of the Bragg reflex with the Scherrer equation (Equation 2.19),

$$D_{hkl} = \frac{K\lambda}{\Delta(2\theta)\cos(\theta_0)}. \tag{2.19}$$

K is the Scherrer form factor, which is about 0.9. λ is the wavelength of the X-rays and $\Delta(2\theta)$ is the full width half maximum (FWHM) of the Bragg peak found at angle 2θ. If the size of

the crystal decreases, the Bragg peaks tend to broaden. The equation is valid only for the crystallite size in the range of 5 nm to 200 nm.[72] For the position of the Bragg reflexes, the angles can be converted to q values

$$q = \frac{4\pi \sin(\theta)}{\lambda}. \tag{2.20}$$

Bragg reflexes based on both, the angle and q values as well as the relative intensities of the peaks for the wurtzite zinc oxide, which is studied in this thesis, are shown in Table 2.1.

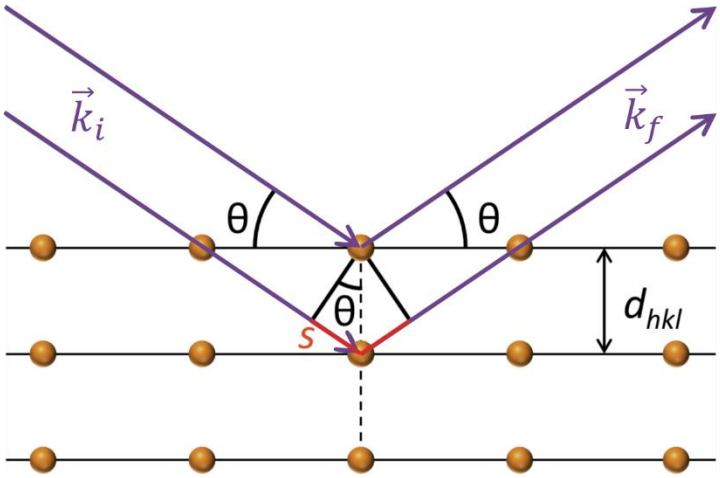

Figure 2.13 Schematic illustration of the Bragg equation. The incoming X-ray beams $\vec{k}_i$ (purple lines) interact with the electron clouds of the atoms as shown in orange circles which are located in regular lattice planes. The distance between these planes is described by the lattice spacing d_{hkl}. The X-ray travels a longer distance, as indicated by the red lines S when interacting with the lower lattice plane. Adapted from Ref.[41]

Table 2.1 Bragg reflexes of wurtzite zinc oxide along with the corresponding relative intensities (obtained from the Joint Committee on Powder Diffraction Standards (JCPDS) database).

crystal order	$2\theta(\lambda_{Cu})$	q[nm^{-1}]	rel. intensity
(100)	31.8°	22.34	57
(002)	34.45°	24.15	44
(101)	36.28°	25.39	100
(102)	47.58°	32.89	23
(110)	56.65°	36.69	32

2.4.3 Grazing-incidence small-angle X-ray scattering

Small-angle X-ray scattering (SAXS) is used to probe the nanostructures shown as solid-state powders or in solutions in transmission geometry. The investigated structure has typically sizes in the range of 10 nm to about 2 μm. For thin films such a transmission geometry is not suitable, because the main scattering information would be contributed by the substrate, while only a small sample volume from the film will add to this. Therefore, grazing-incidence small-angle X-ray scattering (GISAXS) is more suitable, due to a grazing incidence angle of $\alpha_i < 1°$. In this case, a much larger illumination area on the films will be obtained, resulting in a much larger scattering volume. The grazing incidence technique not only increases the intensity of the scattering signal but also provides high statistic for the probed structures.

With GISAXS, diffuse scattering can be detected, which is impossible in the specular measurements as described in section 2.4.1. The scattering geometry is shown in Figure 2.12b. α_i is the incident angle, which is selected when doing measurements. Each outcoming beam can be assigned to two diffuse scattering angles, the one in the xz-plane which is called the exit angle α_f and the other one in the out-of-plane angle in the xy-plane, called ψ. The scattering vector $\vec{q}$ is given by[73]

$$\vec{q} = \frac{2\pi}{\lambda}\begin{pmatrix}\cos(\alpha_f)\cos(\psi_f) - \cos(\alpha_i)\cos(\psi_i)\\ \cos(\alpha_f)\sin(\psi_f) - \cos(\alpha_i)\sin(\psi_i)\\ \sin(\alpha_f) + \sin(\alpha_i)\end{pmatrix} \cong \frac{2\pi}{\lambda}\begin{pmatrix}\cos(\alpha_f)\cos(\psi_f) - \cos(\alpha_i)\\ \cos(\alpha_f)\sin(\psi_f)\\ \sin(\alpha_f) + \sin(\alpha_i)\end{pmatrix}, \tag{2.21}$$

where $\psi_f = \psi$ in the xy-plane, and the incident angle in the xy-plane is typically $\psi_i = 0$. Due to very small angles for GISAXS measurements, the contribution from the q_x component is negligible. The q_y component probes lateral structures and the q_z component is induced by the scattering from the vertical structures perpendicular to the film surface.

To extract structural information about the probed materials by GISAXS measurement, objects with a certain size are used to model the signal collected by a 2D detector. The diffuse scattering factor $P_{diff}(\vec{q})$ (recorded intensity) is approximated by

$$P_{diff}(\vec{q}) \propto NS(\vec{q})F(\vec{q}), \tag{2.22}$$

in which N is the number of the scattering objects. $F(\vec{q})$ is the form factor which describes the certain shape and size of the scattering objects. The interaction of X-rays with the electron cloud of the scattering objects reveals the information of the electron density distribution of these objects. Then, the form factor function can be obtained via the Fourier transform.[74] $S(\vec{q})$

is the structure factor, which is used to describe the spatial distribution of the objects. The diffuse scattering is described within the framework of the distorted wave Born approximation (DWBA). Four scattering events are considered for different modes of reflection and scattering: (1) direct scattering on the detected materials, (2) reflection on the sample substrate and then scattering on the detected materials, (3) scattering on the detected materials and then reflection on the sample substrate, and (4) a combination of the last two points, namely, reflection on the sample substrate, followed by scattering on the detected materials, and then another substrate reflection. Based on these scattering events, the waves interfere coherently, which produces the effective form factor. In the present thesis, cylindrical symmetry is used to describe the form factor. A paracrystalline lattice is assumed to describe the structure factor, where the cylinders have a short-range order rather than a long-range order. To describe the spatial arrangement (structure factor) of the objects, a one-dimensional paracrystal is used, in which the paracrystal objects are arranged periodically and the deviation from the ordered position for the cylinders increases with increasing distance from the target cylinder. With one-dimensional paracrystal, the arrangement is independent of the orientation in the system.

In the present thesis, only the horizontal line cuts at the Yoneda region are modeled to obtain the lateral structures. Therefore, an effective interface approximation can be employed assuming that scattering occurs at only one specific surface, which allows for the decoupling of the height with the radii for the scattering objects.[75] The local monodisperse approximation (LMA) is used to include objects with different sizes. It is assumed that each object only scatters with those of similar form and structure factors, rather than with objects of different form and structure factors. It means that respective objects and structures are independent of each other. Therefore, the total scattered intensity can be regarded as a sum of individual intensities scattered by single domains of monodisperse objects.[76]

2.4.4 Grazing-incidence small-angle neutron scattering

For grazing-incidence small-angle scattering, not only X-rays but also neutrons can be used as a probe. In this case the technique is called GISANS. Most of the theory introduced can be applicable to GISANS because the Helmholtz equation used for X-rays is similar to the Schrödinger equation used for neutrons. However, since X-rays are electromagnetic waves, they interact with the electron clouds, whereas neutrons interact with the atomic nuclei. Therefore, the contrast for a given material is different for X-rays and neutrons. Because the neutron contrast depends on the constitution of the atomic nuclei, the contrast is sensitive to isotopes. In the present thesis, GISANS is performed in a time-of-flight (TOF) mode with a broad spectrum of wavelengths, instead of a monochromatic beam. Determining the energy of

each single incoming neutron by measuring its time of flight allows to obtain a whole set of 2D GISANS patterns at once, with each of them measured with a different effective incident energy. Therefore, GISANS patterns cover different q_y ranges in one measurement, depending on the applied energy binning of the neutrons.

According to the deBroglie wavelength determined by

$$\lambda = \frac{h}{p(v_n)}, \tag{2.23}$$

where h is the Planck's constant, and $p(v_n)$ is the momentum of the neutrons depending on the velocity of the neutrons v_n, neutrons with a long wavelength show a low velocity, which is easier to be influenced by the gravity. Due to the influence of the gravity, the neutrons are deflected into the –z direction on a parabola, indicated in blue in Figure 2.14b.

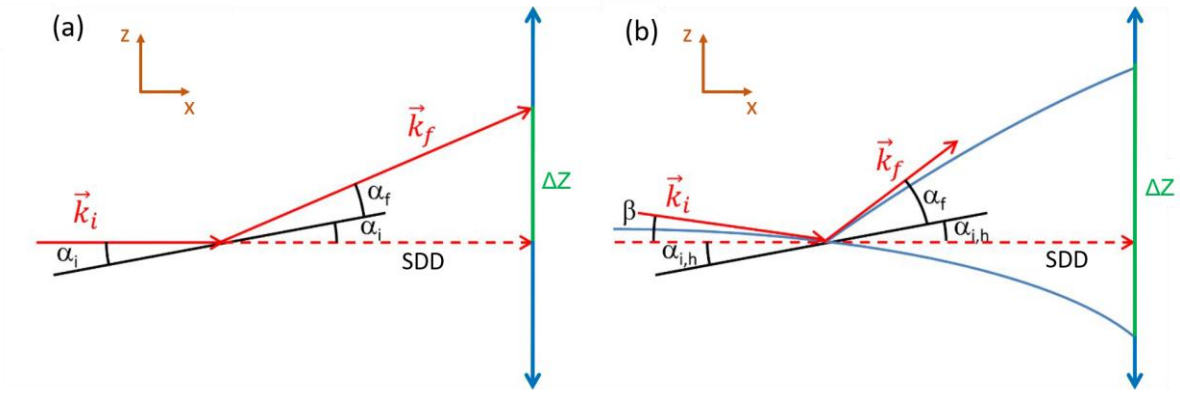

Figure 2.14 Influence of gravity on TOF-GISANS measurement: (a) without and (b) with the influence of gravity in the xz-plane. The detector is indicated in blue with arrows. This picture is based on Ref.[77]

3. Characterization methods

In this chapter, the used characterization techniques are introduced. The structural characterization of the nanostructured ZnO films and the ZnO based active layers are performed via both real- and reciprocal-space imaging methods, which are given in section 3.1. Section 3.2 describes the spectroscopic and electronic characterizations of the ZnO films and the corresponding active layers. For all the mentioned characterizations, the basic working principle and the parameters for measuring are given in the following sections.

3.1 Structural characterization

To improve the photovoltaic performance of the fabricated hybrid solar cells, the morphology, crystallinity and film thickness of the active layers are important to be investigated. In this section, the morphological characterizations including both, surface and inner morphologies are introduced. X-ray diffraction (XRD) to measure the crystalline ZnO is also explained. Besides, height profilometry is described in this section as well.

3.1.1 Optical microscopy

Optical microscopy (OM) can provide us the information on a large length scale, such as the structure and the homogeneity on micrometer length scale as well as the size of the electrodes for solar cells. A series of lenses are used to magnify images of small objects when illuminated with white light. For optical microscopy measurements, an Axiolab A microscope (Carl Zeiss) combined with a PixeLink USB Capture BE 2.6 charge coupled device (CCD) camera is used to collect images with a resolution of 1280×1024 pixels. Various magnifications can be obtained, which is shown in Table 3.1. To analyze the images, the software ImageJ v1.42q[2] is used.

Table 3.1 Resolution of the optical microscope for the different magnifications.

magnification	resolution [μm/px]
1.25x	6.26
2.5x	3.11
10x	0.82
50x	0.17
100x	0.082

3.1.2. Scanning electron microscopy

Scanning electron microscopy (SEM) is another imaging technique but with higher resolution than OM. Instead of using visible light, SEM uses electrons to get the images. With a shorter wavelength of the electrons, SEM can be used to detect the surface morphology on nanometer length scale, therefore providing images of great clarity of the sample surface. In the present work, SEM is widely used to probe the surface morphology of ZnO and the ZnO/P3HT active layers.

To generate the electrons, two ways are generally used. One is produced by a strong electrostatic field (field emission) and the other is from a hot filament (thermionic emission). Then the generated electrons are accelerated with a voltage of several kV, followed by focusing on the sample surface via electrostatic and magnetic lenses. The sample surface is scanned in a line-wise manner. When the incident electrons interact with the sample surface, secondary electrons are emitted from the area very close to the specimen surface and collected by a detector. Generally, beam size, the incident angle between beam and sample surface, and surface morphology have great influence on the intensity of the secondary electrons. Due to the constant beam size and incident angle, the obtained images with different contrasts are mainly determined by the sample's surface. A resolution below 10 nm can be obtained depending on the sample's topography and the materials. In addition, the detected signal is also influenced by the distance between the material and the detector. Higher structures appear brighter because of the detected higher intensity of the secondary electrons. Moreover, the conductivity of the materials also contributes to the contrast of the samples. Materials with different conductivity exhibit different brightness. Besides the generated secondary electrons, the backscattering of the electrons and cathodoluminescence also occur. However, mostly, these are not used to generate images.

In this thesis, a Zeiss Gemini Ultra Plus field emission scanning electron microscope is used at an electron accelerating voltage of 3 kV. All SEM images are processed by the software ImageJ. Silicon substrates are used to measure SEM of samples to prevent over charging.

3.1.3 Atomic force microscopy

Atomic force microscopy (AFM) is a powerful tool to detect the surface morphology of the samples as well as the height of the structures. Both, the inorganic and organic films with structures in a magnification of Angstrom can be investigated. The working principle of AFM is mainly based on the interaction of the surface atoms of the sample and a small tip with a radius of a few nanometers. A close tip-to-surface distance is required. Three modes are commonly used, namely the contact mode, the non-contact mode and the tapping mode.

Among those the tapping mode is used in the present thesis due to the obtained high resolution without damaging the samples or distorting the image data. With tapping mode, the tip is repeatedly touching the sample surface, which is moved in the xy-plane beneath the tip via a piezo controlled stage.

In the present investigations a MFD-3D AFM (Asylum Research) is used in a tapping mode. The used tip, with a curvature radius of 7 nm, is mounted onto a cantilever (OMCL-AC240TS-R3, Asylum Research), with the oscillation being set to a frequency of about 100 kHz. The software Gwyddion 2.31 is used to analyze the images, mainly to extract the height information and the roughness of the samples.

3.1.4 Height profilometry

Profilometry is a useful method to measure the height differences of the samples, especially to measure the film thickness. A DektakXT®stylus profilometer is used in the present thesis. To measure height differences, a diamond-tipped stylus is brought down to contact with the sample surface. The stylus scans the sample's surface by moving the sample, which is mounted on a motorized sample stage, forth and back. The information of the height differences is then converted to a digital signal by a linear variable differential transformer. To investigate the film thickness, a scratch is made on the sample to create a height difference between the film's surface and the substrate. When the stylus scans over the scratch, the height difference between the film surface and the substrate surface is supposed to be the film thickness. For each sample, six scratches are made at different places to get a statistical film thickness value. The used contact force of the stylus onto the sample is 1 mN, and the scan speed is 100 μm s^{-1}.

3.1.5 X-ray diffraction

X-ray diffraction (XRD) is a powerful tool to investigate crystalline materials. One can get information about the crystalline structure, crystal size and the degree of crystallinity. In the present thesis, the crystal structure of ZnO is measured by a Bruker D8 ADVANCE X-ray diffractometer. A copper anode is operated at 40 kV and 40 mA to generate the X-ray beam, which has a wavelength of λ_{Cu,K_a} = 0.1541 nm. The X-rays hit on the sample with an incident angle θ. The specularly reflected beam is detected by a detector located at the same angle θ. The coupled $\theta/2\theta$ mode is applied in the present thesis. Since the ZnO films in the present thesis are very thin, a long measurement about 10 h is performed on the samples. The substrates used for measuring XRD are silicon, which show a strong and typical peak at 2θ=33° position assignable to the (100) Bragg peak. To see the peak of ZnO more clearly, the peak from silicon is not measured. Slits are used to adjust the size and the intensity of the X-ray beam resulting

in different resolution and intensity of the peaks in the XRD measurements. In the present investigations, two slits of 0.6 mm are used to get a good quality of the XRD spectra, with one located between the beam source and the sample and the other between the sample and the detector. The footprint on the sample is usually a horizontally quite broad and vertically narrow beam due to the slits and quite a large incident angle, resulting in a short footprint in beam-direction. Therefore, the size of the sample is required to be sufficient large to ensure the experimental accuracy.

3.1.6 Grazing-incidence small-angle X-ray scattering

Grazing-incidence small-angle X-ray scattering (GISAXS) is used to probe the structural lengths in the range of 1 nm to 1 μm present in the bulk of the films. The theory on this technique is introduced in section 2.4.3. All the measurements shown in this thesis are performed at P03 beamline of PETRA III storage ring at DESY, Hamburg, Germany.

As shown in Figure 3.1, the X-ray beam impinges the sample with a very small angle and then is scattered by the sample. The scattered signal is collected by a 2D detector. In the present investigations, the wavelength of the X-ray beam is constant and the size of the detector is limited. Therefore, the q_y range recorded depends on the sample-detector distance (SDD). In other words, the length scales accessible in the investigated films is determined by the SDD. Generally the SDD is in the range of 3 to 5 m for GISAXS measurements. Because of this long distance between the detector and the sample, an evacuated flight tube is installed in the pathway of the beam to minimize scattering from air. The flight tube can be adjusted according to the SDD before the measurement.

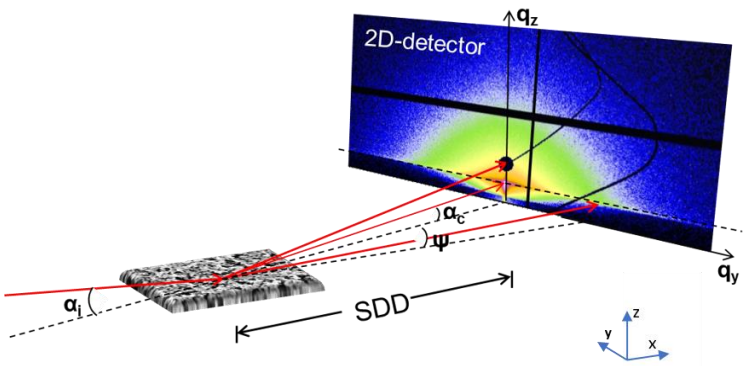

Figure 3.1 Schematic presentation of a grazing-incidence small-angle X-ray scattering (GISAXS) setup with a general SDD in the range of 3-5 m and a characteristic incident angle below 1 deg..

The incident angle is carefully selected to penetrate the whole thickness of the films with high sensitivity. Therefore, the incident angle should be larger than the critical angle of the investigated films, but not a very high angle (normally less than 1°), which would decrease the intensity of the signal. For the GISAXS measurement, two kinds of detectors are used to record the scattered signal. One is the Pilatus 1M (Dectris) detector (981×1043 pixel arrays), with each pixel possessing a size of 172×172 μm^2. The other one is the Pilatus 300K detector, similar to the 1M detector, but with less pixels (487×619 pixels). To prevent the detector from oversaturation, both the specularly reflected beam and the directly transmitted beam are blocked with beamstops.

Vertical and horizontal line cuts are performed for the 2D GISAXS data with the software DPDAK (Gunthard Benecke, DESY Hamburg & MPIKG Potsdam).[78] Vertical line cuts are done along q_y=0, which provides information about the structure perpendicular to the substrate whereas the horizontal line cuts along the Yoneda peak give information on lateral structures parallel to the substrate. To get a quantitative analysis about the length scale, the horizontal line cuts are fitted with a custom-made program. In this program, the model of distorted wave Born approximation (DWBA) using the effective interface approximation in local monodisperse approximation (LMA), which is introduced in section 2.4.3, is employed. A form factor describes the scattering objects (cylinder in this case) whereas the structure factor defines the distance between two neighboring objects. More details about the fitting are given in section 2.4.3.

3.1.7 Grazing-incidence small-angle neutron scattering

Grazing-incidence small-angle neutron scattering (GISANS) in time-of-flight mode (TOF-GISANS) is performed at the REFSANS instrument at the Heinz Maier-Leibnitz Zentrum, Garching, Germany.[79, 80] The basic setup for the GISANS measurement is very similar to that for GISAXS measurement. However, instead of a monochromatic neutron beam, a beam of neutrons with a wide range of wavelengths from 0.2 to 1.9 nm is used. A high-speed double chopper system is employed to define the neutron pulses. The neutron spectra are sliced into 22 wavelength channels with a wavelength resolution of $\Delta\lambda/\lambda$=10% for each channel.[81] By varying the wavelength of the neutrons, TOF-GISANS can provide us different (q_y, q_z) ranges in one measurement instead of varying the incident angle. Therefore, a wide range of length scales can be obtained via one TOF-GISANS measurement at a constant incident angle. The scattering signal is recorded on a two-dimensional (2D) ^{3}He detector with a SDD of 10.5 m.[79] A beamstop is installed at the direct beam position in front of the detector to avoid saturation. The incident angle of the incoming neutron beam is kept at a constant value of 0.38°. This

value is chosen to investigate the inner structure of the films at short wavelengths, and the surface morphology at long wavelengths. Therefore, both the surface and the inner morphology can be accessed with the variable neutron wavelengths in one TOF-GISANS measurement. Due to the relatively low neutron flux, the counting time for each sample is 20 h to obtain sufficient statistics. The substrates used in this thesis are large silicon substrates with a size of 60×60 mm^2.

To do the vertical and horizontal line cuts, the software Fit2D (Andy Hammersley, 1987-2005, ESRF, Grenoble) is used. From the vertical line cuts, the SLD of the probed samples including the ZnO based hybrid films can be precisely determined from the evaluation of the wavelength-dependent critical angles. In detail, the extracted critical angles are plotted as a function of the neutron wavelength and then a linear function is used to fit that. From the slope, one can obtain the SLD value according to Equation 2.17 in section 2.4.3. The fitting procedure of horizontal line cuts from the TOF-GISANS data is similar to that of GISAXS data, with extracting the length scales out of the fits.

3.2 Spectroscopic and electronic characterizations

In this section, the optical absorption, optoelectronic properties and conductivity measurements used to probe the mesoporous ZnO and ZnO/P3HT active layers are described. Moreover, the electronic characterizations of the efficiency and impedance of the complete photovoltaic devices are also introduced in this section.

3.2.1 UV-Vis spectroscopy

Two different PerkinElmer UV-Vis spectrometers, the Lambda 35 and Lambda 650S, are used in the present thesis. Both of them are equipped with a halogen lamp and a deuterium lamp to cover a complementary light spectrum from ultraviolet to visible light. The lamp of Lambda 35 is automatically switched at a wavelength of 326 nm and Lambda 650S at 320 nm, respectively.

Glass substrates are used to prepare a thin film on and the software UV Winlab is used to control the spectrometer. All the measurements in the present thesis are performed in a transmission mode. Grating monochromators are used to generate monochromatic beams. The monochromatic beam is split into two beams with same intensity before it reaches the sample, with one beam going through the probed sample and the other as a reference beam. Two separated detectors (photodiodes) are installed to detect the intensity of these two beams. The intensity for the reference beam is considered as 100% transmission as there is no absorption along this pathway whereas the intensity for the other beam should be smaller than 100%

transmission due to the absorption or scattering of the measured samples. Therefore, the absorbance *A* can be determined by using

$$A(\lambda) = -\log_{10}(\frac{I_t(\lambda)}{I_0(\lambda)}) = \alpha(\lambda)dlog_{10}e. \quad (3.1)$$

This is called Beew-Lambert's law, where $I_0(\lambda)$ and $I_t(\lambda)$ are the initial and transmitted intensities, respectively, $\alpha(\lambda)$ is the material specific absorption coefficient, d is the film thickness and *e* is the Euler's number.

In order to remove the absorption of the glass substrate, it is important to mention that all the absorption for the detected samples is obtained by removing the absorption of a bare glass substrate manually. As glass substrates show an absorption below 290 nm, the transmission measurements are performed above 290 nm to avoid the influence of the glass absorption.

3.2.2 Photoluminescence spectroscopy

Photoluminescence (PL) is light emission from the samples upon photoexcitation. After absorbing photons by the semiconductor materials, photons with a longer wavelength will be emitted. In the present thesis, PL spectra are recorded with a Fluorolog-3 FL3-22 (Horiba Jobin Yvon GmbH) spectrometer equipped with a water-cooled R928 PMT photomultiplier tube mounted at a 90° angle. A Xenon discharge lamp is used as the light source. Samples are excited with a monochromatic beam with a wavelength of 460 nm. Information of the exciton dissociation for the ZnO/P3HT hybrid films can be revealed by recording the emitted PL signal. For the ZnO/P3HT bulk heterojunction films a decreasing intensity of the PL signal indicates a reduced recombination of the generated charge carriers in the active layer. This is known as PL quenching. The charge carriers are spatially separated and transported far from each other, therefore leading to the decreased probability for recombination. From PL analysis, the improved charge carrier yield and the transport behavior in solar cells can be investigated. Moreover, samples are excited at a wavelength of 325 nm to investigate the defects induced emission in the ZnO films by investigating the electron transferring from sub-bands to valence band.

3.2.3 Electrochemical impedance spectroscopy

Impedance is a measure of the ability of a circuit to resist the flow of the electrical current. Unlike resistance, impedance exhibits much more complex behavior to an AC voltage, not limited by the simplifying properties. It is a powerful tool for investigating the response of an electrochemical system to an applied potential and for unraveling complex non-linear processes. The frequency dependence of this impedance can reveal underlying chemical processes on a

surface. In the present thesis, the kinetics of the interfacial charge transfer process in the ZnO based ssDSSCs are probed. The charge transfer process at the interface in the active layers are investigated. The data are collected with an electrochemical workstation under simulated AM1.5 solar illumination (100 mW cm^{-2}) with a solar simulator (Solar Constant by K. H. Steuernagel Lichttechnik GmbH) at open-circuit potential. All the measurements are performed at ambient temperature and humidity.

3.2.4 I-V characterization

To characterize the photovoltaic performance of ssDSSCs, I-V curves are probed with a Keithley 2400 sourcemeter. An external bias is applied to probe the devices under simulated solar illumination. AM 1.5 solar illumination with the light intensity of 100 mW cm^{-2} is provided by the solar simulator Solar Constant 1200 (K.H. Steuernagel Lichttechnik GmbH) equipped with a rare earth Xenon lamp. A silicon-based calibration solar cell (WPVS Reference Solar Cell Typ RS-ID-3 by Fraunhofer ISE) is used to calibrate the light power density to 1000 W m^{-2}.

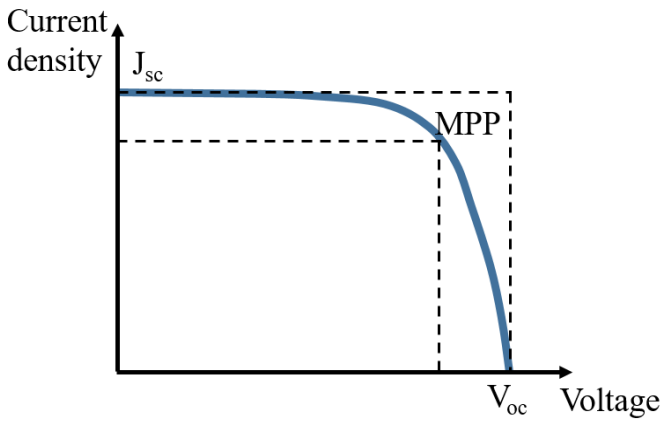

Figure 3.2 An illustration of an I-V curve of a solar cell. The V_{oc}, J_{sc} and maximal power point (MPP) are indicated. The small and large rectangles indicate the maximal output power and the theoretical maximal output power, respectively. Adapted from Ref.[82]

From the I-V curves as shown in Figure 3.2, typical parameters (including the open circuit voltage V_{oc} for J=0, the short-cut current density J_{sc} for V = 0 and the maximum power point MPP where the power density $P = J*V$ is maximum), which are important to investigate the photovoltaic performance, can be extracted. In principle, V_{oc} depends on the band states of the n- and p-type semiconductors in the active layers, whereas J_{sc} is determined by many factors, such as exciton generation, the following charge carrier generation, transportation and

extraction. The fill factor (*FF*) can be calculated from the ratio between the power at the MPP (indicated by the small rectangle) and the theoretical maximum possible power of $P_{max}=J_{sc}*V_{oc}$ (indicated by the large rectangle) as shown in

$$FF = \frac{P_{MPP}}{P_{max}} = \frac{V_{MPP}J_{MPP}}{V_{oc}J_{sc}} . \quad (3.2)$$

The power conversion efficiency (*PCE*) is obtained from the ratio of the output power (P_{out}) and the input power (P_{in}) for the devices as shown in

$$PCE = \frac{P_{out}}{P_{in}} = \frac{V_{oc}J_{sc}FF}{P_{AM1.5}}, \quad (3.3)$$

with the input power density in the present thesis following $P_{AM1.5}$ = 100 mW cm^{-2}.

3.2.5 External quantum efficiency

The external quantum efficiency (EQE) indicates the amount of current that the solar cell will produce when it is irradiated by photons of a particular wavelength. With integrating the efficiency over the whole solar electromagnetic spectrum, the amount of current produced when exposed to sunlight can be evaluated. The EQE can be determined by the ratio of the number of charge carriers to the incident photon numbers as written in

$$EQE = \frac{electrons/sec}{photons/sec} = \frac{(current)/(charge\ of\ one\ electron)}{(total\ power\ of\ photons)/(energy\ of\ one\ photon)}. \quad (3.4)$$

Therefore, the EQE depends on both the light absorption and the charge carrier generation. To improve the EQE, more photons should be absorbed by the active layer to provide the opportunity to generate more charge carriers. The ideal EQE graph should be a square shape with 100% efficiency at each wavelength. However, for most solar cells the EQE is reduced due to many factors. The same mechanisms that affect the *PCE* also affect the EQE value.

In the present thesis, the EQE is measured with the aid of the "Quantum Efficiency/IPCE Measurement Kit". The used light source is a 300-watt Xenon arc lamp. Monochromatic light illuminates on the sample. Before the measurement the calibration is performed with a silicon reference diode. The software Oriel's TracQ Basic is used to adjust the measurement parameters.

4. Sample preparation

In this chapter, the materials and the processing route for the preparation of ZnO and for the fabrication of the corresponding solid-state dye-sensitized solar cells (ssDSSCs) are described. Moreover, the materials and processing routes for nanostructured ZnO/P3HT/P3HT-*b*-PEO active layers which show great promise in hybrid bulk heterojunction solar cells (HBSCs) are also given in this part.

Details about the materials used in the preparation process are given in section 4.1 along with the general specifications and characteristics of the different materials. Section 4.2 describes the processing of the fabricated samples. The ZnO mesoporous nanostructures prepared from a diblock copolymer assisted sol-gel method are introduced in section 4.2.1. Section 4.2.2 illustrates the various steps used to assemble the devices of ssDSSCs. The sol-gel synthesis of ZnO/P3HT/P3HT-*b*-PEO nanostructures for the application as active layers for HBSCs is described in section 4.2.3.

4.1 Materials

In this section, materials including inorganic metal oxide precursors, diblock copolymers which act as structure-directing agents, dye molecules, and p-type semiconductor are introduced.

Inorganic metal oxide precursors

As the precursor of ZnO, zinc acetate dihydrate (ZAD) is used in this work. It is purchased from Sigma-Aldrich (99.999% trace metals basis). The chemical formula is $Zn(CH_3COO)_2 \cdot 2H_2O$. It appears as white powder with a relative density of 1.84 g cm^{-3}. The chemical structure is illustrated in Figure 4.1a. The coordination geometry around the Zn atom is octahedral, as the Zn atom is bound to six oxygen atoms. Two oxygen atoms are provided by the two water molecules and four oxygen atoms by the acetate ligands (two O atoms per acetate group). It crystallizes in a monoclinic unit cell. For ZnO derived from ZAD, typically it crystallizes as wurtzite polymorph. Another precursor used is anhydrous zinc acetate (ZA), which is also purchased from Sigma-Aldrich (99.99% trace metals basis), with the formula of $Zn(CH_3COO)_2$. In anhydrous zinc acetate, the zinc is coordinated to four oxygen atoms to give a tetrahedral environment. These tetrahedral polyhedra are then interconnected by acetate ligands to give a range of polymeric structures as shown in Figure 4.1b.

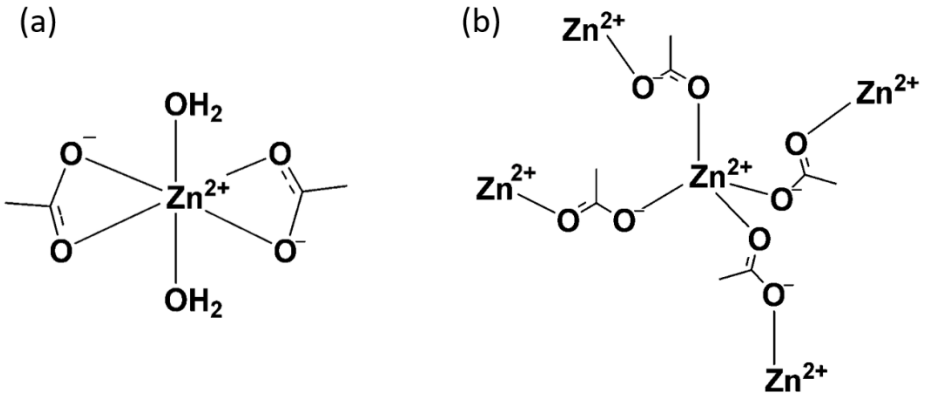

Figure 4.1 Chemical structure of the precursors for ZnO: (a) zinc acetate dihydrate (ZAD), (b) zinc acetate (ZA).

Diblock copolymer templates

For the mesoporous ZnO nanostructures, the diblock copolymers polystyrene-*block*-polyethylene oxide (PS-*b*-PEO) and polystyrene-*block*-4-polyvinylpyridine (PS-*b*-P4VP) are used as structure-directing templates in combination with sol-gel synthesis route to govern the length scales of the obtained ZnO nanostructures. Both of these polymers are purchased from Polymer Source Inc., Canada and used as received. The chemical structures are drawn in Figure 4.2. For the PS-*b*-PEO we used, the value of average molecular weights, M_n are 20.5 and 8 kg mol^{-1} for the PS and PEO blocks, respectively, with a polydispersity of 1.02. For PS-*b*-P4VP (M_n: 11.8-*b*-10.8 kg mol^{-1}), the polydispersity index is 1.12.

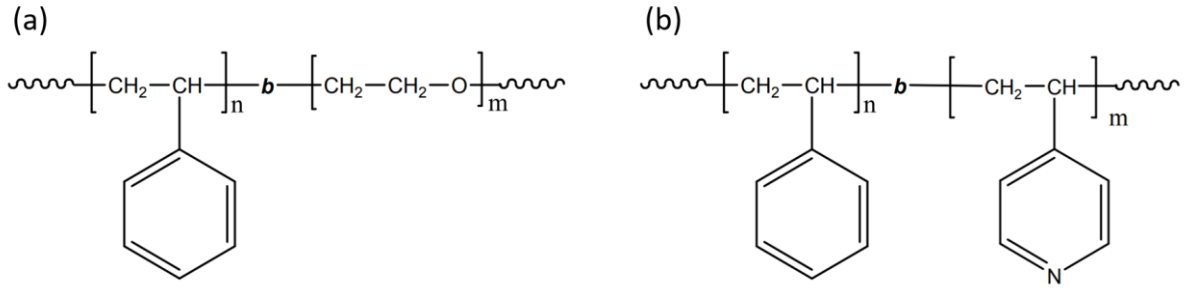

Figure 4.2 Chemical structures of the diblock copolymer templates used in this thesis: (a) PS-b-PEO, and (b) PS-b-P4VP. The degree of polymerization for the individual monomer unit is depicted by n and m.

The diblock copolymer P3HT-*b*-PEO is employed to modify the interfaces of the n-type semiconductor ZnO and p-type semiconductor P3HT in the active layers in HBSCs. Moreover, the length scales of ZnO and P3HT domains can be tuned by the selection of specific synthesis parameters. It is purchased from Polymer Source Inc., Canada, with the number average molecular weights, M_n = 3 kg mol^{-1} for the P3HT block and 90 kg mol^{-1} for the PEO block, respectively. The chemical structure of P3HT-*b*-PEO is shown in Figure 4.3.

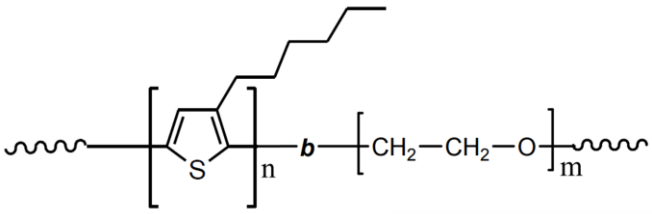

Figure 4.3 Chemical structures of the diblock copolymer P3HT-b-PEO used in this study. The degree of polymerization for the individual monomer unit is depicted by n and m.

Dye

In ssDSSCs, dye molecules are used to absorb light and then generate excitons. 5-[[4-[4-(2,2-Diphenylethenyl)phenyl]-1,2,3,3a,4,8b-hexahydrocyclopent[b]indol-7-yl]methylene]-2-(3-octyl-4-oxo-2-thioxo-5-thiazolidinylidene)-4-oxo-3-thiazolidineacetic acid (D205) is a pure organic dye without any metals inside. It is a purple indoline dye. As shown in Figure 4.4, in the center, the indoline group acts as an electron donating group. The cyanoacrylic acid serves as an electron accepting group, which is conjugated to the indoline group. The pendant carboxylic acid in this functional group benefits the anchoring of the dye molecules to the polar surface of ZnO. The rhodanine ring is beneficial for high electron injection yields. The phenyl rings show advantages to stabilize the central part.

D205 used in the study is purchased from Sigma Aldrich and used directly without any further treatment. 0.3 mM D205 and 0.6 mM chenodeoxycholic acid are dissolved in a mixture of acetonitrile and tert-butanol at a volume ratio of 1:1. Chenodeoxycholic acid is beneficial for hindering the aggregation of dye molecules. The aggregation decreases the probability for dye molecules to bind to the ZnO surface. Moreover, the π-stacked aggregation of dyes on the nanostructured ZnO photoanodes tends to hamper efficient photocurrent generation from dye molecules. Thus, reducing dye-aggregation through the addition of chenodeoxycholic acid is crucial during the fabrication of ssDSSCs. The final solution is stored away from light at room temperature.

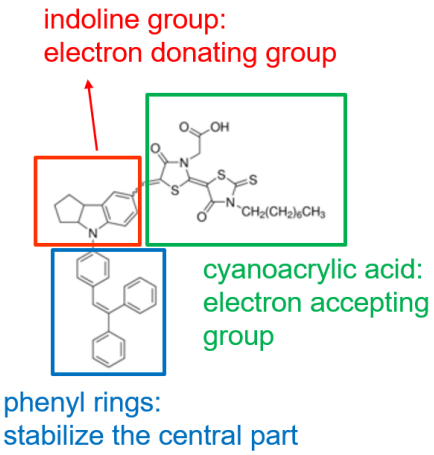

Figure 4.4 Chemical structures of D205 used in the study. The functional groups is indicated in the figure.

p-type semiconductors

Besides the n-type semiconductor, the p-type semiconductor is also important. It is used to provide a pathway for positive charge carriers to be extracted to their corresponding electrode. In this work, 2,2',7,7'-tetrakis(N,N di-p-methoxyphenylamine)9,9'-spiro-bi-fluorene (spiro-OMeTAD) is used. The chemical structure is shown in Figure 4.5a. For spiro-OMeTAD itself, the charge carrier mobility (in the order of 10^{-4} cm^2 V^{-1} s^{-1}) is low. To overcome this problem, 4-tert-Butylpyridine (4-TBP) and bis(trifluoromethane)sulfonimide lithium salt (Li-TFSI) are used to make a p-doping to improve the performance of ssDSSCs, in which 4-TBP hinders the recombination of charge carriers, while Li-TFSI increases the charge carrier density. For preparing the spiro-OMeTAD solution, 320 mg of spiro-OMeTAD, 4 mL chlorobenzene, 114 µL of 4-TBP, and 70 µL of Li-TFSI stock solution (520 mg mL^{-1} in acetonitrile) are mixed in a small bottle under nitrogen atmosphere.

For the active layers in HBSCs, a conducting polymer poly(3-hexyl-thiophene) (P3HT) is used. The chemical structure is shown in Figure 4.5b. P3HT consists of thiophene rings (the backbones) which are responsible for the conductivity of P3HT, and alkyl chains of six carbon atoms (side chains) which make the polymer soluble in organic solvents. It shows a band gap of 1.9 eV, with a HOMO of -5.2 eV and a LUMO of -3.3 eV. P3HT is a widely used electron donor material in organic photovoltaics (OPV), ssDSSCs and HBSCs.

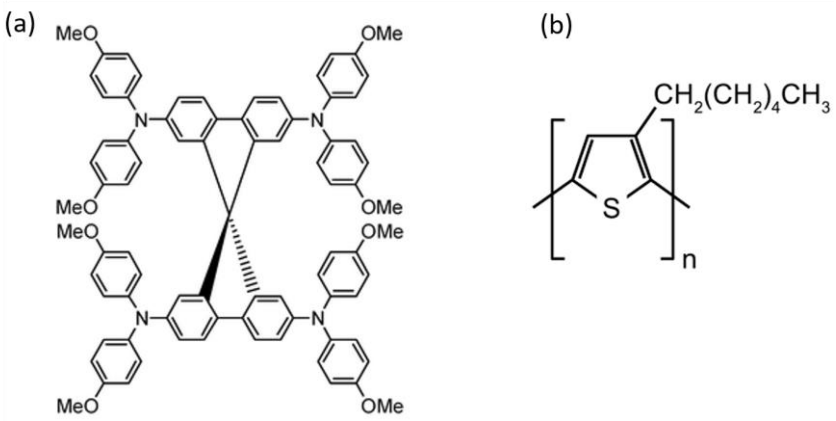

Figure 4.5 Chemical structures of the p-type semiconductors used in this study: (a) spiro-OMeTAD, and (b) P3HT. The degree of polymerization for the individual monomer unit is depicted by n.

4.2 Processing

For ZnO films and the corresponding ssDSSCs, several steps are involved to produce the final samples, including the preparation of the compact ZnO layer, mesoporous ZnO layer, backfilling of dye molecules and p-type semiconductors into the ZnO mesopores, and metal-electrode evaporation. Moreover, the steps of fabricating nanostructured active layers for HBSCs are described in this section as well.

4.2.1 Preparation of mesoporous nanostructures

The mesoporous ZnO films are synthesized from a sol-gel method assisted with a diblock copolymer. Two diblock copolymers are used as a template. One is PS-*b*-PEO, which makes it more likely to form foam-like structure with the used molecular weight M_n being 20.5-*b*-8 kg mol^{-1}. The other one is PS-*b*-P4VP, through which sponge-like ZnO structures are expected.

Substrate cleaning

The substrates used in the study are glass substrates (26 × 76 mm^2, Carl Roth GmbH) and silicon substrates (wafer with a diameter of 100 mm, (100)-orientation, Si-Mat), which are cut into smaller pieces with dimensions required for a specific experiment, using a glass cutter or a diamond. The substrates are then cleaned in an acid bath. 54 mL deionized water (H_2O), 84 mL hydrogen peroxide (H_2O_2, 30%), and 198 mL sulfuric acid (H_2SO_4, 96%) are mixed in that order, during which H_2SO_4 is added into the solution very slowly with the temperature always below 40 °C. After finishing the addition of the H_2SO_4, the temperature of the bath is elevated

to 80 °C slowly. Once the temperature is attained, the pre-cut substrates which are stacked in a teflon holder beforehand are soaked into the bath for 15 min. Then the substrates are taken out and put into a water bath subsequently. Afterwards, the substrates are frequently rinsed with deionized water, followed by drying them with an oil-free nitrogen flow.

Spin coating

Spin coating is one of the commonly used deposition methods to obtain a uniform thin film on a flat substrate. It is a fast non-equilibrium process which can be divided into three steps. First, the majority of the coating material is flung off the substrate due to the high angular speed. It is difficult to get a homogeneous film with a low-speed spinning (below 800 rpm), which is therefore not recommended. Second, the process is dominated by convection, which makes the majority of the solvent evaporate rapidly. Finally, the remaining solvent evaporates and a homogeneous thin film can be obtained on the substrate. One can adjust the film thickness simply by changing the angular speed as a higher speed results in a thinner film to some extent. Moreover, the concentration and the viscosity of the solution as well as the type of the solvent we used also have a great effluence on the film thickness. An empirical formula in case of films derived from pure polymer solutions is used to estimate the film thickness

$$d = C\omega^{-1/2} c_0 M_w^{1/4}, \tag{4.1}$$

with C being an empirical constant, ω the angular speed, c_0 the solution concentration, and M_w the molecular weight of the polymer.

In this study, a Delta 6 RC TT (Süss MicroTec Lithography GmbH) spin coater is used. The parameters of spin coating, including acceleration speed, angular speed of rotation and rotation time, are pre-set. The pre-cleaned substrate is placed on the rotation table of the spin-coater and is then held via an applied vacuum. The substrate should be horizontal to the ground. Next, a suitable amount of solution is loaded to cover the substrate and the spin coating process is started. Once the rotation stops, the sample is dismounted from the spin-coater and its back side is wiped with a clean tissue to remove residual solution.

Sol-gel synthesis templated with PS-*b*-PEO

To prepare the sol-gel solution of ZnO templated with PS-*b*-PEO, a so-called good-poor solvent pair is introduced. The good solvent dissolves both the blocks of the polymer well, which in present case is N,N-dimethylformamide (C_3H_7NO from Carl Roth GmbH; abbreviated as DMF, 99.8%). The poor solvent, in this case ethanolamine (MEA, 98%), only can dissolve the PEO blocks, which makes the PS blocks shrink and form the cores while the

PEO blocks form the coronas, hence resulting in dispersed micelles in the solution. In the study, the precursor for ZnO we used is zinc acetate dihydrate (ZAD, 99.999% trace metals basis), which is a commonly used precursor for ZnO. When the precursor is introduced to the solution, they prefer to incorporate into the PEO block via hydrogen bonds, electrostatic and Van-der-Waals interactions. To describe the steps in detail, a schematic illustration of the various steps involved in the synthesis route is shown in Figure 4.6. First, PS-*b*-PEO (200 mg) and ZAD (483 mg) are each dissolved separately in DMF (2 mL), and stirred for half an hour to get clear homogeneous solutions. The two solutions are filtered using a polytetrafluoroethylene (PTFE) filter with 0.45 µm pore diameter to remove the large particles which are not dissolved in the solution. 129 µL of MEA is then added to the polymer solution and stirred for half an hour further. Both, the polymer and precursor solutions, are then mixed together with the aid of a syringe pump, PHD 2000 infuse/withdraw, Harvard Apparatus, by using a constant infuse rate of 1 mL min^{-1} and then stirred at 80 °C for 1 h on a heated magnetic stirring plate. The final solution obtained is spin-coated (1000 rpm, 60 s) onto the pre-cleaned silicon (100) or glass substrate for further characterization. Directly after spin-coating the composite films are annealed at different temperatures for 1 h on a heating plate, which is an essential step to improve the self-assembly process of the diblock copolymer and to benefit the crystallization of ZnO.

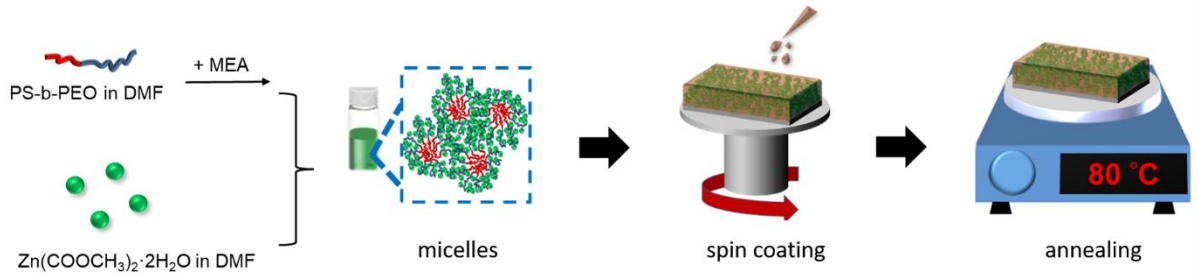

Figure 4.6 Schematic overview of the sol-gel synthesis of ZnO using PS-b-PEO as a template. Reprinted with permission from Ref.[83]

Sol-gel synthesis templated with PS-*b*-P4VP

Another diblock copolymer PS-*b*-P4VP with a molecule weight Mn of 11.8-*b*-10.8 kg mol^{-1} is also used as a template to tune the structure of ZnO films. Similarly, microphase separation is induced via the good-poor solvent pair of DMF and MEA. In this case, the precursor, still ZAD, is preferentially grown in the P4VP block. Again, the synthesis procedure for the ZnO preparation is a sol-gel process, but assisted with PS-*b*-P4VP. Typically, 120 mg ZAD is dissolved in 0.5 mL DMF, stirred for 30 min and then filtered using 0.45 µm Teflon filters.

Separately, different amounts of PS-*b*-P4VP (10 mg, 30 mg, 50 mg, and 70 mg) are dissolved in DMF (0.5 mL) and stirred for 30 min and then filtered using 0.45 µm Teflon filters. Next, 32 µL of MEA are added to the PS-*b*-P4VP solution and stirred for an additional 30 min, which leads to the formation of PS-*b*-P4VP micelles in the good-poor solvent pair mixture. Afterwards, the ZAD solution and the polymer solution are mixed together and then stirred for an additional 1 h. All the solutions are prepared and processed at ambient conditions. For film deposition, spin coating at 1000 rpm for 60 s is used on precleaned silicon (100) or glass substrates. The obtained thin films are thermally annealed at 160 °C or 240 °C for 1 h.

Sintering and UV-irradiation

To get pure ZnO films without any polymers inside, it is required to remove the polymers from the hybrid films. Sintering and UV-irradiation are most commonly used techniques to remove the polymers. UV light interacts with the bonds in the polymer to form free radicals, which then react further with oxygen in the atmosphere. Thus, long chain polymers are depolymerized into small molecules.[84] For the ZnO films templated by PS-*b*-PEO, UV-irradiation is performed for 24 h. To remove the template of PS-*b*-P4VP, two methods were applied. One is UV-irradiation for 24 h. The other one is sintering, which is carried out at 400 °C for 30 min with a heating rate of 375 °C h^{-1}. Sintering of the films is performed in air in a tube furnace by GERO or Hereaus instruments. After sintering the samples, they are allowed to cool to room temperature in the furnace. Afterwards, the nanoporous ZnO films can be obtained.

4.2.2 Solar cell assembly

ssDSSCs are fabricated with mesoporous ZnO nanostructures and spiro-OMeTAD as negative and positive charge carrier transport material, respectively. Dye molecules, D205 in this case, are attached to the surface of ZnO to absorb light. The typical steps involved in the fabrication process are demonstrated in Figure 4.7. The details about each layer are described below.

Substrate preparation

For the fabrication of ssDSSCs, a transparent electrode is used as the bottom electrode. Fluorine-doped tin oxide (FTO) coated glass sheets are purchased from Solaronix with a size of 10×10 cm^2. The resistance is about 15 Ω $□^{-1}$. The FTO substrates are cut to a suitable size to fit the size of the holder for gold evaporation and the final device measurement. To start the substrate preparation, first a small stripe of FTO is etched away as shown in Figure 4.7a to avoid short circuits in the device. Zinc powder and HCl (12 M) are used to etch away FTO which is about half the size of the electrodes. DI water is used to remove the remaining zinc

powder and the acid. To get clean substrates for the following deposition of the functional layers, four organic solvents are used in sequence in an ultrasonic bath for 10 min. The solvents I used are Alconox® detergent solution (16 mg mL^{-1}), ethanol (99.8%), acetone (99.9%), and 2-propanol (99.8%). An oil-free nitrogen flow is used to dry these substrates. To remove the impurities and contaminants from the substrate further, oxygen plasma is performed for 10 min.

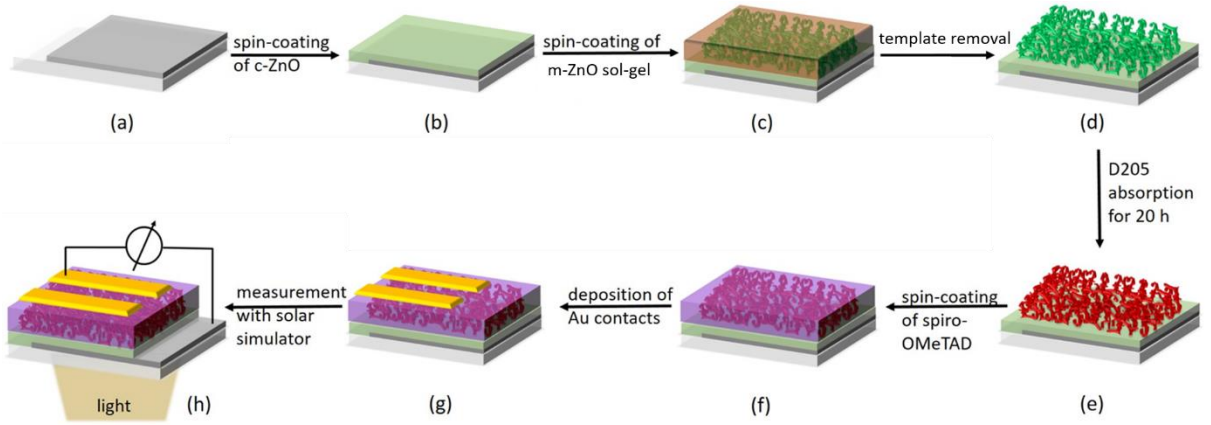

Figure 4.7 Schematic representation of the steps involved in the fabrication of a ssDSSC based on the nanostructured ZnO films. (a) Etching of FTO coated on glass substrates. (b) Formation of compact ZnO layer as a hole blocking layer. (c) Deposition of ZnO/diblock copolymer hybrid films from a diblock copolymer assisted sol-gel synthesis. (d) Removal of the diblock copolymer resulting in a mesoporous ZnO layer. (e) Adsorption of dye molecules into the nanostructured ZnO. (f) Backfilling of the ZnO structure with spiro-OMeTAD as the positive charge carrier transport material. (g) Evaporation of a gold back contact on top to finalize the solar cells. (h) Solar cell characterization under sunlight illumination. Reprinted with permission from Ref.[83]

Compact ZnO layers

The compact ZnO layer is used as hole blocking layer in this study. It is considered as an effective layer to prevent the recombination of the charge carriers at the electrode. It is introduced between the fluorine-doped tin oxide (FTO) and the mesoporous ZnO layer to avoid the transport of positive charge carriers to the FTO electrode. Moreover, due to the presence of the much denser layer of compact ZnO underneath the mesoporous ZnO layer, the probability of short circuits is reduced. Typically, a compact ZnO layer is spin coated following the procedure reported by Heo *et al.*[85] Briefly, 328 mg ZAD and 100 µL MEA are dissolved with vigorous stirring in 2 mL 2-methoxyethanol at 60 °C for 30 min. The ZnO solution is then spin-

coated on a cleaned FTO glass substrate at 2000 rpm for 60 s and finally annealed at 150 °C for 10 min.

Mesoporous ZnO films

Mesoporous ZnO films with different morphologies are prepared on the compact ZnO layer, which is beneficial for adsorbing more dye molecules on the surface of the porous ZnO structures. Two different diblock copolymers are used to tune the structure of the mesoporous ZnO with sol-gel synthesis which is described in section 4.2.1. After spin coating, annealing is performed to improve the self-assembly process, followed by removing the polymer template by UV-irradiation or sintering as demonstrated in section 4.2.1.

Dye loading

For ssDSSCs, the mesoporous ZnO films are required to load dye molecules to absorb visible light. After being treated with oxygen plasma for 10 min to clean the samples, the samples with mesoporous ZnO films are subsequently soaked into the solution of D205 for 20 h at ambient conditions. Afterwards, the samples are taken out from the dye solution and rinsed with acetonitrile to remove the superfluous dyes. Lastly, the dyed samples are dried with nitrogen as shown in Figure 4.7e, and stored in Petri dishes which are wrapped in aluminum foil to protect the sensitive dye from light.

P-type semiconductor backfilling

After loading dye molecules into mesoporous ZnO network, p-type semiconductors are required to be backfilled into the dyed ZnO films. In this case, spiro-OMeTAD solution with the concentration described in section 4.1 is spin-coated on top of the samples at 3000 rpm for 60 s as shown in Figure 4.7f. The details of this procedure is given in section 4.2.1.

Gold electrode

For ssDSSCs, a gold electrode is used as the counter electrode as shown in Figure 4.7g. Gold with about 160-200 mg is thermally evaporated for about 4 min to be deposited on the p-type semiconductor. Gold evaporation can only be started when the pressure in the chamber is less than $3 \cdot 10^{-5}$ mbar. The areas on the samples finally covered by gold are referred as pixels. The active area of one pixel of the solar cell is defined as the overlap of FTO and gold contacts, which is typically around 0.1 cm^2. The accurate area is evaluated via the ImageJ v1.42q software from optical microscopy images of each pixel.

4.2.3 Preparation of nanostructured active layers

The nanostructured ZnO/P3HT/P3HT-*b*-PEO hybrid films are used as active layers for HBSCs. The diblock copolymer P3HT-*b*-PEO is employed as a template in a sol-gel method to fabricate the hybrid films. Two kinds of solutions with different research highlights are prepared. One is prepared for spray coating, which is applied to illustrate the improvement of the morphology and the optoelectronic performance of the ZnO/P3HT films via the introduction of P3HT-*b*-PEO. The other one is prepared for comparison of the films with two coating methods, spin and spray coating, to investigate the influence of the deposition method on the morphology of the ZnO/P3HT/P3HT-*b*-PEO hybrid films. All the hybrid films are prepared at low temperatures.

Spray coating

Spray deposition is a process during which small droplets are dispersed in a gas and deposited on a substrate. A liquid is converted into small droplets with the aid of the energy provided by a compressed carrier gas. This process is referred to as atomization. At the exit point of the nozzle (commonly named as orifice), an angular and downward velocity of the solution caused by the lateral pressure differences drives the droplets apart from each other, widening the so-called spray cone. Therefore, the diameter of the cone enlarges and the density of the droplets decreases. Depending on the liquid inertia, surface tension, and aerodynamic forces on the jet, several spray regimes are identified as shown in Figure 4.8.

- Regime I: dense regime.
  After primary breakup, the collision and coalescence of droplets occur frequently. The droplets easily collide with their neighbors and merge together because of the abundant existence of droplets.
- Regime II: intermediate regime.
  In this regime, the dispersed phase dynamics is dominated by the continuous phase turbulence. The collision and coalescence of droplets can be neglected since the single droplet is far away from its neighbors.
- Regime III: dilute regime.
  In this regime, the continuous phase turbulence scarcely exists. Small and isolated droplets are presented instead. The spray cone is wide which enables a homogeneous deposition of the film. But the amount of the material that reaches the substrate is significantly reduced.

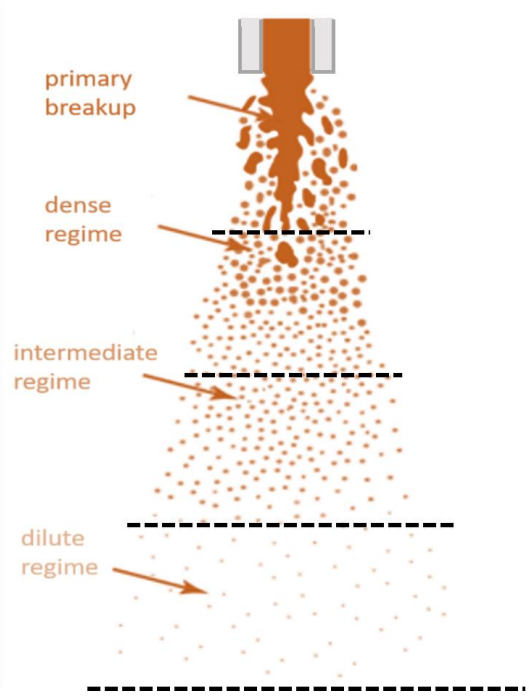

Figure 4.8 Schematic illustration of liquid atomization with three flow regimes. This picture is based on Ref.[86]

During spray coating, the nozzle-to-substrate distance, the pressure of the carrier gas, the orifice diameter, the flow rate of the solution, and the temperature of the substrate are the key parameters to control the solvent evaporation of the droplets. For example, if solvent evaporates completely during the droplet transport period, a layer of powders rather than a film is obtained on the substrate. A very small amount of solvent makes the formation of a continuous film possible since the droplets stick to the substrate and enable them to fuse with pre-arrived droplets. In the present thesis, a spray gun is mounted on a spray setup. The spray nozzle is perpendicular to the pre-cleaned substrate which is kept at 80 °C. The nozzle-to-substrate distance is 16 cm and the pressure of the carrier gas is kept at 2 bar during the whole spray coating process. The flow rate of the coating solution is adjusted to be 20-25 μL s^{-1}. Instead of a continuous spray deposition, a spray protocol of 10 s spray shots and 10 s pause between subsequent shots is used.

Sol-gel synthesis of ZnO/P3HT/P3HT-*b*-PEO

To investigate the morphology and corresponding optoelectronic performance improvement of the ZnO/P3HT active layers for the application in HBSCs via the introduction of P3HT-*b*-PEO, both the ZnO/P3HT and ZnO/P3HT/P3HT-*b*-PEO solutions are prepared by a sol-gel method, followed by spray coating to form films. Typically, 10 mg of P3HT and an appropriate amount

of the diblock copolymer P3HT-*b*-PEO are dissolved in a 4 mL mixture solution of DCB and DMSO (volume ratio of 7:1). The solution is stirred for 30 min at 80 °C to dissolve both, the P3HT and the PEO components completely in the solution. At the same time, 50 mg zinc acetate is dissolved in a different vial in the same mixed solvent and stirred for 30 min at 80 °C. Afterwards, 19.76 µL of MEA is added to the polymer solution and stirred for further 30 min at 80 °C. In the next step, both solutions are mixed together using a syringe pump, PHD 2000 infuse/withdraw, Harvard Apparatus, by using a constant infuse rate of 1 mL min^{-1} and then stirred for 1 h at 80 °C. Therefore, the sol–gel is obtained with P3HT as a charge carrier transport material and PEO chains as a template into which the precursor of ZnO is preferentially incorporated. Spray deposition is carried out subsequently onto pre-cleaned silicon (100) and glass substrates, which are kept at 80 °C. The obtained composites are then annealed at different temperatures below 160 °C for half an hour to obtain the final hybrid films.

To further investigate the ZnO/P3HT/P3HT-*b*-PEO hybrid films, ZnO/P3HT/P3HT-*b*-PEO solutions with various ZnO concentrations are prepared via the sol-gel method and the influence of the deposition method to the morphology of the active layers is investigated as well. The preparation procedures are similar to the sol-gel method described above. For spin coating, the solutions are prepared as follows. 20 mg of P3HT and 4 mg of P3HT-*b*-PEO are dissolved in a 2 mL mixture of DCB and DMSO (with a volume ratio of 7:1). The solution is stirred for 30 min to dissolve both polymers. At the same time, an appropriate amount of zinc acetate is dissolved in a separate vial in the same solvent mixture and stirred for 30 min. Afterwards, 24 µL of MEA is added to the polymer solution and stirred further for 30 min. After mixing the zinc acetate solution with the polymer solution, further stirring for 1 h is carried out. All the stirring procedures are performed at 80 °C. Spin coating is carried out under ambient conditions at 1500 rpm for 60 sec. For spray coating, the initial solution is diluted two times with the DCB/DMSO mixture solvent to avoid any blockage of the spray gun. The parameters used for the spray coating setup are described above. Finally, the spin and spray coated films are annealed at 80 °C for 30 min to obtain well-organized hybrid films.

5. Nanostructured ZnO films templated with PS-*b*-PEO

Parts of this chapter have been published in the article: Morphology control of low temperature fabricated ZnO nanostructures for transparent active layers in all solid-state dye-sensitized solar cells (K. Wang *et al.*, J. Mater. Chem. A, 2018, 6, 4405-4415, DOI: 10.1039/c7ta10654h).

In the last few decades, dye-sensitized solar cells (DSSCs) have shown great promise in the solar energy conversion field due to their convenient and low-cost fabrication.[4, 87-89] An efficiency of over 13% has been achieved with a liquid electrolyte DSSC.[5] Nevertheless, these DSSCs suffer from cycling stability problems resulting from electrolyte leakage and corrosion.[19, 90] Many researchers have replaced liquid electrolytes with quasi-solid electrolytes to improve the stability. However, a more promising approach is to use a solid-state p-type semiconductor to build all solid-state DSSCs (ssDSSCs). P3HT is one of the most commonly used p-type semiconductors to transport the positive charge carriers to the corresponding electrode due to its conducting properties.[91, 92] However, due to the limited pore size of the n-type semiconductor, ZnO in this case, spiro-OMeTAD with much smaller molecular weight shows an easier way to be backfilled into the ZnO films.[15, 93] Doped with TBP and Li-TFSI, the properties of the hole mobility and conductivity improves significantly. Typically, a ssDSSC involves a wide band gap semiconducting nanostructured metal oxide film as a negative charge carrier transport material, a dye molecule as a sensitizer, and a p-type organic semiconductor as a positive charge carrier transport material. In the present work, ZnO is used as an n-type semiconductor mainly due to the good electron mobility and low crystallization temperature.[19, 94, 95] It is reported that ZnO can crystallize below 100 °C.[96-98] The low crystallization temperature makes it possible to fabricate lightweight and flexible solar cells on polymer substrates, which are heat-sensitive and will undergo thermal degradation at high temperatures. Moreover, low temperature fabrication is beneficial for reducing the fabrication cost and payback time as well.

Regarding ZnO nanostructures fabricated at low temperatures, most reports are about one-dimensional (1D) crystalline ZnO, such as nanowires and nanorods.[99-104] These 1D nanostructures are reported to show a high conductivity.[99, 104, 105] However, for ssDSSCs, such 1D nanostructures have limitations with respect to their surface-area-to-volume-ratio, which is a drawback for having a maximum amount of adsorbed dye molecules. Therefore, in the

present work, a novel route is introduced to fabricate different morphologies of three-dimensional (3D) mesoporous ZnO (m-ZnO) nanostructures (including foam-like, worm-like and sphere-like structures) through a sol-gel method with processing temperatures well below 200 °C. The resulting 3D ZnO nanostructures are expected to offer a large surface to load dye molecules and also a large interface between ZnO and dyes, which is beneficial for improving the charge carrier density, and thus, attain higher photocurrents and efficiencies.

PS-*b*-PEO is used as a template to design the morphology of the ZnO nanostructures. Through the so-called good-poor solvent pair, microphase separation is induced. Due to the competing forces arising from the enthalpic contribution of mixing and the entropic penalty associated with elongating the polymer chains, the adopted structures depend on the annealing temperature greatly. A fabrication route of ZnO nanostructures is given in section 5.1. Both the surface and the inner morphology of ZnO films are detected with real space imaging techniques and grazing-incidence small-angle X-ray scattering (GISAXS) as described in section 5.2. The conductivity and optoelectronic properties of ZnO films are given in section 5.3. Moreover, on the basis of these film morphologies, all ssDSSCs are fabricated with every layer deposited at low temperatures. These ssDSSCs all show a transparent active layer, which demonstrates the possibility for building-integrated solar cells. Section 5.4 demonstrates that morphology control of the ZnO thin films at low temperature via polymer assisted sol-gel method results in improved photovoltaic performance of ssDSSCs.

5.1 Fabrication route of ZnO nanostructures

The ZnO nanostructures in this work are fabricated with a sol-gel method combined with the diblock copolymer PS-*b*-PEO which acts as a template. A schematic representation of the steps involved in making foam-like ZnO nanostructures at 80 °C via PS-*b*-PEO assisted sol-gel route, including a subsequent all ssDSSC fabrication, is shown in Figure 5.1. First, a solution containing micelles is prepared (Figure 5.1a), with PS block as the core and PEO block as the corona. The zinc precursor prefers to incorporate into the PEO block. The solution is spin-coated on pre-cleaned substrates to get thin composite films of ZnO and polymer (Figure 5.1b) and annealed for 1 h (Figure 5.1c) to improve the self-assembly of the nanostructure. After removing the PS-*b*-PEO template by UV-irradiation (Figure 5.1d), the resulting mesoporous ZnO films (Figure 5.1e) are used for further characterizations. For ssDSSCs, the device layout (Figure 1f) is FTO/compact ZnO (c-ZnO)/m-ZnO/dye/spiro-OMeTAD/Au on glass. The annealing temperature plays a crucial role to control the ZnO morphology, which also causes great differences in the device performance.

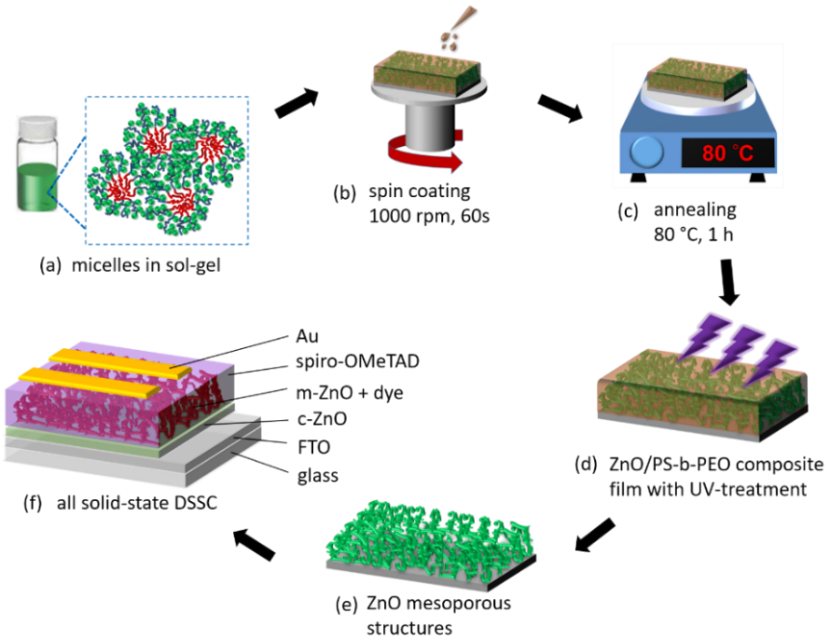

Figure 5.1 Schematic representation of (a-e) the steps involved in the fabrication of the mesoporous ZnO films and of (f) the corresponding all solid-state DSSC. The annealing temperature, here 80 °C is varied. Reprinted from Ref.[83] *with permission from The Royal Society of Chemistry.*

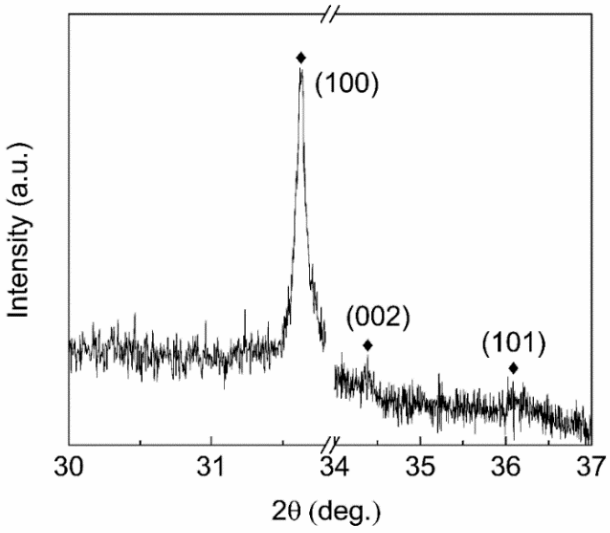

Figure 5.2 XRD pattern of mesoporous ZnO film annealed at 80 °C after polymer removal. The Bragg peaks at 31.6, 34.4, and 36.1 deg. correspond to crystal planes of (100), (002) and (101), respectively. The curve is interrupted from 32.5 to 34 deg. to remove the strong Bragg peak of the Si substrate. Diamonds indicate the Bragg peaks of ZnO wurtzite phase. Reprinted from Ref.[83] *with permission from The Royal Society of Chemistry.*

The XRD data of the foam-like ZnO films, which are prepared at 80 °C and shown in Figure 5.2, reveal the formation of wurtzite phase of ZnO, which is the most suitable ZnO phase for DSSCs because of its superior charge transport properties.[106]

5.2 Surface and inner morphology

Regarding ssDSSCs, both the surface and the inner morphology are important since the dye molecules need to be infiltrated into the pores and the interfaces between ZnO and dyes play a critical role in exciton separation. Moreover, the generated charge carriers are required to be transported along the corresponding p-type and n-type semiconductors to their corresponding electrode. It is reported that the inner morphology might also be different from the surface morphology which makes the investigation of both surface and inner morphology necessary. The static investigation of ZnO films with variable morphologies, which are fabricated at different annealing temperatures, are given in section 5.2.1. Section 5.2.2 reveals the kinetic evolution of the worm-like structure.

5.2.1 Static investigation of ZnO films annealed at different temperatures

In this section, both the surface and inner morphologies of the mesoporous ZnO films prepared at different annealing temperatures are presented. When increasing the annealing temperature, the morphology changes from foam-like, worm-like, to sphere-like structures, which indicates the importance of the annealing temperature to the morphology of the ZnO films templated by PS-*b*-PEO. In this section, all the detected films are pure ZnO films without any polymers inside.

Surface morphology

SEM images of the ZnO nanostructures annealed at different temperatures are presented in Figure 5.3. All the films presented are treated with UV-irradiation to remove the diblock copolymer from the films. It is shown that the morphology changes dramatically when increasing the annealing temperature, indicating that the annealing temperature plays a great importance in the morphology tuning. At 80 °C (Figure 5.3a), the ZnO films exhibit a high interconnectivity of foam-like structures, which provides a continuous pathway for electron transport and a good percolation path for the backfilling of spiro-OMeTAD. The introduction of amphiphilic diblock copolymer PS-*b*-PEO induces a micro-phase separation with the aid of the so-called good-poor solvent pair of DMF and MEA. The preferential incorporation of ZnO into the PEO part enables control of the ZnO nanostructures. The foam-like structure of ZnO films is similar to the reported structure.[107] When increasing the temperature to 100 °C (Figure

5.3b), some large ZnO particles appear at the surface randomly. Upon increasing the temperature further to 120 °C (Figure 5.3c) and 140 °C (Figure 5.3d), the films show a worm-like structure. Small particles interconnect with each other, therefore forming curved lines. In this case, the ZnO films provide a good pathway for negative charge carriers to be extracted to the corresponding electrode, which is beneficial for application in ssDSSCs. With the temperature increasing to 160 °C (Figure 5.3e) and 200 °C (Figure 5.3f), it is observed that sphere-like structures with a high monodispersity are present at the surface.

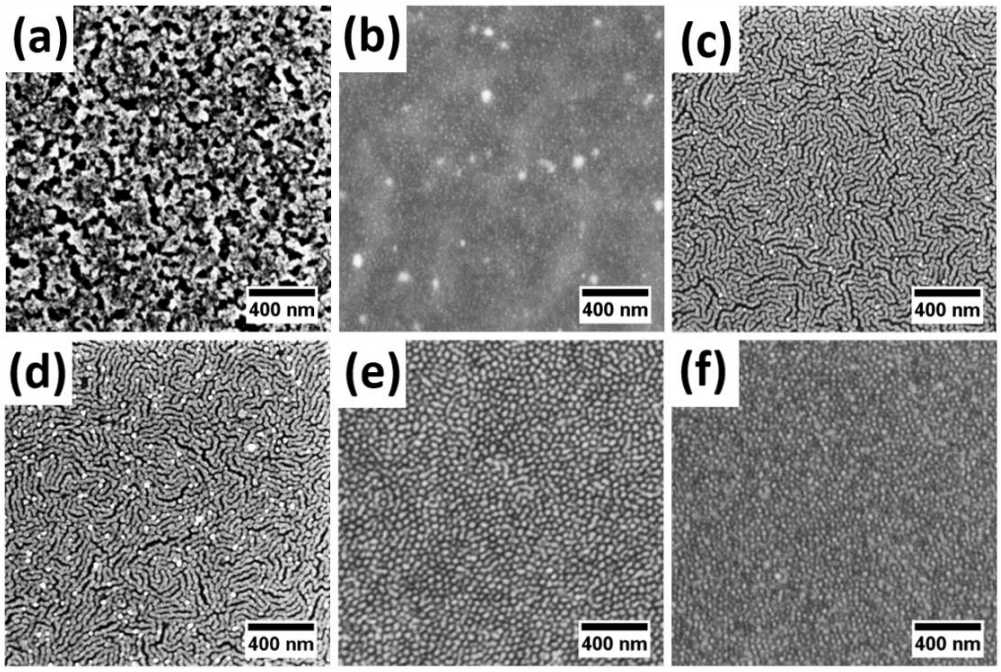

Figure 5.3 SEM images of mesoporous ZnO films with different morphologies which are annealed at different temperatures: (a) 80 °C, (b) 100 °C, (c) 120 °C, (d) 140 °C, (e) 160 °C, and (f) 200 °C. Reproduced from Ref.[83] with permission from The Royal Society of Chemistry.

The SEM images with various magnifications for the worm-like ZnO films are shown in Figure 5.4. At low magnification (Figure 5.4a), the SEM image indicates a very homogeneous film. When enlarging the image further (Figure 5.4b and c), it is clearer to observe that the nanoworms are formed due to the connection of the small ZnO nanoparticles.

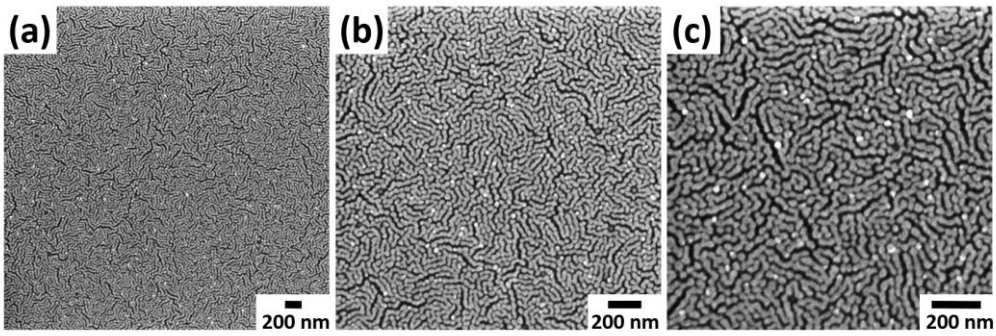

Figure 5.4 SEM images of worm-like ZnO films which are obtained at 120 °C under different magnifications.

With respect to the process of the structural change, many parameters, such as the evaporation rate of the solvent, the different compatibility of the two blocks in the diblock copolymer, and the decreased mobility induced by the ZnO particles in the ZnO/PS-*b*-PEO hybrid films, may have an influence on the final morphology of the ZnO films. Among these parameters, one of the most important reasons for the morphology change might be due to the decreased compatibility between the PS and the PEO blocks when increasing the annealing temperature. During the annealing process, the phase transitions are highly dependent on three characteristic temperatures, namely the melting temperature (T_m) of the PEO block, the glass transition temperature (T_g) of PS block and the order-disorder transition temperature (T_{ODT}) of PS-*b*-PEO.[108] At 80 °C, a temperature higher than T_m of the PEO block, but lower than T_g of the PS block, the morphology is similar to that of the as-cast hybrid films (Figure 5.8a), which can be explained by the lack of mobility of the PS block. The relatively fixed position of PS and ZnO particles prevent an efficient structural reorganization. Thus, the ZnO films are present at the same state with the as-cast foam-like structure. When the films are annealed at 100 °C, which is around the T_g of the PS block, the PS block start to soften and the degree of structural reorganization improves greatly. The ZnO particles prefer to decrease the surface energy, thus, forming the aggregated randomly dispersed ZnO particles. Upon increasing the temperature to 120 °C, the Flory-Huggins interaction parameter decreases and the compatibility of the PS and PEO blocks increases.[109] The worm-like structures form which is influenced by the mobility prevention induced by ZnO particles in the films. When increasing the temperature to 200 °C, the compatibility between the PS and the PEO blocks increases further, which makes the morphology of the diblock copolymer change from an ordered phase to a disordered phase. Small ZnO nanoparticles are observed with a random dispersion, forming a disordered sphere-like structure.

Optical microscopy (OM) images of the ZnO films with different morphologies are shown in Figure 5.5. The uniformity of the films on micrometer length scale can be observed. The ZnO films annealed at 80 (Figure 5.5a), 120 (Figure 5.5c), 140 (Figure 5.5d), 160 (Figure 5.5e) and 200 °C (Figure 5.5f) appear homogeneous, which is consistent with the SEM results. However, the ZnO films annealed at 100 °C (Figure 5.5b) show many light spots which are marked with black arrows. These spots reveal some aggregations of ZnO particles during the structure transition process, which agrees with the SEM results as well.

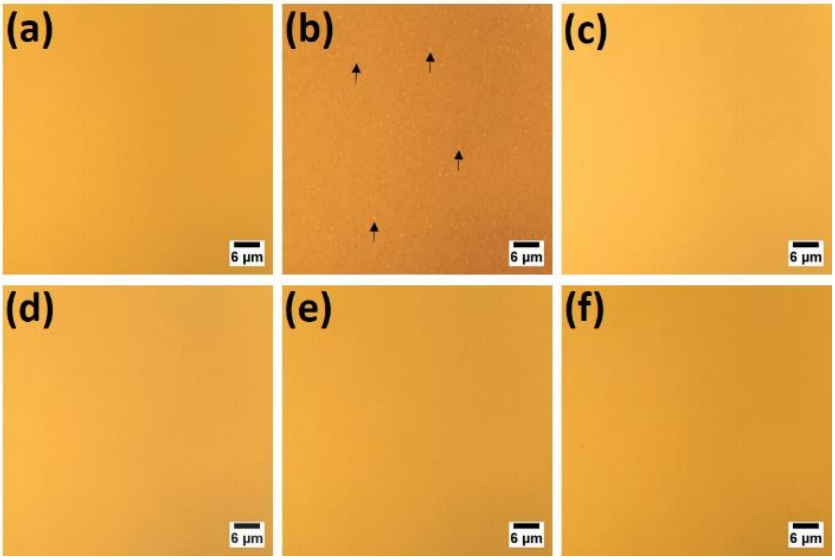

Figure 5.5 OM images of mesoporous ZnO films annealed at different temperatures: (a) 80 °C, (b) 100 °C, (c) 120 °C, (d) 140 °C, (e) 160 °C, and (f) 200 °C. Black arrows in (b) indicate some of the light spots, implying large scale aggregation. Reprinted from Ref.[83] with permission from The Royal Society of Chemistry.

Inner morphology

GISAXS is a powerful tool to investigate the morphology buried in the films.[76, 110] It can detect structure length scales ranging from nanometer to micrometer.[111] Due to the small incident angle, the footprint on the sample can be much larger than the area detected with SEM measurement, which gives statistical information. The collected two-dimensional (2D) GISAXS data of the ZnO films with multiple morphologies are shown in Figure 5.6. As seen in the 2D data, the signal is dominated by the reflected beam, with the most intensive peak being located at the position with the exit angle equal to the incident angle, which is called specular beam. A beamstop is used to block the specular beam to prevent the oversaturation of

the detector and accordingly make the contrast of the scattering signal clearer to eyes. Between the sample horizon and the specular beam, the Yoneda peak, which is located at the position of critical angle, is observed. Along the Yoneda peak position, a lateral scattering signal from ZnO nanostructures is observed in the 2D GISAXS data. The different scattering signal at the Yoneda peak position indicates that the ZnO nanostructures annealed at different temperatures show different lateral structures. To analyze quantitatively, horizontal line cuts are performed along the Yoneda peak as marked by a red arrow in Figure 5.6a.

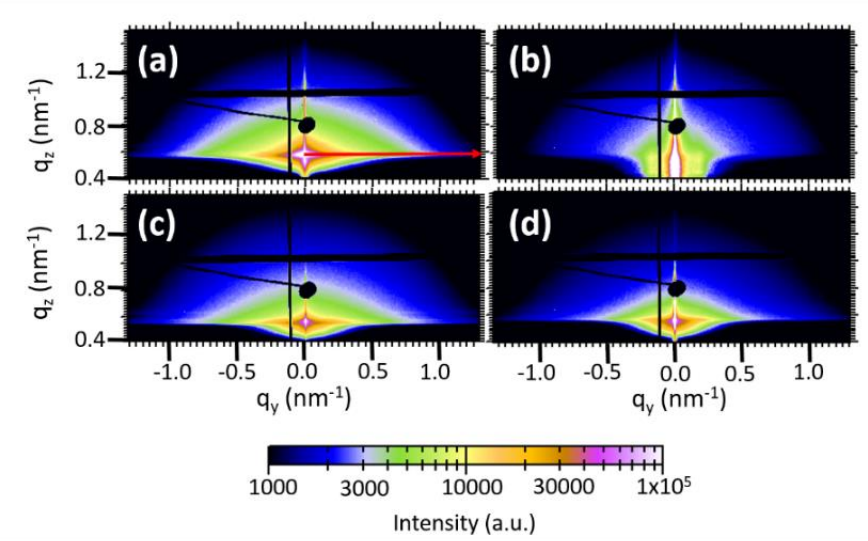

Figure 5.6 2D GISAXS data of mesoporous ZnO films annealed at different temperatures: (a) 80 °C, (b) 120 °C, (c) 160 °C, and (d) 200 °C. The specular peak is shielded by a beamstop. The red arrow indicates the place where the horizontal line cuts are performed. All the images have the same intensity scale as shown in the scale bar. Reprinted from Ref.[83] with permission from The Royal Society of Chemistry.

Figure 5.7 shows the horizontal line cuts of ZnO films annealed at different annealing temperatures. Different from the other three curves, the horizontal line cut obtained from the 120 °C annealed films shows a distinct peak at about 0.15 nm^{-1} of q_y. This indicates that the worm-like structure shows a more ordered structure in the lateral direction compared with the ZnO films with foam-like and sphere-like structures. To get the information of the length scale, the effective interface approximation of the distorted wave Born approximation (DWBA) is used to fit the data, with the local monodisperse approximation (LMA).[112] This means that the total scattering signal can be approximated by incoherently superposing the scattering intensities of the individual substructures that appear within the film, if the length scales of the distinct substructures are sufficiently different. In this model, three such distinct substructures

are approximated by standing cylinders with Gaussian distribution for the form and structure factors. On one hand, the form factors denote the shape of these scattering objects in the film which in the present case is ascribed to the ZnO clusters. The diameters of these cylindrical objects obtained from the fits denote the size of the ZnO clusters. The structure factors obtained from the fits, on the other hand, account for the center-to-center distance between the scattering objects. Values of the form and the structure factors are then used to extract the average pore size of the ZnO films:

Pore size = (center-to-center distance between the nanoparticles - 2×radius of the clusters).

Based on these calculations, the cluster sizes and pore sizes of the mesoporous ZnO films are obtained. For the foam-like structures of ZnO films prepared at 80 °C, the ZnO clusters show three average sizes which are all below 100 nm. The small- and middle-sized pores are mesopores while the large-sized pores are macropores. Both the presence of these two kinds of pores are beneficial for improving the surface of the ZnO films and for loading the dye molecules and backfilling with the spiro-OMeTAD for application in ssDSSCs. When the annealing temperature increases to 120 °C, the ZnO films show small-sized clusters around 3 nm, middle-sized clusters around 15 nm, and large-sized clusters around 118 nm. The small-sized clusters correspond to the small ZnO nanoparticles which connect with each other to form the worm-like structures. These worm-like structures are referred as middle-sized clusters. The presence of large-sized clusters might be resulted from some aggregations of the worms. Regarding pore size, the worm-like structure of ZnO films prepared at 120 °C show larger average small-sized pores. This is supposed to benefit the infiltration of dye molecules and spiro-OMeTAD. When increasing the temperature further to 200 °C, both the large clusters and the pores show a decrease trend, suggesting the preference to form smaller ZnO clusters with high monodispersity in the films. This changing trend is consistent with the SEM data, indicating that the inner morphology is similar to the surface for all the ZnO films.

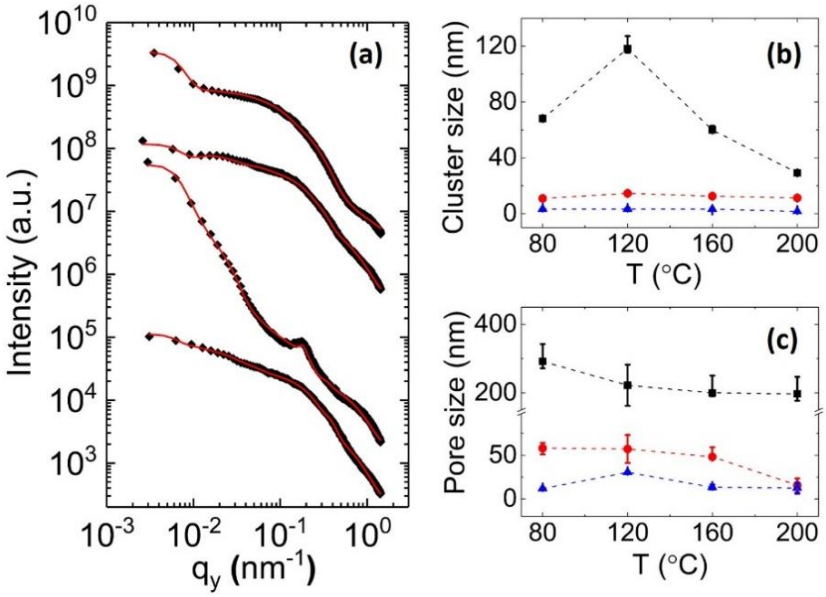

Figure 5.7 (a) Horizontal line cuts (black diamonds) of the 2D GISAXS data of mesoporous ZnO films annealed at different temperatures: 80 °C, 120 °C, 160 °C, and 200 °C from bottom to top. The red lines represent the fits to the data. All curves are shifted along the intensity axis for clarity of the presentation. Extracted characteristic length scales: (b) cluster size and (c) pore size in the ZnO thin films as a function of annealing temperature. Blue triangles indicate small-sized structures, red circles indicate middle-sized structures and black squares indicate large-sized structures. Reprinted from Ref.[83] with permission from The Royal Society of Chemistry.

5.2.2 Evolution of worm-like structure

The worm-like structure of the ZnO films prepared at 120 °C shows an interconnected structure. Compared with other samples, the worm-like structure also possesses larger small-sized pores, which would make the subsequent backfilling steps more effective, therefore resulting in a more well-defined ZnO/dye/spiro-OMeTAD interface. Thus, the worm-like structure seems more promising for application in ssDSSCs. In this section, the kinetic evolution of the worm-like structure formation process is investigated. All the results shown in this section are based on the hybrid films of ZnO/PS-*b*-PEO as the diblock copolymer PS-*b*-PEO plays a significant role in the kinetic evolution during the annealing process.

Surface morphology

SEM images of several stages involved in the formation process of the worm-like structures are shown in Figure 5.8. The morphology changes remarkably during the first 2 min (Figure

5.8a-d) and then only shows changes on the large scale from 2 min to 8 min (Figure 5.8e-g). After 8 min (Figure 5.8h-j), the morphology remains constant. For the films without any annealing (Figure 5.8a), it shows an interconnected 3D structure. This structure was already reported by using the same diblock copolymer.[113] This suggests the interconnected foam-like structure can be realized by a sol-gel method in combination with PS-*b*-PEO templating. After keeping the samples at 120 °C for 0.5 min (Figure 5.8b), some ZnO particles start to aggregate with each other to form large clusters. This might be resulted from many factors. The evaporation of the residual solvent in the films and the suddenly increasing mobility of both PS and PEO blocks might lead to the aggregation of the ZnO. When increasing the annealing time to 1 min (Figure 5.8c), more large domains appear at the surface. The worm-like structure is observed until annealing for 2 min (Figure 5.8d). Some large clusters are still at the surface and they even grow to larger ones. This might be due to the Ostwald ripening which plays an important role during the growth of the large particles. Since small particles are energetically less stable than the well-ordered ones and packed in the interior, they prefer to grow on the surface of the large particles. Upon increasing the annealing time to 8 min (Figure 5.8g), the worm-like structure almost stays constant and the large clusters vanish gradually. The large clusters change to worm-like structure gradually from the edge to the center as shown in Figure 5.8f and g. After annealing for 15 min (Figure 5.8g), it shows a very homogeneous worm-like structure. No large clusters are observed anymore. From 15 min to 60 min (Figure 5.8h-j), the worm-like structure keeps constant and no morphology change is observed, indicating the morphology transition from foam-like to worm-like structure finishes at 15 min at 120 °C.

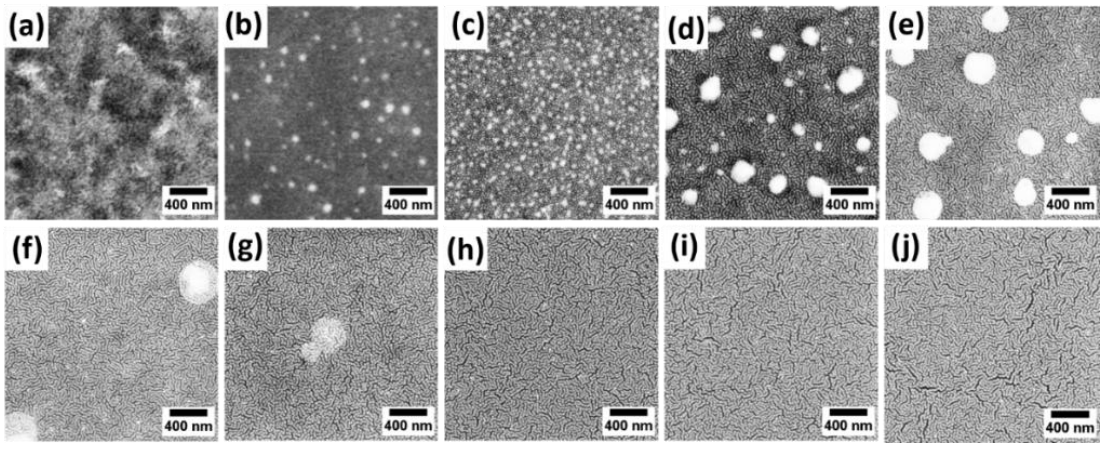

Figure 5.8 SEM images of the ZnO/PS-b-PEO hybrid films annealed at 120 °C for different times: (a) 0 min, (b) 0.5 min, (c) 1 min, (d) 2 min, (e) 3 min, (f) 5 min, (g) 8 min, (h) 15 min, (i) 30 min and (j) 60 min. Reprinted from Ref.[83] with permission from The Royal Society of Chemistry.

Inner morphology

GISAXS measurements are performed to investigate the evolution of worm-like structure buried in the films. Figure 5.9a-j show the 2D GISAXS data of different stages towards the formation of worm-like structure. The scattering data changes significantly during the first 8 min (Figure 5.9a-g), and then almost keeps constant from 15 min on (Figure 5.9h-j). A semicircular scattering pattern is observed for all samples, which suggests that the morphology in the films is generally isotropic. However, from 2 min on, the 2D data show two vertically scattering signals known as Bragg rods as marked by the white boxes in Figure 5.9d. This indicates the appearance of a vertically oriented structure with respect to the substrate.[107, 114] Combined with the SEM results, it is concluded that the vertically oriented structure originates from the worm-like structure. The worm-like structures are partly perpendicular to the substrate. Moreover, the morphology transition from foam-like to worm-like structure starts at 2 min.

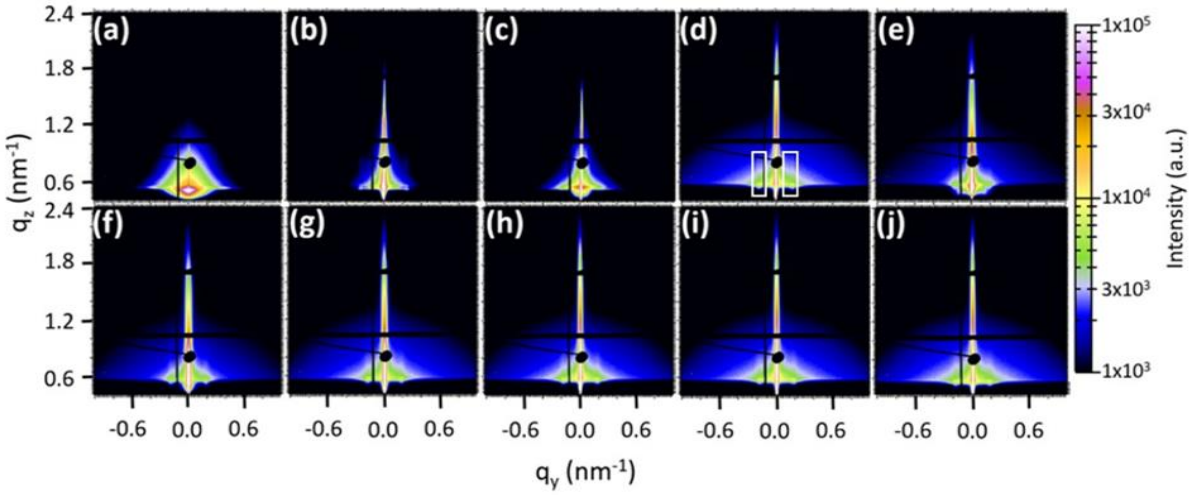

Figure 5.9 2D GISAXS data of ZnO/PS-b-PEO films annealed at 120 °C for different times: (a) 0 min, (b) 0.5 min, (c) 1 min, (d) 2 min, (e) 3 min, (f) 5 min, (g) 8 min, (h) 15 min, (i) 30 min and (j) 60 min. The specular peak is blocked by a beamstop. All the images have the same intensity scale as shown in the scale bar. The white boxes in (d) indicate the two vertical Bragg rods. Reproduced from Ref.[83] with permission from The Royal Society of Chemistry.

Horizontal line cuts are performed along the Yoneda peak (Figure 5.10a). The curves show a significant change during the first 2 min. It is worth noting that a distinct peak is observed at about 0.2 nm^{-1} of q_y for the curves annealed for over 2 min. This peak is originated from the Bragg rods.

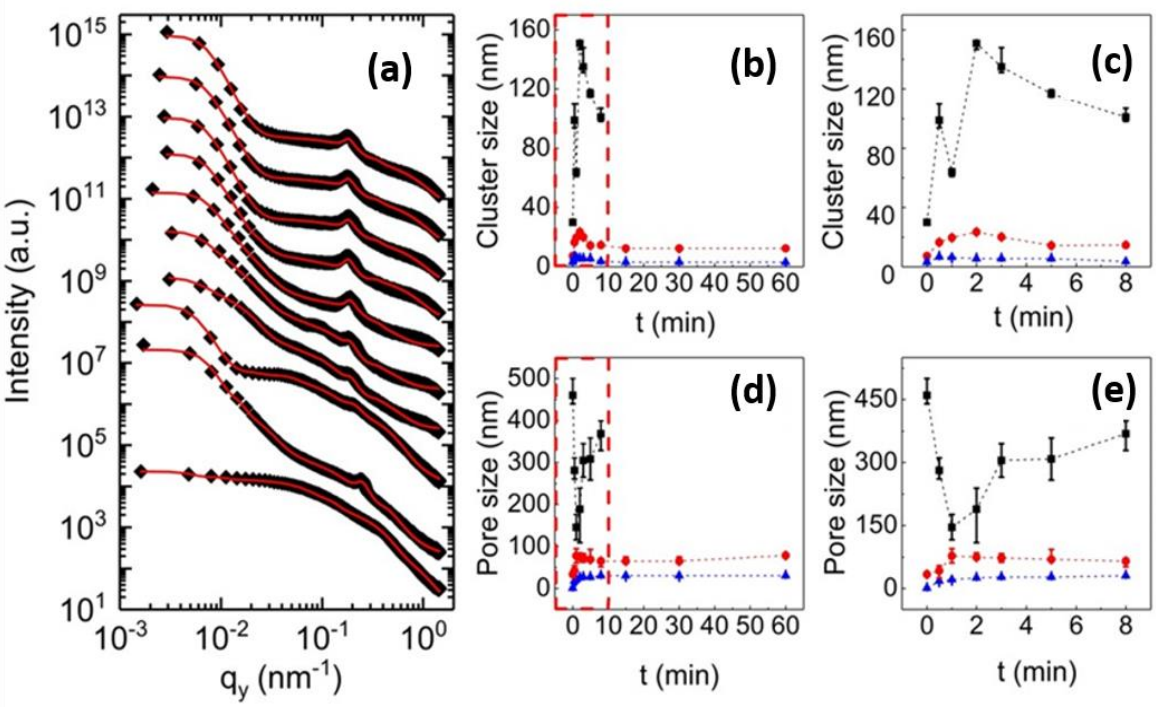

Figure 5.10 (a) Horizontal line cuts of the 2D GISAXS data for ZnO/PS-b-PEO films annealed at 120 °C for increasing time from bottom to top. The red lines represent the fits to the data. All curves are shifted along the intensity axis for clarity of the presentation. Extracted characteristic length scales: (b and c) ZnO cluster size and (d and e) pore size in the ZnO/PS-b-PEO films as a function of increasing annealing time. (c and e) correspond to the cluster size and pore size of the first 8 min in the red boxes in (b and d), respectively. Blue triangles indicate small-sized structures, red circles indicate middle-sized structures and black squares indicate large-sized structures. Reproduced from Ref.[83] with permission from The Royal Society of Chemistry.

To obtain the average cluster and pore size of the ZnO films for different annealing times, the horizontal line cuts are fitted with the same model described above. The average cluster size and average pore size are plotted as a function of the annealing time (Figure 5.10b and d, respectively). To fit the cuts, three structures are required for the curves annealed for the first 8 min, whereas two structures for the curves after 8 min are sufficient. After 8 min, the large-sized structures disappear, indicating that no large clusters are present in the films anymore. Instead, only the worm-like structure exists in the films. This is consistent with the morphology changes observed from the SEM images. During the first 2 min, the large-sized clusters become larger expect for that annealed for 1 min (Figure 5.10c, a zoom-in of the first 8 min indicated in the red box in Figure 5.10b). When increasing the time further to 8 min, the large-sized clusters show decreased size and then vanish after 8 min. While for the large-sized pores

(Figure 5.10e, a zoom-in of the first 8 min indicated in the red box in Figure 5.10d), they first decrease before 1 min, followed by increasing until 8 min, indicating that large-sized ZnO clusters first become more and larger at 0.5 min, and then become smaller and denser at 1 min. Afterwards, the large clusters become larger and sparser at 2 min and then a little smaller and even sparser from 2 min to 8 min. Both the small-sized and middle-sized structures show an increased cluster and pore size, which may indicate that the crystallization and the formation of the mesopores worm-like structure are improved during this process. From 2 min on, both the cluster size and the pore size almost stay constant.

For the final ZnO/PS-*b*-PEO films annealed for 60 min, the 2D GISAXS data differ from that of the pure ZnO film (Figure 5.6b). This might be resulted from the removal of the polymer template, which slightly changes the contrast and the morphology. Nevertheless, the two vertical Bragg rods are preserved after polymer removal and the position of the Bragg rods remains the same, implying the conservation of the worm-like structure after polymer removal, which is observed in the SEM images. It is important to note that the ZnO/PS-*b*-PEO films show two structures whereas the pure worm-like ZnO films show three average structures. This might be explained by the aggregation of some worms caused by the removal of the polymer template. Moreover, although the small-sized structures for ZnO in hybrid films and in pure ZnO films are similar (3 nm for the cluster size and 30 nm for the pore size), the pure worm-like ZnO films show larger middle-sized cluster sizes (15 nm *vs.* 12 nm) and smaller pore sizes (57 nm *vs.* 78 nm) than the worm-like ZnO/PS-*b*-PEO composite films. This can be attributed to the collapse of the ZnO films to some extent. The fusion of the ZnO structures makes the average pore size smaller and the cluster size larger during polymer removal.[115-118]

5.3 Conductivity and optoelectronic properties of ZnO films

To apply the ZnO films in ssDSSCs, the conductivity and the optoelectronic properties are of great importance. In this section, these properties are explored on the basis of the pure ZnO films with multiple morphologies.

5.3.1 Sheet resistance

The conductivity of the ZnO films is investigated by measuring the sheet resistance. Figure 5.11 shows the plot of the sheet resistance as a function of the annealing temperature. Although the crystallinity of ZnO is generally supposed to be improved by increasing the annealing temperature, the sheet resistance decreases first, followed with increasing values, revealing that the worm-like structure annealed at 120 °C possesses the lowest sheet resistance. The best

conductivity of the worm-like structure may be induced by better interconnected network structure as compared with the other samples.

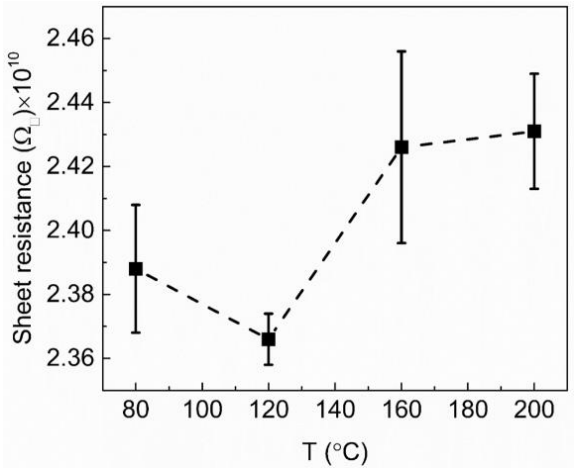

Figure 5.11 Sheet resistance of mesoporous ZnO films prepared at different annealing temperatures, which is plotted as a function of annealing temperature. The dashed line is a guide to the eyes. Reprinted from Ref.[83] with permission from The Royal Society of Chemistry.

5.3.2 Optoelectronic properties

Figure 5.12 shows the photoluminescence (PL) spectra of mesoporous ZnO films annealed at 80 and 120 °C after polymer removal, which are the most promising samples due to the larger mesopore size for backfilling as compared to the structures prepared at other temperatures. The films are excited at the wavelength of 325 nm. Two prominent peaks are observed in the range of 345-600 nm. The peak at about 350 nm is caused by the radiative recombination of electrons from the conduction band with holes from the valence band. While the other broad peak located at about 530 nm may be caused by defect induced emission. Compared with the ZnO films annealed at 80 °C, the films at 120 °C show weaker intensity for the defects, indicating less defects in the worm-like structure.

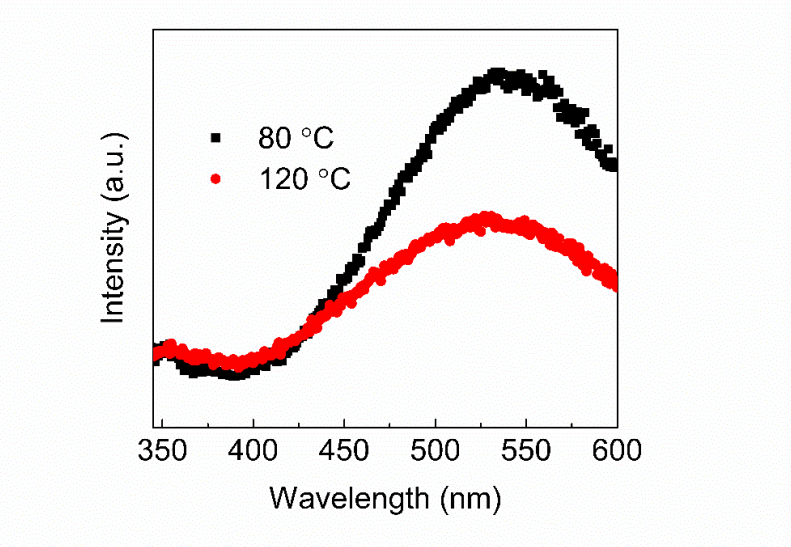

Figure 5.12 PL spectra of mesoporous ZnO films annealed at 80 and 120 °C as indicated after polymer removal (λ_{Ex}=325 nm). Reprinted from Ref.[83] with permission from The Royal Society of Chemistry.

Time resolved photoluminescence measurements are performed to investigate the charge separation at the interface between dye molecules and ZnO. Figure 5.13 shows the time resolved PL spectra of D205 on different mesoporous ZnO films and that on glass as a comparison. A biexponential decay function is used to fit the curves with Fluofit software. The average lifetime and the fitting results are shown as dashed yellow lines. Compared with the PL decay lifetime of D205 on glass (2.1 ns), the lifetime of D205 on ZnO films shows a increasing trend with temperature, *i.e.*, 1.1 ns for samples prepared at 80 °C and 120 °C, 1.4 ns for 160 °C and 1.5 ns for 200 °C. It implies that D205 loaded in 80 °C and 120 °C annealed ZnO films shows the most effective exciton separation. This might be due to the better interconnected network in the foam- and worm-like structures. Nevertheless, due to the larger amount of defects in the 80 °C annealed samples, the exciton separation in the 120 °C annealed samples seems more efficient, which favors the improvement of the photovoltaic performance. The reason for this may be due to two aspects. One is that the worm-like structure prepared at 120 °C shows larger small-sized pores, which is beneficial for forming a more effective interface for exciton separation. The other is the better vertically oriented structure in the worm-like structure, making the electron transport to the corresponding electrode more efficient.

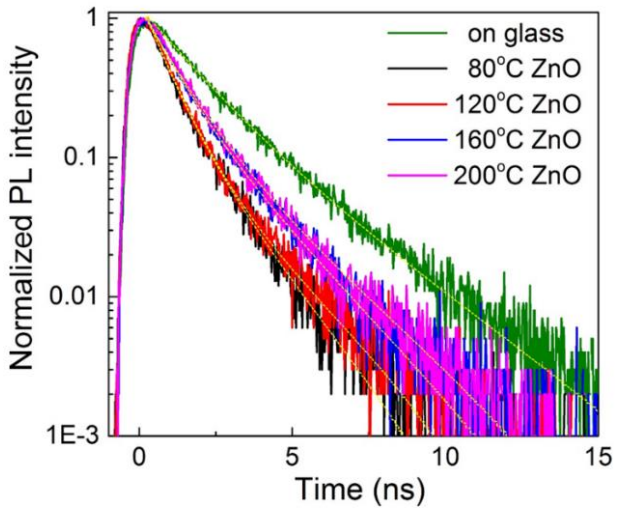

Figure 5.13 Time resolved PL spectra of D205 on glass and on mesoporous ZnO films prepared at different annealing temperatures as indicated. The curves are fitted with biexponential decay function to obtain the average lifetime. The fits are shown as dashed yellow lines. Reprinted from Ref.[83] with permission from The Royal Society of Chemistry.

5.4 Solar cell performance

To investigate the solar cell performance, ssDSSCs based on ZnO films with foam-like, worm-like and sphere-like structures prepared at 80, 120, 160, and 200 °C are fabricated. The device layout is FTO/compact ZnO/m-ZnO/dye/spiro-OMeTAD/Au on glass. Each layer for the ssDSSCs is prepared at relatively low temperature. Therefore, these devices show great promise for application in flexible solar cells, where the substrate is sensitive to high temperatures. The photovoltaic performance based on ZnO films with different morphologies is given in section 5.4.1. Section 5.4.2 describes the long-term stability of the ssDSSCs based on the worm-like structure.

5.4.1 Influence of annealing temperature

The annealing temperature has a great influence on the morphology of the ZnO films as shown in section 5.2.1. In this part, the corresponding photovoltaic performance is investigated. UV-Vis spectra, current density-voltage curves (I-V curves), incident photon-to-current efficiency (IPCE) and electrochemical impedance spectra (EIS) are measured in this section.

Transparency

Optical images of the ssDSSCs based on ZnO films with different morphologies are shown in Figure 5.14a-d. All ssDSSCs are very transparent (excluding the area with gold contact). Only a slight color of light purple is observed which is originated from the color of D205. Further differences in color is not observed for the ssDSSCs fabricated from different ZnO films. To see the transparency quantitatively, UV-Vis spectra are measured (excluding the gold contact) and the transmittance of the four solar cells is shown in Figure 5.14e. The absorption in the range of 465-610 nm is mainly originated from the dye molecules D205. The high absorption at 390 nm is due to the absorption of both D205 and ZnO films. The high transmittance (above 90%) in the range of 427-800 nm, indicates that the active layers in the ssDSSCs show high transparency in the visible light region. The transparency of the active layers makes them promising for applications in building integrated solar cells. Moreover, it is shown that the solar cells (excluding the gold contact) prepared from ZnO annealed at 80 °C and 120 °C have a higher dye absorption peak as compared with those from 160 °C and 200 °C annealed ZnO films. This indicates that the ZnO films annealed at 80 °C and 120 °C increase the probability for dye molecules being loaded in the films, which might be due to larger meso-pore size as compared to the ZnO films annealed at 160 °C and 200 °C.

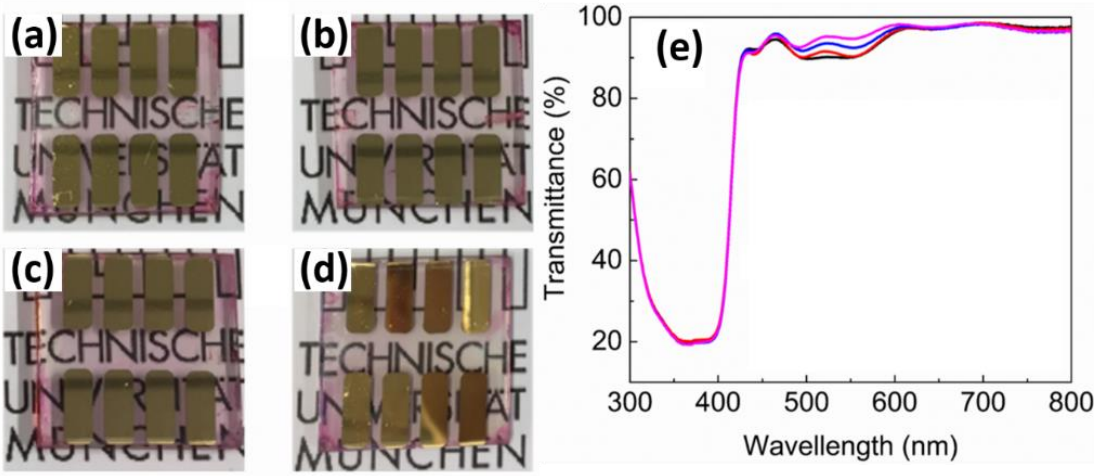

Figure 5.14 (a-d) Optical images of ssDSSCs based on ZnO prepared at different annealing temperatures: (a) 80 °C, (b) 120 °C, (c) 160 °C, (d) 200 °C. (e) Transmittance spectra of ssDSSCs excluding top contacts prepared from ZnO films annealed at different temperatures: 80 °C (indicated by black curves), 120 °C (red), 160 °C (blue), and 200 °C (magenta). Adapted from Ref.[83] with permission from The Royal Society of Chemistry.

I-V curves

The current density-voltage (I-V) curves of the ssDSSCs prepared from ZnO films annealed at different temperatures are given in Figure 5.15. It is observed that the ssDSSCs based on the ZnO films annealed at 120 °C show a larger maximum output power as compared to other ssDSSCs indicating a larger power conversion efficiency.

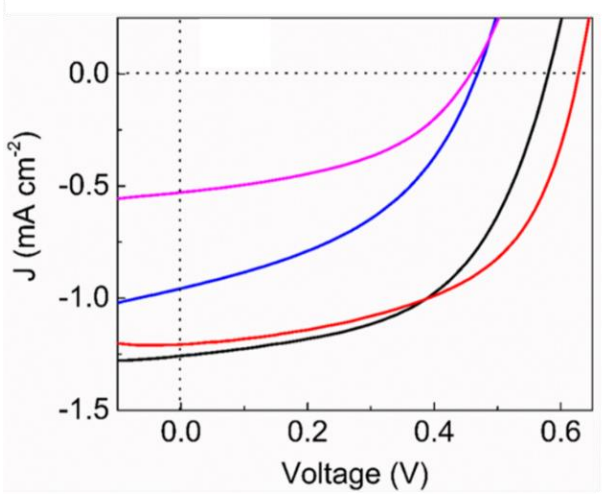

Figure 5.15 Current density-voltage characteristics of ssDSSCs based on ZnO prepared at different annealing temperatures: 80 °C (indicated by black curves), 120 °C (red), 160 °C (blue), and 200 °C (magenta). Reproduced from Ref.[83] with permission from The Royal Society of Chemistry.

The photovoltaic parameters including short-circuit current density (J_{sc}), open-circuit voltage (V_{oc}), fill factor (*FF*) and power conversion efficiency (*PCE*) are extracted from the I-V curves (Figure 5.16), which are obtained from 12 pixels. It is observed that the annealing temperature of the ZnO films has a great influence on the ssDSSC performance. Figure 5.16b shows that the *PCE* of the ssDSSCs based on 120 °C annealed ZnO films (average value: 0.42%, highest value: 0.45%) is higher than those from the other devices. When increasing the annealing temperature of the ZnO films to 160 °C and 200 °C, the corresponding ssDSSCs show a decreased *PCE*. This changing trend is similar to those of J_{sc}, V_{oc} and FF. The efficiency we obtained in this work is not extensively high, which is mainly due to the transparent active layers.[99, 104, 119, 120] Upon further characterizations, the following incident photon-to-current efficiencies without and with normalized values are given below.

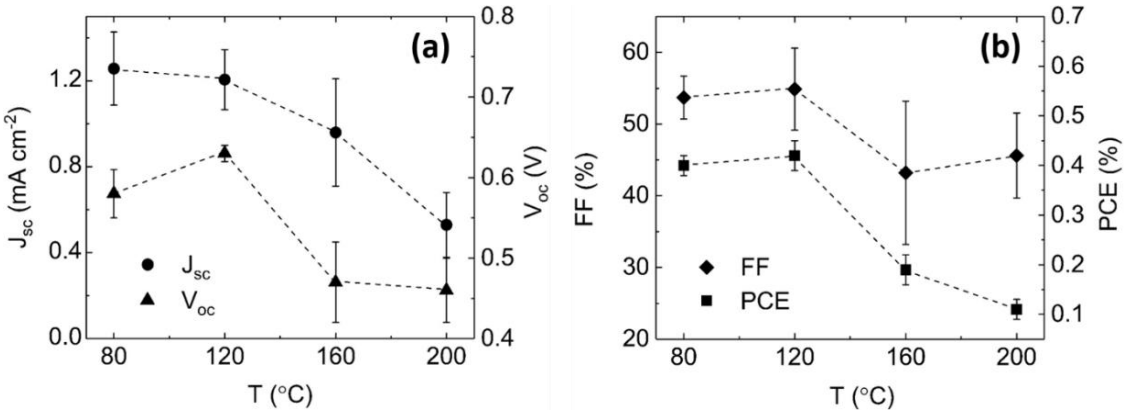

Figure 5.16 (a) J_{sc} (circles, dataset at the top) and V_{oc} (triangles, dataset at the bottom), (b) FF (diamonds, dataset at the top) and PCE (squares, dataset at the bottom) extracted from I-V curves of the DSSCs based on ZnO prepared at different annealing temperatures as indicated. The lines are guides to the eye. Reprinted from Ref.[83] with permission from The Royal Society of Chemistry.

Incident photon-to-current efficiency

To investigate the photovoltaic properties at different wavelengths, incident photon-to-current efficiency (IPCE) measurements are performed (Figure 5.17a). Two absorption peaks in the range of 300 to 600 nm are observed, which coincides with the absorption spectra of the used D205 dye molecules. The IPCE values are lower than the reported values. This is mainly because the active layer in this work is of high transparency for the visible light as described above. Thus, the IPCE normalized by (1-transmittance) (Figure 5.17b) seems more reasonable to investigate the performance of the devices. We can observe that the efficiency improves significantly in the wavelength range of 450 to 650 nm in these normalized IPCE curves. For the ZnO annealed at different temperatures, the normalized IPCE of the corresponding ssDSSCs first increases and then decreases. At 590 nm, the highest efficiency of 98.2% is obtained for the ssDSSCs prepared from ZnO annealed at 120 °C, which is much higher than the other ssDSSCs based on ZnO annealed at other temperatures. It shows that at 590 nm, the normalized IPCE of the ssDSSCs prepared from ZnO films with 80 °C, 160 °C and 200 °C are 65.5%, 58.9% and 46.6%, respectively.

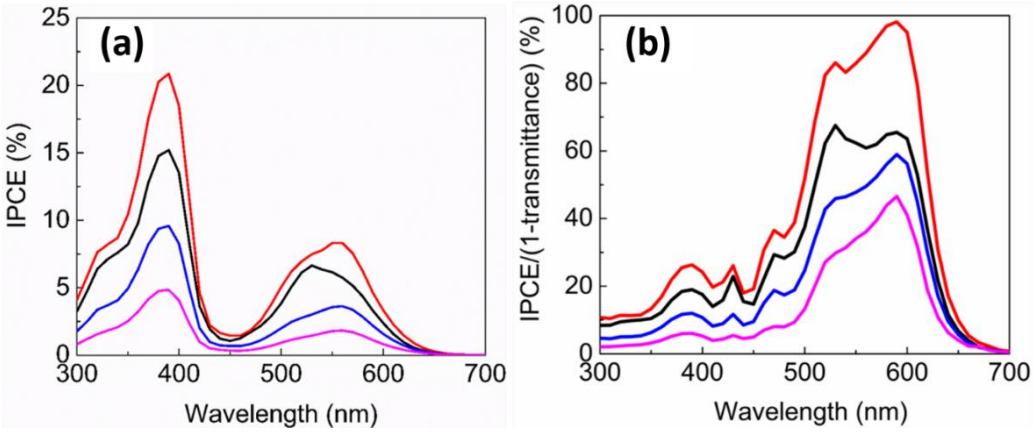

Figure 5.17 (a) IPCE spectra; and (b) IPCE normalized by (1-transmittance) of ssDSSCs based on ZnO prepared at different annealing temperatures: 80 °C (indicated by black curves), 120 °C (red), 160 °C (blue), and 200 °C (magenta). Reproduced from Ref.[83] with permission from The Royal Society of Chemistry.

The best photovoltaic performance of the ssDSSCs based on the 120 °C annealed ZnO films may be because of the larger mesopore size as shown in section 5.2.1 and the better conductivity of the ZnO films annealed at 120 °C. Larger mesopores are beneficial for backfilling of spiro-OMeTAD after loading dye molecules, which results in a better ZnO/dye/spiro-OMeTAD interface and therefore an improved photovoltaic performance as reported by Rawolle et al. in the case of TiO_2 films.[121] Moreover, the ZnO films annealed at 120 °C show a worm-like morphology which is better vertically oriented than the other morphologies as described in section 5.2.1. This contributes significantly to the improvement of the charge carrier transport towards the corresponding electrodes.

Electrochemical impedance spectra

The electrochemical impedance spectra (EIS) are shown in Figure 5.18 to probe the kinetics of the interfacial charge carrier transfer process in ssDSSCs. An equivalent circuit (on the top of Figure 5.18a) is used to fit the Nyquist plots. It is shown that all the EIS spectra exhibit two arcs. In the high frequency region, the arc is attributed to charge transfer at the back contact/n-type semiconductor interface (R_1), whereas the arc in the low frequency region is resulted from the charge transfer at the ZnO/dye/n-type semiconductor interface (R_2).[17, 122, 123] The ssDSSCs from 120 °C annealed ZnO films show much smaller R_2 as compared with others, which implies that the ssDSSCs based on worm-like structure possess lower hole-electron recombination, therefore resulting in a better efficiency. Table 5.1 gives the corresponding values of R_1 and R_2.

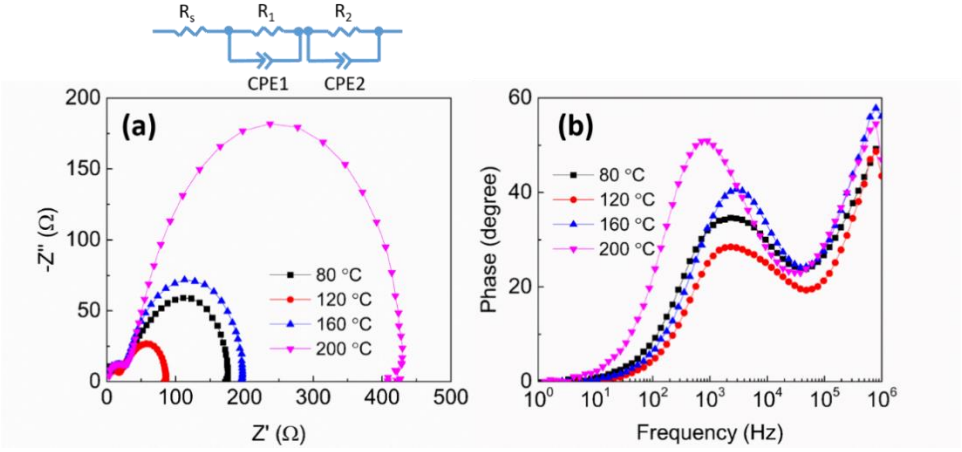

Figure 5.18 EIS analysis of DSSCs based on ZnO prepared at different annealing temperatures as indicated. (a) Nyquist plots (ontop showing equivalent circuit model used for the DSSCs in this study). (b) Bode phase plots. Reprinted from Ref.[83] with permission from The Royal Society of Chemistry.

The corresponding Bode phase plots of the EIS spectra for the ssDSSCs are shown in Figure 5.18b. The characteristic frequency peaks for the ssDSSCs first decrease from 80 °C to 120 °C and then increase when the annealing temperature increases to 160 °C as shown in Table 5.1. The electron lifetime for recombination (τ) of ssDSSCs is calculated by

$$\tau = 1/2\pi f_{\max}, \tag{5.1}$$

where f_{max} is the corresponding characteristic low-frequency peaks.[124]

The recombination lifetime for ssDSSCs can be obtained from this equation. The values are shown in Table 5.1. Compared with the recombination lifetime for ssDSSCs from 80 and 160 °C annealed ZnO, the one for ssDSSCs from 120 °C annealed ZnO shows a longer lifetime. This could effectively reduce the electron recombination and consequently lead to a significant enhancement of the device efficiency.

For ssDSSCs prepared from 200 °C annealed ZnO, lower frequency but higher charge transfer resistance at the ZnO/dye/n-type semiconductor interface is shown. This can be explained by the smaller pore sizes of the sphere-like ZnO structure at 200 °C, which results in a bad backfilling of the spiro-OMeTAD, therefore leading to poor charge injection to spiro-OMeTAD and low probability of charge recombination as well.

Table 5.1. EIS parameters of DSSCs based on ZnO prepared at different annealing temperatures as indicated. Reprinted from Ref.[83] with permission from The Royal Society of Chemistry.

DSSCs on different ZnO	R_1 (Ω)	R_2 (Ω)	f_{max} (Hz)	τ (ms)
80 °C	25.2	153.6	2302	0.069
120 °C	20.7	65.4	1823	0.087
160 °C	28.5	170.1	2910	0.055
200 °C	29.4	403.7	905	0.180

5.4.2 Long-term stability

The long-term stability of one ssDSSC based on 120 °C annealed ZnO film is shown in Figure 5.19. The normalized *PCE*, J_{sc}, V_{oc}, and *FF* are shown from top to the bottom. For the ssDSSCs, the fabrication, storage, and characterization process are conducted under ambient air conditions and undergo no encapsulation step. After 20 days, the *PCE*, J_{sc}, V_{oc}, and *FF* only slightly decrease with values of 90.4%, 92.8%, 101.6% and 96.0% of the initial values, respectively. Even after 120 days, the PCE still remains 79.4% (T80) which is significantly more stable than commonly reported in case of liquid electrolyte DSSCs.[125-128] The loss of the *PCE* mainly results from the decrease of the current density. The I-V curves after storing the ssDSSC for 0, 10, 20, 30 and 120 days are shown in Figure 5.20. The curves show similar shape except the slightly decreasing current density. The stability could be further improved by encapsulation.

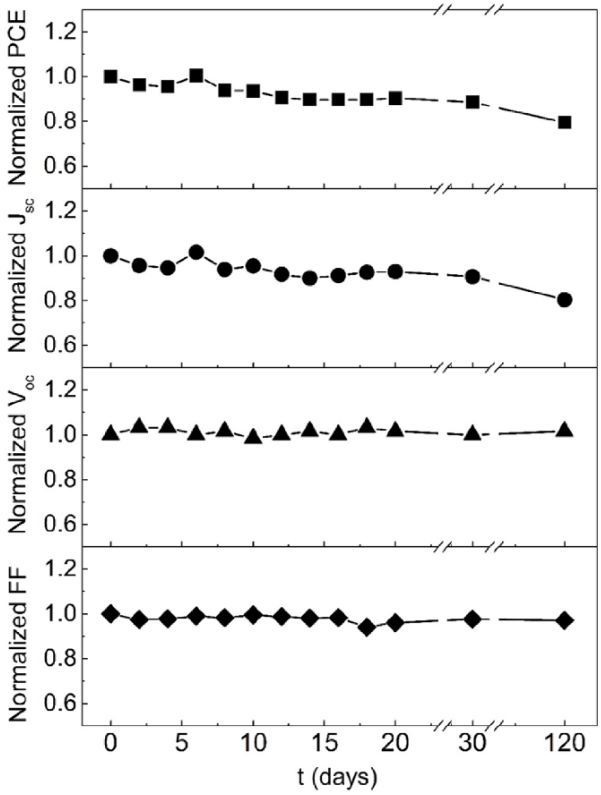

Figure 5.19 Long-term stability (PCE, J_{sc}, V_{oc}, and FF from top to bottom, respectively) of one ssDSSC based on 120 °C annealed ZnO film at ambient air condition. The lines are guides to the eye. Reprinted from Ref.[83] with permission from The Royal Society of Chemistry.

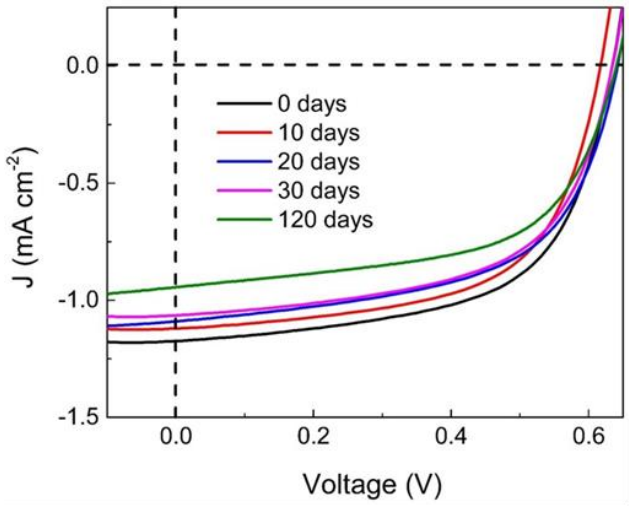

Figure 5.20 Current-voltage characteristics of one ssDSSC based on 120 °C annealed ZnO film measured after several days as indicated to study aging. Reprinted from Ref.[83] with permission from The Royal Society of Chemistry.

5.5 Summary

In this part, ZnO films with multiple morphologies (including foam-like, worm-like and sphere-like structures) are fabricated via sol-gel method in combination with a diblock copolymer templating. XRD reveals the formation of the wurtzite ZnO at 80 °C. All the fabrication processes for the different ZnO films are well below 200 °C and the annealing temperature shows great importance for morphology tuning. The surface and inner morphologies are detected by SEM and GISAXS, respectively, which reveals that the morphology changes from foam-like, worm-like, to sphere-like structures when increasing the annealing temperature. Moreover, the evolution of the worm-like structure while increasing the annealing time is investigated and the underlying self-assembly process is well observed by both SEM and GISAXS techniques. In addition, the ZnO films annealed at 120 °C show the lowest sheet resistance as compared with those annealed at 80 °C, 160 °C and 200 °C, indicating the improvement of charge transport by tuning the ZnO morphology. Time resolved photoluminescence measurements imply that D205 loaded in 120 °C annealed ZnO films shows the most effective exciton separation, which favors the improvement of the photovoltaic performance. Furthermore, ssDSSCs with transparent active layers are fabricated with these tunable ZnO films. For all ssDSSCs, every layer is deposited at low temperature, which shows great promise for applications in flexible solar cells. Since the worm-like structures of ZnO films have larger meso-pore sizes, the backfilling of dye molecules and spiro-OMeTAD is easier, thereby providing a better interface for charge separation between ZnO and dyes and for charge transfer from dye molecules to spiro-OMeTAD. The worm-like structure annealed at 120 °C has an interconnected 3D structure which is better ordered and vertically oriented as compared with other samples, thus, leading to lowest charge transfer resistance and recombination at the interfaces of ZnO/dye/spiro-OMeTAD as indicated by electrochemical impedance spectra. By tuning the annealing temperature of the ZnO films, an almost four times improvement of the *PCE* is found for the ssDSSCs based on the worm-like ZnO films. Almost 100% of the charge separation and collection efficiency for the absorbed photons by D205 is observed at 590 nm for the worm-like based ssDSSCs. Apart from this, the devices also possess very good stability in ambient air conditions. T80 is achieved even after 120 days for devices without encapsulation, which renders them highly interesting for practical applications, considering that standard encapsulation would enhance lifetime further.

In this work, a low temperature fabrication technique is used, which saves great energy and reduces the payback time significantly. The obtained transparent active layers make it possible for making building-integrated photovoltaic devices. In addition, the inexpensive and scalable sol-gel method for preparing ZnO templated by a diblock copolymer is a good way to

manufacture multiple morphologies to meet various needs and functionalities, not only in solar cells but also can be extended to a low-cost fabrication routine for other energy conversion devices.

6. Nanostructured ZnO films templated with PS-*b*-P4VP

Parts of this chapter have been published in an article: Comparison of UV Irradiation and Sintering on Mesoporous Spongelike ZnO Films Prepared from PS-*b*-P4VP Templated Sol-Gel Synthesis (K. Wang *et al.*, ACS Appl. Nano Mater. 2018, 1, 7139-7148, DOI: 10.1021/acsanm.8b02039).

As mentioned above, DSSCs have attracted great attention and show great potential in the photovoltaic field due to the efficient conversion from solar energy to electricity.[88, 129] Many efforts have been focused on ssDSSCs. Generally, a monolayer of dye molecules is adsorbed on the surface of the n-type semiconductors. The increased surface-area-to-volume-ratio of the mesoporous n-type semiconductors is favorable to adsorb a larger amount of the dye molecules, therefore resulting in a stronger absorption of the sunlight. The large n-type semiconductor/dye interface area also promotes the exciton separation. Moreover, the conductivity of the n-type semiconductor is improved to benefit the charge carrier transport to their corresponding electrode. However, the photovoltaic performance still remains modest. One of the most important issues is the poor efficiency of backfilling for the dye molecules and the p-type semiconductors into the mesoporous inorganic semiconductors, which results in a bad contact between dye molecules and charge carrier transport materials and a poor exciton separation and charge transfer. One possible way to overcome this issue is to tune either the polarities of the p-type semiconductors or the solvent to make it easy to penetrate the pores of the n-type semiconductors. Alternatively one can also use small molecules instead of conjugated polymers to act as the charge carrier transport materials.[130-133] For example, spiro-OMeTAD is widely used in ssDSSCs and perovskite solar cells, which show better photovoltaic performance than that prepared with P3HT. However, the availability of suitable small organic conductors is limited. Precise control over the pore size of the n-type inorganic semiconductors tends to be important in order to obtain highly efficient ssDSSCs. Investigating an optimum pore size is indispensable since the increased pore sizes have the tendency to enhance the backfilling, but on the other hand, may reduce the surface-area-to-volume-ratio, which decreases the charge carrier density separated at the interfaces of the dye molecules and the charge carrier transport materials.

An efficient way to control the pore sizes of the n-type inorganic materials is to use the sol-gel method in combination with a diblock copolymer as a template.[48, 134-136] As reported, many parameters may have an influence on the pore size of the inorganic materials.[107, 137-139] One can tune the pore size of the mesoporous scaffold by changing the weight ratio of the inorganic semiconductors to the template, or by tuning the weight ratio of the two blocks in the polymer template. The solvent or thermal annealing procedure can also greatly influence the pore sizes of the scaffold. In Chapter 5, the pore sizes in different structures are tuned by changing the annealing temperature which is controlled below 200 °C. However, as far as we know, the investigation of different post-treatment techniques, which might have some influence on the pore sizes of the scaffold, has not been reported. UV-irradiation and high temperature sintering are two reported methods to remove the polymer template from the polymer/inorganic semiconductor composite films.[107, 139-143] The polymer template is removed and only mesoporous inorganic thin films are preserved. However, different collapsed states of the inorganic thin films will occur during the respective process.[115, 116, 118, 143] Therefore, the post-treatment method is expected to show a significant influence on the final pore sizes of the inorganic materials.

In this chapter, mesoporous ZnO films are still fabricated by sol-gel synthesis, but templated with a different diblock copolymer polystyrene-*block*-poly(4-vinylpyridine) (PS-*b*-P4VP). Two post-treatment techniques, namely UV-irradiation and high temperature sintering, are used to remove the diblock copolymer template in this part to compare the finally obtained ZnO films which show different pore sizes with different post-treatment techniques. In addition, the influence of the weight ratio of the polymer template to the zinc precursor on the pore sizes of the final ZnO films is also investigated. Scanning electron microscopy (SEM) and atomic force microscopy (AFM) are used to monitor possible changes in the pore sizes at the surface of the ZnO films with different post-treatment methods and an increased template to precursor ratio. The pores buried inside the films are investigated with grazing-incidence small-angle X-ray scattering (GISAXS) which gives high statistical information on the pore sizes. Based on the ZnO films with different pore sizes, ssDSSCs are fabricated and the photovoltaic performances are found improved significantly via tuning the pore size of the ZnO films.

6.1 Fabrication route of ZnO nanostructures

A sol-gel synthesis is employed to fabricate the mesoporous ZnO films with the diblock copolymer PS-*b*-P4VP as a template. Figure 6.1 shows the multiple steps involved in the fabrication process. N, N-dimethylformamide (DMF) is used as a good solvent for both the PS and the P4VP blocks (Figure 6.1b). Moreover, the zinc precursor zinc acetate dihydrate (ZAD)

can also be dissolved in DMF as well (Figure 6.1a). While ethanolamine (MEA) is a poor solvent for the PS block, but a selective solvent for the P4VP block. Therefore, after introducing the poor solvent MEA, the PS blocks shrink and form the cores, whereas the P4VP blocks form the coronas. After mixing the zinc precursor solution and the polymer solution together, the zinc precursor prefers to incorporate into the P4VP blocks. As a result, micelles with zinc precursor present in the sol-gel are formed as shown in Figure 6.1c. After spin-coating the solution on a cleaned silicon (100) or glass substrate (Figure 6.1d), annealing at low temperature is performed to improve the self-assembly of the composite films (Figure 6.1e). Two post-treatment techniques, namely high temperature sintering (Figure 6.1f) and UV-irradiation (Figure 6.1g) which are reported to be efficient ways are employed to remove the polymer template from the composite films.[139, 142-144] Finally, mesoporous ZnO films are realized (Figure 6.1h). More details about the preparation process is described in section 4.2.1.

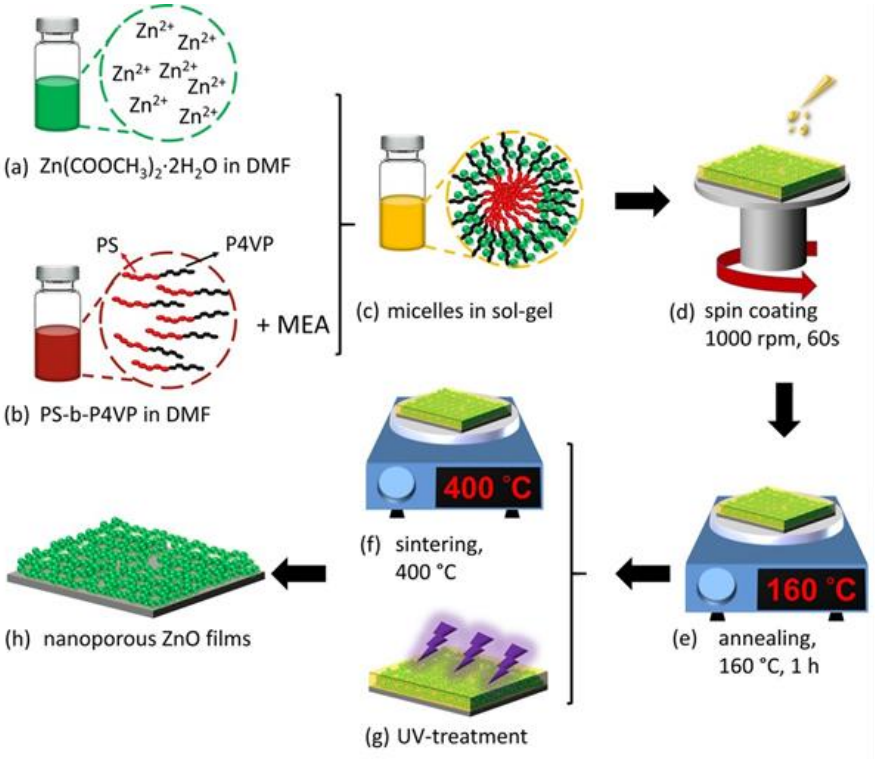

Figure 6.1 Schematic representation of the sol-gel route in combination with PS-b-P4VP templating to prepare ZnO/PS-b-P4VP composite thin films, followed by post-treatment: (f) high temperature sintering or (g) UV-irradiation in order to remove the polymer template. Eventually mesoporous ZnO films are obtained. Reprinted with permission from Ref.[145] Copyright {2018} American Chemical Society.

FT-IR spectra of the films are shown in Figure 6.2 before and after applying the post-treatment method (namely sintering or UV-irradiation) to remove the polymer template. For the films without post-treatment, the curve shows strong absorption peaks at 1621 and 700 cm^{-1}, which are attributed to the stretching modes of pyridine rings and aromatic rings, respectively, indicating the existence of P4VP and PS blocks.[146] In contrast, these peaks disappear for the samples after post-treatment with either sintering or UV-irradiation, suggesting that the polymer template is removed completely by either sintering or UV-irradiation.

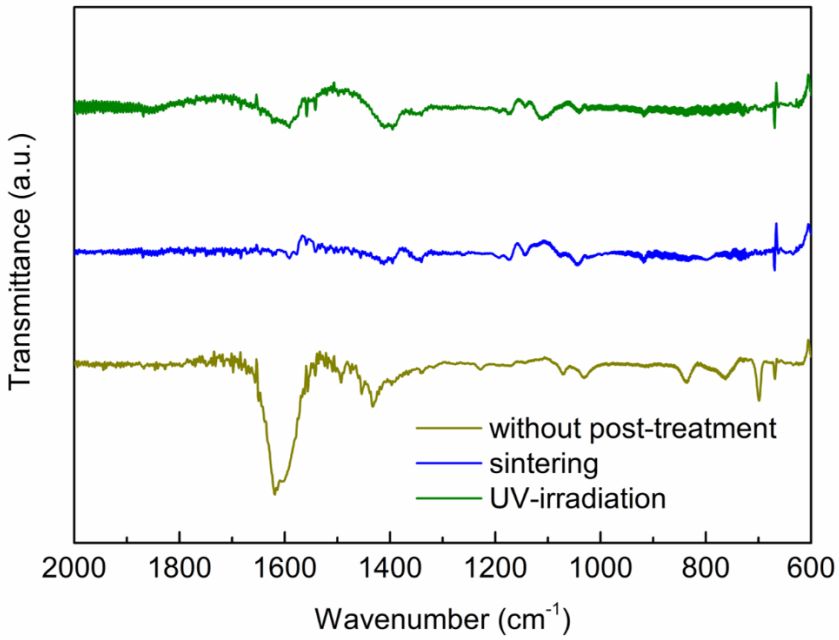

Figure 6.2 FTIR spectra of ZnO/PS-b-P4VP composite films (prepared from the polymer template-to-ZAD ratio of 5:12) without post-treatment and the corresponding ZnO films after polymer extraction via sintering or UV-irradiation. Reprinted with permission from Ref.[145] *Copyright {2018} American Chemical Society.*

Regarding each post-treatment technique, ZnO films with different ratios between template and ZAD are fabricated to investigate the influence of the ratio. Both surface and inner morphologies of the obtained ZnO films are probed and the corresponding ssDSSCs are fabricated, which shows remarkable relationship with the pore sizes of the ZnO films.

6.2 Mesoporous ZnO films via different post-treatment methods

The crystal structure of the mesoporous ZnO films is discussed in section 6.2.1. The surface and inner morphology is described in section 6.2.2 and section 6.2.3, respectively. According

to the morphology changes, the structural evolution affected by the weight ratio of template to the zinc precursor and the post-treatment technique is given in section 6.2.4. Moreover, the optical properties of the obtained ZnO films with different pore sizes are investigated in section 6.2.5.

6.2.1 Crystal structure

XRD data of ZnO/PS-*b*-P4VP and pure mesoporous ZnO films are shown in Figure 6.3 to investigate the information about the crystal structure. For all the three ZnO films three broaden peaks are observed in the range of 30 deg. to 37 deg. which are labeled by diamonds. The Bragg peaks at around 31.6, 34.3, and 36.3 deg. correspond to crystal planes of (100), (002) and (101), respectively. This indicates the formation of the wurtzite phase in the ZnO films. Moreover, compared with the hybrid films, the samples post-treated with UV-irradiation show no difference in the XRD data, suggesting that the crystallization is not improved by UV-irradiation treatment. The peaks for the sintered ZnO films show narrower full width at half maximum than those in the UV-irradiated samples, which demonstrates that the sintered films possess a better crystallization.

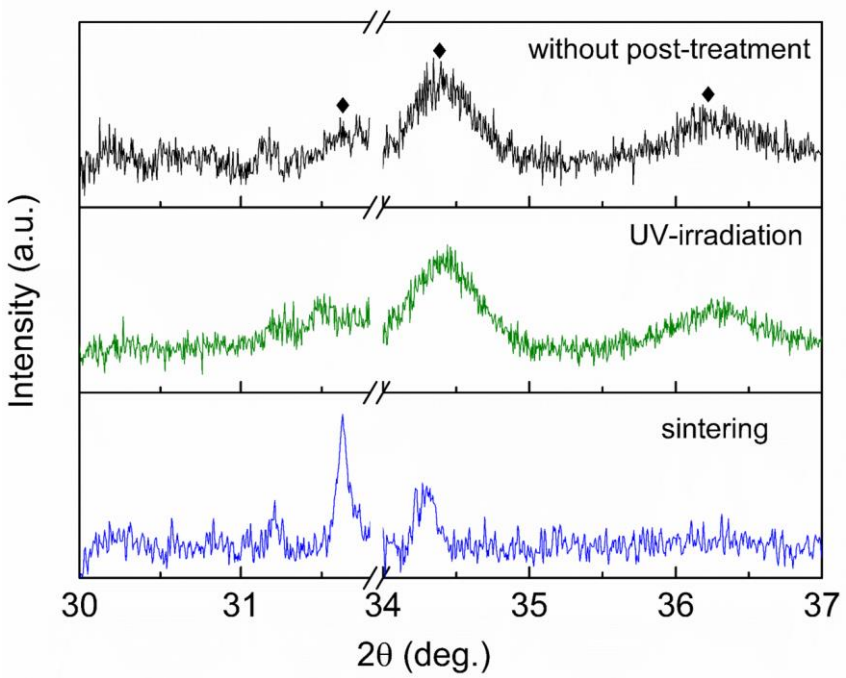

Figure 6.3 XRD patterns of ZnO/PS-b-P4VP (without post-treatment) and mesoporous ZnO films after polymer removal by UV-irradiation and sintering. The curves are interrupted from 31.8 to 34 deg. to remove the strong Bragg peak of the Si substrate. The Bragg peaks of ZnO wurtzite phase are indicated by diamonds. Reprinted with permission from Ref.[145] Copyright {2018} American Chemical Society.

6.2.2 Surface morphology

Both SEM and AFM are used to investigate the surface morphology of the ZnO films treated with different techniques. The morphology of the films upon increasing template-to ZAD ratio is also probed with SEM and AFM.

SEM images of UV-irradiated ZnO films with the ratio of 5:12 are shown in Figure 6.4. At low magnification (Figure 6.4a and b), the sample shows a homogeneous pore structure. The sponge-like structure is clearly observed under higher magnification (Figure 6.4c and d). Figure 6.5 shows the SEM images of both sintered and UV-irradiated ZnO films prepared from different template-to-ZAD ratios. All the ZnO films show an interconnected sponge-like structure, independent of the applied post-treatment method.

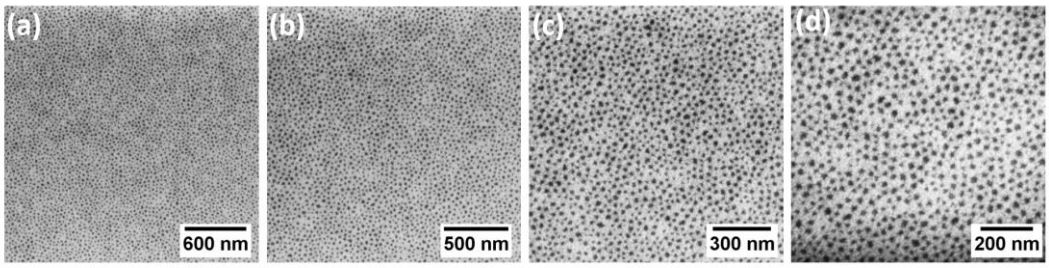

Figure 6.4 SEM images of UV-irradiated ZnO films with the ratio of 5:12 under different magnifications.

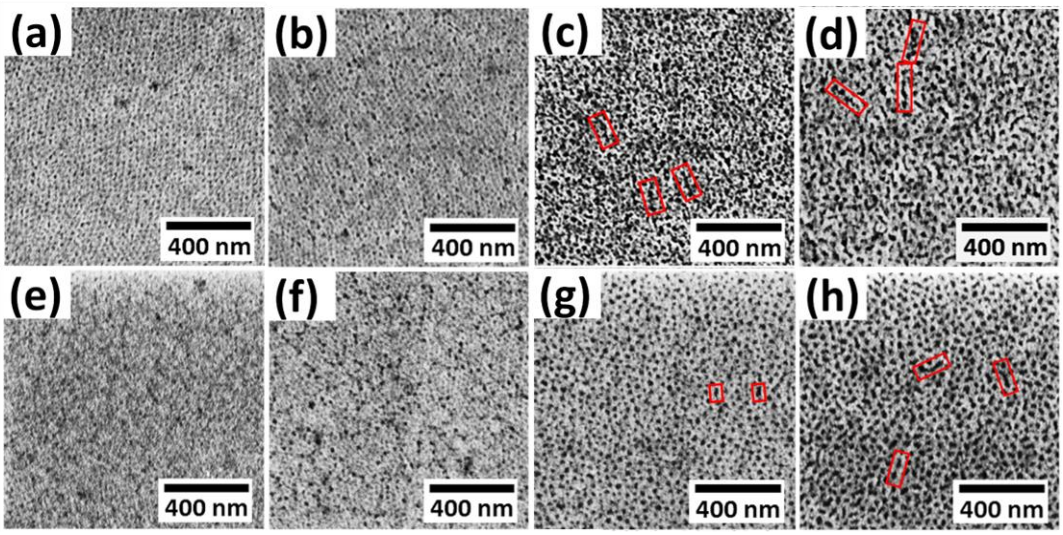

Figure 6.5 SEM images of polymer removed mesoporous ZnO films via (a-d) sintering and (e-h) UV-irradiation with different weight ratios of template to ZAD ($w_{PS\text{-}b\text{-}P4VP}$: w_{ZAD}): (a, e) 1:12, (b, f) 3:12, (c, g) 5:12, (d, h) 7:12. The red rectangles in (c), (d), (g), (h) indicate the connected pores. Reproduced with permission from Ref.[145] *Copyright {2018} American Chemical Society.*

For the sintered ZnO films, upon increasing the template-to-ZAD ratio from 1:12 to 7:12, the pore size increases gradually. With the ratio increasing, it is observed that small pores preferentially grow into large pores and also tend to connect with each other to form larger ones (about 140 nm for the sample of 5:12 and 170 nm for 7:12, marked by red boxes in Figure 6.5c and d). The ZnO films treated with UV-irradiation show a similar tendency when increasing the template-to-ZAD ratio. However, the pore sizes obtained via UV-irradiation are found smaller than the counterparts via sintering. With increasing the template-to-ZAD ratio for the UV-irradiated ZnO films, the small pores become larger and also tend to interconnect with each other to form larger pores (some pore sizes reach about 50 nm for sample with the ratio of 5:12 and 120 nm of 7:12, respectively, as marked by red boxes in Figure 6.5g and h). However, compared with the large pores of the sintered films, the corresponding large pores in the UV-irradiated films are smaller. The decreased pore size can be explained by a collapse that is induced by the polymer removal process. When the template is removed from the composite films, the initial ZnO scaffold inevitably collapses, therefore leading to smaller pore sizes. The irradiated ZnO films show smaller pore sizes than the sintered ones, indicating that the collapse behavior of ZnO films during UV-irradiation is more serious than that during sintering when removing the polymer template from the composite films.

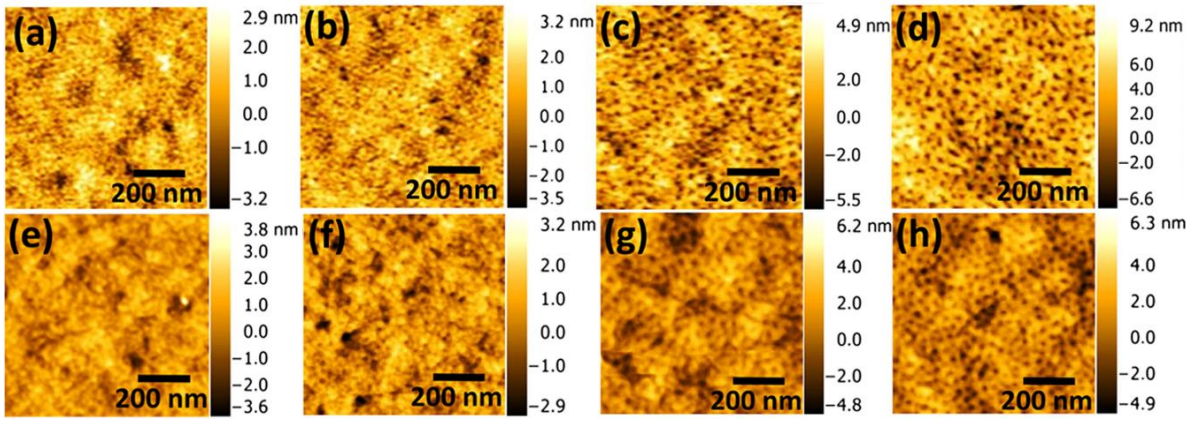

Figure 6.6 AFM images of polymer removed mesoporous ZnO films via (a-d) sintering and (e-h) UV-irradiation with different weight ratios of template to ZAD ($w_{PS\text{-}b\text{-}P4VP}$: w_{ZAD}): (a, e) 1:12, (b, f) 3:12, (c, g) 5:12, (d, h) 7:12. Reproduced with permission from Ref.[145] Copyright {2018} American Chemical Society.

To explore the surface morphology further, AFM measurements are performed for the template removed ZnO films. Figure 6.6 illustrates the topography of the mesoporous ZnO films post-treated with sintering (a-d) and UV-irradiation (e-h). When the ratio of the template increases, the pore sizes of the ZnO films increase independent of the post-treatment method. With small

ratios, the ZnO films seem more compact, which decreases the probability of backfilling for the dyes and charge carrier transport materials. When increasing the pore sizes along increasing the template-to-ZAD ratio, the pore sizes become larger, which benefits the subsequent penetration. This is supposed to provide a more beneficial interface between dye molecules and charge carrier transport materials for exciton separation. When increasing the pore sizes further, the interface may decrease, which decreases the opportunity of the exciton separation again. Compared with the sintered films, the irradiated samples appear to be more compact with the presence of smaller pore sizes. All these observations are consistent with the SEM results.

To investigate the morphology changes further with increasing the template-to-ZAD ratio, SEM and AFM images of 240 °C annealed ZnO films post-treated with UV-irradiation are shown in Figure 6.7 and 6.8, respectively. The morphologies for the ZnO films at 240 °C are quite different from those at 160 °C, which is mainly caused by the increased compatibility at 240 °C. When the template-to-ZAD ratio increases, aggregation of the ZnO clusters is observed and both the ZnO clusters and pores become larger, which is consistent with the morphology evolution trend at 160 °C.

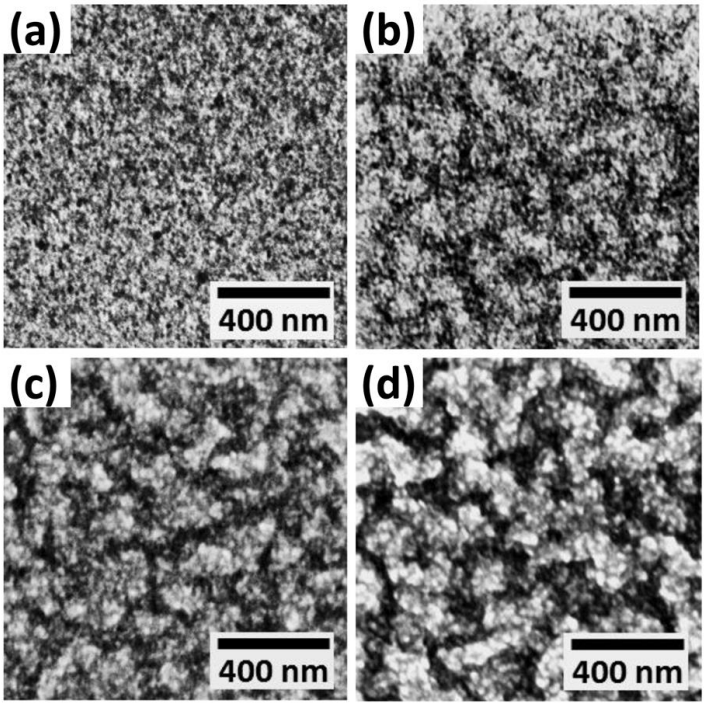

Figure 6.7 SEM images of UV-irradiated mesoporous ZnO films prepared from different ratios of polymer to ZAD at the annealing temperature of 240 °C: (a) $w_{PS\text{-}b\text{-}P4VP}$: w_{ZAD} =1:12, (b) 3:12, (c) 5:12, and (d) 7:12. Reprinted with permission from Ref.[145] *Copyright {2018} American Chemical Society.*

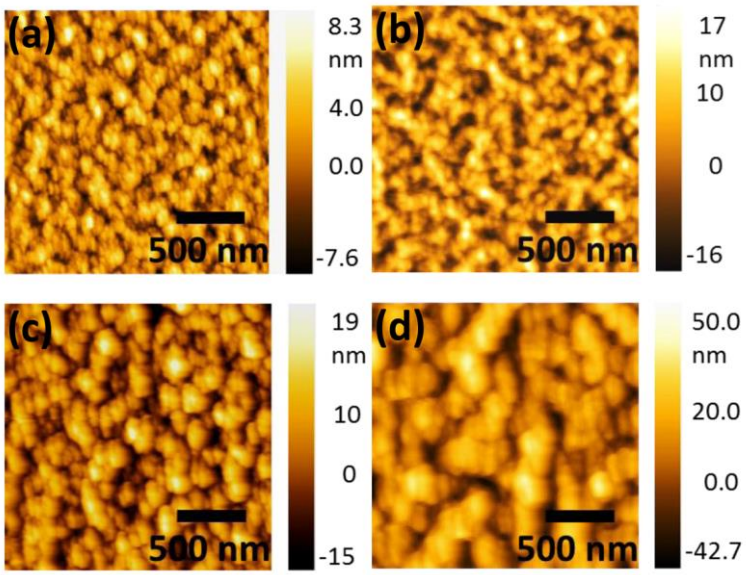

Figure 6.8 AFM images of UV-irradiated mesoporous ZnO films prepared from different ratios of polymer to ZAD at the annealing temperature of 240 °C: (a) $w_{PS\text{-}b\text{-}P4VP}$: w_{ZAD}=1:12, (b) 3:12, (c) 5:12, and (d) 7:12. Reprinted with permission from Ref.[145] *Copyright {2018} American Chemical Society.*

6.2.3 Inner morphology

Apart from the surface morphology, the inner morphology is also significant since both the dye molecules and the p-type semiconductor are required to be backfilled into the mesoporous ZnO films and the exciton separation and charge transfer occur at the interfaces of the dye molecules and the charge carrier transport materials. Moreover, it can happen that the inner morphology may be different from the surface morphology.[147-149] Therefore, investigating the characteristic features of the inner morphology is important. GISAXS is a powerful tool to investigate the inner morphology. The X-ray beam can penetrate the whole film since the incident angle is 0.35° which is higher than the critical angle. Therefore, the inner structure can be probed. Furthermore, a large area of the film is illuminated with X-rays which enables high statistics. Figure 6.9 shows the 2D GISAXS data of the ZnO films (annealed at 160 °C) treated via sintering and UV-irradiation. Two prominent Bragg scattering rods are observed in all the 2D scattering data, indicating that an ordered structure appears perpendicular to the substrate. When increasing the template-to-ZAD ratio, the position of the Bragg rods shifts to a lower q_y value for both sintered and irradiated samples. This reveals that when increasing the template-to-ZAD ratio, larger structures form for both sintered and irradiated ZnO films.

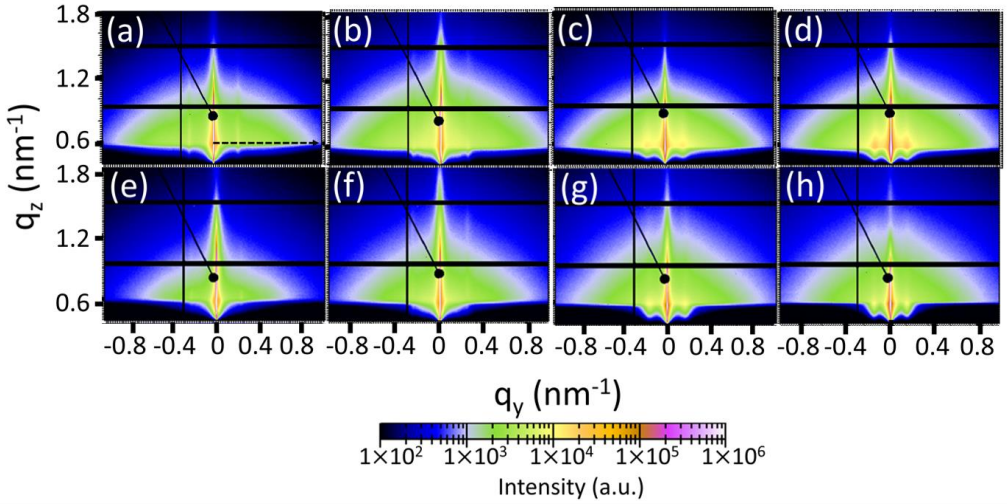

Figure 6.9 2D GISAXS data of polymer removed mesoporous ZnO films (annealed at 160 °C) via (a-d) sintering and (e-h) UV-irradiation with different weight ratios of template to ZAD ($w_{PS\text{-}b\text{-}P4VP}$: w_{ZAD}): (a, e) 1:12, (b, f) 3:12, (c, g) 5:12, (d, h) 7:12. The specular peak is shielded by a beamstop. The black dashed arrow in (a) indicates the Yoneda peak position where horizontal cuts for all the scattering patterns are made. Reproduced with permission from Ref.[145] Copyright {2018} American Chemical Society.

To get the lateral structural information about the ZnO films, horizontal line cuts are performed along the Yoneda peak which is located at the position of the critical angle of the materials (marked by the black dashed line in Figure 6.9a). Through the horizontal line cuts, the structural information parallel to the substrate can be obtained. For the sintered films, the horizontal line cuts show a prominent peak at around 0.2 nm^{-1} as marked by a blue box in Figure 6.10a.These peaks come from the Bragg rods as observed in the 2D scattering data. When increasing the weight ratio of the template, the peak moves to a lower q_y value, implying that the center-to-center distance becomes larger. For the UV-irradiated ZnO films, the horizontal line cuts (Figure 6.10c) show a similar changing trend. To get the length scales in detail, a 1D paracrystal model within the effective interface approximation of the distorted wave Born approximation (DWBA) is used to fit the horizontal line cuts. Similarly to the work in section 5.2.1, a cylindrical geometry is used to present ZnO clusters, with form factors representing the radii of the ZnO clusters, whereas structure factors corresponding to the center-to-center distance of the two neighboring cylinders with similar average sizes.[107, 121] Thus, the average pore size of the ZnO films in the present work can be obtained by the difference of center-to-center distance with the diameter of the clusters via modelling the cuts. To fit the horizontal line cuts well, three structures are required: the large-sized, middle-sized and small-sized structures. The

average small- and middle-pore sizes are extracted and plotted as a function of the weight ratio between the template and ZAD (Figure 6.10b and d). Because the exciton diffusion length is only tens of nanometers, the length scales in the small- and middle-range seem more significant than the large-sized structure. Therefore, the sizes of the large pores are not shown here. As expected, the small- and middle-pores show an increasing pore sizes upon increasing the template-to-ZAD ratio independent of the post-treatment method. Apart from this, the pores in the sintered films are larger than those in the irradiated samples for both small- and middle-sized pores. These results agree with the SEM and AFM data well.

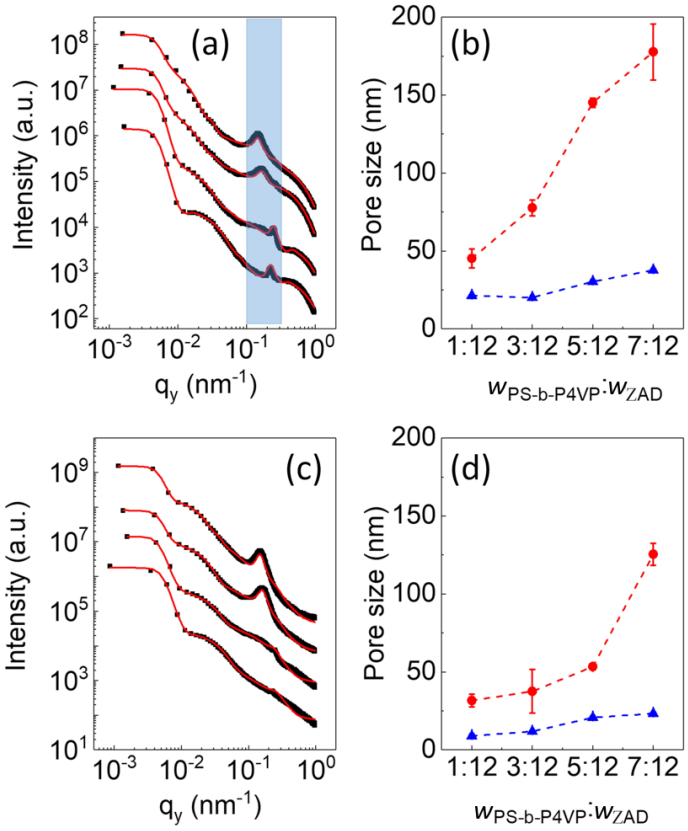

Figure 6.10 Horizontal line cuts obtained from the GISAXS measurements for ZnO films (annealed at 160 °C) with different ratios of polymer to ZAD with $w_{PS\text{-}b\text{-}P4VP}$: w_{ZAD}=1:12, 3:12, 5:12, and 7:12 from bottom to top. Polymer is removed by (a) sintering, and (c) UV-irradiation. The solid red lines indicate the fits to the data. Curves are shifted along the intensity axis for clarity of the presentation. Average pore sizes of polymer removed mesoporous ZnO films by (b) sintering and (d) UV-irradiation extracted from the fits are plotted as a function of the ratio of polymer to ZAD. Triangles indicate small-sized pores (blue) and circles middle-sized pores (red). The dashed lines in (b) and (d) are guides to the eye. Reprinted with permission from Ref.[145] Copyright {2018} American Chemical Society.

6.2.4 Structural evolution

According to the surface and the inner morphology detected by SEM, AFM and GISAXS, the pore sizes of the mesoporous ZnO films increase along increasing the template-to-ZAD ratio. Moreover, the sintered samples show larger pore sizes than those in the irradiated samples. A schematic representation of these changing trend is drawn in Figure 6.11. When the so-called good-poor solvent pair is introduced into the mixture of zinc precursor and diblock copolymer, micelles appear in the solution. As the template-to-ZAD ratio increases, the core size of the micelles increases due to the aggregation of the polymer chains. The ZAD molecules are preferentially located inside the P4VP block in the sol-gel, which also has an influence on the decrease of the mobility of the subsequently deposited films. During the following self-assembly in the annealing process, the mobility of the films is hindered to a large extent. Therefore, the final ZnO films also show increasing pore sizes with increasing the template-to-ZAD ratio from 1:12 to 7:12 after removing the template. In addition, the template removal method is also important to the pore sizes of the final ZnO films. The mechanism processes of polymer degradation via UV-irradiation and sintering are different and complicated. Two main processes occur during thermal degradation. At low temperatures, the materials on the substrate are stabilized, and at high temperatures actual degradation takes place. The low temperature increase rate in the pre-sintering process contributes to the films stabilization, thus decreasing the collapse of ZnO films. However, under UV-irradiation, photooxidative degradation of the polymers directly occurs, resulting into free radicals and small molecules. Therefore, more serious collapse and smaller pore sizes are observed in the final UV-irradiated ZnO films.

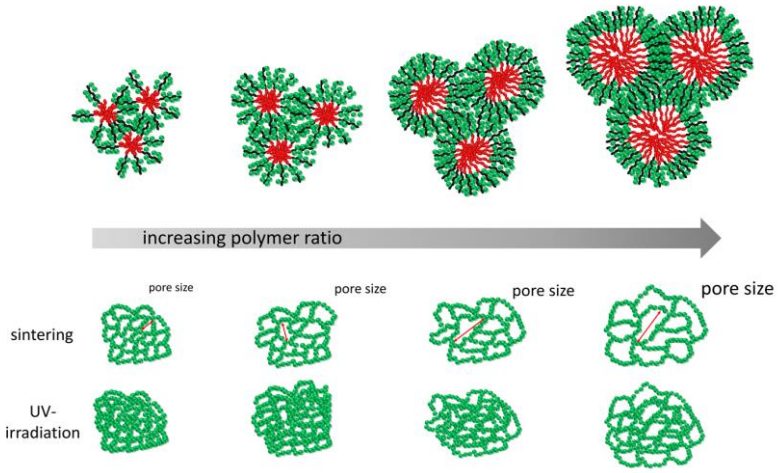

Figure 6.11 Schematic illustration of the structural evolution of ZnO/PS-b-P4VP micelles in sol-gel and the mesoporous ZnO films treated via sintering and UV-irradiation. Reprinted with permission from Ref.[145] *Copyright {2018} American Chemical Society.*

To further investigate the collapse behavior of the ZnO films via sintering and UV-irradiation, the film thickness is measured and plotted as a function of the template-to-ZAD ratio (Figure 6.12). When the template-to-ZAD ratio increases, the thickness of the ZnO films increases as well. Since the concentration in the sol-gel increases and all films are spin-coated via the identical protocol, therefore resulting in increasing film thickness. Moreover, the UV-irradiated samples show thinner films as compared with the corresponding films with sintering. UV-irradiation makes the ZnO films collapse in a more severe way than sintering during the template removal process.

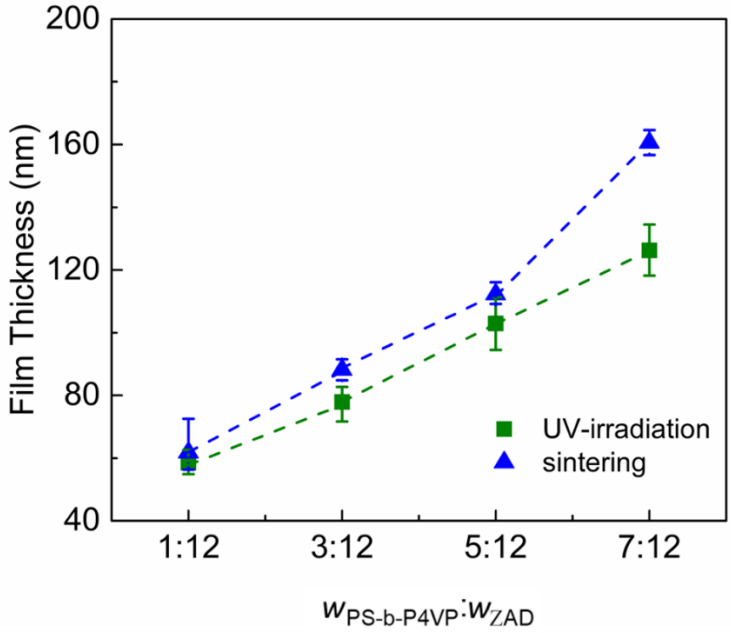

Figure 6.12 Film thickness of mesoporous ZnO films (annealed at 160 °C) plotted as a function of the ratio of polymer to ZAD. The dashed lines are guides to the eye. Reprinted with permission from Ref.[145] *Copyright {2018} American Chemical Society.*

6.2.5 Optical properties

UV-Vis spectra are employed for the ZnO films to investigate the light absorption in the UV-Vis region and the band gap as well. The transmittance of the ZnO films (annealed at 160 °C) post-treated with sintering and UV-irradiation is shown in Figure 6.13a and b, respectively. All the ZnO films show an absorption in the UV region and the transmittance intensity decreases with increasing the template-to-ZAD ratio, which is independent of the post-treatment method we used. This might be due to the increasing film thickness when the ratio increases from 1:12 to 7:12. On the other hand, in the visible region, almost 100% transmittance is observed for all the ZnO films, indicating a very good transparency in the visible range, which does not hinder

the absorption of photons for dye molecules. For the normally obtained wurtzite phase of ZnO films,[83, 150] the Tauc's equation (Equation 6.1) is used

$$\alpha h\nu = A(h\nu - E_g)^n, \quad (6.1)$$

in which A is a constant, $h\nu$ is the photon energy, E_g is the allowed band gap and n = 1/2 for direct transition.[151] $(\alpha h\nu)^2$ is plotted as a function of photon energy in Figure 6.13c and d and the band gap of ZnO films can be obtained from the x-axis intercept of the corresponding linear fits (in the dashed lines), which is around 3.3 eV for all the ZnO films post-treated with either sintering or UV-irradiation.

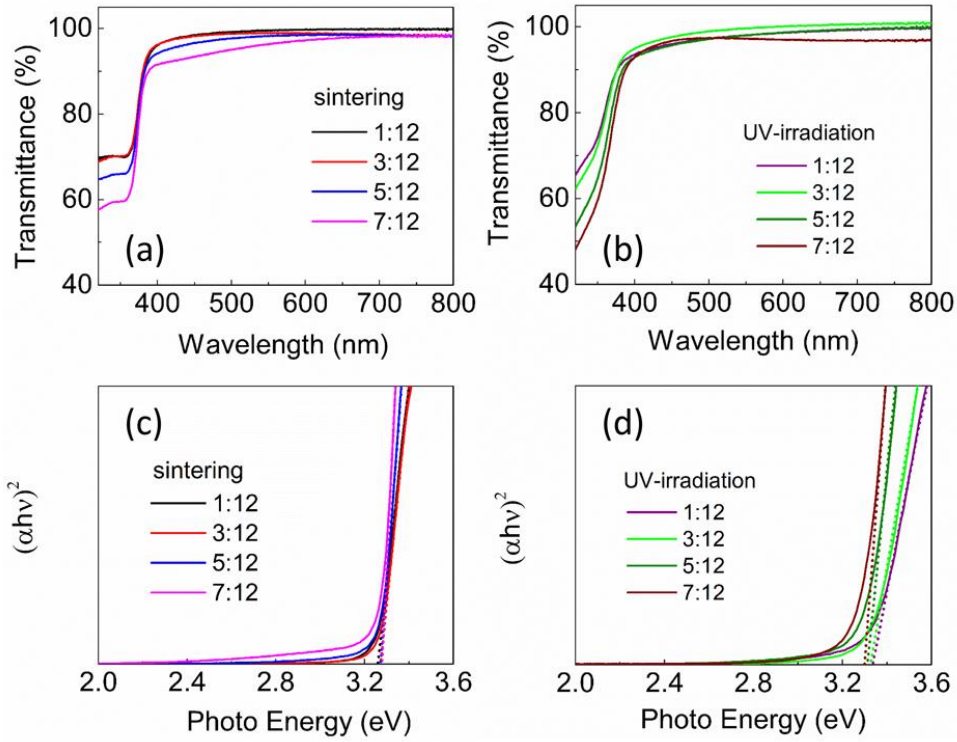

Figure 6.13. Transmittance spectra and direct optical band gap transitions $(\alpha h\nu)^2$ as a function of photon energy of mesoporous ZnO films prepared from different ratios of polymer to ZAD as indicated at the annealing temperature of 160 °C: (a) and (c) post-treated by sintering, and (b) and (d) post-treated by UV-irradiation. Reprinted with permission from Ref.[145] Copyright {2018} American Chemical Society.

6.3 Solar cell performance

To investigate the photovoltaic performance of the complete devices, ssDSSCs are fabricated on the basis of the ZnO films prepared from different template-to-ZAD ratios in section 6.3.1. The device layout is shown in Figure 6.14a. It is FTO/compact ZnO/mesoporous ZnO/D205/spiro-OMeTAD/Au. For more detailed description about the fabrication of the ssDSSCs, it is given in section 4.2.2. Moreover, the photovoltaic performance of ssDSSCs based on ZnO films post-treated with sintering and UV-irradiation is compared in section 6.3.2 as well.

6.3.1 Influence of weight ratio

The photovoltaic performance is characterized by the current density-voltage characteristics (I-V curves). Figure 6.14b shows the I-V curves of the ssDSSCs fabricated from the sintered ZnO films. The shape of the curves changes greatly, with the curve obtained from the template-to-ZAD ratio of 5:12 possessing the largest covering area. When increasing the ratio from 1:12 to 7:12, the V_{oc} increases gradually. To see the photovoltaic parameters more intuitively, the four parameters, J_{sc}, V_{oc}, FF and PCE are plotted as a function of the template-to-ZAD ratio as shown in Figure 6.14c and d. Due to the much thinner ZnO films than the reported value, the efficiency obtained in this work is not so high.[15, 152-154] However, the changing trend of the photovoltaic performance based on ZnO films can be well represented in this work. The V_{oc} increases from 0.44 ± 0.01 eV to 0.66 ± 0.01 eV with increasing the ratio ($w_{PS\text{-}b\text{-}P4VP}$: w_{ZAD}) from 1:12 to 7:12. This can be explained by the larger pore sizes which makes more efficient backfilling and thicker ZnO films which are beneficial for loading more dye molecules in the mesoporous ZnO, therefore contributing to the improvement of V_{oc}. While increasing the template-to-ZAD ratio from 1:12 to 7:12, the PCE first increases and then decreases, with a highest PCE at around 0.47% for the ssDSSCs based on ZnO films prepared from 5:12. The PCE changes in the same routine with that of J_{sc}. As investigated in both the surface morphology and the inner morphology, the pore sizes increase with increasing the template-to-ZAD ratio. When the ratio increases from 1:12 to 5:12, the increasing pore sizes provide a better pathway for dye molecules and spiro-OMeTAD to be penetrated into the ZnO films. The effective connection between dye molecules and charge carrier transport materials at the interface is improved, therefore improving the probability for the exciton separation and charge transfer at the interfaces. Moreover, the increased ZnO film thickness within a certain range (about 2 μm) also promotes this process, thereby increasing the generated free charge carrier density. However, if the pore sizes increase further (for the sample with the template-to-ZAD ratio of 7:12), the interface area is supposed to decrease, which decreases the interfaces for the

exciton separation. Although the ZnO film is thicker and with larger pores the penetration of spiro-OMeTAD become more efficient, the decreased interface area hinders the improvement of the photovoltaic performance in this case. Therefore, the PCE and the J_{sc} decrease when increasing the ratio to 7:12.

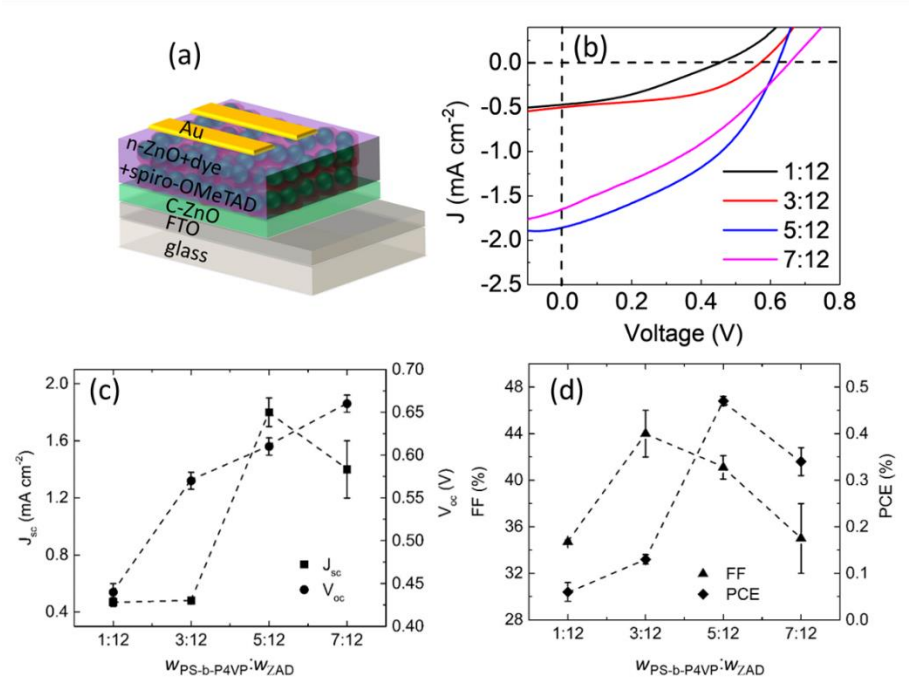

Figure 6.14 (a) Schematic representation of a ssDSSC setup; (b) Current density–voltage characteristics of ssDSSCs based on sintered mesoporous ZnO films prepared from different polymer to ZAD ratios; (c) J_{sc} and V_{oc}, and (d) FF and PCE extracted from I-V curves of the ssDSSCs based on sintered mesoporous ZnO films plotted as a function of the ratio of polymer to ZAD. The dashed lines are guides to the eye. Reproduced with permission from Ref.[145] *Copyright {2018} American Chemical Society.*

6.3.2 Influence of post-treatment technique

For the ssDSSCs based on ZnO films with the template-to-ZAD ratio of 5:12 post-treated with different techniques, the I-V curves are shown in Figure 6.15. Compared with the ssDSSCs from irradiated films, those from sintered samples show much larger covered area, which indicates a much better photovoltaic performance. The corresponding parameters are shown in Table 6.1. The ssDSSCs based on sintered ZnO films show much higher *PCE* (0.47 ± 0.01%) than those from UV-irradiated ZnO films (0.2 ± 0.04%). This is mainly due to the improvement of the J_{sc}. The ssDSSCs from sintered ZnO films exhibit over twice of J_{sc} than those from irradiated samples. The improvement in *PCE* and J_{sc} can be explained by the larger pore sizes

of the sintered ZnO films than those from the irradiated samples. The penetration of dye molecules and spiro-OMeTAD is improved and hence results in a better contact of ZnO/dye/spiro-OMeTAD interfaces. Moreover, the sintered ZnO films show a better crystallization as compared to the UV-irradiated ZnO, which would decrease the traps in the films. This favors the speed up of the charge transport process in ssDSSCs, thus reducing exciton recombination at the ZnO/dye interface and improving the photovoltaic performance.

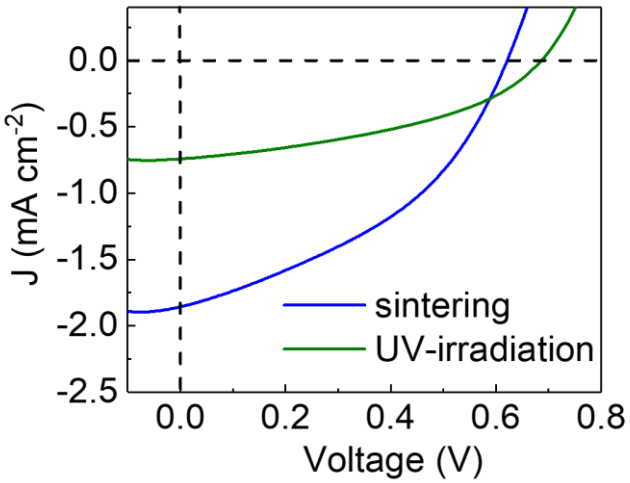

Figure 6.15 Current density–voltage characteristics of ssDSSCs based on different post-treated mesoporous ZnO films prepared from $w_{PS\text{-}b\text{-}P4VP}$: w_{ZAD}=5:12. Reprinted with permission from Ref.[145] Copyright {2018} American Chemical Society.

Table 6.1 Device parameters extracted from I-V curves of ssDSSCs based on different post-treated mesoporous ZnO films annealed at 160 °C with $w_{PS\text{-}b\text{-}P4VP}$: w_{ZAD}=5:12. Reprinted with permission from Ref.[145] Copyright {2018} American Chemical Society.

post-treatment	J_{sc} (mA cm^{-2})	V_{oc} (V)	*FF* (%)	*PCE* (%)
UV-irradiation	0.8 ± 0.2	0.68 ± 0.01	39.6 ± 2.0	0.20 ± 0.04
sintering	1.8 ± 0.1	0.61 ± 0.01	41.1 ± 1.0	0.47 ± 0.01

Electrochemical impedance spectra (EIS) are shown in Figure 6.16 to investigate the interfacial charge carrier transfer process. Compared to the UV-irradiated ZnO based devices, those based on the sintered ZnO films show a smaller charge transfer resistance (R_{ct}) at the ZnO/dye/HTM interface, which indicates a lower probability of the hole-electron recombination action in the

devices fabricated from the sintered ZnO films. The Bode phase plots of the EIS spectra are shown in Figure 6.16b. The devices based on UV-irradiated samples show a higher characteristic frequency peak than the sintered samples, demonstrating that the electron life time for the recombination (τ) is reduced when changing the post-treatment method from UV-irradiation to sintering according to Equation 5.1. Therefore, it promotes the improvement of the photovoltaic performance of the ssDSSCs based on the sintered ZnO films.

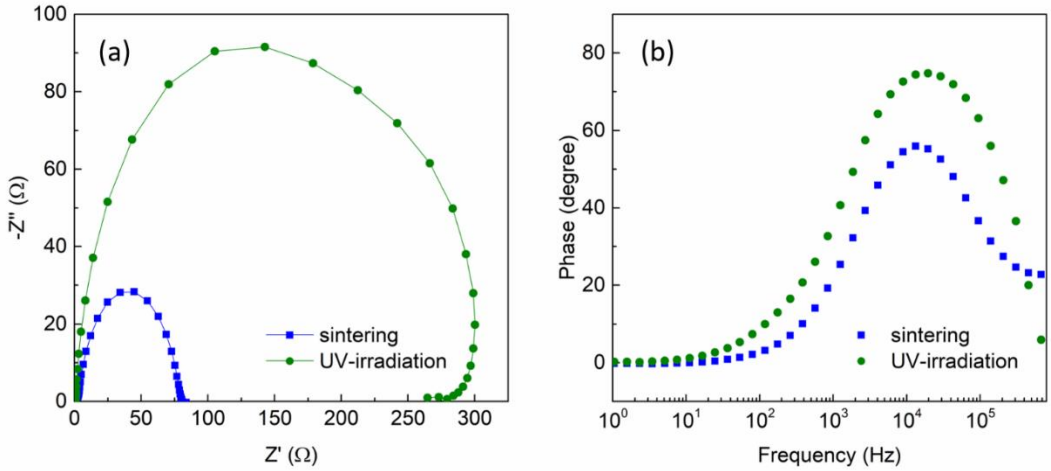

Figure 6.16 EIS analyses of DSSCs based on ZnO films post-treated with sintering and UV-irradiation as indicated. (a) Nyquist plots; (b) Bode phase plots. Reprinted with permission from Ref.[145] Copyright {2018} American Chemical Society.

6.3.3 Long-term stability

For solar cell devices, apart from the efficiency which determines the photovoltaic performance, another feature, namely the long-term stability, also plays a critical role for real application. In this work, the stability is measured under ambient air conditions without any encapsulation. Figure 6.17 shows the decays of *PCE*, J_{sc}, V_{oc} and *FF* along the measurement time for the ssDSSCs based on the sintered ZnO films prepared from the ratio of 5:12. The mostly stable parameter is V_{oc}, which remains constant after 80 days. For the *PCE*, after 80 days, it still remains 92.6% of the initial efficiency. It changes in the same way as J_{sc} and *FF*. Moreover, the initial increased *PCE* might be resulted from the improved penetration of spiro-OMeTAD into the mesoporous ZnO films and the "activation" of the entire electrode.[155] For the I-V curves obtained at different times as indicated in Figure 6.18, the shape of the curves looks similar, except a slight change for the J_{sc}, V_{oc} and *FF*.

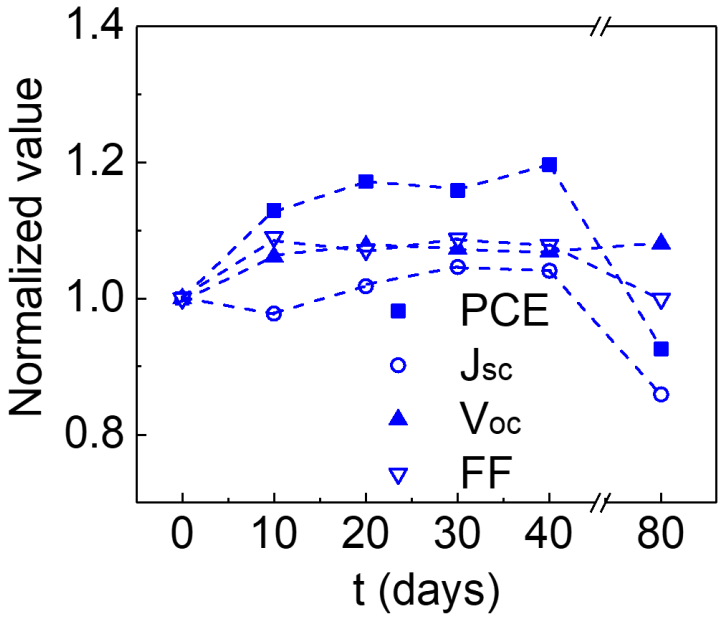

Figure 6.17 Stability of ssDSSCs based on sintered mesoporous ZnO films prepared from $w_{PS\text{-}b\text{-}P4VP}$: w_{ZAD}=5:12. The dashed lines are guides to the eye. Reprinted with permission from Ref.[145] Copyright {2018} American Chemical Society.

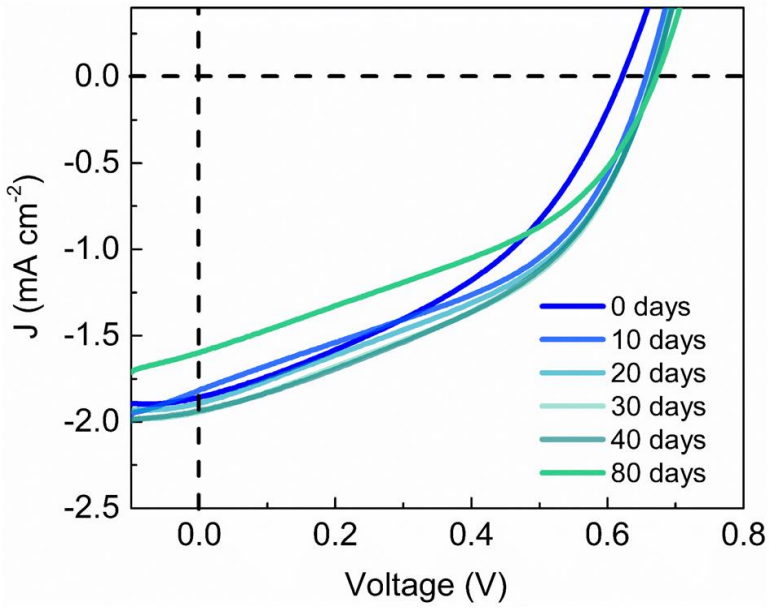

Figure 6.18 Current-voltage characteristics of ssDSSCs based on sintered mesoporous ZnO films annealed at 160 °C with $w_{PS\text{-}b\text{-}P4VP}$: w_{ZAD}=5:12. Reprinted with permission from Ref.[145] Copyright {2018} American Chemical Society.

6.4 Summary

In this part, the pore sizes of the ZnO films are investigated, which is significant for the penetration of dye molecules and the p-type semiconductors when application in ssDSSCs. A sol-gel synthesis is combined with a diblock copolymer PS-*b*-P4VP, which acts as a template, to control the morphology of the ZnO films. Although the sponge-like structure is obtained independent of the post-treatment technique and the changing ratio between the template and the zinc precursor, the pore sizes changes significantly. Both, SEM and AFM measurements reveal that ZnO films post-treated with UV-irradiation show smaller pore sizes at the surface than those treated with sintering. GISAXS measurement also exhibits that the pores buried in the films show smaller sizes for the UV-irradiated samples as compared with those in the sintered films. The decreased pore sizes for the UV-irradiated samples mainly originate from the more severe collapse of the ZnO scaffold during the template removal process than those in the sintered samples. Apart from this, the template-to-zinc precursor ratio also plays an important role in the pore sizes tuning. When increasing the template-to-ZAD ratio, the pore sizes increase gradually for the ZnO films regardless of the post-treatment technique. The increasing pore sizes benefit the penetration of the dye molecules and the p-type semiconductors, therefore improving the probability for exciton separation and charge transfer at the interfaces between dye molecules and charge carrier transport materials. However, it also decreases the interface area, which is required for exciton separation. Eventually, the corresponding ssDSSCs are fabricated. For application in photovoltaic devices, the band gap of ZnO is determined by UV-Vis measurements and 3.3 eV is found for all the prepared ZnO films, which indicates the successful preparation of semiconductive ZnO with a suitable band gap for an electron transport layer. The photovoltaic performance shows a close relationship with the pore sizes of the ZnO films. With the increase of pore sizes for sintered ZnO films, the efficiency of the corresponding device initially increases and then decreases, with an optimal efficiency at the ratio of $w_{\text{PS-}b\text{-P4VP}}$: w_{ZAD}=5:12. Compared with ssDSSCs based on the UV-irradiated ZnO films, those from sintered ZnO films show a higher efficiency which may originate from the larger pore sizes of the ZnO films, therefore improving the probability of backfilling of dye molecules and p-type semiconductors. In addition, ssDSSCs based on the optimal pore sizes show a very good long-term stability. Despite all steps (including fabrication, storage and characterization) of the ssDSSCs are conducted under ambient air conditions, it still remains 92.6% of the initial efficiency after 80 days.

We demonstrate the importance of the pore sizes of the ZnO films with respect to the application in ssDSSCs. By varying the post-treatment technique the pore sizes can be tuned,

which provides a reliable preparation route, gives control over the ZnO film morphology and eventually improves the photovoltaic performance of the ssDSSCs.

7. ZnO/P3HT hybrid film modification with P3HT-*b*-PEO

Parts of this chapter have been published in the article: Tuning of the Morphology and Optoelectronic Properties of ZnO/P3HT/P3HT-*b*-PEO Hybrid Films via Spray Deposition Method (K. Wang *et al.*, ACS Appl. Mater. Interfaces 2018, 10, 20569-20577, DOI: 10.1021/acsami.8b05459).

Block copolymers, with two or more blocks of different polymerized monomers covalently bound with each other, show great potential for many foreseeable applications, such as solar cells, sensors, drug deliveries, *etc*.[156-158] Due to the competing forces originating from the enthalpy contribution of mixing and the entropy penalty associated with elongating the polymer chains, the obtainable structures exhibit a well-defined ordered structure on the nanometer length scale via microphase separation.[109, 159] With block copolymers, apart from the combination of distinct properties of each blocks, an interesting nanoscale assembly phenomena due to the covalent bonds can also be accessed.

Among the block copolymers, the simplest and most commonly used classes are di- and tri-block copolymers. Manifold morphologies can be obtained via self-assembly process, *e.g.* spheres, cylinders, lamellae, and bicontinuous structures.[91, 135, 160] Based on these different morphologies, one important application of block copolymers is their use as a template for synthesis of inorganic nanomaterials.[134, 139, 161, 162] Kim *et al.* prepared mesoporous ZnO films by depositing ZnO precursors onto porous PS templates, which were fabricated beforehand by removing the other block in the diblock copolymer of polystyrene-block-poly(methyl methacrylate) (PS-*b*-PMMA) or polystyrene-block-polyisoprene (PS-*b*-PI).[114] Finally, the PS block was removed as well to get pure nanostructured ZnO films. Another route, which seems more efficient, is sol-gel synthesis, where the amphiphilic block copolymer serves as a template and is introduced into the sol-gel together with the ZnO precursor. With the introduction of the so-called good-poor solvent pair, micelles are formed in the solution with metal oxides prefer to incorporate in one of the blocks. Therefore, various morphologies can be obtained for the metal oxides via self-assembly process. In chapter 5 and 6, diblock copolymers of PS-*b*-PEO and PS-*b*-P4VP are used to tune the morphology of the mesoporous ZnO films. Different structures with tunable pore sizes are obtained via changing the annealing temperature, the precursor ratio and the post-treatment method. These copolymers provide many possibilities to

change the structure of metal oxides, which also shows great potential for application in HBSCs.[136]

To improve the photovoltaic performance of HBSCs, the surface area of the inorganic semiconductors needs to be improved since excitons can only separate at the interfaces between the inorganic semiconductor and the p-type conducting polymers generating free charge carriers. Moreover, it is beneficial if the inorganic materials can form an interconnected structure in which the free charge carriers can travel to their corresponding electrode. Thus, the structure of the inorganic semiconductors is of high importance. A good way to control the morphology of the inorganic semiconductor films is to use sol-gel synthesis which is assisted with amphiphilic diblock copolymers. It is demonstrated in chapter 5 that a microphase separation of PS-*b*-PEO, which is induced by a good-poor solvent pair, enables to control the morphology of the interconnected network ZnO nanostructures with tunable surface area and interconnected network structure.[48] The PEO block plays an important role to control the morphology of the ZnO films since during the self-assembly process zinc precursor is grown on the PEO block preferentially. In contrast, the only task of PS is to enable microphase separation to form well-defined nanostructures. To make hybrid solar cells, the block copolymer need to be removed after the desired morphology is achieved due to its insulating property. Generally further steps, such as calcination, UV-irradiation or toxic solvents are used to remove the polymer inside the films, which are energy- and time-consuming. Moreover, nanopore penetration with a p-type semiconductor is also required to build a hybrid solar cell, which is still a challenge due to potentially unfavorable interaction of the polymer solution with the metal oxide nanostructure as well as steric problems of the conjugated polymer induced by the metal oxide nanostructure.[81, 163, 164] Thus, replacing the PS block with a p-type semiconducting polymer seems quite promising. In this case, neither template removal steps nor backfilling procedures are needed any more. P3HT is a commonly used conjugated polymer to extract the positive charge carriers to their corresponding electrode. Unlike the routines for regular organic solar cells, if we directly mix the ZnO particles with P3HT, non-continuous large domains will form, instead of a well-mixed blend due to the incompatibility of these inorganic and organic materials. Such large and non-connected domains are not useful for hybrid solar cells, because they will hinder exciton separation and charge carrier transport.[165, 166] To solve this problem, a different type of block copolymer, with one block being conductive, for example P3HT is used. Due to the covalently bonding of the two blocks, microphase separation will occur and exhibit nanoscale structures.[167]

In this part, not PS-*b*-PEO, but P3HT-*b*-PEO is used to act as a template, in which P3HT acts as the charge carrier transport material and light absorber, and PEO serves as a template for

ZnO synthesis. The ZnO particles and P3HT can directly form heterojunction in the hybrid solar cells via the self-assembly process without requirement for further polymer removal or nanopore penetration. In a simple one-step approach, ZnO nanoparticles are directly synthesized in the PEO block during the sol-gel process and form the heterojunction with the interface with P3HT. Spray coating is used to deposit the composite solutions on the substrates, which is simple, low-cost and up-scalable.[168, 169] Both, the surface and inner morphologies of the composite films are studied and the corresponding optoelectronic properties and solar cell performance are also investigated.

7.1 Fabrication route of hybrid films

For preparing the ZnO/P3HT-*b*-PEO hybrid films, several steps are performed as following. Figure 7.1 shows a schematic representation of the preparation process. Section 4.2.3 describes the sample preparation in more detail. In this work, the mixture solvent of DCB and DMSO is used instead of pure DCB or pure DMSO solvent. This is mainly due to the different solubility of the P3HT, PEO and zinc oxide precursor. P3HT can only be dispersed in the nonpolar solvent, whereas the other materials only in polar solvents. Moreover, the two solvents possess a similar boiling point, which is important to obtain a homogeneous film during spray coating. For preparing the composite solution, first the polymers (P3HT and P3HT-*b*-PEO), and the zinc oxide precursor are dispersed in the mixed solvent separately, followed by mixing these two solutions under stirring. Afterwards, spray coating is performed at 80 °C. The solvent evaporation from the droplets during the whole spray process is considered as an important factor for determination of the spray parameters. A more detailed description and the used spray parameters are given in section 4.2.3. Finally annealing is performed at different temperatures (all below 240 °C) to investigate the morphology influenced by annealing temperature. The weight ratio of ZnO and P3HT is kept at 2:1 while the amount of the diblock copolymer P3HT-*b*-PEO is changed to investigate its influence on the film morphology. The crystalline structures of P3HT and ZnO in the hybrid films are investigated by XRD measurement as shown in Figure 7.2. The prominent peak in Figure 7.2 is attributed to the (100) plane of P3HT, corresponding to the chain-chain interlayer distance. In Figure 7.2b, three characteristic peaks are observed, which indicates the wurtzite phase of ZnO prepared from sol-gel synthesis. This phase is considered as beneficial for charge transport properties.[106]

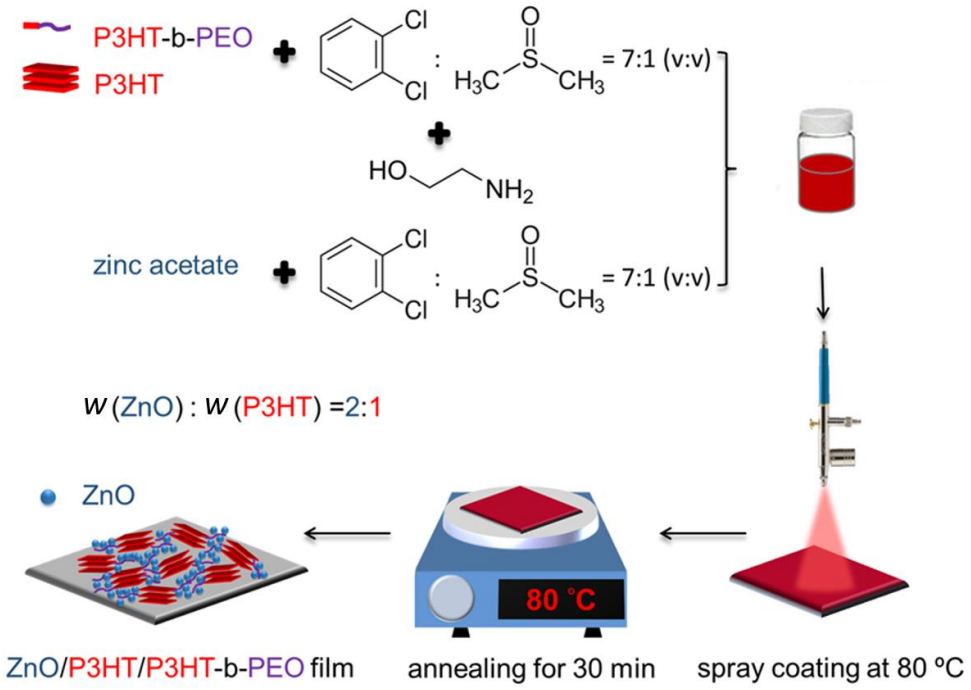

Figure 7.1 Schematic representation of the steps involved in the fabrication of the ZnO/P3HT/P3HT-b-PEO hybrid films via spray coating and subsequent thermal annealing (for example at 80 °C). Reprinted with permission from Ref.[150] *Copyright (2018) American Chemical Society.*

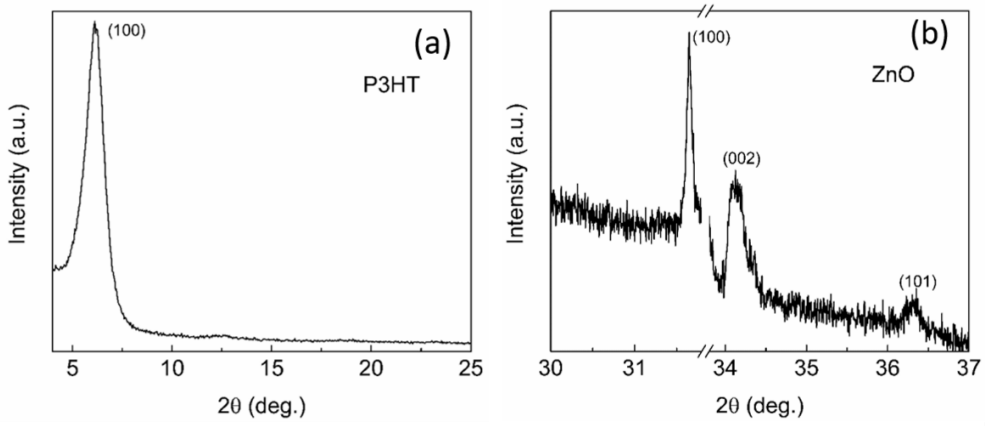

Figure 7.2 XRD pattern of 80 °C annealed ZnO/P3HT/P3HT-b-PEO films with a ratio of w_{ZnO}*:* w_{P3HT}*:* $w_{P3HT\text{-}b\text{-}PEO}$ *= 2:1:1. The prominent peaks correspond to (a) P3HT and (b) wurtzite ZnO, respectively. In the curve in (b) the strong Bragg peak of the Si substrate is not shown in the range from 31.8 to 33.8 degrees. Reprinted with permission from Ref.*[150] *Copyright (2018) American Chemical Society.*

7.2 Film morphology influenced by weight ratio

To investigate the morphology of the samples with and without the diblock copolymer P3HT-*b*-PEO, SEM measurements are performed to probe the surface structure. Moreover, the surface morphology of the ZnO/P3HT/P3HT-*b*-PEO hybrid films influenced by the amount of the diblock copolymer is also investigated and the corresponding analysis is given in section 7.2.1. With respect to the active layer for application in hybrid bulk heterojunction solar cells, the interfaces between ZnO and P3HT are mostly present in the films, and can therefore not be observed with surface sensitive measurement techniques like SEM. Thus, GISAXS is used to probe the morphology buried in the films in section 7.2.2.

7.2.1 Surface morphology

The surface morphology is investigated by the optical microscope (OM). For the ZnO/P3HT/P3HT-*b*-PEO hybrid films annealed at 80 °C with the ratio of 2:1:0, the sample shows a homogeneous film at low magnification (Figure 7.3a and b). Under high magnification, plenty of coffee rings are observed at the surface (Figure 7.3c, d and Figure 7.4a), which are resulted from the complicated spray process. From the OM images obtained from the hybrid films with different ratios (Figure 7.4a-d), it is hard to see any difference between the surface morphology. This is mainly because of the potential different structures in smaller length scale, which is regularly impossible to be observed with OM.

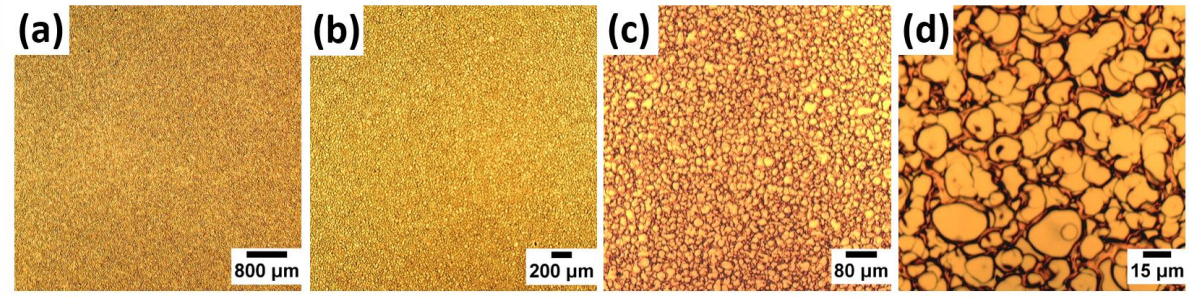

Figure 7.3 OM images of the spray coated ZnO/P3HT/P3HT-b-PEO hybrid films with the ratio of w_{ZnO}: w_{P3HT}: $w_{P3HT\text{-}b\text{-}PEO}$ =2:1:0 and annealing temperature of 80 °C.

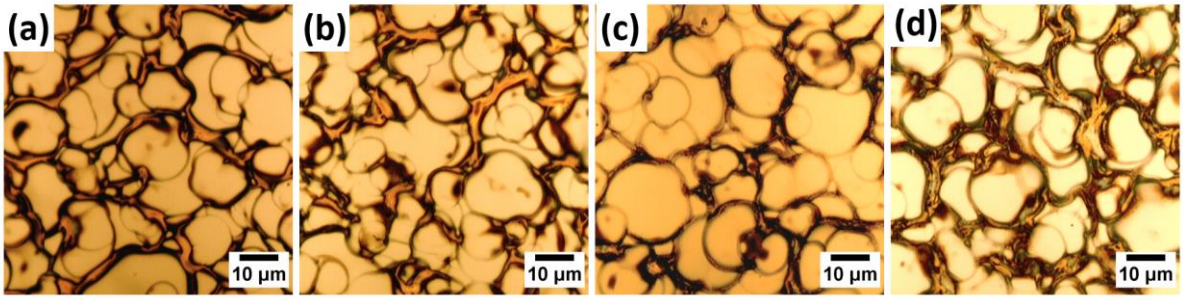

Figure 7.4 OM images of the ZnO/P3HT/P3HT-b-PEO hybrid films deposited by spray coating and annealing at 80 °C. Ratios of w_{ZnO}: w_{P3HT}: $w_{P3HT\text{-}b\text{-}PEO}$ are (a) 2:1:0, (b) 2:1:0.2, (c) 2:1:0.5, and (d) 2:1:1.

To further investigate the surface morphology in the nanometer length scale, the ZnO/P3HT/P3HT-*b*-PEO hybrid films are investigated by SEM measurements (Figure 7.5). Due to the different electron density of ZnO and polymers, the SEM images show large contrast, with the bright phase being ZnO particles and polymers present in the darker regions. It is observed that all the SEM images show an interconnected network structure for ZnO nanoparticles, which provides a good pathway for electrons to be extracted to the corresponding electrode. Similarly, the P3HT shows an interconnected structure as well, which is beneficial for the positive charge carrier transport.[170] For the ZnO/P3HT hybrid films without the addition of the diblock copolymer P3HT-*b*-PEO, large domains for both ZnO and P3HT are observed. Both, ZnO and P3HT domains prefer to aggregate with their phase due to the incompatibility of the two materials. In contrast, the hybrid films with the diblock copolymer inside (Figure 7.5b-d) show much smaller ZnO and P3HT domain sizes and more homogeneous films. Instead of aggregating into large domains, ZnO is enriched in the PEO block preferentially. Therefore, the morphology of ZnO nanoparticles is tuned via microphase separation of the diblock copolymer and the ZnO particles show a much smaller and increased monodispersity for the sizes compared with the film without the diblock copolymer. Moreover, in the diblock copolymer P3HT-*b*-PEO, the P3HT block will be embedded into the P3HT homopolymer, whereas the PEO block acts as a template for growing ZnO, which plays an important role in modifying the interfaces of ZnO and P3HT. Thus, it provides an approach to make a good blend of ZnO and P3HT on a controlled nanometer length scale. When increasing the ratio of the diblock copolymer from 0.2 to 1, both, the ZnO nanoparticles and the distance between neighboring ZnO become smaller. This is supposed to provide a larger interface between ZnO and P3HT, and thus, is beneficial for the exciton separation. For the samples with

a ratio of diblock copolymer being 1, a very homogeneous film with the smallest ZnO domains is observed.

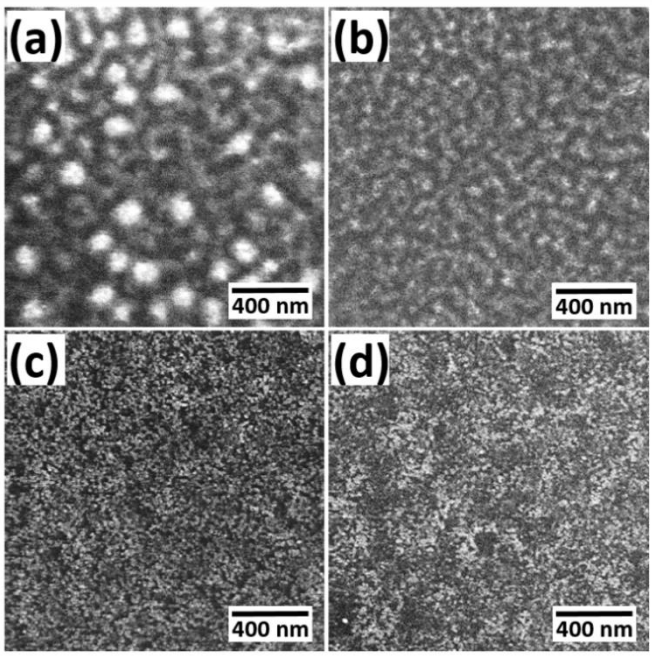

Figure 7.5 SEM images of the ZnO/P3HT/P3HT-b-PEO hybrid films deposited by spray coating and annealing at 80 °C. Ratios of w_{ZnO}: w_{P3HT}: $w_{P3HT\text{-}b\text{-}PEO}$ are (a) 2:1:0, (b) 2:1:0.2, (c) 2:1:0.5, and (d) 2:1:1. ZnO appears bright and polymer phase dark. Reprinted with permission from Ref.[150] Copyright (2018) American Chemical Society.

To investigate the surface morphology on a larger scale, SEM images with different magnifications are shown in Figure 7.6 for the sample with the diblock copolymer ratio of 1. Despite that coffee rings are present at the surface of the hybrid films on the micrometer length scale (Figure 7.6b), which mainly originates from the complicated flow behaviors during the spray deposition process,[171-173] a very homogeneous film can still be observed at lower magnification on the nanometer length scale (Figure 7.6a). This homogeneous and interconnected network structure on the nanometer length scale is beneficial for improving the interface for exciton separation and the pathway for free charge carriers extraction.

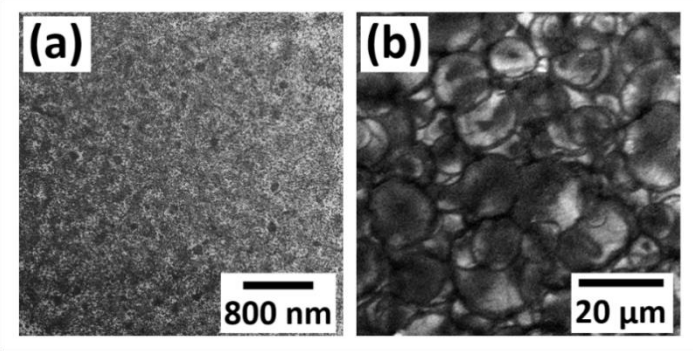

Figure 7.6 SEM images with different magnifications of sprayed ZnO/P3HT/P3HT-b-PEO hybrid films with a ratio of w_{ZnO}: w_{P3HT}: $w_{P3HT\text{-}b\text{-}PEO}$ = 2:1:1 processed at 80 °C: (a) on nanometer length scale, and (b) on micrometer length scale. Reprinted with permission from Ref.[150] Copyright (2018) American Chemical Society.

7.2.2 Inner morphology

GISAXS is used to probe the morphology buried in the films. Figure 7.7 shows the 2D GISAXS data for the ZnO/P3HT/P3HT-*b*-PEO hybrid films with different ratios. In the images, the specular peak is covered by a beamstop to avoid oversaturation and the damage to the detector, and in turn highlights the scattered signal at the Yoneda peak region,[174-177] which shows an intensive peak at the position of the material's critical angle. The X-rays can penetrate the whole film if the incident angle is larger than the critical angle.[178, 179] In this case, the inner structure buried in the films can be detected. Generally, we can get the vertical structure information from the scattering signal in the vertical direction (along q_z) and lateral structure information from the horizontal direction (along q_y). For the samples with different diblock copolymer ratios, although the scattering signals in the vertical direction are similar, the patterns in the horizontal direction along the Yoneda peak region are quite different. It scatters more widely when increasing the ratio of the diblock copolymer, which indicates the existence of smaller structure scales in the films.

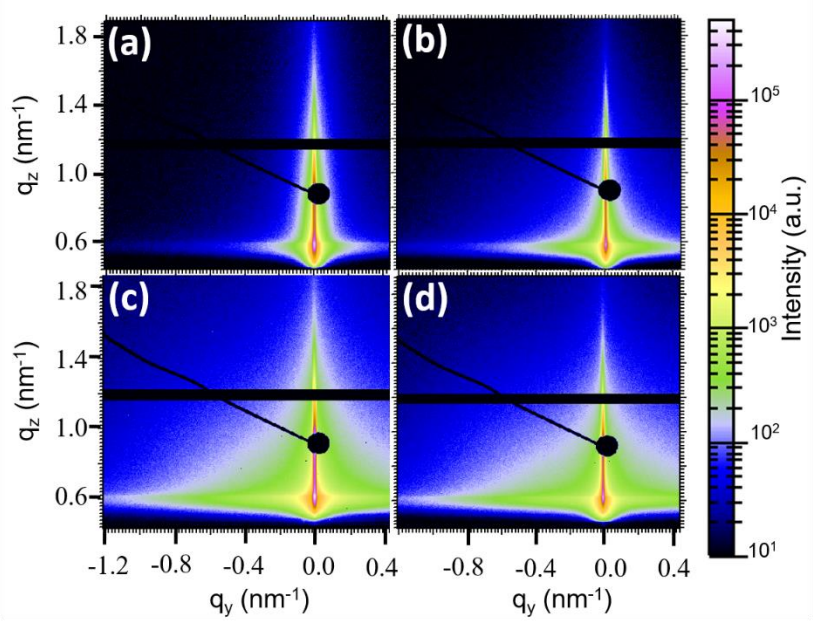

Figure 7.7 2D GISAXS data of the ZnO/P3HT/P3HT-b-PEO hybrid films deposited by spray coating and annealing at 80 °C. Ratios of w_{ZnO}: w_{P3HT}: $w_{P3HT\text{-}b\text{-}PEO}$ = (a) 2:1:0, (b) 2:1:0.2, (c) 2:1:0.5, and (d) 2:1:1 are shown. The specular peak is blocked by a beamstop. All the images have the same intensity scale as shown in the scale bar. Reprinted with permission from Ref.[150] *Copyright (2018) American Chemical Society.*

Vertical line cuts for the samples with different ratios of diblock copolymer are performed along the vertical direction at q_y=0 (Figure 7.8a). At the exit angle being 0°, it indicates the sample horizon, which is along the sample plane. No signal is detected at the position marked by a grey box due to the gap of the detector below the sample horizon. The sudden drop in intensity at around 0.4° for all curves is resulted from the shielding of the specular beam with a beamstop. The region between the sample horizon and the specular beam is dominated by the Yoneda peak. A prominent peak at 0.133°~0.138° (marked with blue strip) originates from the critical angle of the SiO_x/Si substrate. This is consistent with the theoretical value.[139] For P3HT, the theoretical critical angle is about 0.098°,[179] which is shown in red in Figure 7.8a. The Yoneda peak of P3HT is hardly visible, due to the high signal arising from the vertical scattering of the substrate.

Along the Yoneda peak position of the P3HT, horizontal line cuts are performed for the four hybrid films with different weight ratios of the diblock copolymer. A dominant shoulder at high q_y value is observed in Figure 7.8b, which indicates the presence of small P3HT domain sizes in the hybrid films. In addition, the peak position shifts to larger q_y value with increasing the diblock copolymer ratio, which implies the P3HT domain sizes become smaller.

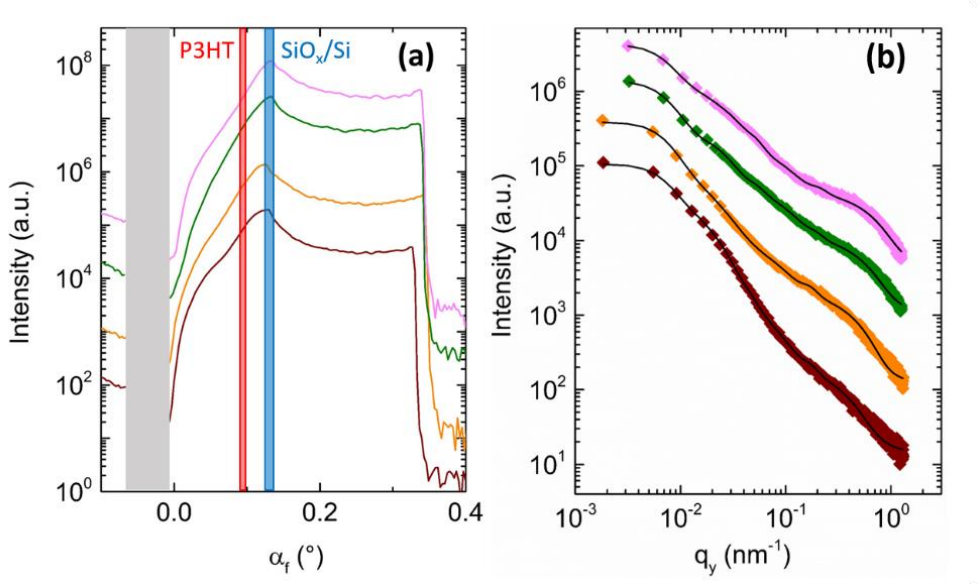

Figure 7.8 (a) Vertical line cuts at q_y = 0 nm^{-1} and (b) horizontal line cuts of the 2D GISAXS data (symbols) along with the fits (black curves) for the ZnO/P3HT/P3HT-b-PEO hybrid films deposited by spray coating and annealing at 80 °C with w_{ZnO}: w_{P3HT}: $w_{P3HT\text{-}b\text{-}PEO}$ = 2:1:0, 2:1:0.2, 2:1:0.5 and 2:1:1 from bottom to top. In (a) the grey shaded region is the detector gap and the red and blue shaded regions are the critical angle regions of P3HT and SiO_x/Si, respectively. The intensity decrease at about 0.4° in (a) is due to the shielding of the specular beamstop. Reprinted with permission from Ref.[150] Copyright (2018) American Chemical Society.

To get the length scale quantitatively, the horizontal line cuts are fitted with the same model as described in the last two sections. Namely, a one-dimensional paracrystal model is assumed and three types of cylindrically shaped objects in the framework of the distorted wave Born approximation (DWBA) and local monodisperse approximation (LMA) is used to fit the curves.[73] P3HT domains are represented by the cylindrical objects and therefore two kinds of characteristic length scales can be extracted from the fits. The diameter of the cylinders represents the P3HT domain size, which can be calculated from two times of the obtained form factor. The length scale of ZnO/PEO domain sizes can be attained from the difference between the structure factor and two times of the radius of the cylinders. The obtained P3HT domain sizes and the ZnO/PEO domain sizes are plotted as a function of the ratio of the diblock copolymer P3HT-*b*-PEO in Figure 7.9a and b, respectively. With the introduction of the diblock copolymer, both, the P3HT and the ZnO/PEO domains become smaller for large-, middle- and small-sized structures. This is due to the interface compatibilizer effect and the self-assembly process of the diblock copolymer. When increasing the ratio of the diblock

copolymer, all the three structures for P3HT show a decreased P3HT domain sizes. While the ZnO/PEO domains show a non-monotonous change for the three structures. When increasing the ratio of the diblock copolymer, the middle- and large-sized domains show slightly increased sizes in spite of the almost constant small-sized domains. This might result from the increased amount of PEO block in the hybrid films. While the P3HT domains show decreasing sizes along with increasing the ratio of the diblock copolymer. The P3HT domains in the film with a weight ratio of w_{ZnO}: w_{P3HT}: $w_{P3HT\text{-}b\text{-}PEO}$ = 2:1:1 exhibit the smallest sizes (large domain size: 82 nm, middle domain size: 24 nm, small domain size: 4 nm). As the exciton diffusion length for P3HT is about 10 nm,[180, 181] the sample with the diblock copolymer ratio of 1 is expected to improve the exciton separation performance due to the smaller P3HT domain sizes as compared with those in other hybrid films.

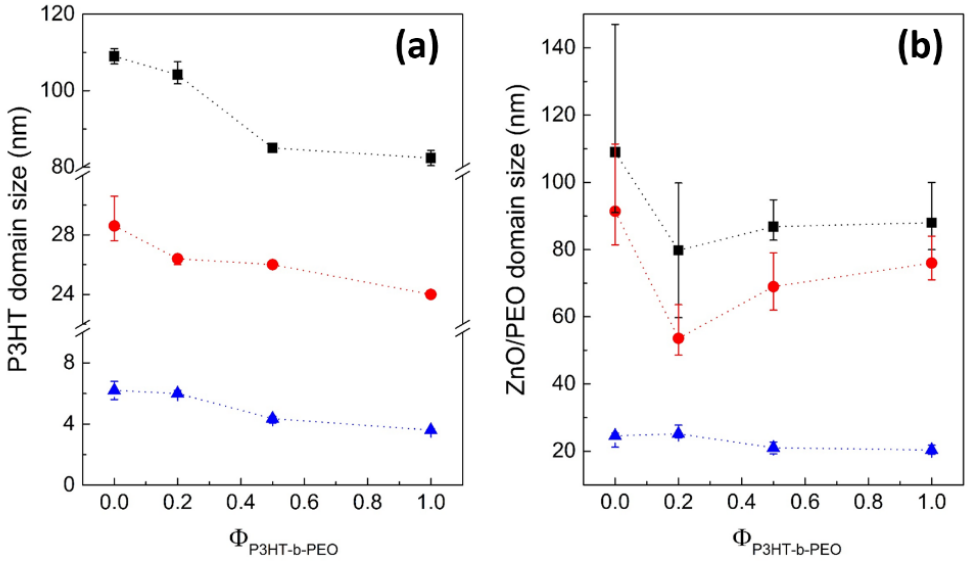

Figure 7.9 (a) P3HT domain size and (b) ZnO/PEO domain size in the ZnO/P3HT/P3HT-b-PEO hybrid films as a function of P3HT-b-PEO weight ratio. Triangles (blue) indicate small-sized structures, circles (red) middle-sized structures and squares (black) large-sized structures. Reprinted with permission from Ref.[150] Copyright (2018) American Chemical Society.

7.3 Film morphology influenced by annealing temperature

Apart from the ratio of the diblock copolymer, the annealing temperature is also important for the morphology of the hybrid films due to the self-assembly process during annealing. In this section, both, the surface and inner morphologies influenced by the annealing temperature are discussed.

7.3.1 Surface morphology

The surface morphology of the hybrid films with the ratio of w_{ZnO}: w_{P3HT}: $w_{P3HT\text{-}b\text{-}PEO}$ = 2:1:1 annealed at different temperatures of 80 °C, 120 °C and 160 °C are shown in Figure 7.10 and 7.11. Coffee rings are observed in the OM images (Figure 7.10), which are resulted from the spray process as discussed above. To investigate the morphology on the nanometer length scale, SEM images are shown in Figure 7.11. With increasing the annealing temperature, the interconnected network structure is preserved. However, the ZnO domain sizes become much larger. Part of the ZnO particles tend to aggregate with each other to form large particles. This is due to a kinetic process which drives the system towards an equilibrium structure via thermal annealing. Different states are achieved after fixed time of annealing in the underlying kinetics.

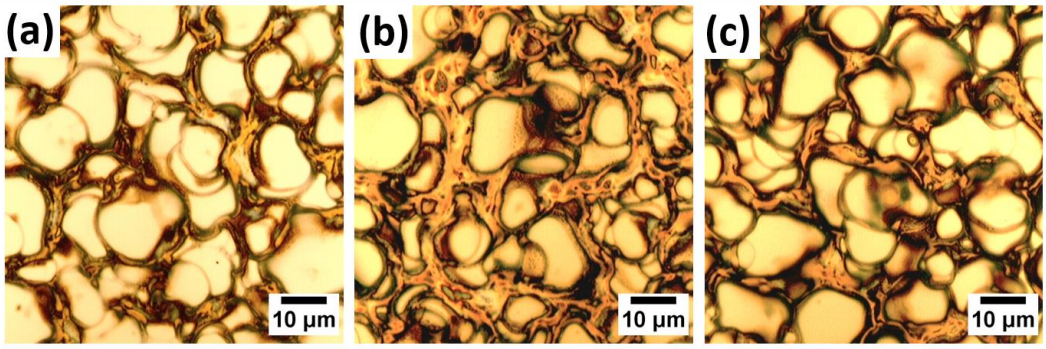

Figure 7.10 OM images of ZnO/P3HT/P3HT-b-PEO hybrid films with w_{ZnO}: w_{P3HT}: $w_{P3HT\text{-}b\text{-}PEO}$= 2:1:1 annealed at (a) 80 °C, (b) 120 °C, and (c) 160 °C for 0.5 hours.

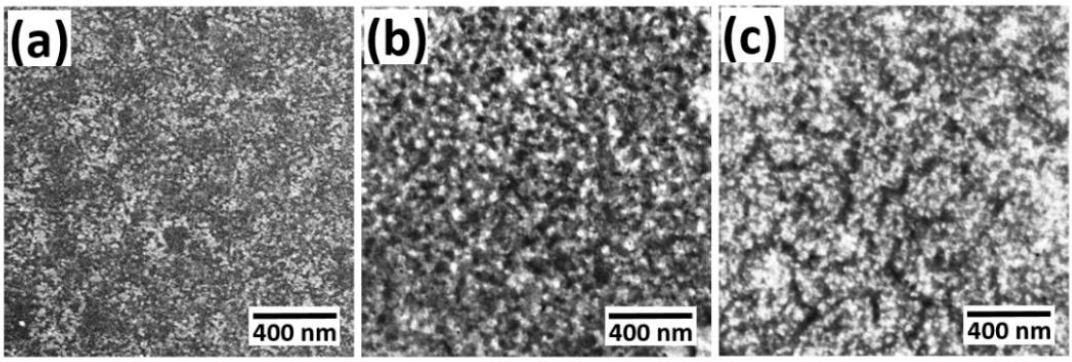

Figure 7.11 SEM images of ZnO/P3HT/P3HT-b-PEO hybrid films with w_{ZnO}: w_{P3HT}: $w_{P3HT\text{-}b\text{-}PEO}$= 2:1:1 annealed at (a) 80 °C, (b) 120 °C, and (c) 160 °C for 0.5 hours. Reprinted with permission from Ref.[150] Copyright (2018) American Chemical Society.

7.3.2 Inner morphology

The inner morphologies for the hybrid films with the ratio of w_{ZnO}: w_{P3HT}: $w_{P3HT\text{-}b\text{-}PEO}$ = 2:1:1 annealed at different temperatures are investigated by GISAXS measurements, with the 2D GISAXS data shown in Figure 7.12. Horizontal line cuts are performed along the Yoneda peak region and are plotted for the hybrid films with different annealing temperatures (Figure 7.13). An intensive shoulder at a high q_y value about 0.6 nm^{-1} is observed for all three cuts. With increasing the annealing temperature, this peak position keeps constant, which indicates a constant domain size of the small-structured P3HT domains. However, another shoulder at smaller q_y (about 0.03 nm^{-1}) shifts to smaller q_y values, implying an increase of the large-sized P3HT domains with the annealing temperature increasing from 80 °C to 160 °C. The same model as described in section 7.2.2 is used to fit the cuts. The fits (black) are shown together with the cuts in Figure 7.13a. Figure 7.13b and c show the plots of the P3HT domain sizes and ZnO/PEO domain sizes as a function of the annealing temperatures, respectively. For the P3HT domain sizes, despite that the small-sized structure keeps constant, both the middle- and large-sized domains show increasing sizes when the annealing temperature goes from 80 °C to 160 °C. Therefore, the hybrid films annealed at 80 °C is expected to possess the best exciton separation as compared with the samples annealed at higher temperatures due to the small exciton diffusion length of P3HT. For the ZnO/PEO domains, all of the three kinds of structures show an increase in size when increasing the annealing temperature. All of these results agrees with the SEM results, indicating that the structures inside the hybrid films follow similar kinetics as the surface structures.

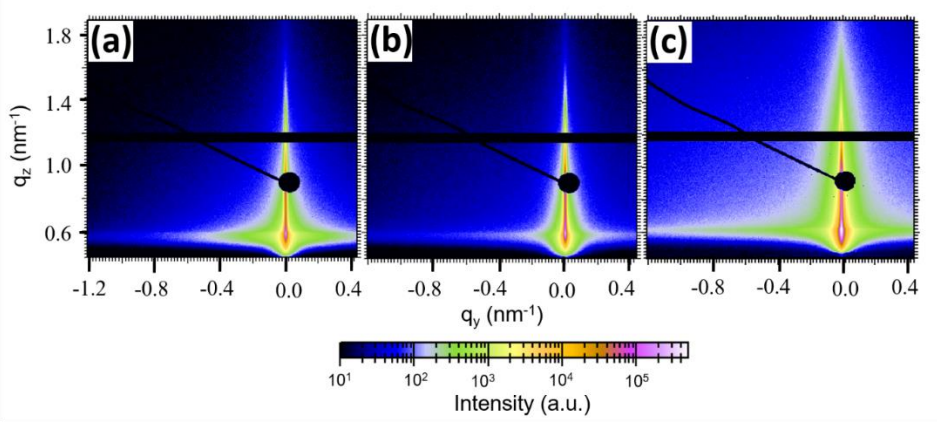

Figure 7.12 2D GISAXS data of sprayed ZnO/P3HT/P3HT-b-PEO hybrid films with a ratio of w_{ZnO}: w_{P3HT}: $w_{P3HT\text{-}b\text{-}PEO}$ = 2:1:1 processed at different annealing temperatures: (a) 80 °C, (b) 120 °C, and (c) 160 °C. Reprinted with permission from Ref.[150] Copyright (2018) American Chemical Society.

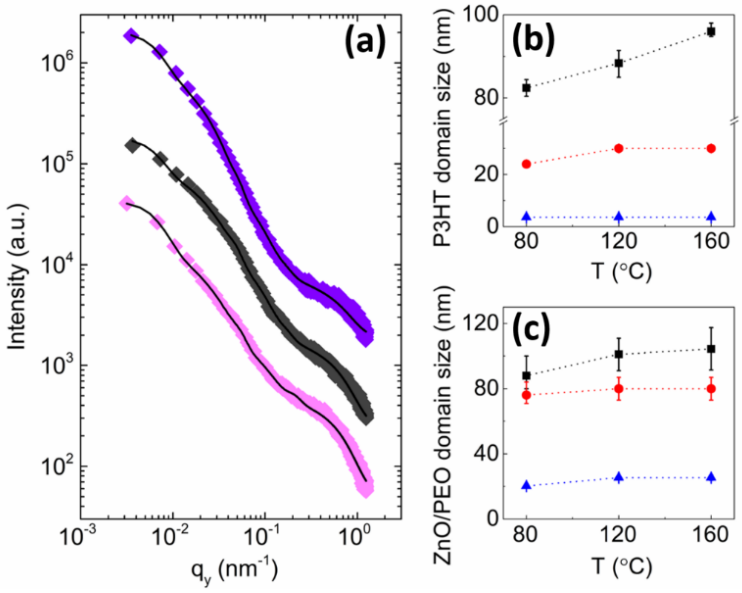

Figure 7.13 (a) Horizontal line cuts of the 2D GISAXS data (symbols) shown with their corresponding fits (black curves) for the ZnO/P3HT/P3HT-b-PEO hybrid films deposited by spray coating with w_{ZnO}: w_{P3HT}: $w_{P3HT\text{-}b\text{-}PEO}$ = 2:1:1 after annealing at different temperatures: 80 °C, 120 °C, and 160 °C from bottom to top. (b) P3HT domain size and (c) ZnO/PEO domain size in the ZnO/P3HT/P3HT-b-PEO hybrid films as a function of increasing annealing temperature. Triangles (blue) indicate small-sized structures, circles (red) middle-sized structures and squares (black) large-sized structures. Reprinted with permission from Ref.[150] *Copyright (2018) American Chemical Society.*

7.4 Optoelectronic properties

In this section, UV-Vis absorption and photoluminescence (PL) measurements are performed, which is helpful to investigate the aggregation of P3HT in the hybrid films, exciton separation and the charge transfer along the p-type and n-type semiconductors.

UV-Vis spectra for the samples with different weight ratios at 80 °C and for the films with the ratio of w_{ZnO}: w_{P3HT}: $w_{P3HT\text{-}b\text{-}PEO}$ = 2:1:1 at different annealing temperatures are shown in Figure 7.14a and b, respectively. An absorption at about 330 nm is observed for all curves, which originates from the exciton absorption. This is consistent with the reported value, which indicates the successful synthesis of ZnO nanoparticles.[166, 182, 183] The absorption shoulders at 518, 550 and 600 nm are assigned to 0-2, 0-1 and 0-0 transitions in P3HT.[184, 185] The shoulder at 600 nm originates from the intermolecular π-π stacking of P3HT and the peak position is not shifted when changing the weight ratio or increasing the annealing temperature. This indicates a similar P3HT crystallization for all of the hybrid films. Moreover, the ZnO particles mainly

absorb the light in the UV region and therefore do not hinder the absorption of P3HT (used as light absorber for application in solar cells). Meanwhile, the ZnO nanoparticles act as an additional UV filter to prevent the degradation of the P3HT caused by the high-energy photons.

The PL measurements are excited at 460 nm with the emission recorded in the range of 550-850 nm. Figure 7.14c shows that with the introduction of the diblock copolymer P3HT-*b*-PEO, the hybrid films exhibit a better fluorescence quenching as compared to the ZnO/P3HT films. This enhanced quenching is mainly attributed to the smaller P3HT domain sizes and the more efficient charge transfer at the interfaces between ZnO and P3HT due to the interfacial compatibilizer of the diblock copolymer. Therefore, the exciton separation at the interfaces is improved. Increasing the ratio of the diblock copolymer enhances the quenching, indicating a higher exciton separation yield and a more efficient charge transfer process. For the hybrid films with the ratio of the diblock copolymer being 1, it shows best exciton separation at the interfaces. Figure 7.14d shows the PL quenching of the hybrid films with different annealing temperatures. When increasing the annealing temperature, the PL intensity increases, indicating the films annealed at 80 °C exhibit a better heterojunction than the films annealed at higher temperatures.

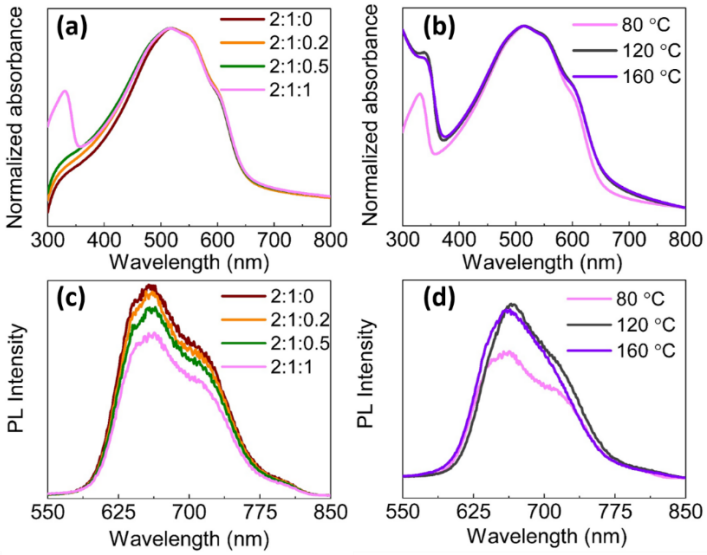

Figure 7.14 (a, b) UV-Vis and (c, d) PL spectra of ZnO/P3HT/P3HT-b-PEO hybrid films (a,c) annealed at 80 °C with different compositions w_{ZnO}*:* w_{P3HT}*:* $w_{P3HT\text{-}b\text{-}PEO}$ *= 2:1:0, 2:1:0.2, 2:1:0.5, and 2:1:1 and (b, d) for fixed composition* w_{ZnO}*:* w_{P3HT}*:* $w_{P3HT\text{-}b\text{-}PEO}$ *= 2:1:1 under different annealing temperatures: 80 °C, 120 °C, and 160 °C. Reprinted with permission from Ref.*[150] *Copyright (2018) American Chemical Society.*

In addition, the PL spectra excited by the wavelength of 325 nm is obtained for the films with the ratio of w_{ZnO}: w_{P3HT}: $w_{P3HT\text{-}b\text{-}PEO}$ = 2:1:1 annealed at 80 °C (Figure 7.15). An intensive peak at about 386 nm is observed, which is caused by the radiative recombination. The electrons excited into the conduction band will recombine with the holes left in the valence band and therefore light is emitted. In the region with relatively higher wavelength, no clear peak is observed, which implies that the defects in the hybrid films are very low.[166, 186, 187]

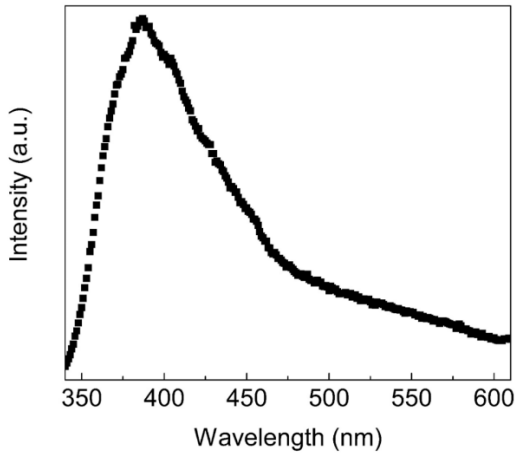

Figure 7.15 PL spectrum of ZnO/P3HT/P3HT-b-PEO hybrid films annealed at 80 °C having a ratio of w_{ZnO}: w_{P3HT}: $w_{P3HT\text{-}b\text{-}PEO}$ = 2:1:1. (λ_{Ex} = 325 nm). Reprinted with permission from Ref.[150] Copyright (2018) American Chemical Society.

7.5 Solar cell performance

HBSCs are fabricated based on the 80 °C annealed ZnO/P3HT/P3HT-*b*-PEO hybrid films and the layout is glass//FTO//compact ZnO//ZnO/P3HT/P3HT-*b*-PEO//P3HT//Au (Figure 7.16a). To avoid the recombination at both, transparent and Au electrode, a compact ZnO layer on top of FTO and a P3HT layer above the active layer are spin coated, respectively. The measured I-V curves are shown in Figure 7.16b. The photovoltaic performance of ZnO/P3HT/P3HT-*b*-PEO based solar cell device is better than that of the one fabricated from ZnO/P3HT, which indicates the importance of the addition of P3HT-*b*-PEO in the active layer. Compared with the devices without P3HT-*b*-PEO, the HBSCs based on the active layer with P3HT-*b*-PEO shows much higher J_{sc} as shown in Table 7.1, which is resulted from the modified interfaces of ZnO and P3HT. The decreased P3HT domain sizes lead to increased probability for exciton separation, contributing to larger charge carrier density. Moreover, the V_{oc} and FF are also improved with the introduction of the diblock copolymer in the active layer. From the measured I-V curves, a PCE of the ZnO/P3HT/P3HT-*b*-PEO based solar cells (0.07± 0.01%) is calculated,

which is higher than those from ZnO/P3HT (0.02±0.01%). The increased photovoltaic performance for application in HBSCs indicates that the improved morphology of the active layer modified by the diblock copolymer P3HT-*b*-PEO plays a significant role in increasing the photovoltaic performance.

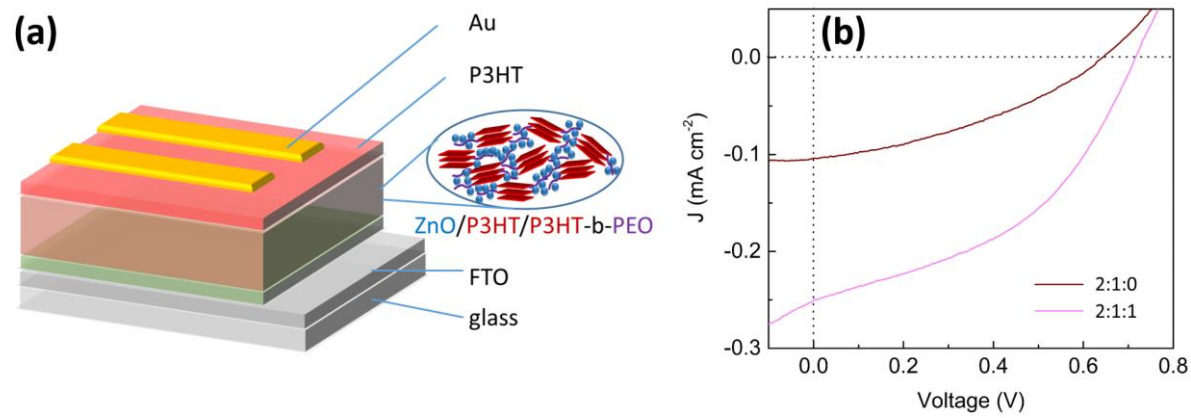

Figure 7.16 (a) Schematic representation of a HBSC setup. (b) Current density–voltage characteristics of HBSCs based on 80 °C annealed ZnO/P3HT/P3HT-b-PEO hybrid films with different ratios.

Table 7.1 Device parameters extracted from I-V curves of HBSCs based on 80 °C annealed ZnO/P3HT/P3HT-b-PEO hybrid films with different ratios.

devices	J_{sc} (mA cm^{-2})	V_{oc} (V)	FF (%)	PCE (%)
2:1:0	0.1 ± 0.01	0.6 ± 0.13	35.0 ± 5.0	0.02 ± 0.01
2:1:1	0.2 ± 0.05	0.7 ± 0.02	42.0 ± 3.0	0.07 ± 0.01

7.6 Summary

In this chapter, ZnO/P3HT hybrid films are modified with the introduction of the diblock copolymer P3HT-*b*-PEO, which serves as a compatibilizer to improve the morphology of the hybrid films as well as the interfaces of the bulk heterojunction. The hybrid films of ZnO/P3HT/P3HT-*b*-PEO are successfully fabricated through a sol-gel synthesis, in which the zinc precursor is directly grown onto the PEO block, which acts as a template to control the morphology of ZnO nanoparticles. In addition, P3HT can be used as a light absorber and a charge carrier transport material. Spray deposition is employed to fabricate the thin films from the sol-gel, which is promising for preparing active layers on a large scale. The surface and the

inner morphologies of the hybrid films are investigated by SEM and GISAXS, respectively. With the addition of the diblock copolymer, the interconnected network structure is sustained, which is beneficial for charge carriers to be extracted along the ZnO and P3HT to their corresponding electrode. Both, the P3HT and ZnO domains become smaller because of the self-assembly of the diblock copolymer which hinders the chemically incompatible two components from forming large integrated domains. Moreover, when increasing the ratio of the diblock copolymer, the P3HT domains show a decreasing sizes whereas the ZnO/PEO domains show an increase for the average structures. Therefore, the samples with the ratio of w_{ZnO}: w_{P3HT}: $w_{P3HT\text{-}b\text{-}PEO}$ = 2:1:1 show improved exciton separation and charge carrier transport, which is supported by the PL results. However, when increasing the annealing temperature of the hybrid films, both, P3HT and ZnO particles tend to aggregate with each other because of the underlying kinetics of the films. The aggregated domains hinder the improvement of the exciton separation when aiming at an application in solar cells, which is revealed by the reduced PL quenching as well. To conclude, the morphology of the hybrid films is improved by the introduction of the diblock copolymer P3HT-*b*-PEO and by controlling the annealing temperature. The samples with the ratio of w_{ZnO}: w_{P3HT}: $w_{P3HT\text{-}b\text{-}PEO}$ = 2:1:1 annealed at 80 °C reveal the optimal exciton separation due to the best PL quenching.

Applying the sol-gel synthesis combined with the diblock copolymer P3HT-*b*-PEO, active layers of ZnO/P3HT on nanometer length scale are fabricated for application in bulk heterojunction solar cells. Based on this simple route, bulk heterojunction solar cells are successfully fabricated. Since the fabrication in this work is performed using low temperatures (well below 160 °C), it provides a promising route for a potential large scale preparation of hybrid solar cells on flexible substrates.

8. Morphology tuning of ZnO/P3HT/P3HT-*b*-PEO hybrid films via spray and spin coating

Parts of this chapter have been prepared as a manuscript: Morphology Tuning of ZnO/P3HT/P3HT-*b*-PEO Hybrid Films via Spray and Spin Coating, which is presently to be submitted.

Hybrid materials have attracted great attention in several fields, such as optoelectronics, photocatalysis, biomedical sensors, energy storage and conversion in recent years.[188-194] The multiple kinds of functional nanoparticles doped in the polymer matrixes provide various improved properties including promising thermal, mechanical, electric, optical and magnetic properties.[195-198] Based on the optoelectronic properties, one of the most important applications are the hybrid bulk junction solar cells (HBSCs), which show many advantages due to the direct combination of inorganic and organic materials. Compared with the conventional inorganic solar cells, HBSCs are light-weight, flexible and low-cost.[199, 200] Moreover, HBSCs show higher stability compared to organic solar cells due to the introduction of the inorganic materials, which acts as a framework and avoids the morphological aging which usually occurs in organic solar cells.[200-202]

Generally, HBSCs are composed of a blend of conjugated polymers and inorganic semiconducting materials. The large interface area between these two network components provides an increased probability for the excitons to be separated into the charge carriers within the lifetime as compared with the conventional bilayer heterojunction layout. The generated excitons can only be split at the interfaces of donor and acceptor within their lifetime and the exciton diffusion length in donor materials is limited within tens of nanometers.[180, 181] Thus, tuning the morphologies of the donor and acceptor plays an important role in improving the performance of HBSCs. Based on extensive studies, the morphology can be tailored by the material synthesis and the deposition method.

In a blend of inorganic and organic components, these two components tend to form large domains due to an energetically unfavorable interaction of the polymer with the inorganic semiconducting nanoparticles, which reduces the opportunity for exciton separation in HBSCs. Interface modifications can be a good way to solve this problem. With the introduction of a diblock copolymer, instead of an uncontrolled macrophase separation in a blend, microphase separation will occur due to the covalently bound two blocks of the block copolymer. Therefore,

due to the self-assembly process, diblock copolymers are deemed to be a promising addition to modify the morphology of the films by modifying the interfaces of the organic and inorganic materials.[165, 166, 203, 204] For example, ZnO/P3HT interfaces can be modified with the diblock copolymer P3HT-*b*-PEO. Li *et al.* and Shi *et al.* first dispersed ZnO (prepared beforehand via a sol-gel method) in chlorobenzene and then mixed ZnO, P3HT and P3HT-*b*-PEO as a blend.[165, 166] In this case, two steps are required as it is quite challenging to dissolve ZnO in the same solvent as the polymers. The solvents for dissolving functional inorganic materials and polymers are typically different due to the different polarities of the two components. Normally, p-type semiconducting polymers are dissolved in unipolar solvents, such as chlorobenzene, dichlorobenzene, folurene *etc*. whereas n-type semiconducting inorganic materials are dissolvable in polar solvents, such as DMF and DMSO. Therefore, in the present work, a solvent mixture of dichlorobenzene (DCB) and dimethyl sulfoxide (DMSO) is used to dissolve all the materials. With this mixed solvent, the sol-gel solution containing ZnO, P3HT and P3HT-*b*-PEO can be obtained with the zinc precursor directly growing in the PEO blocks (acting as a template). Thus, the hybrid active layer is fabricated in a much simpler route, namely a one pot synthesis, as compared to approaches from the literature. Meanwhile, the self-assembly of the diblock copolymer helps to control the morphology of the inorganic semiconductors and the semiconducting polymers on a nanometer length scale, which is beneficial to increase the interface area, thereby improving the exciton separation.

Deposition methods, such as the commonly used blade-coating, printing, spray deposition, and spin coating to fabricate sol-gel thin films, also play a crucial role in the morphology tuning. Spin-coating is easy to operate and also shows high deposition uniformity and fast processing times whereas spray coating is also a widely used technique due to the possibility for large scale production and a reduced material consumption as compared to the spin coating.[91, 205] Moreover, spray coating can be used to deposit films on non-flat surface. Continuous films with a homogeneous morphology can be realized via each of these methods. However, the obtained morphology via the different deposition methods may vary, as the morphology is influenced by the interactions of the liquid flow with the substrate and the air, the evaporation rate, and the nature of the blend system. Extensive work has been done on the morphological tuning of the active layers via these deposition methods. However, few studies make a direct comparison of the morphologies obtained by varying the deposition method.

In chapter 7, spray coating is used to deposit the ZnO/P3HT/P3HT-*b*-PEO solution as an active layer and it is demonstrated that the introduction of the diblock copolymer P3HT-*b*-PEO improves the interfaces of ZnO and P3HT greatly due to the compatibility effect and the self-assembly of the diblock copolymer. In this chapter, different deposition methods, namely spray

and spin coating, are used to compare the effect on the obtained film morphology of the active layer. Moreover, spray coated films prepared from sol-gel with different ZnO ratios are investigated, which influences the morphology significantly.

8.1 Fabrication route

The schematic representation for fabricating the ZnO/P3HT/P3HT-*b*-PEO hybrid films is shown in Figure 8.1. Sol-gel synthesis is used to prepare the ZnO/P3HT/P3HT-*b*-PEO solutions with the procedure being similar to that in section 7.1. Two different deposition methods, spray and spin coating, are used separately to compare the resulting film morphology. A more detailed description about spin-coating and the used spray parameters are given in chapter 4. Finally, annealing is performed at 80 °C to improve equilibrium during the self-assembly process. The weight ratio between P3HT and the diblock copolymer is constant while the amount of the zinc precursor changes to investigate the influence of the amount of ZnO on the hybrid films.

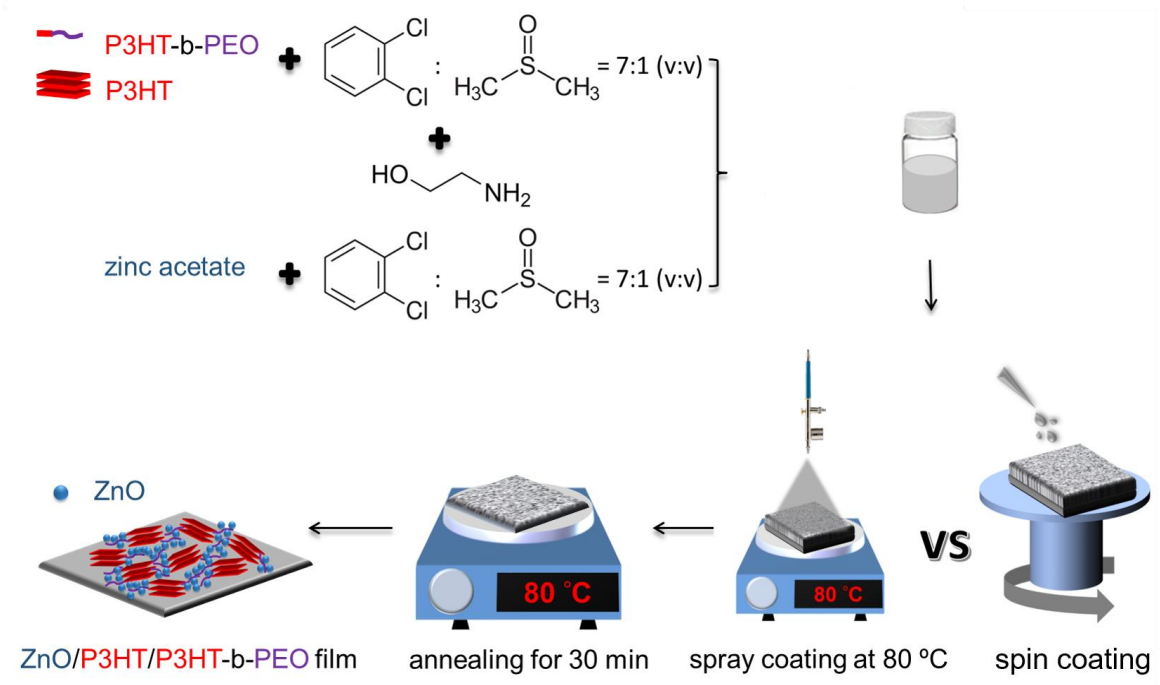

Figure 8.1 Schematic representation of the steps involved in the fabrication of the ZnO/P3HT/P3HT-b-PEO hybrid films via spray and spin coating and subsequent thermal annealing at 80 °C. Reprinted from Ref.[206]

8.2 Morphology tuning by deposition method

In order to investigate the morphology of the hybrid films coated via different deposition methods, both surface and inner structures are probed with OM, SEM and TOF-GISANS, respectively. In section 8.2.1, the surface morphology of the spray and spin coated films is discussed in detail. TOF-GISANS is a powerful tool to investigate the inner structure statistically, which is described in section 8.2.2.

8.2.1 Surface morphology

OM images of ZnO/P3HT/P3HT-*b*-PEO hybrid films with the ratio of w_{ZnO}: w_{P3HT}: $w_{P3HT\text{-}b\text{-}PEO}$ = 4:5:1 deposited by spray and spin coating are shown in Figure 8.2a-b. It is observed that the surface morphologies for the spray and spin coated films on a micrometer length scale are quite different in spite of the same ratio of the three components. For the spray coated samples, many coffee rings appear at the surface. Actually, these coffee rings are commonly observed for spray coated films as reported in the literature because of the complicated flow behavior in the liquid layer.[171-173, 207, 208] In the present thesis, the situation is complicated due to the multicomponent solution used for spray deposition. Having the substrate at elevated temperature causes fast evaporation of residual solvent during spray deposition and thereby limits the probability of equilibrating height difference via vertical flow. Therefore, spray coating creates less homogeneous films on a micrometer length scale as compared with spin coating. No coffee rings are observed for the hybrid films via spin coating. Instead, some black spots are randomly distributed at the surface which might be attributed to the aggregations of ZnO nanoparticles.

To investigate the surface morphology on a nanometer length scale, SEM images of the spray and spin coated hybrid films with the ratio of w_{ZnO}: w_{P3HT}: $w_{P3HT\text{-}b\text{-}PEO}$ = 4:5:1 are shown in Figure 8.2c-d. Due to the different electron densities of ZnO and the polymers, they show different contrasts, with ZnO appearing bright and polymers dark. For both, the spray and spin coated samples, they show a well-mixed structure on a nanometer length scale. This is expected to increase the interface area between the ZnO nanoparticles and P3HT, therefore leading to the modification of the exciton separation. Both, the ZnO and the P3HT phase tend to interconnect in each phase, favoring the extraction of the charge carriers to the corresponding electrode. Moreover, the spin coated samples show much smaller ZnO domain sizes than the counterpart produced via spray coating, which is expected to increase the interface area further, and therefore, is supposed to improve the exciton separation when application in HBSCs.

The surface on both, micrometer and nanometer length scale, is more homogeneous and has smaller domain sizes in case of the spin coated films. Although spray coating leads to a rougher

surface, it is promising for application on a large scale for industrial production. Therefore, the morphology of the spray coated films is optimized further.

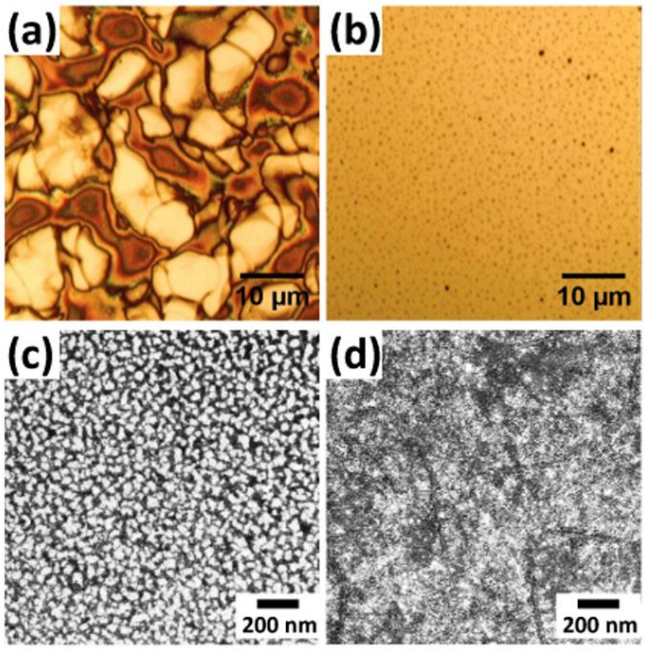

Figure 8.2 OM (a, b) and SEM (c, d) images of the ZnO/P3HT/P3HT-b-PEO hybrid films deposited by (a, c) spray coating and (b, d) spin coating. Reprinted from Ref.[206]

8.2.2 Inner morphology

TOF-GISANS is performed to investigate the inner morphology of the hybrid films deposited via both coating methods. With the TOF mode, a broad spectrum of neutron wavelengths is used instead of a monochromatic neutron beam. Therefore, a whole set of scattering patterns can be achieved via subsequent slicing the scattering data in wavelength channels. In this case, each pattern covers a different range of scattering vectors, which makes it possible to detect multiple structures with a wide length scale in one TOF-GISANS measurement. Moreover, due to the variable wavelengths, the critical angle changes, and we can detect both the surface and inner morphology even at a constant incident angle.[209] Figure 8.3 shows selected 2D TOF-GISANS data of the spray and spin coated hybrid films with the ratio of w_{ZnO}: w_{P3HT}: $w_{P3HT\text{-}b\text{-}PEO}$ = 4:5:1 at different wavelengths. The sample horizon exhibits the minimum intensity, which is marked by a black dashed line. Below the sample horizon, the scattering pattern is given by the transmitted intensity, with the direct beam shielded by a beamstop to avoid oversaturation of the detector. Above the sample horizon, it is due to the reflected intensity. An intense peak is found at the position of the exit angle (α_f) equal to the incident angle (α_i). It is observed that the specular beam slightly shifts to smaller scattering angles with increasing the neutron

wavelength. This is mainly due to the effect of gravity on the neutron beam, which is corrected in the analysis. At low neutron wavelengths, the Yoneda peak is observed between the sample horizon and the specular peak. It is located at the position of the critical angle α_c, and it moves to higher scattering angles with increasing neutron wavelength due to the increasing value of α_c. For neutrons with long wavelength, as the position of the Yoneda peak gradually overlaps with the specular beam, it cannot be observed clearly. In this case, only the surface morphology can be detected.

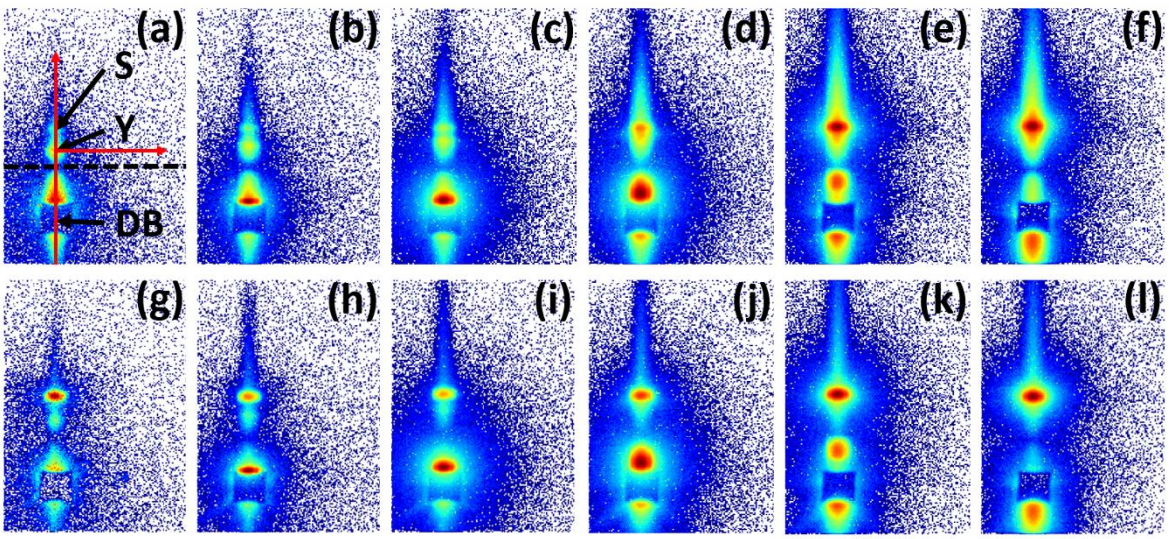

Figure 8.3 Selected 2D GISANS data of the ZnO/P3HT/P3HT-b-PEO hybrid films deposited by (a-f) spray coating and (g-l) spin coating obtained from the TOF-GISANS measurements. The average neutron wavelength from left to right is (a, g) 0.38 nm, (b, h) 0.46 nm, (c, i) 0.57 nm, (d, j) 0.69 nm, (e, k) 0.85 nm, and (f, l) 1.03 nm, respectively. The direct beam is blocked by a beamstop. The dashed black line in (a) indicates the sample horizon. S, Y and DB in (a) represent specular peak, Yoneda peak and direct beam, respectively. The red arrows along the vertical and horizontal directions indicate the places where the vertical and horizontal cuts are performed. Reprinted from Ref.[206]

To get the information of the film structure perpendicular to the substrate, vertical line cuts are performed along q_y=0, which is marked by a red vertical arrow in Figure 8.3a. Figure 8.4 shows the obtained vertical cuts for the spray and spin coated films with the ratio of w_{ZnO}: w_{P3HT}: $w_{P3HT\text{-}b\text{-}PEO}$ = 4:5:1. The neutron wavelength increases from bottom to top. A drop in intensity at $\alpha_i + \alpha_f = 0.38°$ is found for all curves, which is marked by a black dashed line. This indicates the sample horizon. On the left of the sample horizon ($\alpha_i + \alpha_f < 0.38°$), transmitted intensity can be observed, with the direct beam covered by a beamstop, indicated by a gray box. On the

right of the sample horizon ($\alpha_i + \alpha_f > 0.38°$), the reflected signal is detected. An intensive peak at $\alpha_i + \alpha_f = 0.76°$, twice the value of the incident angle, is observed for all curves. This is the specular peak (marked by a green line), with the exit angle equal to the incident angle. Compared with the spray coated samples, the spin coated films show a more intense specular beam, especially at small neutron wavelengths. This increased specular reflection is caused by the increased homogeneity of the hybrid films via spin coating as compared with those via spray as observed in the OM and SEM images. Between the sample horizon and the specular peak, another peak (marked by a red dashed line) is found. This is the Yoneda peak. By increasing the wavelength of the neutrons, the Yoneda peak become ambiguous as it becomes gradually larger and finally overlaps with the specular peak at high wavelength.

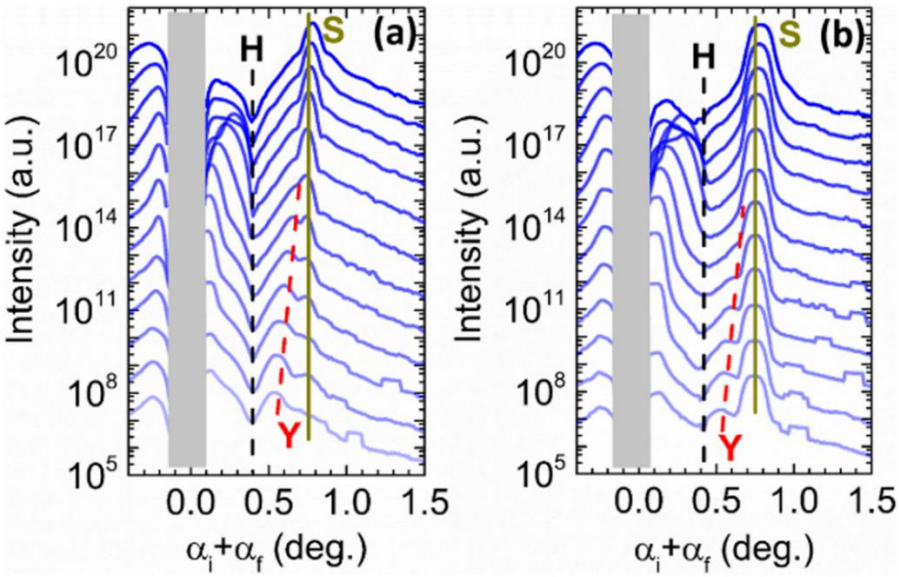

Figure 8.4 Vertical line cuts of the 2D GISANS data for the ZnO/P3HT/P3HT-b-PEO hybrid films deposited by (a) spray coating and (b) spin coating obtained from the 2D GISANS scattering pattern. From bottom to top, the average neutron wavelength increases from 0.38 to 1.14 nm. All cuts are shifted along the y axis for clarity. The region shielded by a beamstop is illustrated in gray. The dashed black line, the dashed red line, and the solid dark yellow line indicate the sample horizon, the shifting of the Yoneda peak for the hybrid film, and the specular peak, respectively. Reprinted from Ref.[206]

The Yoneda peak positions are extracted from the vertical line cuts of the 2D GISANS data of the spray and spin coated samples and are plotted as a function of the neutron wavelength (Figure 8.5). For the spray and spin coated hybrid films, the data are fitted with a line according to

$$\alpha_c = \lambda\sqrt{\frac{\rho}{\pi}}, \tag{8.1}$$

where ρ is the neutron scattering length density (SLD) of the material.[210] The detected angles can only be obtained from the vertical line cuts at low neutron wavelength and not high neutron wavelength since the Yoneda peak overlaps with the specular peak at high wavelength. According to Equation 8.1, the critical angle increases linearly with increasing the neutron wavelength. Under a constant wavelength, a higher critical angle can be obtained for the materials with higher SLD. From the fits, it is observed that the Yoneda peak positions of the spray and spin coated films are larger than the counterpart of the bulk P3HT, PEO and smaller than that from bulk ZnO. This implies that ZnO and P3HT are successfully mixed in the hybrid films. Moreover, the linear slope is slightly smaller for the spin coated films (~0.43 deg. nm^{-1}) as compared to the spray coated samples (~0.47 deg. nm^{-1}). According to Equation 8.1, a smaller SLD (~1.77×10^{-4} nm^{-2}) is obtained for the spin coated samples. The obtained smaller SLD for spin-coated films as compared to that of spray coated samples shows that with different deposition methods also different hybrid films are formed.

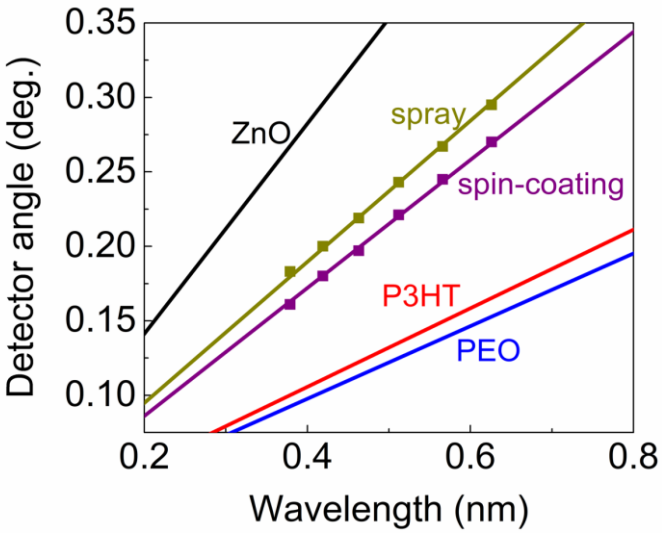

Figure 8.5 Experimental Yoneda peak positions (the solid squares) of the hybrid films deposited by spray and spin coating (dark yellow: spray coated samples, purple: spin coated samples) obtained from the vertical line cuts at the corresponding wavelengths and the linear fits to the data (the solid lines). Theoretical critical angles of bulk ZnO, P3HT and PEO as a function of wavelength are shown in black, red and blue lines, respectively. Reprinted from Ref.[206]

Horizontal line cuts are performed along the Yoneda region to investigate the inner structure parallel to the substrate.[121, 211] Figure 8.6 shows the horizontal line cuts for the spray and spin coated hybrid films with the ratio of w_{ZnO}: w_{P3HT}: $w_{P3HT\text{-}b\text{-}PEO}$ = 4:5:1. With increasing the neutron wavelength, the detected q_y range changes to smaller q_y, which makes it possible to probe a wide length scale of the structures with one TOF-GISANS measurement. To fit the data, the model of the distorted wave Born approximation (DWBA) is used. We assume cylindrical-shaped scattering objects, in the framework of the local monodisperse approximation (LMA) distributed on a one-dimensional paracrystal lattice to determine the most prominent length scales of the spatial distances and diameters of the detected domains.[73] Thus, the radius of the scattering objects and the corresponding center-to-center distances can be extracted from the form factor and the structure factor, respectively. For the spray coated hybrid films, three structures are used to fit all the curves measured at different neutron wavelengths. In contrast, only two structures are required to fit the horizontal line cuts of the spin coated samples. This indicates a more uniform size distribution of the domains in the spin coated films than those in the spray coated ones. Moreover, for the spray coated films, the sizes of the small- and middle-sized domains are 30±7 nm and 59±9 nm, respectively. These values are larger than the small-sized domains (27±3 nm) in the spin coated films. For the application in HBSCs, the smaller domain sizes help improving the probability for the generated excitons to reach an interface within their lifetime and therefore being separated into free charge carriers. Since the exciton diffusion length for P3HT is only about 10 nm,[180] the large-sized domains are not so significant. Therefore, the large structures obtained from the fits are not compared for the spray and spin coated samples. The different domain sizes in the spray and spin coated films illustrate that the deposition method has a great influence on the final morphology of the hybrid films. In case of short wavelength, the critical angle is far below the incident angle, and the inner morphology can be detected. At long wavelength, the critical angle is close to or even larger than the incident angle. In this case, the neutrons are surface sensitive and the surface morphology can be investigated. For both spray and spin coated films, the same fitting results are employed for the curves under different wavelengths, implying that the morphology buried in the films is consistent with the surface morphology independently of the deposition method.

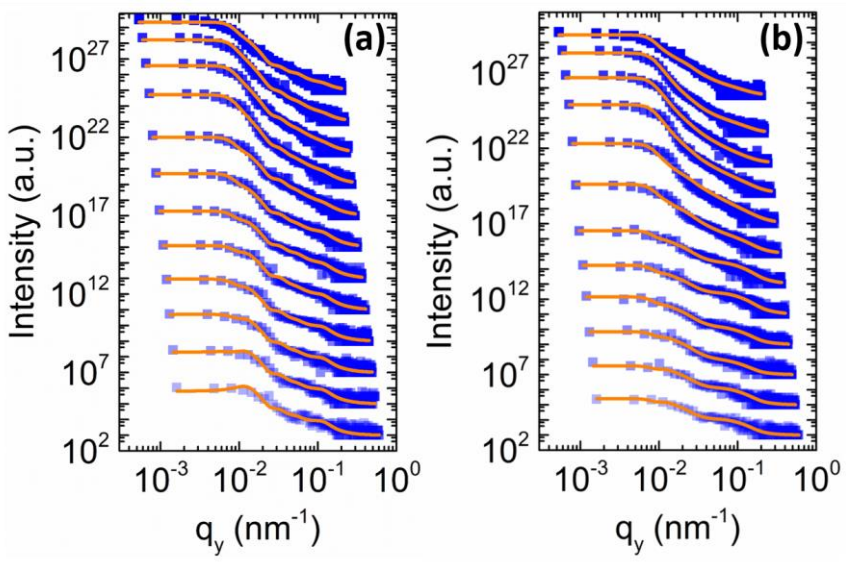

Figure 8.6 Horizontal line cuts of the 2D GISANS data for the ZnO/P3HT/P3HT-b-PEO hybrid films deposited by (a) spray coating and (b) spin coating obtained from the 2D GISANS scattering pattern. The solid curves are the fits using the geometry of cylindrical scattering objects on a 1D paracrystal lattice as described in the text. From bottom to top, the average neutron wavelength increases from 0.379 to 1.141 nm. The different q_y ranges result from the variable neutron wavelength. All cuts are shifted along the y axis for clarity. Reprinted from Ref.[206]

8.3 Morphology tuning by changing ratio

From the direct comparison, the spin coated ZnO/P3HT/P3HT-*b*-PEO hybrid films are supposed to be superior in the application as HBSCs due to the larger interface between the ZnO particles and P3HT and the smaller obtained domain sizes. However, spin coating is quite challenging when producing films on a large scale as even on curved interfaces. In contrast to that, spray coating seems more significant for an up-scalable production routine. Therefore, the film morphology via spray coating is investigated further by tuning the weight ratio of the zinc precursor during the sol-gel synthesis. Both, the surface and inner morphologies of the sprayed films with different ZnO ratios are discussed. Moreover, the film thickness is also described in section 8.3.3.

8.3.1 Surface morphology

SEM images of the spray coated films with different ZnO ratios are shown in Figure 8.7. It is observed that the ZnO particles tend to interconnect to form a network structure in the matrix

of the polymers in the hybrid films, which is expected to provide a good pathway for the charge carriers to be extracted through the ZnO and P3HT to their corresponding electrode. For the hybrid films with the ratio of 1:5:1 (Figure 8.7a), some small ZnO domains are observed. Apart from this, large domains are also present at the surface. In the spray coating process, aggregation of the ZnO particles occurs. Thus, even though the ZnO ratio is decreased, the hybrid films prepared via spray coating are still less homogeneous as compared with the spin coated films. Moreover, the aggregation becomes more severe when increasing the ratio of the ZnO. This behavior may be explained by a stronger interaction between ZnO nanoparticles and the PEO block with increasing the concentration of the reactant. When the ratio increases to 4:5:1 (Figure 8.7d), most of the PEO blocks are saturated with ZnO due to the high concentration of the zinc precursor in the sol-gel solution. It indicates that the morphology of the ZnO/P3HT/P3HT-*b*-PEO hybrid films can be easily tuned via the ratio of ZnO in the hybrid films with ZnO, P3HT, and P3HT-b-PEO components.

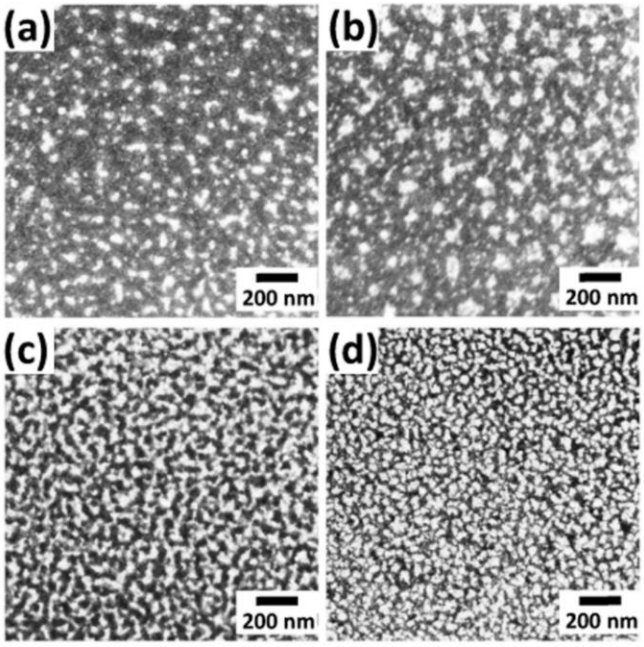

Figure 8.7 SEM images of spray coated ZnO/P3HT/P3HT-b-PEO hybrid films with different ratio of w_{ZnO}*:* w_{P3HT}*:* $w_{P3HT\text{-}b\text{-}PEO}$ *= (a) 1:5:1, (b) 2:5:1, (c) 3:5:1, (d) 4:5:1. Reprinted from Ref.*[206]

OM images for the spray coated films with different ZnO ratios are shown in Figure 8.8 to investigate the surface morphology on the micrometer length scale. It is observed that coffee rings are present at the surface for all the films prepared via spray coating. When increasing the ratio of ZnO, more coffee rings are observed, causing larger surface roughness. This might

be due to the increasing viscosity in the solution with increasing concentration of the zinc precursor. Having the composite at high viscosity further limits the probable equilibrium of the thickness in the vertical direction with respect to the substrate.

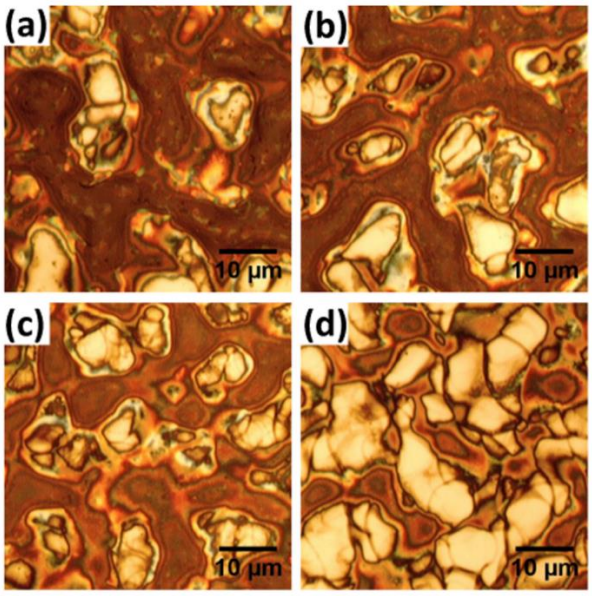

Figure 8.8 OM images of sprayed ZnO/P3HT/P3HT-b-PEO hybrid films with different ratio of w_{ZnO}*:* w_{P3HT}*:* $w_{P3HT\text{-}b\text{-}PEO}$ *= (a) 1:5:1, (b) 2:5:1, (c) 3:5:1, (d) 4:5:1. Reprinted from Ref.*[206]

8.3.2 Inner morphology

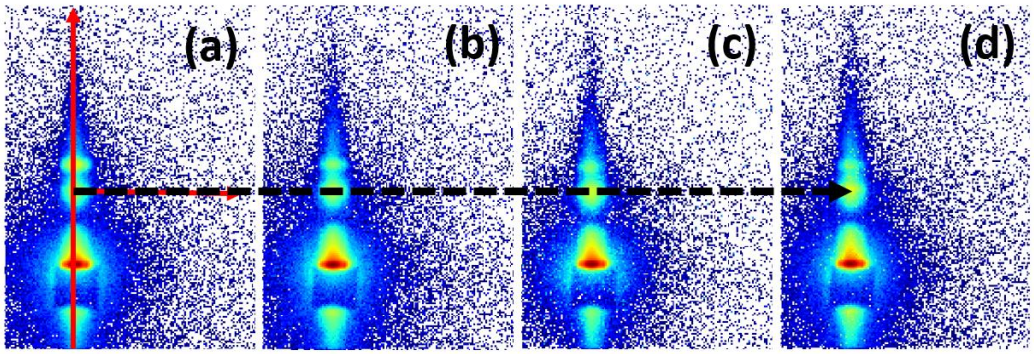

Figure 8.9 Selected 2D GISANS data of the spray coated ZnO/P3HT/P3HT-b-PEO hybrid films with different weight ratios of w_{ZnO}*:* w_{P3HT}*:* $w_{P3HT\text{-}b\text{-}PEO}$*: (a) 1:5:1, (b) 2:5:1, (c) 3:5:1, and (d) 4:5:1. The average neutron wavelength is 0.46 nm. The direct beam is covered by a beamstop. The red arrows along the vertical and horizontal directions indicate the places where the vertical and horizontal cuts are performed. The black dashed arrow indicates the position of the Yoneda peak. Reprinted from Ref.*[206]

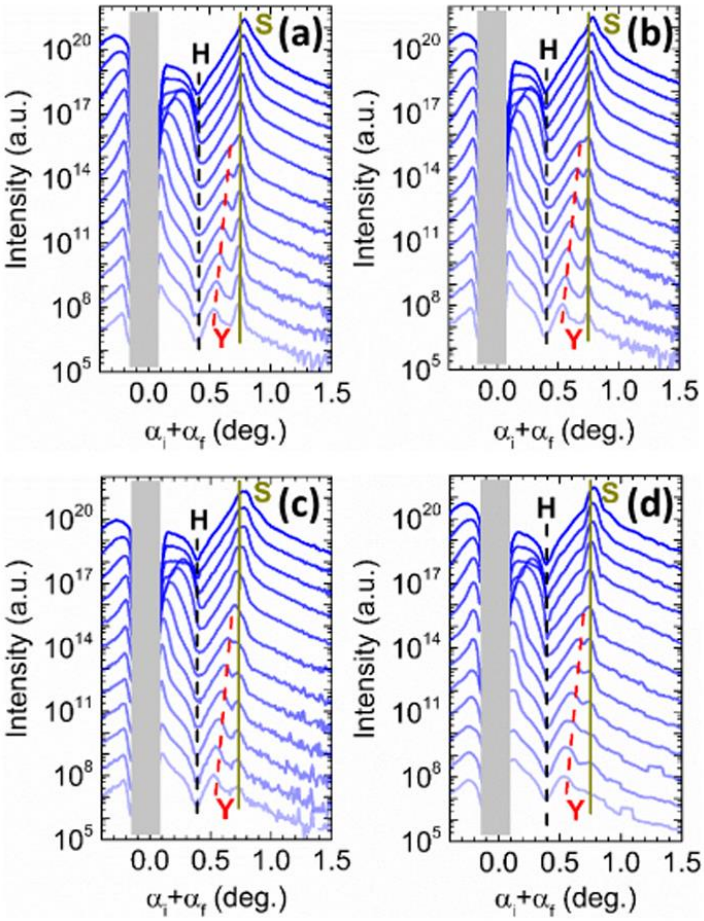

Figure 8.10 Vertical line cuts of the 2D GISANS data for the sprayed ZnO/P3HT/P3HT-b-PEO hybrid films with different weight ratio of w_{ZnO}: w_{P3HT}: $w_{P3HT\text{-}b\text{-}PEO}$: (a) 1:5:1, (b) 2:5:1, (c) 3:5:1, and (d) 4:5:1. From bottom to top, the average neutron wavelength increases from 0.379 to 1.141 nm. All cuts are shifted along the y axis for clarity. The region shielded by a beamstop is illustrated in gray. The dashed black line, the dashed red line, and the solid dark yellow line denote the sample horizon, the shifting of the Yoneda peak for the hybrid film and the specular peak, respectively. Reprinted from Ref.[206]

To see the shift of the critical angles in more detail, the detected Yoneda peak positions are extracted and plotted as a function of neutron wavelength as shown in Figure 8.11a. The experimental data are fitted with a line according to Equation 8.1. The increasing slope of the fitted line indicates the increasing SLD of the detected materials. Thus, the SLD of the hybrid materials follows SLD_{P3HT}, $SLD_{PEO} < SLD_{1:5:1} < SLD_{2:5:1} < SLD_{3:5:1} < SLD_{4:5:1} < SLD_{ZnO}$, which indicates the successful well-mixed hybrid films. Since the SLD of ZnO is larger than the SLD of the polymers, the SLD of the hybrid films increase when increasing the ratio of the ZnO in

the hybrid films. The corresponding SLD calculated from the linear fits are plotted as a function of the weight ratio as shown in Figure 8.11b. The SLD increases from 1.8 x 10^{-4} nm^{-2} to 2.2 x 10^{-4} nm^{-2} when increasing the ratio of w_{ZnO}: w_{P3HT}: $w_{P3HT\text{-}b\text{-}PEO}$ from 1:5:1 to 4:5:1.

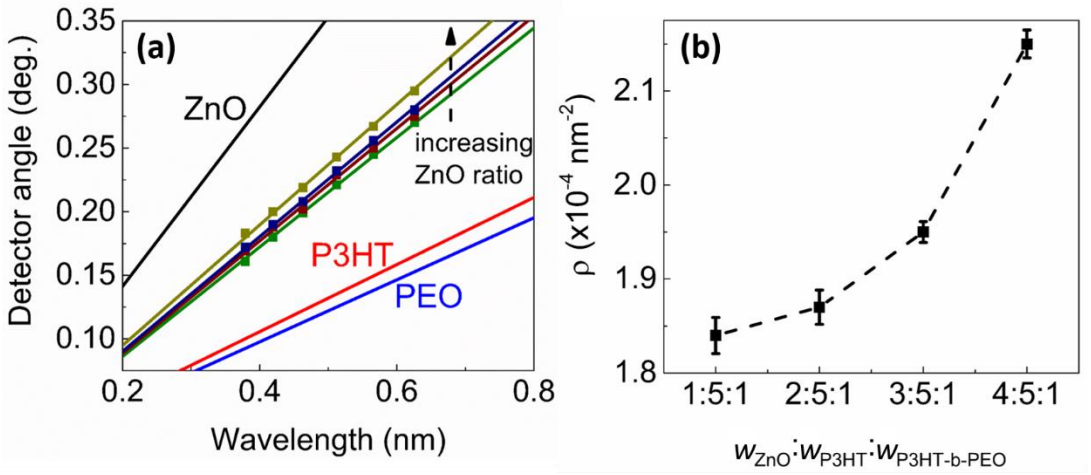

Figure 8.11 (a) The experimental Yoneda peak positions (the solid squares) of the hybrid films with different weight ratio of w_{ZnO}: w_{P3HT}: $w_{P3HT\text{-}b\text{-}PEO}$ (green: 1:5:1, brown: 2:5:1, dark blue: 3:5:1, and dark yellow: 4:5:1) obtained from the vertical line cuts at the corresponding wavelengths and the corresponding linear fits (the solid lines). Ideally expected critical angles of ZnO, P3HT and PEO as a function of wavelength are shown as black, red and blue lines, respectively. (b) SLD values extracted from the linear fits of the spray coated samples for different weight ratios of ZnO. Reprinted from Ref.[206]

Horizontal line cuts are performed along the Yoneda region of the spray coated hybrid films with different weight ratios. As shown in Figure 8.12, all curves are fitted using the same model as described in section 8.2.2. Compared with the spin coated samples with two structures fitting the horizontal line cuts, three are still required for all the spray coated hybrid films. This implies the poor monodispersity of the domain sizes in spray coated films even if it is improved by decreasing the ZnO ratio. In Figure 8.12, the fitted curves are in excellent agreement with the experimental data. When increasing the neutron wavelength, the detected q_y range shifts to smaller value, which widens the length scale being detected. As described above, at short neutron wavelengths, inner morphologies are able to be detected, whereas at long neutron wavelengths, it is impossible to detect the inner morphology. Instead, only the surface morphology can be probed. In Figure 8.12, the same structural sizes are obtained from each fitted curve for experimental data obtained at different neutron wavelength. This indicates the consistency of the surface and inner morphology. As for application in HBSCs, the exciton

diffusion length of P3HT is only about 10 nm. Therefore, the small- and middle-sized structures are supposed to be more important than the large-sized structure.

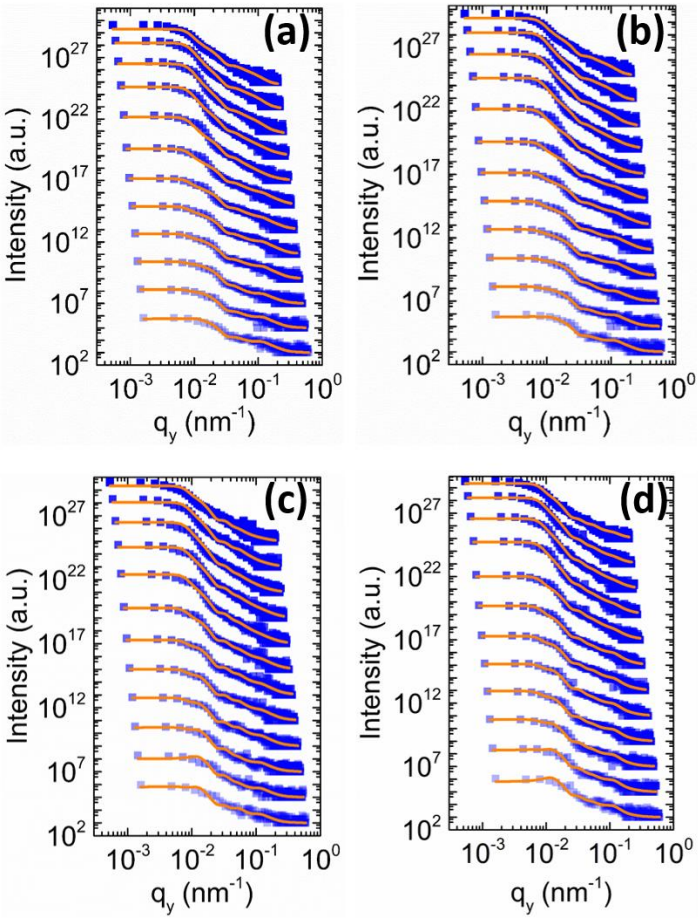

Figure 8.12 Horizontal line cuts of the 2D GISANS data for the ZnO/P3HT/P3HT-b-PEO hybrid films with different weight ratios of w_{ZnO}: w_{P3HT}: $w_{P3HT\text{-}b\text{-}PEO}$: (a) 1:5:1, (b) 2:5:1, (c) 3:5:1, and (d) 4:5:1. The solid curves are the fits using the geometry of cylindrical scattering objects distributed on a 1D paracrystal lattice as described in the text. From bottom to top, the average neutron wavelength increases from 0.38 to 1.14 nm. The different q ranges result from the variable neutron wavelengths. All cuts are shifted along the y axis for clarity. Reprinted from Ref.[206]

Figure 8.13 shows the average domain sizes of extracted small- and middle-domain structures. When the weight ratio of ZnO increases, both the middle- and small-domain sizes increase, indicating that the ZnO particles tend to aggregate to form larger domains. The spray coated films with a ratio of w_{ZnO}: w_{P3HT}: $w_{P3HT\text{-}b\text{-}PEO}$ = 1:5:1 exhibit much smaller domain sizes (20±3 nm for the small-sized domains, and 43±7 nm for the middle-sized domains) as compared with the other samples. Therefore, the spray coated samples with the ratio of 1:5:1 would show a

most suitable domain size for improving the interfaces of ZnO and P3HT, thus, revealing an advantage of promoting the exciton separation for applications in HBSCs. In addition, the samples with the ratio of 1:5:1 show smaller size difference of the middle-sized domains and the small-sized domains as compared with other samples, which indicates a better monodispersity of the fabricated films with the ratio of 1:5:1.

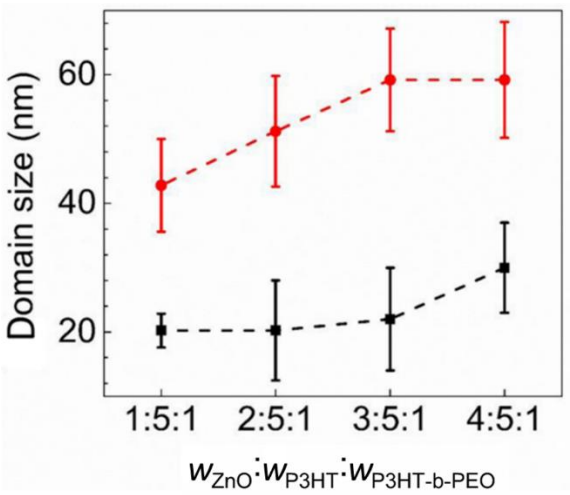

Figure 8.13 Domain size of the spray coated ZnO/P3HT/P3HT-b-PEO hybrid films with different ratio of w_{ZnO}: w_{P3HT}: $w_{P3HT\text{-}b\text{-}PEO}$ extracted from the fits to the corresponding horizontal line cuts. Squares (black) indicate small-sized structures and circles (red) middle-sized structures. Reprinted from Ref.[206]

8.3.3 Film thickness

Apart from the morphology, the film thickness is supposed to be influenced by the weight ratio as well. Figure 8.14 shows the film thickness for the spray coated films with different weight ratios. The large error bars represent the different values measured at different positions due to the very rough surface from coffee ring patterns. With increasing the weight ratio of the ZnO, the film thickness increase significantly from 130 nm to about 350 nm. The higher concentration of the zinc precursor during the sol-gel synthesis results in more metal oxide being deposited at constant flow volumes.

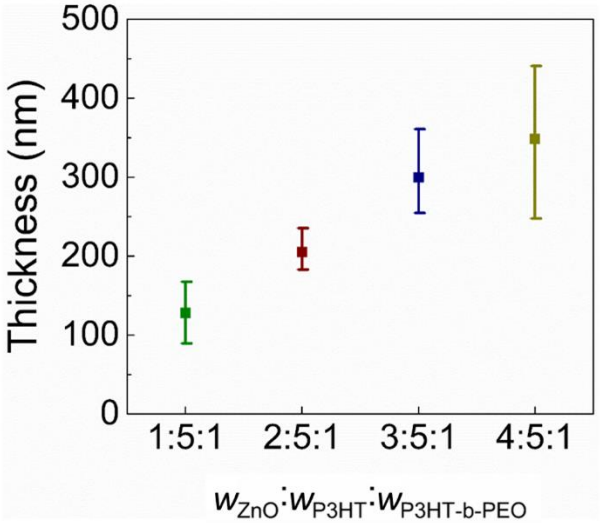

Figure 8.14 Film thickness of the spray coated samples for different weight ratios of ZnO. Reprinted from Ref.[206]

8.4 Summary

In this work, a simple route for fabricating ZnO/P3HT/P3HT-*b*-PEO hybrid films is introduced. The films are successfully prepared by a sol-gel synthesis with the diblock copolymer P3HT-*b*-PEO as an interface compatibilizer. In a well-mixed solvent of DCB and DMSO, the zinc precursor directly grows in the PEO blocks which act as a template while the P3HT blocks can be used to absorb light and transport charge carriers. Via the self-assembly process of the diblock copolymer, a well-mixed blend of ZnO/P3HT on a nanometer length scale is achieved. Moreover, two deposition methods, namely spray and spin coating, are used to deposit the sol-gel onto a substrate to form an active layer used in HBSCs. Both, the surface and inner morphologies are investigated by SEM and TOF-GISANS, respectively. They reveal that the spin coated hybrid films possess a higher homogeneity with smaller domain sizes. Although the spin coated films show promise in increasing the interface area for exciton separation, it is a great challenge to use spin coating for large scale fabrication. Spin coating on curved surface would even be impossible. Therefore, further tuning of the morphology of the spray coated films is performed. It is shown that when increasing the weight ratio of the ZnO inside the hybrid films, the ZnO particles tend to aggregate to form large domains, which hinders the formation of an effective interface for exciton separation. For the spray coated films with the ratio of *w*ZnO: *w*P3HT: *w*P3HT-b-PEO = 1:5:1, they show decreased domain sizes and better monodispersity as compared with the spray coated samples with higher ZnO ratios, which would benefit the exciton separation in HBSCs. In summary, the deposition method and the

weight ratio of the components inside the sol-gel system play a great role in the morphology tuning of ZnO/P3HT/P3HT-*b*-PEO hybrid films. When aiming at improving the performance of HBSCs via tuning the morphology of the active layer, this work is significantly important in providing us with a general guideline.

9. Conclusion and outlook

In the present thesis, the structures of ZnO films and of ZnO/P3HT hybrid films are investigated and the photovoltaic performances are improved via tailoring the morphologies accordingly. Two types of photovoltaic devices are explored, namely ssDSSCs and HBSCs. For ssDSSCs, mesoporous ZnO nanostructures are prepared by sol-gel synthesis. The morphology of the ZnO films is tailored by a diblock copolymer which acts as a template. By backfilling with dye molecules and p-type organic semiconductors into the mesoporous ZnO structures, which provide a rigid scaffold, DSSCs are fabricated. The photovoltaic performance of the devices is investigated. It is revealed that the optoelectronic properties and photovoltaic performance are highly linked with the morphology of the nanostructured ZnO films. Regarding HBSCs, the bulk heterojunction ZnO/P3HT is prepared directly as a blend. It is demonstrated that with the addition of the diblock copolymer P3HT-*b*-PEO, the interface of ZnO and P3HT is modified. Accordingly, the optoelectronic properties are improved. For both DSSCs and HBSCs, all these experiment results indicate the importance of the morphology of the ZnO and the ZnO-based active layers to the photovoltaic performance.

To tune the mesoporous ZnO morphology based on the interconnected network structures, a method combining sol-gel chemistry and diblock copolymer PS-*b*-PEO is used. Via increasing the annealing temperature the ZnO films change from foam-like, worm-like, to sphere-like structures. All the ZnO films with these morphologies are prepared at low temperature, which is cost-effective. Moreover, for fabricating ssDSSCs, every layer is deposited at low temperature which makes it promising to be used in flexible solar cells. With tuning the morphology of the ZnO films, the performance of the ssDSSCs improves significantly, with the ssDSSCs based on the worm-like structures exhibiting highest *PCE* due to the appropriate mesopore size and the better ordered interconnected network structures. In addition, a good long-term stability of the ssDSSCs is obtained even without special encapsulation.

For ssDSSCs it is revealed that the pores in the mesoporous ZnO films with appropriate sizes are important to improve the photovoltaic performance, due to the challenging steps in backfilling during the fabrication of solar cells. Increasing the pore size favors the backfilling of the dye molecules and p-type organic semiconductors, but on the other hand also decreases the surface-to-volume-ratio. Sol-gel synthesis combined with PS-*b*-P4VP templating is employed to tune the pore sizes of the mesoporous ZnO films. The obtained pore sizes with two post-treatment methods, namely UV-irradiation and sintering, are compared. It is revealed

that the sintered ZnO films show a larger pore size than the UV-irradiated samples. Moreover, both the surface and the inner morphology shows that the pore size increases when increasing the template-to-ZnO precursor ratio. Accordingly, the photovoltaic performance of the fabricated ssDSSCs shows a strong correlation with the nanopore size of the ZnO films. When increasing the pore sizes of the ZnO films, the efficiency first increases and then decreases, showing an optimal efficiency with the appropriate pore sizes.

In the active layer ZnO/P3HT, for application in HBSCs, a diblock copolymer P3HT-*b*-PEO with a functional block is used as a template as well as a compatibilizer. It is shown that with P3HT-*b*-PEO the domain sizes of both the P3HT and the ZnO decrease, which promotes the exciton separation due to the increased interface. PL measurements also reveal that upon increasing the ratio of the diblock copolymer the quenching becomes stronger, indicating a higher charge separation yield and a better charge transfer process. However, when increasing the annealing temperature, aggregation of both P3HT and ZnO domains appear, resulting in a decreased PL quenching.

Due to the great impact of the deposition method on the film deposition, two different film deposition techniques, namely spin and spray coating, are used to compare the morphology of the obtained ZnO/P3HT films modified by P3HT-*b*-PEO. Both, the surface and the inner morphology investigated by SEM and TOF-GISANS, respectively, shows that the spin coated samples possess smaller domains and higher monodisperse distribution than the spray coated films. Moreover, it is found that for the spray coated samples the domain sizes decrease and the aggregation becomes less when decreasing the amount of the ZnO. It is revealed that both the deposition method and the amount of the ZnO turn out to be significant parameters to tune the morphology of the ZnO/P3HT hybrid films.

All the above mentioned projects explore the way to tune the morphology of the ZnO and ZnO/P3HT films and the corresponding influence of the morphology to the photovoltaic performance for application in solar cells. Diblock copolymers play an important role in tailoring the morphology of the films with sol-gel synthesis. The preparations at low temperature are carried out, which is promising for future flexible solar cell fabrication. The morphology of the hybrid films prepared at low temperature is also compared with that obtained with high temperature sintering. It is demonstrated that the morphology of the ZnO films and also the ZnO/P3HT hybrid films plays a significant role in the photovoltaic performance improvement.

With respect to future investigations, many research approaches can still be explored in the hybrid solar cells due to the advantages resulting from the combination of inorganic and

organic materials. As the methods used in this thesis are mostly at low temperature and the mesoporous ZnO structure is not favorable to crystallize, the crystallization issue is therefore still challenging. Improving the crystallinity of the ZnO films is expected to improve the electron mobility further, and resulting in less charge carrier recombination at the interfaces of the n-type and the p-type semiconductors. Moreover, the film thickness also influences the photovoltaic performance of solar cells. For example, for ssDSSCs, the optimal thickness for the ZnO films should be on the order of micrometer length scale. It is simple to increase the film thickness via spray coating. In contrast, it is challenging to improve it with spin coating due to the redissolving while spin coating layer-by-layer. In the future study, deposition methods which can be used to produce large scale films can be explored. Since the synthesis method used in the present thesis is the sol-gel method, it provides the possibility to produce the active layers on a large scale with all types of wet-composite deposition. The other techniques, such as printing, and blade-casting can also be investigated and will likely also give rise to other morphologies.

Bibliography

1. Becquerel, A. E., Mémoire sur les effets électriques produits sous l'influence des rayons solaires. *Comptes Rendus des Séances Hebdomadaires* 1839, 9, 561-567.
2. Green, M. A., The path to 25% silicon solar cell efficiency: History of silicon cell evolution. *Progress in Photovoltaics: Research and Applications* 2009, 17, 183-189.
3. Chiang, C. K.; Fincher, C.; Park, Y.; Heeger, A. J.; Shirakawa, H.; Louis, E. J. C.; Gau, S.; G. MacDiarmid, A., Electrical conductivity in doped polyacetylene. *Physical Review Letters* 1977, 39, 1098-1101.
4. O'Regan, B.; Grätzel, M., A low-cost, high-efficiency solar cell based on dye-sensitized colloidal TiO_2 films. *Nature* 1991, 353, 737.
5. Mathew, S.; Yella, A.; Gao, P.; Humphry-Baker, R.; Curchod, B. F. E.; Ashari-Astani, N.; Tavernelli, I.; Rothlisberger, U.; Nazeeruddin, M. K.; Grätzel, M., Dye-sensitized solar cells with 13% efficiency achieved through the molecular engineering of porphyrin sensitizers. *Nature Chemistry* 2014, 6, 242.
6. Babelon, P.; Dequiedt, A. S.; Mostéfa-Sba, H.; Bourgeois, S.; Sibillot, P.; Sacilotti, M., SEM and XPS studies of titanium dioxide thin films grown by MOCVD. *Thin Solid Films* 1998, 322, 63-67.
7. Wang, F.; Shi, Z.; Gong, F.; Jiu, J.; Adachi, M., Morphology control of anatase TiO_2 by surfactant-assisted hydrothermal method. *Chinese Journal of Chemical Engineering* 2007, 15, 754-759.
8. Zhu, J.; Deng, Z.; Chen, F.; Zhang, J.; Chen, H.; Anpo, M.; Huang, J.; Zhang, L., Hydrothermal doping method for preparation of Cr^{3+}-TiO_2 photocatalysts with concentration gradient distribution of Cr^{3+}. *Applied Catalysis B: Environmental* 2006, 62, 329-335.
9. Gu, D.-E.; Yang, B.-C.; Hu, Y.-D., V and N co-doped nanocrystal anatase TiO_2 photocatalysts with enhanced photocatalytic activity under visible light irradiation. *Catalysis Communications* 2008, 9, 1472-1476.
10. Linsebigler, A. L.; Lu, G.; Yates, J. T., Photocatalysis on TiO_2 surfaces: principles, mechanisms, and selected results. *Chemical Reviews* 1995, 95, 735-758.
11. Henderson, M. A., Photooxidation of Acetone on TiO_2(110): Conversion to acetate via methyl radical ejection. *The Journal of Physical Chemistry B* 2005, 109, 12062-12070.
12. Guldin, S.; Kohn, P.; Stefik, M.; Song, J.; Divitini, G.; Ecarla, F.; Ducati, C.; Wiesner, U.; Steiner, U., Self-cleaning antireflective optical coatings. *Nano Letters* 2013, 13, 5329-5335.
13. Hartmann, P.; Lee, D.-K.; Smarsly, B. M.; Janek, J., Mesoporous TiO_2: comparison of classical sol−gel and nanoparticle based photoelectrodes for the water splitting reaction. *ACS Nano* 2010, 4, 3147-3154.
14. Liu, Y.; Yang, Y., Recent progress of TiO_2-based anodes for Li ion batteries. *Journal of Nanomaterials* 2016, 2016, 15.
15. Xu, C.; Wu, J.; Desai, U. V.; Gao, D., High-efficiency solid-state dye-sensitized solar cells based on TiO_2-coated ZnO nanowire arrays. *Nano Letters* 2012, 12, 2420-2424.
16. Hwang, D.; Kim, D. Y.; Jang, S.-Y.; Kim, D., Superior photoelectrodes for solid-state dye-sensitized solar cells using amphiphilic TiO_2. *Journal of Materials Chemistry A* 2013, 1, 1228-1238.

17. Deng, J.; Zheng, Y.-Z.; Hou, Q.; Chen, J.-F.; Zhou, W.; Tao, X., Solid-state dye-sensitized hierarchically structured ZnO solar cells. *Electrochimica Acta* 2011, 56, 4176-4180.
18. O'Regan, B.; Schwartz, D. T.; Zakeeruddin, S. M.; Gratzel, M., Electrodeposited nanocomposite n-p heterojunctions for solid-state dye-sensitized photovoltaics. *Advanced Materials* 2000, 12, 1263.
19. Lin, C.-Y.; Lai, Y.-H.; Chen, H.-W.; Chen, J.-G.; Kung, C.-W.; Vittal, R.; Ho, K.-C., Highly efficient dye-sensitized solar cell with a ZnO nanosheet-based photoanode. *Energy & Environmental Science* 2011, 4, 3448-3455.
20. Law, M.; Greene, L. E.; Johnson, J. C.; Saykally, R.; Yang, P. D., Nanowire dye-sensitized solar cells. *Nat Mater* 2005, 4, 455-459.
21. Baxter, J. B.; Walker, A. M.; Ommering, K. V.; Aydil, E. S., Synthesis and characterization of ZnO nanowires and their integration into dye-sensitized solar cells. *Nanotechnology* 2006, 17, S304.
22. Boucharef, M.; Di Bin, C.; Boumaza, M. S.; Colas, M.; Snaith, H. J.; Ratier, B.; Boucle, J., Solid-state dye-sensitized solar cells based on ZnO nanocrystals. *Nanotechnology* 2010, 21, 205203.
23. Tao-Hua, L.; Hung-Jue, S.; Xing, C., ZnO and conjugated polymer bulk heterojunction solar cells containing ZnO nanorod photoanode. *Nanotechnology* 2011, 22, 285401.
24. J.M.G. Cowie, V. A., Polymers: chemistry and physics of modern materials. *Chemical Rubber Company (CRC) press* 2007.
25. Bower, D. I., An introduction to polymer physics. *Cambridge University press* 2002.
26. Fougnies, C.; Dosière, M.; Koch, M. H. J.; Roovers, J., Morphological study and melting behavior of narrow molecular weight fractions of poly(aryl ether ether ketone) (PEEK) annealed from the glassy state. *Macromolecules* 1998, 31, 6266-6274.
27. Sirringhaus, H.; Brown, P. J.; Friend, R. H.; Nielsen, M. M.; Bechgaard, K.; Langeveld-Voss, B. M. W.; Spiering, A. J. H.; Janssen, R. A. J.; Meijer, E. W.; Herwig, P.; de Leeuw, D. M., Two-dimensional charge transport in self-organized, high-mobility conjugated polymers. *Nature* 1999, 401, 685.
28. Kobashi, M.; Takeuchi, H., Inhomogeneity of Spin-Coated and Cast Non-Regioregular Poly(3-hexylthiophene) Films. Structures and electrical and photophysical properties. *Macromolecules* 1998, 31, 7273-7278.
29. Strobl, G., The physics of polymers: concepts for understanding their structures and behavior. *Springer Berlin Heidelberg*: 2007.
30. Fromhold, A. T., Stress in dielectric contact layers on metals. *Surface Science* 1972, 29, 396-410.
31. Sarkar, K. Nanostructured zinc oxide films for application in photovoltaics. Technische Universität München, Ph. D. thesis 2014.
32. Flory, P. J., Thermodynamics of high polymer solutions. *The Journal of Chemical Physics* 1942, 10, 51-61.
33. Huggins, M. L., thermodynamics properties of solutions of long-chain compounds. *Annals of the New York Academy of Sciences* 1942, 43, 1-32.
34. Bates, F. S.; Fredrickson, G. H., Block Copolymer thermodynamics: theory and experiment. *Annual Review of Physical Chemistry* 1990, 41, 525-557.
35. Tseng, Y.-C.; Darling, S. B., Block copolymer nanostructures for technology. *Polymers* 2010, 2, 470-489.
36. Ward, M. D.; Horner, M. J., Structure and order in soft matter: symmetry transcending length scale. *CrystEngComm* 2004, 6, 401-407.
37. Mai, Y.; Eisenberg, A., Self-assembly of block copolymers. *Chemical Society Reviews* 2012, 41, 5969-5985.

38. Corvazier, L.; Messé, L.; L O Salou, C.; Young, R.; Fairclough, P.; Ryan, A., Lamellar phases and microemulsions in model ternary blends containing amphiphilic block copolymers. *Journal of Materials Chemistry*, 2001, 11, 2864-2874.
39. Johansson, T.; Mammo, W.; Svensson, M.; Andersson, M.; Inganas, O., Electrochemical bandgaps of substituted polythiophenes. *Journal of Materials Chemistry*, 2003, 13, 1316-1323.
40. Dong, H.; Zhu, H.; Meng, Q.; Gong, X.; Hu, W., Organic photoresponse materials and devices. *Chemical Society Reviews* 2012, 41, 1754-1808.
41. Niedermeier, M. A. Novel structuring routines of titania films for application in photovoltaics. Ph.D., Technische Universität München, Ph. D. thesis 2013.
42. Nelson, J., Polymer:fullerene bulk heterojunction solar cells. *Materials Today* 2011, 14, 462-470.
43. Chang, J.; Waclawik, E. R., Colloidal semiconductor nanocrystals: controlled synthesis and surface chemistry in organic media. *RSC Advances* 2014, 4, 23505-23527.
44. Özgür, Ü.; Alivov, Y. I.; Liu, C.; Teke, A.; Reshchikov, M. A.; Doğan, S.; Avrutin, V.; Cho, S. J.; Morkoç, H., A comprehensive review of ZnO materials and devices. *Journal of Applied Physics* 2005, 98, 041301.
45. Zhang, Y.; Chung, J.; Lee, J.; Myoung, J.; Lim, S., Synthesis of ZnO nanospheres with uniform nanopores by a hydrothermal process. *Journal of Physics and Chemistry of Solids* 2011, 72, 1548-1553.
46. Fang, B.; Zhang, C.; Zhang, W.; Wang, G., A novel hydrazine electrochemical sensor based on a carbon nanotube-wired ZnO nanoflower-modified electrode. *Electrochimica Acta* 2009, 55, 178-182.
47. Yao, Q.; Wang, C.; Fan, B.; Wang, H.; Sun, Q.; Jin, C.; Zhang, H., One-step solvothermal deposition of ZnO nanorod arrays on a wood surface for robust superamphiphobic performance and superior ultraviolet resistance. *Scientific Reports* 2016, 6, 35505.
48. Orilall, M. C.; Wiesner, U., Block copolymer based composition and morphology control in nanostructured hybrid materials for energy conversion and storage: solar cells, batteries, and fuel cells. *Chemical Society Reviews* 2011, 40, 520-535.
49. Lim Soo, P.; Eisenberg, A., Preparation of block copolymer vesicles in solution. *Journal of Polymer Science Part B: Polymer Physics* 2004, 42, 923-938.
50. Brinker, C. J.; Lu, Y.; Sellinger, A.; Fan, H., Evaporation-induced self-assembly: nanostructures made easy. *Advanced Materials* 1999, 11, 579-585.
51. Rawolle, M.; Braden, E. V.; Niedermeier, M. A.; Magerl, D.; Sarkar, K.; Fröschl, T.; Hüsing, N.; Perlich, J.; Müller-Buschbaum, P., Low-temperature route to crystalline titania network structures in thin films. *ChemPhysChem* 2012, 13, 2412-2417.
52. Choi, S. Y.; Mamak, M.; Speakman, S.; Chopra, N.; Ozin, G. A., Evolution of nanocrystallinity in periodic mesoporous anatase thin films. *Small* 2004, 1, 226-232.
53. Oregan, B.; Gratzel, M., A low-cost, high-efficiency solar-cell based on dye-sensitized colloidal TiO_2 films. *Nature* 1991, 353, 737-740.
54. Gunaratna, N.; Kumara, G., Solid state solar cells based on TiO_2 sensitized with natural pigment extracted from anthurium. *International Journal of Scientific and Research Publications*, 2013, 3, 1-5.
55. Gerischer, H.; Willig, F. In reaction of excited dye molecules at electrodes, *Physical and Chemical Applications of Dyestuffs*, Berlin, Heidelberg, 1976, 31-84.
56. Robertson, N., Optimizing dyes for dye-sensitized solar cells. *Angewandte Chemie International Edition* 2006, 45, 2338-2345.
57. Heimer, T. A.; Bignozzi, C. A.; Meyer, G. J., Molecular level photovoltaics: the electrooptical properties of metal cyanide complexes anchored to titanium dioxide. *The Journal of Physical Chemistry* 1993, 97, 11987-11994.

58. Islam, A.; Sugihara, H.; Hara, K.; Singh, L. P.; Katoh, R.; Yanagida, M.; Takahashi, Y.; Murata, S.; Arakawa, H.; Fujihashi, G., Dye sensitization of nanocrystalline titanium dioxide with square planar platinum(II) diimine dithiolate domplexes. *Inorganic Chemistry* 2001, 40, 5371-5380.
59. Hasselmann, G. M.; Meyer, G. J., Diffusion-limited interfacial electron transfer with large apparent driving forces. *The Journal of Physical Chemistry B* 1999, 103, 7671-7675.
60. Bessho, T.; Constable, E. C.; Graetzel, M.; Hernandez Redondo, A.; Housecroft, C. E.; Kylberg, W.; Nazeeruddin, M. K.; Neuburger, M.; Schaffner, S., An element of surprise-efficient copper-functionalized dye-sensitized solar cells. *Chemical Communications* 2008, 3717-3719.
61. Ferrere, S.; Gregg, B. A., Photosensitization of TiO_2 by [FeII(2,2'-bipyridine-4,4'-dicarboxylic acid)$_2$(CN)$_2$]: band selective electron injection from ultra-short-lived excited states. *Journal of the American Chemical Society* 1998, 120, 843-844.
62. Clifford, J. N.; Martínez-Ferrero, E.; Viterisi, A.; Palomares, E., Sensitizer molecular structure-device efficiency relationship in dye sensitized solar cells. *Chemical Society Reviews* 2011, 40, 1635-1646.
63. Hagberg, D. P.; Yum, J.-H.; Lee, H.; De Angelis, F.; Marinado, T.; Karlsson, K. M.; Humphry-Baker, R.; Sun, L.; Hagfeldt, A.; Grätzel, M.; Nazeeruddin, M. K., Molecular engineering of organic sensitizers for dye-sensitized solar cell applications. *Journal of the American Chemical Society* 2008, 130, 6259-6266.
64. Higashino, T.; Imahori, H., Porphyrins as excellent dyes for dye-sensitized solar cells: recent developments and insights. *Dalton Transactions* 2015, 44, 448-463.
65. Ragoussi, M.-E.; Ince, M.; Torres, T., Recent advances in phthalocyanine-based sensitizers for dye-sensitized solar cells. *European Journal of Organic Chemistry* 2013, 2013, 6475-6489.
66. Rehm, J. M.; McLendon, G. L.; Nagasawa, Y.; Yoshihara, K.; Moser, J.; Grätzel, M., Femtosecond electron-transfer dynamics at a sensitizing dye-semiconductor (TiO_2) interface. *The Journal of Physical Chemistry* 1996, 100, 9577-9578.
67. Zhao, W.; Jun Hou, Y.; Song Wang, X.; Wen Zhang, B.; Cao, Y.; Yang, R.; Bo Wang, W.; Rui Xiao, X., Study on squarylium cyanine dyes for photoelectric conversion. *Solar Energy Materials and Solar Cells* 1999, 58, 173-183.
68. Ferrere, S.; Gregg, B. A., Large increases in photocurrents and solar conversion efficiencies by UV illumination of dye sensitized solar cells. *The Journal of Physical Chemistry B* 2001, 105, 7602-7605.
69. Horiuchi, T.; Miura, H.; Uchida, S., Highly efficient metal-free organic dyes for dye-sensitized solar cells. *Journal of Photochemistry and Photobiology A: Chemistry* 2004, 164, 29-32.
70. Henry, J. S.; Robin, H.-B.; Peter, C.; Ilkay, C.; Shaik, M. Z.; Michael, G., Charge collection and pore filling in solid-state dye-sensitized solar cells. *Nanotechnology* 2008, 19, 424003.
71. Dosch, H.; Batterman, B. W.; Wack, D. C., Depth-controlled grazing-incidence diffraction of synchrotron X-radiation. *Physical Review Letters* 1986, 56, 1144-1147.
72. Holzwarth, U.; Gibson, N., The Scherrer equation versus the Debye-Scherrer equation. *Nature Nanotechnology* 2011, 6, 534.
73. Lazzari, R., IsGISAXS: a program for grazing-incidence small-angle X-ray scattering analysis of supported islands. *Journal of Applied Crystallography* 2002, 35, 406-421.
74. Naudon, A.; Babonneau, D.; Thiaudière, D.; Lequien, S., Grazing-incidence small-angle X-ray scattering applied to the characterization of aggregates in surface regions. *Physica B: Condensed Matter* 2000, 283, 69-74.

75. Müller-Buschbaum, P., A basic introduction to grazing incidence small-angle X-ray scattering. *Applications of Synchrotron Light to Scattering and Diffraction in Materials and Life Sciences*, 2009, 61-89.
76. Renaud, G.; Lazzari, R.; Leroy, F., Probing surface and interface morphology with Grazing Incidence Small Angle X-Ray Scattering. *Surface Science Reports* 2009, 64, 255-380.
77. Rawolle, M. Structuring and filling of titania films for applications in photovoltaics. *Technische Universität München*, Ph. D. thesis 2013.
78. Benecke, G.; Wagermaier, W.; Li, C.; Schwartzkopf, M.; Flucke, G.; Hoerth, R.; Zizak, I.; Burghammer, M.; Metwalli, E.; Müller-Buschbaum, P.; Trebbin, M.; Förster, S.; Paris, O.; Roth, S. V.; Fratzl, P., A customizable software for fast reduction and analysis of large X-ray scattering data sets: applications of the new DPDAK package to small-angle X-ray scattering and grazing-incidence small-angle X-ray scattering. *Journal of Applied Crystallography* 2014, 47, 1797-1803.
79. Kampmann, R.; Haese-Seiller, M.; Kudryashov, V.; Deriglazov, V.; Tristl, M.; Daniel, C.; Toperverg, B.; Schreyer, A.; Sackmann, E., The potential of the horizontal reflectometer REFSANS/FRM-II for measuring low reflectivity and diffuse surface scattering. *Physica B: Condensed Matter* 2004, 350, E763-E766.
80. Kampmann, R.; Haese-Seiller, M.; Kudryashov, V.; Nickel, B.; Daniel, C.; Fenzl, W.; Schreyer, A.; Sackmann, E.; Rädler, J., Horizontal TOF-neutron reflectometer REFSANS at FRM-II Munich/Germany: First tests and status. *Physica B: Condensed Matter* 2006, 385, 1161-1163.
81. Kaune, G.; Haese-Seiller, M.; Kampmann, R.; Moulin, J.-F.; Zhong, Q.; Müller-Buschbaum, P., TOF-GISANS investigation of polymer infiltration in mesoporous TiO_2 films for photovoltaic applications. *Journal of Polymer Science Part B: Polymer Physics* 2010, 48, 1628-1635.
82. Bartesaghi, D.; Pérez, I. d. C.; Kniepert, J.; Roland, S.; Turbiez, M.; Neher, D.; Koster, L. J. A., Competition between recombination and extraction of free charges determines the fill factor of organic solar cells. *Nature Communications* 2015, 6, 7083.
83. Wang, K.; Körstgens, V.; Yang, D.; Hohn, N.; Roth, S. V.; Müller-Buschbaum, P., Morphology control of low temperature fabricated ZnO nanostructures for transparent active layers in all solid-state dye-sensitized solar cells. *Journal of Materials Chemistry A* 2018, 6, 4405-4415.
84. Bolon, D. A.; Kunz, C. O., Ultraviolet depolymerization of photoresist polymers. *Polymer Engineering & Science* 1972, 12, 109-111.
85. Heo, J. H.; Lee, M. H.; Han, H. J.; Patil, B. R.; Yu, J. S.; Im, S. H., Highly efficient low temperature solution processable planar type $CH_3NH_3PbI_3$ perovskite flexible solar cells. *Journal of Materials Chemistry A* 2016, 4, 1572-1578.
86. Menon, S.; Ranjan, R., Spray Combustion in Swirling Flow. In coarse grained simulation and turbulent mixing, *Cambridge University Press: Cambridge*, 2016, 351-392.
87. Hardin, B. E.; Snaith, H. J.; McGehee, M. D., The renaissance of dye-sensitized solar cells. *Nat Photon* 2012, 6, 162-169.
88. Hagfeldt, A.; Boschloo, G.; Sun, L.; Kloo, L.; Pettersson, H., Dye-sensitized solar cells. *Chemical Reviews* 2010, 110, 6595-6663.
89. Grätzel, M., Dye-sensitized solar cells. *Journal of Photochemistry and Photobiology C: Photochemistry Reviews* 2003, 4, 145-153.
90. Chung, I.; Lee, B.; He, J.; Chang, R. P. H.; Kanatzidis, M. G., All-solid-state dye-sensitized solar cells with high efficiency. *Nature* 2012, 485, 486.
91. Song, L.; Wang, W.; Körstgens, V.; González, D. M.; Yao, Y.; Minar, N. K.; Feckl, J. M.; Peters, K.; Bein, T.; Fattakhova-Rohlfing, D.; Santoro, G.; Roth, S. V.; Müller-

Buschbaum, P., Spray deposition of titania films with incorporated crystalline nanoparticles for all-solid-state dye-sensitized solar cells using P3HT. *Advanced Functional Materials* 2016, 26, 1498-1506.
92. Lee, T.-H.; Sue, H.-J.; Cheng, X., Solid-state dye-sensitized solar cells based on ZnO nanoparticle and nanorod array hybrid photoanodes. *Nanoscale Research Letters* 2011, 6, 517.
93. Cai, N.; Moon, S.-J.; Cevey-Ha, L.; Moehl, T.; Humphry-Baker, R.; Wang, P.; Zakeeruddin, S. M.; Grätzel, M., An organic D-π-A dye for record efficiency solid-state sensitized heterojunction solar cells. *Nano Letters* 2011, 11, 1452-1456.
94. Law, M.; Greene, L. E.; Johnson, J. C.; Saykally, R.; Yang, P., Nanowire dye-sensitized solar cells. *Nature Materials* 2005, 4, 455.
95. Boucharef, M.; Bin, C. D.; Boumaza, M. S.; Colas, M.; Snaith, H. J.; Ratier, B.; Bouclé, J., Solid-state dye-sensitized solar cells based on ZnO nanocrystals. *Nanotechnology* 2010, 21, 205203.
96. Segawa, H.; Sakurai, H.; Izumi, R.; Hayashi, T.; Yano, T.; Shibata, S., Low-temperature crystallization of oriented ZnO film using seed layers prepared by sol–gel method. *Journal of Materials Science* 2011, 46, 3537-3543.
97. Elkady, M. F.; Shokry Hassan, H.; Hafez, E. E.; Fouad, A., Construction of zinc oxide into different morphological structures to be utilized as antimicrobial agent against multidrug resistant bacteria. *Bioinorganic Chemistry and Applications* 2015, 2015, 536854.
98. Yunus, S. H. A.; Sahdan, M. Z.; Ichimura, M.; Supee, A.; Rahim, S., Structural studies of ZnO nanostructures by varying the deposition parameters. *AIP Conference Proceedings* 2017, 1788, 030101.
99. Plank, N. O. V.; Howard, I.; Rao, A.; Wilson, M. W. B.; Ducati, C.; Mane, R. S.; Bendall, J. S.; Louca, R. R. M.; Greenham, N. C.; Miura, H.; Friend, R. H.; Snaith, H. J.; Welland, M. E., Efficient ZnO nanowire solid-state dye-sensitized solar cells using organic dyes and core−shell nanostructures. *The Journal of Physical Chemistry C* 2009, 113, 18515-18522.
100. Yu, H.; Zhang, Z.; Han, M.; Hao, X.; Zhu, F., A general low-temperature route for large-scale fabrication of highly oriented ZnO nanorod/nanotube arrays. *Journal of the American Chemical Society* 2005, 127, 2378-2379.
101. Pal, U.; Santiago, P., Controlling the morphology of ZnO nanostructures in a low-temperature hydrothermal process. *The Journal of Physical Chemistry B* 2005, 109, 15317-15321.
102. Tong, Y.; Liu, Y.; Dong, L.; Zhao, D.; Zhang, J.; Lu, Y.; Shen, D.; Fan, X., Growth of ZnO nanostructures with different morphologies by using hydrothermal technique. *The Journal of Physical Chemistry B* 2006, 110, 20263-20267.
103. Wang, Z.; Qian, X.-f.; Yin, J.; Zhu, Z.-k., Large-Scale Fabrication of Tower-like, Flower-like, and tube-like ZnO arrays by a simple chemical solution route. *Langmuir* 2004, 20, 3441-3448.
104. Muguerra, H.; Berthoux, G.; Yahya, W. Z. N.; Kervella, Y.; Ivanova, V.; Bouclé, J.; Demadrille, R., Electrodeposited ZnO nanowires as photoelectrodes in solid-state organic dye-sensitized solar cells. *Physical Chemistry Chemical Physics* 2014, 16, 7472-7480.
105. Lai, M.-H.; Tubtimtae, A.; Lee, M.-W.; Wang, G.-J., ZnO-nanorod dye-sensitized solar cells: new structure without a transparent conducting oxide layer. *International Journal of Photoenergy* 2010, 2010.
106. Peng, W.; Qu, S.; Cong, G.; Wang, Z., Synthesis and structures of morphology-controlled ZnO nano- and microcrystals. *Crystal Growth & Design* 2006, 6, 1518-1522.

107. Sarkar, K.; Schaffer, C. J.; González, D. M.; Naumann, A.; Perlich, J.; Müller-Buschbaum, P., Tuning the pore size of ZnO nano-grids via time-dependent solvent annealing. *Journal of Materials Chemistry A* 2014, 2, 6945-6951.
108. Hsiao, M.-S.; Zheng, J. X.; Leng, S.; Van Horn, R. M.; Quirk, R. P.; Thomas, E. L.; Chen, H.-L.; Hsiao, B. S.; Rong, L.; Lotz, B.; Cheng, S. Z. D., Crystal orientation change and its origin in one-dimensional nanoconfinement constructed by polystyrene-block-poly(ethylene oxide) single crystal mats. *Macromolecules* 2008, 41, 8114-8123.
109. Swann, J. M. G.; Topham, P. D., Design and application of nanoscale actuators using block-copolymers. *Polymers* 2010, 2, 454-469.
110. Müller-Buschbaum, P., The active layer morphology of organic solar cells probed with grazing incidence scattering techniques. *Advanced Materials* 2014, 26, 7692-7709.
111. Müller-Buschbaum, P.; Casagrande, M.; Gutmann, J.; Kuhlmann, T.; Stamm, M.; Krosigk, G. v.; Lode, U.; Cunis, S.; Gehrke, R., Determination of micrometer length scales with an X-ray reflection ultra small-angle scattering set-up. *Europhysics Letters* 1998, 42, 517.
112. Salditt, T.; Metzger, T. H.; Peisl, J.; Reinker, B.; Moske, M.; Samwer, K., Determination of the height-height correlation-function of rough surfaces from diffuse-X-ray scattering. *Europhys Lett* 1995, 32, 331-336.
113. Niedermeier, M. A.; Tainter, G.; Weiler, B.; Lugli, P.; Müller-Buschbaum, P., Fabrication of hierarchically structured titania thin films via combining nano-imprint lithography with block copolymer assisted sol-gel templating. *Journal of Materials Chemistry A* 2013, 1, 7870-7873.
114. Kim, E.; Vaynzof, Y.; Sepe, A.; Guldin, S.; Scherer, M.; Cunha, P.; Roth, S. V.; Steiner, U., Gyroid-structured 3D ZnO networks made by atomic layer deposition. *Advanced Functional Materials* 2014, 24, 863-872.
115. Choi, S. Y.; Mamak, M.; Speakman, S.; Chopra, N.; Ozin, G. A., Evolution of nanocrystallinity in periodic mesoporous anatase thin films. *Small* 2005, 1, 226-232.
116. Stefik, M.; Song, J.; Sai, H.; Guldin, S.; Boldrighini, P.; Orilall, M. C.; Steiner, U.; Gruner, S. M.; Wiesner, U., Ordered mesoporous titania from highly amphiphilic block copolymers: tuned solution conditions enable highly ordered morphologies and ultra-large mesopores. *Journal of Materials Chemistry A* 2015, 3, 11478-11492.
117. Karakaya, C.; Türker, Y.; Dag, Ö., Molten-salt-assisted self-assembly (MASA)-synthesis of mesoporous metal titanate-titania, metal Sulfide-titania, and metal selenide-titania thin films. *Advanced Functional Materials* 2013, 23, 4002-4010.
118. Fattakhova-Rohlfing, D.; Zaleska, A.; Bein, T., Three-dimensional titanium dioxide nanomaterials. *Chemical Reviews* 2014, 114, 9487-9558.
119. Bu, I. Y. Y.; Cole, M. T., One-pot synthesis of intercalating ZnO nanoparticles for enhanced dye-sensitized solar cells. *Materials Letters* 2013, 90, 56-59.
120. Suresh, S.; Pandikumar, A.; Murugesan, S.; Ramaraj, R.; Paul Raj, S., Metal-free low-cost organic dye-sensitized ZnO-nanorod photoanode for solid-state solar cell. *Materials Express* 2011, 1, 307-314.
121. Rawolle, M.; Sarkar, K.; Niedermeier, M. A.; Schindler, M.; Lellig, P.; Gutmann, J. S.; Moulin, J.-F.; Haese-Seiller, M.; Wochnik, A. S.; Scheu, C.; Müller-Buschbaum, P., Infiltration of polymer hole-conductor into mesoporous titania structures for solid-state dye-sensitized solar cells. *ACS Applied Materials & Interfaces* 2013, 5, 719-729.
122. Dualeh, A.; Moehl, T.; Nazeeruddin, M. K.; Grätzel, M., Temperature dependence of transport properties of spiro-MeOTAD as a hole transport material in solid-state dye-sensitized solar cells. *ACS Nano* 2013, 7, 2292-2301.

123. Tao, X.; Ruan, P.; Zhang, X.; Sun, H.; Zhou, X., Microsphere assembly of TiO_2 mesoporous nanosheets with highly exposed (101) facets and application in a light-trapping quasi-solid-state dye-sensitized solar cell. *Nanoscale* 2015, 7, 3539-3547.
124. Yang, W.-G.; Wan, F.-R.; Chen, Q.-W.; Li, J.-J.; Xu, D.-S., Controlling synthesis of well-crystallized mesoporous TiO_2 microspheres with ultrahigh surface area for high-performance dye-sensitized solar cells. *Journal of Materials Chemistry* 2010, 20, 2870-2876.
125. Sun, K. C.; Sahito, I. A.; Noh, J. W.; Yeo, S. Y.; Im, J. N.; Yi, S. C.; Kim, Y. S.; Jeong, S. H., Highly efficient and durable dye-sensitized solar cells based on a wet-laid PET membrane electrolyte. *Journal of Materials Chemistry A* 2016, 4, 458-465.
126. Kar, P.; Maji, T. K.; Sarkar, P. K.; Sardar, S.; Pal, S. K., Direct observation of electronic transition-plasmon coupling for enhanced electron injection in dye-sensitized solar cells. *RSC Advances* 2016, 6, 98753-98760.
127. Sardar, S.; Ghosh, S.; Remita, H.; Kar, P.; Liu, B.; Bhattacharya, C.; Lemmens, P.; Kumar Pal, S., Enhanced photovoltage in DSSC: synergistic combination of silver modified TiO_2 photoanode and low cost counter electrode. *RSC Advances* 2016, 6, 33433-33442.
128. Chen, S.; Xu, A.; Tao, J.; Tao, H.; Shen, Y.; Zhu, L.; Jiang, J.; Wang, T.; Pan, L., In-situ and green method to prepare Pt-free Cu_2ZnSnS_4 (CZTS) counter electrodes for efficient and low cost dye-sensitized solar cells. *ACS Sustainable Chemistry & Engineering* 2015, 3, 2652-2659.
129. Odobel, F.; Le Pleux, L.; Pellegrin, Y.; Blart, E., New photovoltaic devices based on the sensitization of p-type semiconductors: challenges and opportunities. *Accounts of Chemical Research* 2010, 43, 1063-1071.
130. Hagen, J.; Schaffrath, W.; Otschik, P.; Fink, R.; Bacher, A.; Schmidt, H.-W.; Haarer, D., Novel hybrid solar cells consisting of inorganic nanoparticles and an organic hole transport material. *Synthetic Metals* 1997, 89, 215-220.
131. Senadeera, G. K. R.; Jayaweera, P. V. V.; Perera, V. P. S.; Tennakone, K., Solid-state dye-sensitized photocell based on pentacene as a hole collector. *Solar Energy Materials and Solar Cells* 2002, 73, 103-108.
132. Salbeck, J.; Yu, N.; Bauer, J.; Weissörtel, F.; Bestgen, H., Low molecular organic glasses for blue electroluminescence. *Synthetic Metals* 1997, 91, 209-215.
133. Bach, U.; Lupo, D.; Comte, P.; Moser, J. E.; Weissortel, F.; Salbeck, J.; Spreitzer, H.; Gratzel, M., Solid-state dye-sensitized mesoporous TiO_2 solar cells with high photon-to-electron conversion efficiencies. *Nature* 1998, 395.
134. Guldin, S.; Huttner, S.; Tiwana, P.; Orilall, M. C.; Ulgut, B.; Stefik, M.; Docampo, P.; Kolle, M.; Divitini, G.; Ducati, C.; Redfern, S. A. T.; Snaith, H. J.; Wiesner, U.; Eder, D.; Steiner, U., Improved conductivity in dye-sensitised solar cells through block-copolymer confined TiO_2 crystallisation. *Energy & Environmental Science* 2011, 4, 225-233.
135. Cheng, Y.-J.; Gutmann, J. S., Morphology phase diagram of ultrathin anatase TiO_2 Films templated by a single PS-b-PEO block copolymer. *Journal of the American Chemical Society* 2006, 128, 4658-4674.
136. Rawolle, M.; Niedermeier, M. A.; Kaune, G.; Perlich, J.; Lellig, P.; Memesa, M.; Cheng, Y.-J.; Gutmann, J. S.; Müller-Buschbaum, P., Fabrication and characterization of nanostructured titania films with integrated function from inorganic-organic hybrid materials. *Chemical Society Reviews* 2012, 41, 5131-5142.
137. Liu, Z.; Li, Y.; Zhao, Z.; Cui, Y.; Hara, K.; Miyauchi, M., Block copolymer templated nanoporous TiO_2 for quantum-dot-sensitized solar cells. *Journal of Materials Chemistry* 2010, 20, 492-497.

138. Lim, J. Y.; Lee, C. S.; Lee, J. M.; Ahn, J.; Cho, H. H.; Kim, J. H., Amphiphilic block-graft copolymer templates for organized mesoporous TiO_2 films in dye-sensitized solar cells. *Journal of Power Sources* 2016, 301, 18-28.
139. Sarkar, K.; Rawolle, M.; Niedermeier, M. A.; Wang, W.; Herzig, E. M.; Korstgens, V.; Buffet, A.; Roth, S. V.; Müller-Buschbaum, P., A quantitative approach to tune metal oxide network morphology based on grazing-incidence small-angle X-ray scattering investigations. *Journal of Applied Crystallography* 2014, 47, 76-83.
140. li, X.; Fu, J.; Steinhart, M.; Ha Kim, D.; Knoll, W., Au/titania composite nanoparticle arrays with controlled size and spacing by organic-inorganic nanohybridization in thin film block copolymer templates. *Bulletin-Korean Chemical Society* 2007, 28, 1015-1020.
141. Haseloh, S.; Choi, S. Y.; Mamak, M.; Coombs, N.; Petrov, S.; Chopra, N.; Ozin, G. A., Towards flexible inorganic "mesomaterials": one-pot low temperature synthesis of mesostructured nanocrystalline titania. *Chemical Communications* 2004, 1460-1461.
142. Sun, Z.; Kim, D. H.; Wolkenhauer, M.; Bumbu, G. G.; Knoll, W.; Gutmann, J. S., Synthesis and photoluminescence of titania nanoparticle arrays templated by block-copolymer thin films. *ChemPhysChem* 2006, 7, 370-378.
143. Song, L.; Abdelsamie, A.; Schaffer, C. J.; Körstgens, V.; Wang, W.; Wang, T.; Indari, E. D.; Fröschl, T.; Hüsing, N.; Haeberle, T.; Lugli, P.; Bernstorff, S.; Müller-Buschbaum, P., A low temperature route toward hierarchically structured titania films for thin hybrid solar cells. *Advanced Functional Materials* 2016, 26, 7084-7093.
144. Haseloh, S.; Choi, S. Y.; Mamak, M.; Coombs, N.; Petrov, S.; Chopra, N.; Ozin, G. A., Towards flexible inorganic “mesomaterials”: one-pot low temperature synthesis of mesostructured nanocrystalline titania. *Chemical Communications* 2004, 1460-1461.
145. Wang, K.; Xia, S.; Cao, W.; Hohn, N.; Grott, S.; Kreuzer, L.; Schwartzkopf, M.; Roth, S. V.; Müller-Buschbaum, P., Comparison of UV-irradiation and sintering on mesoporous sponge-like ZnO films prepared from PS-b-P4VP templated sol-gel synthesis. *ACS Applied Nano Materials* 2018. DOI: 10.1021/acsanm.8b02039.
146. Du, B.; Chen, X.; Zhao, B.; Mei, A.; Wang, Q.; Xu, J.; Fan, Z., Interfacial entrapment of noble metal nanoparticles and nanorods capped with amphiphilic multiblock copolymer at a selective liquid–liquid interface. *Nanoscale* 2010, 2, 1684-1689.
147. Ruderer Matthias, A.; Guo, S.; Meier, R.; Chiang, H. Y.; Körstgens, V.; Wiedersich, J.; Perlich, J.; Roth Stephan, V.; Müller-Buschbaum, P., Solvent-induced morphology in polymer-based systems for organic photovoltaics. *Advanced Functional Materials* 2011, 21, 3382-3391.
148. Einollahzadeh-Samadi, M.; Dariani, R. S.; Paul, A., Tailoring morphology, structure and photoluminescence properties of anodic TiO_2 nanotubes. *Journal of Applied Crystallography* 2017, 50, 1133-1143.
149. Hoppe, H.; Sariciftci, N. S., Morphology of polymer/fullerene bulk heterojunction solar cells. *Journal of Materials Chemistry* 2006, 16, 45-61.
150. Wang, K.; Bießmann, L.; Schwartzkopf, M.; Roth, S. V.; Müller-Buschbaum, P., Tuning of the morphology and optoelectronic properties of ZnO/P3HT/P3HT-b-PEO hybrid films via spray deposition method. *ACS Applied Materials & Interfaces* 2018, 10, 20569-20577.
151. Yu, C.-F.; Sung, C.-W.; Chen, S.-H.; Sun, S.-J., Relationship between the photoluminescence and conductivity of undoped ZnO thin films grown with various oxygen pressures. *Applied Surface Science* 2009, 256, 792-796.
152. Lancelle-Beltran, E.; Prené, P.; Boscher, C.; Belleville, P.; Buvat, P.; Sanchez, C., All-solid-state dye-sensitized nanoporous TiO_2 hybrid solar cells with high energy-conversion efficiency. *Advanced Materials* 2006, 18, 2579-2582.

153. Cao, Y.; Saygili, Y.; Ummadisingu, A.; Teuscher, J.; Luo, J.; Pellet, N.; Giordano, F.; Zakeeruddin, S. M.; Moser, J. E.; Freitag, M.; Hagfeldt, A.; Grätzel, M., 11% efficiency solid-state dye-sensitized solar cells with copper(II/I) hole transport materials. *Nature Communications* 2017, 8, 15390.
154. Chergui, Y.; Nehaoua, N.; Mekki, D. E., Photovoltaic characteristics of ZnO nanotube dye-sensitized solar cells and TiO_2 nanostructure. *Research and Reviews: Journal of Material Sciences* 2013, 01, 18-24.
155. Venkata-Haritha, M.; Gopi, C. V. V. M.; Kim, S.-K.; Lee, J.-c.; Kim, H.-J., Solution-processed morphology-controllable nanosphere structured highly efficient and stable nickel sulfide counter electrodes for dye- and quantum dot-sensitized solar cells. *New Journal of Chemistry* 2015, 39, 9575-9585.
156. Schaffer, E.; Thurn-Albrecht, T.; Russell, T. P.; Steiner, U., Electrically induced structure formation and pattern transfer. *Nature* 2000, 403, 874-877.
157. Thurn-Albrecht, T.; Schotter, J.; Kästle, G. A.; Emley, N.; Shibauchi, T.; Krusin-Elbaum, L.; Guarini, K.; Black, C. T.; Tuominen, M. T.; Russell, T. P., Ultrahigh-density nanowire arrays grown in self-assembled diblock copolymer templates. *Science* 2000, 290, 2126.
158. Chai, J.; Buriak, J. M., Using cylindrical domains of block copolymers To self-assemble and align metallic nanowires. *ACS Nano* 2008, 2, 489-501.
159. Matsen, M. W.; Bates, F. S., Unifying weak- and strong-segregation block copolymer theories. *Macromolecules* 1996, 29, 1091-1098.
160. Discher, D. E.; Eisenberg, A., Polymer vesicles. *Science* 2002, 297, 967.
161. Suresh, V.; Huang, M. S.; Srinivasan, M. P.; Krishnamoorthy, S., In situ synthesis of high density sub-50 nm ZnO nanopatterned arrays using diblock copolymer templates. *ACS Applied Materials & Interfaces* 2013, 5, 5727-5732.
162. Kamcev, J.; Germack, D. S.; Nykypanchuk, D.; Grubbs, R. B.; Nam, C.-Y.; Black, C. T., Chemically enhancing block copolymers for block-selective synthesis of self-assembled metal oxide nanostructures. *ACS Nano* 2013, 7, 339-346.
163. Lai, C.-H.; Lee, W.-F.; Wu, I. C.; Kang, C.-C.; Chen, D.-Y.; Chen, L.-J.; Chou, P.-T., Highly luminescent, homogeneous ZnO nanoparticles synthesized via semiconductive polyalkyloxylthiophene template. *Journal of Materials Chemistry* 2009, 19, 7284-7289.
164. Schmidt-Mende, L.; Grätzel, M., TiO_2 pore-filling and its effect on the efficiency of solid-state dye-sensitized solar cells. *Thin Solid Films* 2006, 500, 296-301.
165. Shi, Y.; Li, F.; Chen, Y., Controlling morphology and improving the photovoltaic performances of P3HT/ZnO hybrid solar cells via P3HT-b-PEO as an interfacial compatibilizer. *New Journal of Chemistry* 2013, 37, 236-244.
166. Li, F.; Shi, Y.; Yuan, K.; Chen, Y., Fine dispersion and self-assembly of ZnO nanoparticles driven by P3HT-b-PEO diblocks for improvement of hybrid solar cells performance. *New Journal of Chemistry* 2013, 37, 195-203.
167. Niedermeier, M. A.; Rawolle, M.; Lellig, P.; Körstgens, V.; Herzig, E. M.; Buffet, A.; Roth, S. V.; Gutmann, J. S.; Fröschl, T.; Hüsing, N.; Müller-Buschbaum, P., Low-temperature sol-gel synthesis of nanostructured polymer/titania hybrid films based on custom-made poly(3-Alkoxy Thiophene). *ChemPhysChem* 2013, 14, 597-602.
168. Sahay, P. P.; Tewari, S.; Nath, R. K., Optical and electrical studies on spray deposited ZnO thin films. *Crystal Research and Technology* 2007, 42, 723-729.
169. Dedova, T.; Volobujeva, O.; Klauson, J.; Mere, A.; Krunks, M., ZnO nanorods via spray deposition of solutions containing zinc chloride and thiocarbamide. *Nanoscale Research Letters* 2007, 2, 391-396.
170. Zhang, J.; Cai, W.; Huang, F.; Wang, E.; Zhong, C.; Liu, S.; Wang, M.; Duan, C.; Yang, T.; Cao, Y., Synthesis of quinoxaline-based donor−acceptor narrow-band-gap polymers

and their cyclized derivatives for bulk-heterojunction polymer solar cell applications. *Macromolecules* 2011, 44, 894-901.
171. Lee, J.-h.; Sagawa, T.; Yoshikawa, S., Morphological and topographical characterizations in spray coated organic solar cells using an additional solvent spray deposition. *Organic Electronics* 2011, 12, 2165-2173.
172. Liu, S.; Zhang, X.; Yin, M.; Feng, H.; Zhang, J.; Zhang, L.; Xie, W., Coffee-ring-free ultrasonic spray coating single-emission layers for white organic light-emitting devices and their energy-transfer mechanism. *ACS Applied Energy Materials* 2018, 1, 103-112.
173. Fukuda, T.; Sato, A., Fluorene bilayer for polymer organic light-emitting diode using efficient ionization method for atomized droplet. *Organic Electronics* 2015, 26, 1-7.
174. Kim, K.; Fang, Y.-K.; Kwon, W.; Pyo, S.; Chen, W.-C.; Ree, M., Tunable electrical memory characteristics of brush copolymers bearing electron donor and acceptor moieties. *Journal of Materials Chemistry C* 2013, 1, 4858-4868.
175. Waters, H.; Kettle, J.; Chang, S.-W.; Su, C.-J.; Wu, W.-R.; Jeng, U. S.; Tsai, Y.-C.; Horie, M., Organic photovoltaics based on a crosslinkable PCPDTBT analogue; synthesis, morphological studies, solar cell performance and enhanced lifetime. *Journal of Materials Chemistry A* 2013, 1, 7370-7378.
176. Kaune, G.; Memesa, M.; Meier, R.; Ruderer, M. A.; Diethert, A.; Roth, S. V.; D'Acunzi, M.; Gutmann, J. S.; Müller-Buschbaum, P., Hierarchically structured titania films prepared by polymer/colloidal templating. *ACS applied materials & interfaces* 2009, 1, 2862-2869.
177. Jurow, M. J.; Hageman, B. A.; DiMasi, E.; Nam, C.-Y.; Pabon, C.; Black, C. T.; Drain, C. M., Controlling morphology and molecular packing of alkane substituted phthalocyanine blend bulk heterojunction solar cells. *Journal of Materials Chemistry A* 2013, 1, 1557-1565.
178. Müller-Buschbaum, P., Grazing incidence small-angle X-ray scattering: an advanced scattering technique for the investigation of nanostructured polymer films. *Analytical and Bioanalytical Chemistry* 2003, 376, 3-10.
179. Müller-Buschbaum, P., The active layer morphology of organic solar cells probed with grazing incidence scattering techniques. *Advanced Materials* 2014, 26, 7692-7709.
180. Kurrle, D.; Pflaum, J., Exciton diffusion length in the organic semiconductor diindenoperylene. *Applied Physics Letters* 2008, 92, 133306.
181. Wang, H.; Wang, H.-Y.; Gao, B.-R.; Wang, L.; Yang, Z.-Y.; Du, X.-B.; Chen, Q.-D.; Song, J.-F.; Sun, H.-B., Exciton diffusion and charge transfer dynamics in nano phase-separated P3HT/PCBM blend films. *Nanoscale* 2011, 3, 2280-2285.
182. Wang, L.; Zhao, D.; Su, Z.; Shen, D., Hybrid polymer/ZnO solar cells sensitized by PbS quantum dots. *Nanoscale Research Letters* 2012, 7, 106.
183. Wahab, H. A.; Salama, A. A.; El-Saeid, A. A.; Nur, O.; Willander, M.; Battisha, I. K., Optical, structural and morphological studies of (ZnO) nano-rod thin films for biosensor applications using sol gel technique. *Results in Physics* 2013, 3, 46-51.
184. Yu, X.; Xiao, K.; Chen, J.; Lavrik, N. V.; Hong, K.; Sumpter, B. G.; Geohegan, D. B., High-performance field-effect transistors based on polystyrene-b-poly(3-hexylthiophene) diblock copolymers. *ACS Nano* 2011, 5, 3559-3567.
185. Gu, Z.; Tan, Y.; Tsuchiya, K.; Shimomura, T.; Ogino, K., Synthesis and characterization of poly(3-hexylthiophene)-b-polystyrene for photovoltaic application. *Polymers* 2011, 3.
186. Zhang, L.; Yin, L.; Wang, C.; lun, N.; Qi, Y.; Xiang, D., Origin of visible photoluminescence of ZnO quantum dots: defect-dependent and size-dependent. *The Journal of Physical Chemistry C* 2010, 114, 9651-9658.
187. Yousefi, R.; Jamali-Sheini, F.; Cheraghizade, M.; Khosravi-Gandomani, S.; Sáaedi, A.; Huang, N. M.; Basirun, W. J.; Azarang, M., Enhanced visible-light photocatalytic

activity of strontium-doped zinc oxide nanoparticles. *Materials Science in Semiconductor Processing* 2015, 32, 152-159.
188. Sofos, M.; Goldberger, J.; Stone, D. A.; Allen, J. E.; Ma, Q.; Herman, D. J.; Tsai, W.-W.; Lauhon, L. J.; Stupp, S. I., A synergistic assembly of nanoscale lamellar photoconductor hybrids. *Nature Materials* 2008, 8, 68.
189. Jia, L.; Zhao, G.; Shi, W.; Coombs, N.; Gourevich, I.; Walker, G. C.; Guerin, G.; Manners, I.; Winnik, M. A., A design strategy for the hierarchical fabrication of colloidal hybrid mesostructures. *Nature Communications* 2014, 5, 3882.
190. Cho, S.; Choi, W., Solid-phase photocatalytic degradation of PVC–TiO_2 polymer composites. *Journal of Photochemistry and Photobiology A: Chemistry* 2001, 143, 221-228.
191. Vendamme, R.; Onoue, S.-Y.; Nakao, A.; Kunitake, T., Robust free-standing nanomembranes of organic/inorganic interpenetrating networks. *Nature Materials* 2006, 5, 494.
192. Song, Q.; Cao, S.; Zavala-Rivera, P.; Ping Lu, L.; Li, W.; Ji, Y.; Al-Muhtaseb, S. A.; Cheetham, A. K.; Sivaniah, E., Photo-oxidative enhancement of polymeric molecular sieve membranes. *Nature Communications* 2013, 4, 1918.
193. Gómez-Romero, P.; Chojak, M.; Cuentas-Gallegos, K.; Asensio, J. A.; Kulesza, P. J.; Casañ-Pastor, N.; Lira-Cantú, M., Hybrid organic–inorganic nanocomposite materials for application in solid state electrochemical supercapacitors. *Electrochemistry Communications* 2003, 5, 149-153.
194. Wang, X.; Kim, K.; Wang, Y.; Stadermann, M.; Noy, A.; Hamza, A. V.; Yang, J.; Sirbuly, D. J., Matrix-assisted energy conversion in nanostructured piezoelectric arrays. *Nano Letters* 2010, 10, 4901-4907.
195. Fahmi, A.; Pietsch, T.; Mendoza, C.; Cheval, N., Functional hybrid materials. *Materials Today* 2009, 12, 44-50.
196. Hoffmann, F.; Cornelius, M.; Morell, J.; Fröba, M., Silica-based mesoporous organic–inorganic hybrid materials. *Angewandte Chemie International Edition* 2006, 45, 3216-3251.
197. Hata, E.; Mitsube, K.; Momose, K.; Tomita, Y., Holographic nanoparticle-polymer composites based on step-growth thiol-ene photopolymerization. *Opt. Mater. Express* 2011, 1, 207-222.
198. Sanchez, C.; Julian, B.; Belleville, P.; Popall, M., Applications of hybrid organic-inorganic nanocomposites. *Journal of Materials Chemistry* 2005, 15, 3559-3592.
199. Wright, M.; Uddin, A., Organic-inorganic hybrid solar cells: A comparative review. *Solar Energy Materials and Solar Cells* 2012, 107, 87-111.
200. Huynh, W. U.; Dittmer, J. J.; Alivisatos, A. P., Hybrid nanorod-polymer solar cells. *Science* 2002, 295, 2425.
201. Liu, Z.; Sun, Y.; Yuan, J.; Wei, H.; Huang, X.; Han, L.; Wang, W.; Wang, H.; Ma, W., High-efficiency hybrid solar cells based on polymer/PbS_xSe_{1-x} nanocrystals benefiting from vertical phase segregation. *Advanced Materials* 2013, 25, 5772-5778.
202. Sun, B.; Snaith, H. J.; Dhoot, A. S.; Westenhoff, S.; Greenham, N. C., Vertically segregated hybrid blends for photovoltaic devices with improved efficiency. *Journal of Applied Physics* 2004, 97, 014914.
203. Lin, Y.; Wei, Q.; Qian, G.; Yao, L.; Watkins, J. J., Morphology control in TiO_2 nanorod/polythiophene composites for bulk heterojunction solar cells using hydrogen bonding. *Macromolecules* 2012, 45, 8665-8673.
204. Moshonov, M.; Frey, G. L., Directing hybrid structures by combining self-assembly of functional block copolymers and atomic layer deposition: a demonstration on hybrid photovoltaics. *Langmuir* 2015, 31, 12762-12769.

205. Razza, S.; Castro-Hermosa, S.; Di Carlo, A.; Brown, T. M., Large-area deposition, coating, printing, and processing techniques for the upscaling of perovskite solar cell technology. *APL Materials* 2016, 4, 091508.
206. Kun Wang, N. H., Lucas P. Kreuzer, Tobias Widmann, Jean-Francois Moulin, Martin Haese , Peter Müller-Buschbaum, Morphology tuning of ZnO/P3HT/P3HT-b-PEO hybrid films via spray and spin coating. to be submitted.
207. Das, S.; Yang, B.; Gu, G.; Joshi, P. C.; Ivanov, I. N.; Rouleau, C. M.; Aytug, T.; Geohegan, D. B.; Xiao, K., High-performance flexible perovskite solar cells by using a combination of ultrasonic spray-coating and low thermal budget photonic curing. *ACS Photonics* 2015, 2, 680-686.
208. Deegan, R. D.; Bakajin, O.; Dupont, T. F.; Huber, G.; Nagel, S. R.; Witten, T. A., Capillary flow as the cause of ring stains from dried liquid drops. *Nature* 1997, 389, 827.
209. Müller-Buschbaum, P.; Kaune, G.; Haese-Seiller, M.; Moulin, J. F., Morphology determination of defect-rich diblock copolymer films with time-of-flight grazing-incidence small-angle neutron scattering. *Journal of Applied Crystallography* 2014, 47, 1228-1237.
210. Müller-Buschbaum, P.; Metwalli, E.; Moulin, J. F.; Kudryashov, V.; Haese-Seiller, M.; Kampmann, R., Time of flight grazing incidence small angle neutron scattering. *The European Physical Journal Special Topics* 2009, 167, 107-112.
211. Salditt, T.; Brotons, G., Biomolecular and amphiphilic films probed by surface sensitive X-ray and neutron scattering. *Analytical and Bioanalytical Chemistry* 2004, 379, 960-973.

List of publications

Publications related to the dissertation

- K. Wang, V. Körstgens, D. Yang, N. Hohn, S. Roth, P. Müller-Buschbaum, "Morphology control of low temperature fabricated ZnO nanostructures for transparent active layers in all solid-state dye-sensitized solar cells", J. Mater. Chem. A 6 (2018), 4405.
- K. Wang, L. Bießmann, M. Schwartzkopf, S. V. Roth, P. Müller-Buschbaum, "Tuning of the morphology and optoelectronic properties of ZnO/P3HT/P3HT-b-PEO hybrid films via spray deposition method", ACS Appl. Mater. Interfaces 10 (2018), 20569.
- K. Wang, S. Xia, W. Cao, N. Hohn, S. Grott, L. P. Kreuzer, M. Schwartzkopf, S. V. Roth, P. Müller-Buschbaum, "Comparison of UV Irradiation and Sintering on Mesoporous Spongelike ZnO Films Prepared from PS-b-P4VP Templated Sol-Gel Synthesis", ACS Appl. Nano Mater. 1 (2018), 7139.
- K. Wang, N. Hohn, L. P. Kreuzer, T. Widmann, J.-F. Moulin, P. Müller-Buschbaum, "Morphology tuning of ZnO/P3HT/P3HT-b-PEO hybrid films via spray and spin-coating", to be submitted.

Further publications

- Y. Tong, M. Fu, E. Bladt, H. Huang, A. F. Richter, K. Wang, P. Müller-Buschbaum, S. Bals, P. Tamarat, B. Lounis, J. Feldmann, L. Polavarapu, "Chemical cutting of perovskite nanowires into single-photon emissive low-aspect ratio $CsPbX_3$ (X= Cl, Br & I) nanorods" Angew. Chem. Int. Ed. 130 (2018), 16326.
- Y. Tong, E.-P. Yao, A. Manzi, E. Bladt, K. Wang, M. Döblinger, S. Bals, P. Müller-Buschbaum, A. Urban, L. Polavarapu, J. Feldmann, "Spontaneous self-assembly of perovskite nanocrystals into electronically coupled supercrystals: toward filling the green gap" Adv. Mater. 30 (2018), 1801117.
- B. Bohn, Y. Tong, M. Gramlich, M. Lai, M. Döblinger, K. Wang, R. Hoye, P. Müller-Buschbaum, S. Stranks, A. Urban, L. Polavarapu, J. Feldmann, "Boosting tunable blue luminescence of halide perovskite nanoplatelets through post-synthetic surface trap repair" Nano Lett. 18 (2018), 5231.
- N. Hohn, S. J Schlosser, L. Bießmann, S. Grott, S. Xia, K. Wang, M. Schwartzkopf, S. V Roth, P. Müller-Buschbaum, "Readily available titania nanostructuring routines

based on mobility and polarity controlled phase separation of an amphiphilic diblock copolymer" Nanoscale 10 (2018), 5325.

- R. Wang, Y. Tong, A. Manzi, K. Wang, Z. Fu, E. Kentzinger, J. Feldmann, A. S. Urban, P. Müller-Buschbaum, H. Frielinghau, "Preferential orientation of crystals induced by incorporation of organic ligands in mixed-dimensional hybrid perovskite films" Adv. Opt. Mater. 6 (2018), 1701311.
- N. Hohn, S. J. Schlosser, L. Bießmann, L. Song, S. Grott, S. Xia, K. Wang, M. Schwartzkopf, S. V. Roth, P. Müller-Buschbaum, "Impact of catalytic additive on spray deposited and nanoporous titania thin films observed via in situ x-ray scattering: implications for enhanced photovoltaics" ACS Appl. Nano Mater. 1 (2018), 4227.
- Y. Tong, B. Bohn, E. Bladt, K. Wang, P. Müller-Buschbaum, S. Bals, A. S. Urban, L. Polavarapu, J. Feldmann, "From precursor powders to $CsPbX_3$ perovskite nanowires: one-pot synthesis, growth mechanism and oriented self-assembly", Angew. Chem. Int. Ed. 56 (2017), 13887.

Scientific reports

- K. Wang, P. Müller-Buschbaum, "Comparison of UV-Irradiation and Sintering on Mesoporous Sponge-like ZnO Films", Lehrstuhl für Funktionelle Materialien, Annual Report, 2018.
- K. Wang, V. Körstgens, D. Yang, N. Hohn, P. Müller-Buschbaum, "Low temperature fabricated ZnO films for solid-state dye-sensitized solar cells", Lehrstuhl für Funktionelle Materialien, Annual Report, 2017.
- K. Wang, V. Körstgens, L. Bießmann, D. Yang, N. Hohn, P. Müller-Buschbaum, "Nanostructured zinc oxide films for application in hybrid photovoltaics", Lehrstuhl für Funktionelle Materialien, Annual Report, 2016.
- K. Wang, N. Hohn, L. Kreuzer, T. Widmann, M. Haese-Seiller, J.-F. Moulin, P. Müller-Buschbaum, "Block copolymer based hybrid nanostructures for application in solar cells", Heinz Maier-Leibnitz Zentrum, 2016.
- K. Wang, L. Song, P. Müller-Buschbaum, "Nanostructured zinc oxide films for application in hybrid photovoltaics", Lehrstuhl für Funktionelle Materialien, Annual Report, 2015.

Conference talks

- K. Wang, N. Saxena, K. Wienhold, "X-ray reflectivity and neutron reflectivity", E13 Polymer Physics Summer School, Obertauern, Austria. June 2018.

- K. Wang, "Morphology control of zinc oxide nanostructures for application in hybrid solar cells", Lehrstuhl für Funktionelle Materialien, Seminar Talk, Garching, Germany. May 2018.
- K. Wang, V. Körstgens, D. Yang, N. Hohn, S. V. Roth, P. Müller-Buschbaum, "Morphology control of low temperature fabricated ZnO nanostructures for transparent all solid-state dye-sensitized solar cells", DPG-Frühjahrstagung, Berlin, Germany. March 2018.
- K. Wang, Y. Tong, L. Bießmann, S. V. Roth, P. Müller-Buschbaum, "Morphology improvement of ZnO/P3HT-b-PEO bulk heterojunction films using a low temperature route", 3rd internal biennial science meeting of the MLZ, Grainau, Germany. June 2017.
- K. Wang, "Morphology tailoring of ZnO nanostructures for solid-state dye-sensitized solar cells", Lehrstuhl für Funktionelle Materialien, Seminar Talk, Garching, Germany. June 2017.
- K. Wang, L. Bießmann, N. Saxena, "Conducting polymers", E13 Polymer Physics Summer School, Obertauern, Austria. June 2016.
- K. Wang, "Diblock copolymer templated low temperature synthesized ZnO thin films for hybrid solar cells", Lehrstuhl für Funktionelle Materialien, Seminar Talk, Garching, Germany. June 2016.

Conference poster presentations

- K. Wang, L. Bießmann, S. V. Stephan, P. Müller-Buschbaum, "Morphology control of low temperature synthesized ZnO/P3HT-b-PEO films via spray deposition", German Conference for research with Synchrotron Radiation, Neutrons and Ion Beams at large Facilities, Garching, Germany. September 2018.
- K. Wang, Y. Tong, L. Bießmann, S. V. Stephan, P. Müller-Buschbaum, "Morphology modification of ZnO/P3HT hybrid films via P3HT-b-PEO films", DPG-Frühjahrstagung, Dresden, Germany. March 2017.
- K. Wang, Y. Tong, L. Bießmann, S. V. Stephan, P. Müller-Buschbaum, "Morphology control of ZnO/P3HT/P3HT-b-PEO films via spray deposition", 6th SolTech Conference: Solar Technologies go Hybrid, Munich, Germany. October 2017.
- K. Wang, Y. Tong, L. Song, L. Bießmann, S. Xia, J. Schlipf, C. J. Schaffer, P. Müller-Buschbaum, "Nanostructured zinc oxide films for application in hybrid photovoltaics", DPG-Frühjahrstagung, Regensburg, Germany. March 2016.
- K. Wang, L. Song, L. Bießmann, S. Xia, J. Schlipf, C. J. Schaffer, P. Müller-

Buschbaum, “Zinc oxide nanostructures for application in hybrid bulk heterojunction solar cells”, GISAS summer school: experiments and analysis, Garching, Germany. July 2016.

Acknowledgments

First of all, I really want to thank Prof. Dr. Peter Müller-Buschbaum for giving me the opportunity to work in E13 of physics department in Technische Universität München. Many thanks to him for providing me the nice topic related to the functional materials applied in photovoltaics, for offering the chances to work with advanced equipments and for applying for the treasurable beamtime opportunities for me. Moreover, he often encourages me to attend international conferences. He is very supportive in scientific research and always try his best to help me. He is always there to discuss with me, give me suggestions and help me to improve myself. Especially, many thanks to him for recommending me to continue my scientific work. Many thanks to him for helping with my postdoc application.

Moreover, I would like to thank my collaborators during my PhD study. I am sincerely grateful to Prof. Dr. Jochen Feldmann and Dr. Lakshminarayana Polavarapu in Ludwig-Maximilians-Universität München (LMU) for providing us a good cooperation. Many thanks to Dr. Yu Tong in their group for the nice measurements of SEM and optical spectroscopy and thanks for the helpful discussions for my PhD work. I am grateful to Prof. Dr. Alexander Holleitner and Peter Weiser in WSI for the access to AFM measurements.

I would like to thank the beamline scientists in both DESY, Hamburg, and MLZ, Garching. They supported me to learn and practice a lot to gain the knowledge and experience of the X-ray and neutron scattering technique. I want to thank the people who were involved in no specific order: Prof. Dr. Stephan V. Roth, Dr. Matthias Schwartzkopf, Dr. Jean-Francois Moulin. Moreover, I cannot accomplish my measurements at beamline successfully without the help of my colleagues in E13. Therefore I really want to thank Volker Körstgens, Lorenz Bießmann, Nuri Hohn, Dan Yang, Senlin Xia, Sebastian Grott, Lucas P. Kreuzer and Tobias Widmann for their kind help and nice discussion and wonderful time spent with them. Especially thanks to Volker Körstgens and Lorenz Bießmann, who show me how to do the GISAXS and GIWAXS measurement at DESY in Hamburg.

I am thankful to the contributions from my colleagues in E13. I would like to thank Prof. Dr. Christine Papadakis for recommending me in my postdoc position application. She is so nice and warm-hearted to help me with the application. I also want to thank Wei Cao and Dr. Rui Wang for showing me how to measure the AFM. Many thanks to Dr. Ezzeldin Metwalli Ali, Dr. Lin Song, Senlin Xia and Johannes Schlipf for helping me with the GISAXS, GIWAXS and XRD measurements in E13 group. Also, I would like to thank Lucas P. Kreuzer for the

FTIR measurement, Simon Jakob Schaper for helping to setup the EIS equipment. Special thanks to Dr. Lin Song for nice discussions for my papers, showing me how to fabricate ssDSSCs and helping to solve the problems I came across.

I am sincerely grateful to Nitin Saxena, Lorenz Bießmann, Simon Jakob Schaper, Wei Chen, Lucas P. Kreuzer, Tobias Widmann, Volker Körstgens, Shaleahk Wilson and Senlin Xia for improving my thesis. Especially thank Simon Jakob Schaper and Nitin Saxena for helping me with translation of my abstract from English to German.

During my PhD study, I really appreciate the nice atmosphere in our group. I am quite grateful to my kind colleagues. In no specific order, I want to thank the colleagues not mentioned yet: Dr. Eva M. Herzig, Dr. Weijia Wang, Dr. Bo Su, Dr. Daniel Moseguí González, Dr. Xiaohan Zhang, Franziska Löhrer, Nian Li, Xinyu Jiang, Shanshan Yin, Shambhavi Pratap, Kerstin Wienhold, Julian Heger, Lennart Reb and so on. They are so kind, warm-hearted, diligent and knowledgeable. I really appreciate the wonderful time with them.

Besides, I want to thank the China Scholarship Council (CSC) for funding my Ph.D. study. My PhD work was supported by fundings from TUM.solar in the context of the Bavarian Collaborative Research Project “Solar Technologies Go Hybrid” (SolTech), International Research Training Groups 2022 Alberta/Technical University of Munich International Graduate School for Environmentally Responsible Functional Hybrid Materials (ATUMS) and the Nanosystems Initiative Munich (NIM). Many thanks for their financial support.

Last but not least, I quite appreciate the contributions of my family and friends. They are always there to encourage me when I am down and also share their happiness with me. Their passion, patience, trust always motivate me to improve myself in both scientific work and everyday life. During my PhD study, I particularly want to thank my husband Dr. Yu Tong, who gave me a lot of helpful suggestions and accompanied me to live a wonderful life in Germany.